Measurement of electroweak parameters in the Z boson decays into tau leptons and Detector tests for the upgrade of the CMS tracker for the High Luminosity LHC

Clément Grimault

Université de Strasbourg

UNIVERSITÉ DE STRASBOURG

ECOLE DOCTORALE pcp

ÉCOLE DOCTORALE N° 182 : PHYSIQUE ET CHIMIE PHYSIQUE

Institut Pluridisciplinaire Hubert Curien (IPHC), UMR 7178

THÈSE

présentée et soutenue publiquement par :

Clément GRIMAULT

le 31 août 2022

pour obtenir le grade de : **Docteur de l'Université de Strasbourg**

Discipline/Spécialité : Physique des particules

Mesure de paramètres électrofaibles dans les désintégrations du boson Z en leptons tau et tests de détecteurs pour la jouvence du trajectographe de CMS pour le LHC à haute luminosité

Measurement of electroweak parameters in the Z boson decays into tau leptons and Detector tests for the upgrade of the CMS tracker for the High Luminosity LHC

THÈSE dirigée par :

M. Ulrich GOERLACH	Professeur, Institut Pluridisciplinaire Hubert Curien (IPHC)

RAPPORTEUR.EUSE.S :

Mme Lucia DI CIACCIO	Professeure, Laboratoire d'Annecy de Physique des Particules (LAPP)
M. Roberto SALERNO	Chargé de recherches, Laboratoire Leprince-Ringuet (LLR)

AUTRES MEMBRES DU JURY :

M. Jérôme BAUDOT	Professeur, Institut Pluridisciplinaire Hubert Curien (IPHC)
Mme Caroline COLLARD	Directrice de recherches, Institut Pluridisciplinaire Hubert Curien (IPHC)
Mme Irena NIKOLIC	Maître de conférences, Laboratoire de Physique Nucléaire et de Hautes Énergies (LPNHE)

Remerciements

Je suis heureux de présenter ce manuscrit qui signe la fin de mes études en physique des particules, une aventure qui, certes, m'a demandé de sacrifier de nombreuses heures de sommeil et a certainement contribué à quelques cheveux blancs, mais qui s'est avérée être incroyablement enrichissante.

Bien que cela puisse sembler un cliché, je souhaite avant tout exprimer ma profonde reconnaissance envers les enseignants qui ont su me transmettre leur passion pour la physique. Je ne considère pas mon parcours académique comme une simple progression linéaire vers l'obtention d'une thèse. Au contraire, il a été marqué par une série de doutes et de remises en question, que j'ai pu surmonter grâce à des rencontres décisives qui ont contribué à me guider vers la physique des particules. J'en profite alors pour exprimer ma gratitude envers Patrice Sautejeau, mon professeur de physique-chimie au lycée, qui a su renforcer ma passion pour la physique. De même, je remercie chaleureusement Julien Masbou, tuteur de stage et enseignant durant mes années de Master, qui m'a encouragé à poursuivre dans la voie de la recherche et à entreprendre une thèse.

Je souhaite aussi exprimer ma reconnaissance envers les membres du jury pour avoir pris le temps de lire ce manuscrit avec attention et pour m'avoir fait part de leurs remarques constructives.

Enfin, la réussite de cette thèse a été rendue possible grâce à l'implication de mon directeur de thèse, Ulrich. Grâce à lui j'ai pu réaliser une thèse qui m'a permis de combiner deux aspects de la physique des particules: l'analyse de données pour mesurer un paramètre physique, et une partie instrumentale avec la manipulation d'instruments de détection. J'ai été heureux de pouvoir explorer ces deux domaines. Ulrich a toujours été disponible pour moi, y compris en s'adaptant parfois aux horaires de travail "atypiques" d'un doctorant (dimanche et tard dans la nuit!). Tu a toujours pris le temps de discuter avec moi et de m'expliquer certains concepts physiques en t'assurant que je les avais (réellement) compris. Bien sûr tout n'a pas été parfait dans notre collaboration, mais j'ai particulièrement apprécié l'équilibre que nous avons su trouver entre la confiance que tu m'as accordée pour avancer et fournir certains résultats et l'attention et la rigueur que tu portais aux détails pour toujours améliorer la qualité des résultats.

Je tiens également à exprimer ma profonde gratitude envers Daniel et Anne-Catherine, qui ont été successivement responsables du groupe CMS de l'IPHC. Leur bienveillance envers l'ensemble du groupe était remarquable et j'ai été particulièrement touché par le temps qu'Anne-Catherine a consacré à m'aider dans la rédaction de ma thèse.

Au cours de ma thèse, j'ai eu la chance de participer à de nombreuses campagnes de test faisceaux à l'IPHC, qui ont été des moments particulièrement marquants. Je suis très reconnaissant envers mes collègues, les deux Laurent, Christian, Caroline et Jérémy, avec qui j'ai partagé ces expériences, et dont l'implication et l'enthousiasme ont rendu ces moments encore plus mémorables (notamment notre combat commun contre la FEROL!). Merci beaucoup à Caroline et Jérémy pour la confiance qu'ils m'ont accordée en m'impliquant autant que possible dans l'évolution du projet. Je remercie également les opérateurs du cyclotron, Michel, Jacky et Clément, pour leur précieuse collaboration et leur bonne humeur tout au long de ces journées intensives. J'aimerais aussi exprimer ma gratitude à Danek, Nikkie et Sarah, membres de la collaboration CMS, pour leur contribution essentielle à la réussite de ces tests.

Je voudrais également remercier Éric Chabert, avec qui je prenais plaisir à discuter, notamment de notions assez avancées de mon analyse. Seul petit hic, c'est que ses idées et explications étaient si riches que la discussion pouvait parfois se prolonger jusqu'à tard dans l'après-midi! Guillaume, Dylan et moi partagions le même avis pour les futures générations de doctorants: dès que tu franchis la porte du bureau, il faudrait activer un chronomètre!

Enfin, je souhaiterais exprimer ma gratitude envers le post-doctorant Thomas Müller qui supervisait auparavant l'analyse et avec qui j'ai eu la chance de travailler au début de ma thèse. Sa rigueur et son professionnalisme ont été des éléments clés de la réussite de l'analyse.

Avec la crise du COVID-19, la thèse a pris parfois des tournures plus solitaires, notamment lors des confinements où les interactions avec les autres se limitaient à des visioconférences. Les moments de partage entre doctorants avaient alors une importance particulière, et je garde un excellent souvenir de nos pauses déjeuner passées au BDD, en compagnie de Robin, Mario, Lucas et tant d'autres, autour d'un jeu de carte ou d'un jeu de société. Et qui dit jeux de société, dit forcément Dylan! Je tiens à le remercier de nous avoir partagé sa passion et organisé de nombreuses soirées où nous nous servions des derniers neurones encore en état après une journée de travail pour jouer à des jeux experts pendant des heures. Dommage que tu oubliais souvent de nous expliquer une règle qui t'avantageait à la fin de la partie, mais bon on va dire que tu méritais ce privilège pour l'organisation des soirées (je suis mauvais joueur). Et enfin une forte pensée à notre groupe d'amis *AfterGlow* qui s'est formé pendant cette période. On a vécu tellement de bons moments ensemble lors de vancances improvisées au chalet ou en camping. Premièrement, Guillaume, doctorant avec qui j'ai partagé un bureau pendant

près de trois ans. En plus d'être un complice fidèle ne ratant jamais une occasion de partager un café (ou autre boisson alcoolisée à base de plantes), j'ai toujours apprécié sa franchise et nos discussions décalées me manqueront. Julie et Loris, qui sont pour moi indissociables, toujours prêts à nous concocter une playlist très orientée variété française (et on est reparti pour une chenille!). Douja, véritable source d'énergie positive, qui a toujours su partager sa bonne humeur et nous motiver à sortir de notre routine et explorer les restaurants et (surtout) les bars de la ville. Dommage qu'on n'ait pas partagé ce bureau, mais je suis content de te savoir épanouie dans le Sud. Et Alex, cet ami que j'ai rencontré deux ans auparavant à Nantes et retrouvé en doctorat à Strasbourg. Pendant ma thèse, j'ai pu profité des nombreux rôles qu'il a assumés: expert en C++, barista, mixologiste, coach d'escalade (promis, un jour, je pousserai sur mes jambes), mais surtout ami fidèle!

J'aimerais également en profiter pour exprimer toute ma reconnaissance et mon amour envers Marie-Pascale, qui m'a accompagné tout au long de cette expérience. Bien que j'aie dû te convaincre que l'essentiel de mon travail ne se résumait pas à aligner des points noirs sur une courbe rouge (les habitué.e.s du logiciel ROOT comprendront), ta présence à mes côtés a été précieuse et m'a apporté beaucoup de réconfort.

Enfin, je tiens à remercier mes parents et ma sœur, Emma, pour leur soutien inestimable tout au long de mes études, ainsi que leur leur intérêt pour mes sujets d'étude (je n'oublie pas les post-it "matière noire", "CMS", etc. qui traînaient dans la maison). Sans eux, je n'aurais jamais pu accomplir tout ce chemin.

Synthèse de la mesure de la polarisation des leptons taus

Une mesure de la polarisation moyenne des leptons taus $\mathcal{P}_\tau$ est présentée dans cette thèse en utilisant des événements $Z \to \tau\tau$ avec $\sqrt{\hat{s}}$ proche de la masse du boson Z. Les données de collision proton-proton utilisées ont été collectées avec le détecteur CMS en 2016 à une énergie dans le centre de masse de 13 TeV correspondant à une luminosité intégrée de 36,3 fb^{-1}. La mesure est réalisée en utilisant tous les modes de désintégration du lepton tau identifiables avec le détecteur CMS. Des mesures de la polarisation des leptons taus ont été réalisées précédemment auprès du LEP à des énergies dans le centre de masse proche de la masse du boson Z [1–4], et dans l'expérience ATLAS au LHC à $\sqrt{s} = 8$ TeV [5].

La reconstruction des objets s'appuie sur l'algorithme *particle flow* (`PF`) [6] combinant les données des différents sous-détecteurs pour reconstruire muons, électrons et hadrons chargés ou neutres. Ces éléments sont ensuite assemblés pour définir des objets plus complexes, tels que les candidats potentiels d'une désintégration hadronique d'un lepton tau τ_h.

L'identification des modes de désintégration du lepton tau est réalisée grâce à l'algorithme *Hadron-Plus-Strips* (HPS) [7]. Cet outil, optimisé pour reconstruire les modes de désintégration individuels du lepton tau, tire parti de la haute performance de l'algorithme du *particle flow*.

Les gerbes de particules, ou *jets*, sont reconstruites à partir des constituants du *particle flow* en utilisant l'algorithme anti-k_T avec un paramètre de distance R=0,4 . Ces gerbes sont identifiées comme des candidats τ_h si elles contiennent un ou trois hadrons chargés avec une charge totale de $\pm 1e$, et jusqu'à 2 pions neutres. Une importance est accordée aux photons issus de la désintégration du pion neutre $\pi^0 \to \gamma\gamma$, se convertissant principalement en paires électron-positon e^+e^-, en regroupant l'énergie des photons et des électrons dans une bande (*strip*), définie par la pseudorapidité η et l'angle azimuthal ϕ autour de la direction de la gerbe. La taille de la bande est ajustée dynamiquement pour tenir compte des électrons de faible impulsion transverse p_T et des photons pro-

duits par des interactions avec le trajectographe ou par des rayonnements de freinage (*bremsstrahlung*). Ces bandes sont censées représenter les produits de désintégration des pions neutres. En considérant le nombre de bandes reconstruites et les particules chargées, les modes de désintégration du tau suivants sont reconstruits :

- $\tau^- \to \pi^-\nu$: une particule chargée sans aucune bande,
- $\tau^- \to \rho^-\nu \to \pi^-\pi^0\nu$: une particule chargée avec une bande (compatible avec une résonance ρ),
- $\tau^- \to a_1^-\nu \to \pi^-\pi^+\pi^-\nu$: trois particules chargées sans aucune bande (compatible avec une résonance a_1).

Dans cette étude, étant donné que les modes de désintégration du lepton tau présentent des sensibilités variables à la polarisation, une identification précise de ces canaux est cruciale. Pour améliorer la pureté des modes de désintégration identifiés, une analyse multivariée (`MVA-DM`) a été superposée à l'algorithme `HPS`. Cet algorithme a été conçu initialement pour l'analyse CP du Higgs, face à un enjeu similaire de diminution de la sensibilité CP due aux migrations entre les modes reconstruits.

L'algorithme `HPS` éprouve des difficultés à différencier efficacement deux pions neutres et un seul. Les dépôts individuels des pions neutres dans le calorimètre électromagnétique sont souvent trop proches pour être distingués clairement, conduisant à leur regroupement en une seule bande par l'algorithme `HPS`.

Cette limitation entraîne une importante contamination de 32,8% dans le mode de désintégration $\tau^- \to \pi^-\pi^0\nu$ reconstruit par des événements $\tau^- \to \pi^-2\pi^0\nu$, qui a été diminuée à 19,6% grâce à l'algorithme `MVA-DM`. Les autres contaminations importantes sont : les événements $\tau^- \to \pi^-\pi^0\nu$ reconstruits comme $\tau^- \to \pi^-\nu$ et les événements $\tau^- \to 3\pi^\pm\pi^0\nu$ comme $\tau^- \to 3\pi^\pm\nu$, avec des contaminations dans le mode de désintégration d'intérêt respectivement de 29,7% et de 12,5%, améliorées à 16,5% et 9,3% respectivement.

Les états finaux $\tau\tau$ sont classifiés selon le nombre d'électrons et de muons identifiés dans l'événement. Les événements avec un muon et un électron sont catégorisés comme $\tau_e\tau_\mu$. Si un muon et un candidat τ_h sont détectés sans électron, l'événement est classé comme $\tau_\mu\tau_\mathrm{h}$. De même s'il contient un électron sans muon, il est classé comme $\tau_e\tau_\mathrm{h}$. En l'absence d'électron et de muon, mais avec deux candidats τ_h, l'événement est classé comme $\tau_\mathrm{h}\tau_\mathrm{h}$. Quatre états finaux différents étant considérés, il est essentiel de garantir que chaque événements soit sélectionné dans un seul de ces états. Ceci est réalisé en imposant des critères de veto sur les événements avec un lepton supplémentaire ou une paire de di-lepton lors de la dernière étape de sélection des paires pour les quatre canaux d'états finaux. Seuls les états finaux di-τ présentant une masse visible entre 40 et 85 GeV sont sélectionnés afin d'isoler efficacement les désintégrations du boson Z.

Face à une incohérence dans le traitement de l'hélicité du τ entre le générateur MadGraph5 et les désintégrations du lepton tau assurées par Pythia8 dans les simulations officielles de la collaboration CMS, une simulation spécifique a été nécessaire pour le signal Drell-Yan.

Le bruit de fond principal provient des événements *multijet* où un des *jets* est incorrectement identifié comme un candidat τ_{h}, représentant environ 84%, 20% et 16% du bruit de fond attendu respectivement dans les canaux $\tau_{\mathrm{h}}\tau_{\mathrm{h}}$, $\tau_\mu\tau_{\mathrm{h}}$ et $\tau_e\tau_{\mathrm{h}}$. Les événements Drell-Yan peuvent contribuer si un lepton est identifé comme un τ_{h} ou si un *jet* supplémentaire est mal identifié. Ces contributions sont limitées en excluant les événements avec des di-leptons de même saveur et de charges opposées, ainsi qu'en appliquant des discriminants anti-électron et anti-muon aux candidats τ_{h}. Si les échantillons de contrôle des données sont utilisées pour évaluer le bruit de fond *multijet*, d'autres contributions comme $\mathrm{t\bar{t}}$ et les processus électrofaibles s'appuient sur la simulation. Le bruit de fond W+jets est notable dans les états finaux $\tau_\mu\tau_{\mathrm{h}}$ et $\tau_e\tau_{\mathrm{h}}$, représentant respectivement environ 31% et 27% du bruit de fond attendu, et est évalué à partir des données.

Le spin du lepton τ est converti en moment angulaire de ses produits de désintégration, influençant ainsi leurs distributions angulaires relatives et par rapport à la direction de vol du lepton tau. Un angle clé est l'angle θ, défini entre la direction de vol du lepton tau et la direction du hadron (ou du lepton lors d'une désintégration leptonique du lepton tau), observé dans le référentiel propre du lepton tau. En examinant la désintégration $\tau^- \to \pi^-\nu$, il n'y a pas de moment angulaire dans la désintégration à deux corps du τ, et étant donné que le pion n'a pas de spin, la conservation du moment angulaire impose au neutrino d'adopter le spin du lepton τ. Comme l'hélicité du neutrino est toujours gauche, le π^- est principalement émis dans la direction du spin du lepton τ. Ainsi pour un lepton τ avec une hélicité droite, le pion est préférentiellement émis dans la direction de vol du lepton τ. Dans le référentiel propre du lepton τ, le neutrino et le pion sont émis dos à dos. Par conséquent, lors de la désintégration d'un tau avec une hélicité droite, l'angle θ privilégie de petites valeurs, et de grandes valeurs si le lepton τ est d'hélicité gauche. Dans le cas de $\tau^- \to \pi^-\nu$, l'angle θ détient toute l'information sur le spin du lepton tau.

La désintégration en une résonance V de spin 1, ρ ou a_1, présente la simplicité cinématique d'une désintégration à deux corps, similaire à $\tau^- \to \pi^-\nu$. Cependant, elle possède une dynamique plus complexe puisque les résonances ρ et a_1 peuvent avoir des états de spin longitudinaux et transversaux. La conservation du moment angulaire permet aux résonances ρ et a_1 d'avoir des hélicités $\lambda_{\mathrm{V}} = 0$ ou -1. Par conséquent, la sensibilité à l'hélicité du lepton τ dans la désintégration $\tau \to V\nu$ (V = ρ ou a_1) est nettement réduite si seul l'angle θ est analysé. La perte de sensibilité peut être compensée si l'état d'hélicité de la résonance V est déterminé. Le spin de V est converti en moment angulaire total des produits de désintégration, et peut donc être retrouvé en analysant la distribution angulaire des produits de désintégration de V. Deux angles supplémentaires sont définis dans la désintégration $\tau^- \to \rho^-\nu \to \pi^-\pi^0\nu$: l'angle β, représentant l'angle

entre la direction du pion chargé et celle du ρ observé dans le référentiel propre du ρ, et l'angle α. Lors de l'étude de la désintégration $\tau^- \to a_1^-\nu$, trois angles s'ajoutent à l'angle θ. Ces trois angles sont décrits dans le référentiel propre du a_1. La procédure d'intégration de ces angles en une unique variable, nommée ω, est décrite dans cette étude.

Les hélicités des deux leptons τ dans la désintégration $Z \to \tau^-\tau^+$ sont anti-corrélées à 100% dans la limite ultra-relativiste. Ainsi, la séparation des états d'hélicité et, par conséquent, la sensibilité à la mesure de la polarisation peuvent être améliorées en exploitant cette corrélation. La méthode proposée dans Réf. [8] consiste à définir une nouvelle observable optimale en utilisant les deux leptons taus dans la désintégration. En désignant ω_1 et ω_2 comme les observables respectives pour τ^- et τ^+, on peut définir:

$$\Omega = \frac{\omega_1 + \omega_2}{1 + \omega_1\omega_2} \quad .$$

Il convient de souligner que la reconstruction de l'observable optimale ω nécessite la connaissance du référentiel propre du lepton τ (des deux leptons τ pour Ω), ce qui n'est généralement pas une tâche aisée. Lorsque la direction de vol des leptons τ ne peut être mesurée, l'algorithme `SVfit` [9] est utilisé dans cette analyse pour reconstruire la désintégration du lepton τ. Étant donné que ses performances sont limitées dans certaines catégories d'événements, une meilleure sensibilité est obtenue à partir d'observables mesurées directement dans le détecteur, comme l'angle β dans les désintégrations ρ.

La polarisation moyenne du lepton τ, notée $\langle \mathcal{P}_\tau \rangle$, est définie comme suit:

$$\langle P_\tau \rangle = \frac{N(Z \to \tau_R^-\tau_L^+) - N(Z \to \tau_L^-\tau_R^+)}{N(Z \to \tau_R^-\tau_L^+) + N(Z \to \tau_L^-\tau_R^+)} \quad ,$$

où $N(Z \to \tau_R^-\tau_L^+)$ et $N(Z \to \tau_L^-\tau_R^+)$ sont respectivement les nombres d'événements avec un lepton τ^- d'hélicité positive et d'hélicité négative dans l'échantillon de données. Le générateur Monte-Carlo MadGraph5 est employé pour générer les événements $Z \to \tau\tau$. Ces événements sont entièrement simulés dans le détecteur CMS et reconstruits avec le même logiciel que celui utilisé pour les données. Ensuite, les critères de déclenchement (*trigger*), d'identification du lepton τ et de sélection d'événements sont appliqués. Les événements répondant à ces critères sont divisés en deux échantillons d'événements, soit $N_{\text{reco}}(Z \to \tau_R^-\tau_L^+)$ soit $N_{\text{reco}}(Z \to \tau_L^-\tau_R^+)$, en utilisant l'information d'hélicité au niveau du générateur.

La polarisation moyenne au niveau du générateur dépend fortement de l'intervalle de masse sur lequel la moyenne est calculée. Une fenêtre de masse de 75 à 120 GeV est choisie en se basant sur les critères de maximisation de la section efficace tout en conservant une valeur de polarisation moyenne proche de celle au pôle (*tree-level*) du boson Z. Ce dernier point est crucial pour l'extraction de la polarisation et son interprétation en termes d'angle de mélange électrofaible effectif. Pour créer des modèles correspondant à une polarisation nulle dans les événements $Z \to \tau\tau$ dans les données, l'échantillon

Monte-Carlo a été dépolarisé en pondérant les événements pour atteindre une polarisation moyenne au niveau générateur nulle. Ainsi, la différence d'efficacité de sélection entre les échantillons de différentes hélicités et modes de désintégration est prise en compte dans la mesure de la polarisation.

La polarisation moyenne du lepton τ est déduite des données à partir d'un ajustement des distributions des observables optimales en utilisant des modèles pour le signal et le bruit de fond.

$$\mathcal{T}(\text{data}) \overset{\text{ajustement}}{=} \mathcal{T}(\text{signal}, \langle P_\tau \rangle, r) + \mathcal{T}(\text{bdf}) \quad .$$

Le modèle de signal $\mathcal{T}(\text{signal}, \langle P_\tau \rangle, r)$ est divisé en 2 parties, $\mathcal{T}(Z \to \tau_R^- \tau_L^+)$ et $\mathcal{T}(Z \to \tau_L^- \tau_R^+)$, et dépend de deux paramètres d'intérêts : la polarisation moyenne du lepton τ, $\langle \mathcal{P}_\tau \rangle$, et l'intensité du signal r, comme indiqué dans la formule suivante :

$$\mathcal{T}(\text{signal}, \langle P_\tau \rangle, r) = r \cdot \left[\frac{1 + \langle P_\tau \rangle}{2} \cdot \mathcal{T}(Z \to \tau_R^- \tau_L^+) + \frac{1 - \langle P_\tau \rangle}{2} \cdot \mathcal{T}(Z \to \tau_L^- \tau_R^+) \right].$$

La reconstruction par l'algorithme `HPS` des modes de désintégration des leptons τ se désintégrant hadroniquement n'est pas parfaite. Des incertitudes systématiques découlent des éventuelles différences entre les migrations entre les modes de désintégration incluses dans les modèles d'ajustement et leurs équivalents dans les données. L'analyse discutée ici est affectée de deux manières par ces migrations entre les modes de désintégration. Premièrement, les événements sont catégorisés par le mode de désintégration du lepton τ. Les migrations ont des effets sur la normalisation du signal par rapport aux données, entraînant potentiellement des tensions entre les catégories. Deuxièmement, les discriminateurs finaux sont optimisés pour un certain mode de désintégration du lepton τ. Évaluer un discriminateur donné sur des événements avec un mode de désintégration mal identifié pourrait entraîner un effet modifiant la forme et détériorant l'accord des données avec la simulation dans certaines catégories. Le second effet est spécifique à cette analyse et a été étudié en détail. Les modèles simulés sont ajustés aux données dans le canal $\tau_\mu \tau_\text{h}$, où des variations de la contamination relative d'un mode de désintégration reconstruit sont traitées comme des paramètres d'intérêt. Les modèles sont définis en intervalles de la masse visible de $\tau_\mu \tau_\text{h}$ pour le mode de désintégration du tau en un pion chargé, et en intervalles de la masse visible du τ_h dans les désintégrations du tau en ρ et a_1. Les variables x^reco paramètrent la différence entre les données et la simulation de la proportion d'événements reconstruits dans un mode de désintégration donné, provenant de migrations depuis d'autres modes de désintégration générés vers ce mode de désintégration identifié. Lors de l'ajustement, les normalisations relatives sont modifiées afin de préserver le nombre global d'événements.

Les paramètres x^reco sont mesurés simultanément dans le même ajustement global des trois catégories du canal $\tau_\mu \tau_\text{h}$. Les incertitudes systématiques sont identiques à

celles de l'ajustement final de la polarisation, à l'exception des incertitudes liées aux migrations des modes de désintégration. Les paramètres sont mesurés dans les trois modes de désintégration utilisés (h représente hadron) comme suit :

$$x^{\text{reco}}(h^{\pm} \leftarrow h^{\pm}\pi^0) = -0.005^{+0.027}_{-0.028}$$
$$x^{\text{reco}}(h^{\pm}\pi^0 \leftarrow h^{\pm}\pi^0, h^{\pm}\pi^0\pi^0, h^{\pm}\pi^0\pi^0\pi^0) = -0.029^{+0.032}_{-0.028}$$
$$x^{\text{reco}}(h^{\pm}h^{\pm}h^{\pm} \leftarrow h^{\pm}h^{\pm}h^{\pm}\pi^0, h^{\pm}h^{\pm}h^{\pm}\pi^0\pi^0) = -0.014^{+0.037}_{-0.034}$$

Les déviations mesurées dans les données par rapport à la simulation sont toutes compatibles avec 0 à 1σ près. Ces mesures sont converties en incertitudes systématiques pour la mesure de la polarisation.

La fonction de vraisemblance (*likelihood*), incluant les incertitudes statistiques et systématiques, est minimisée pour obtenir la meilleure estimation de la polarisation moyenne. Elle est ensuite représentée en fonction de la polarisation moyenne afin de comparer les performances des différents discriminateurs. Les variables retenues découlent de l'étude de sensibilité effectuée. Un récapitulatif de ces conclusions est fourni dans le tableau suivant :

Canal	**Catégorie**	**Discriminant**	
$\tau_e\tau_\mu$	$e + \mu$	$m_{\text{vis}}(e, \mu)$	masse visible
$\tau_e\tau_{\text{h}}$	$e + a_1$	$\omega(a_1)$	observable optimale avec `SVfit`
	$e + \rho$	$\cos\beta(\rho)$	observable optimale visible
	$e + \pi$	$\omega(\pi)$	observable optimale avec `SVfit`
$\tau_\mu\tau_{\text{h}}$	$\mu + a_1$	$\omega(a_1)$	observable optimale avec `SVfit`
	$\mu + \rho$	$\cos\beta(\rho)$	observable optimale visible
	$\mu + \pi$	$\omega(\pi)$	observable optimale avec `SVfit`
$\tau_{\text{h}}\tau_{\text{h}}$	$a_1 + a_1$	$m_{\text{vis}}(a_1, a_1)$	masse visible
	$a_1 + \pi$	$\Omega(a_1, \pi)$	observable combinée optimale avec `SVfit`
	$\rho + \tau_{\text{h}}$	$\cos\beta(\rho)$	observable optimale visible
	$\pi + \pi$	$m_{\text{vis}}(\pi, \pi)$	masse visible

Une analyse supplémentaire a démontré que la polarisation moyenne est indépendante de la (pseudo-)rapidité du boson Z. Cette étape est essentielle compte tenu de l'impact potentiel de l'acceptance angulaire des leptons taus.

La plus grande précision est observée dans la catégorie $\mu + \rho$, bénéficiant d'une sélection efficace des événements et d'une reconstruction précise de l'observable optimale

$\cos\beta(\rho)$. La sensibilité la plus faible est trouvée dans le canal de désintégration entièrement hadronique, qui est affecté par des seuils de déclenchement élevés et une efficacité de sélection suboptimale.

L'impact de différentes sources d'incertitudes sur la mesure de la polarisation dans l'ajustement final combiné a été étudié. Les amplitudes de ces sources d'incertitudes sont obtenues en effectuant plusieurs ajustements de vraisemblance (*likelihood*) où les groupes d'incertitudes sont fixés individuellement, permettant une évaluation quadratique de leur impact. Les effets liés à la statistique limitée (intervalle par intervalle) des échantillons de données Monte-Carlo ont le plus fort impact. L'incertitude dans la modélisation des migrations entre les modes de désintégration du tau (en particulier dans les catégories $\tau^- \to \rho^-\nu$) demeure une source d'erreur significative, malgré l'utilisation de l'algorithme `MVA-DM` améliorant la performance d'identification des modes. Les autres sources d'incertitude notables concernent l'identification et la correction en énergie du lepton tau, ainsi que la modélisation du bruit de fond *QCD*. Enfin, les incertitudes globales de normalisation (telles que les sections efficaces ou la luminosité) n'ont pas d'impact sur le résulat final.

Le résultat final de l'ajustement dans les données, combinée dans les différentes catégories, pour la polarisation moyenne du lepton τ, sur un intervalle de masse di-tau de 75 à 120 GeV, donne :

$$\langle P_\tau \rangle = -0.147 \pm 0.015 = -0.147 \pm 0.006\,(\text{stat.}) \pm 0.014\,(\text{syst.}) \quad .$$

Afin de procéder à une comparaison directe avec des précédentes mesures au LEP, la polarisation moyenne mesurée $\langle \mathcal{P}_\tau \rangle$ est convertie en valeur de polarisation au pôle du boson Z. La valeur obtenue est:

$$\langle P_\tau \rangle = -0.152 \pm 0.015 = -0.152 \pm 0.006\,(\text{stat.}) \pm 0.014\,(\text{syst.}) \quad .$$

Il convient de noter que la précision de cette mesure est nettement plus grande que celle d'ATLAS, légèrement meilleure que celle de SLD et approche quasiment celles des expériences individuelles au LEP. La combinaison des résultats du LEP et du SLD donne une précision qui est meilleure d'un facteur 3 par rapport à cette unique mesure réalisée avec le LHC.

La polarisation des leptons taus issus de la désintégration des bosons Z est une conséquence directe de la structure de l'interaction faible, à savoir le mélange des champs B^0 et W^0, paramétré par l'angle de mélange électrofaible effectif, $\sin^2\theta_W^{\text{eff}}$. Dans l'analyse, il est impossible de distinguer des événements $Z \to \tau\tau$ et $\gamma \to \tau\tau$, car ils produisent exactement le même état final. Le processus $\gamma \to \tau\tau$ conduit à des leptons τ non polarisés. Comme la fraction relative des événements $Z/\gamma \to \tau\tau$ varie en fonction de l'énergie du système quark-antiquark, $\hat{s}$, la polarisation doit également être considérée en fonction de cette masse, en plus de l'angle de mélange électrofaible effectif et du type de quark q, spécifiant si le boson Z a été produit par une paire de quark *up* ou *down*

: $\mathcal{P}_\tau = \mathcal{P}_\tau(\sin^2\theta_W^{\text{eff}}, \hat{s}, q)$. L'énergie du système quark-antiquark, notée $\hat{s}$, n'est pas accessible dans l'analyse en raison de la présence de neutrinos dans les désintégrations des leptons τ. Ainsi, la polarisation mesurée du lepton τ est une moyenne pondérée sur un intervalle de masse plus large. De la même manière, la polarisation est moyennée sur les saveurs de quarks q. Comme expliqué précédemment, les efficacités pour les leptons taus d'hélicité gauche et droite diffèrent et dépendent également du mode de désintégration. Par conséquent, une méthodologie a été adoptée où des modèles pour les leptons taus d'hélicité gauche et droite sont utilisés pour tenir compte de ces effets. Ces modèles sont normalisés de manière à obtenir une polarisation nulle au niveau générateur pour un intervalle de masse donné, $\sqrt{\hat{s}} \in [75, 120]\,\text{GeV}$. La polarisation extraite par l'ajustement de ces modèles à la distribution des observables optimales correspond alors à la polarisation moyenne dans cette intervalle de masse $\sqrt{\hat{s}}$, et cette valeur moyenne de la polarisation sera liée à l'angle de mélange électrofaible. Des courbes d'étalonnage sont nécessaires pour convertir une valeur de polarisation en un angle de mélange effectif.

La conversion de la polarisation mesurée présentée dans cette thèse en valeur de l'angle de mélange électrofaible effectif donne :

$$\sin^2\theta_W^{\text{eff}} = 0.2308 \pm 0.0019 = 0.2308 \pm 0.0008\,(\text{stat.}) \pm 0.0018\,(\text{syst.}) \quad .$$

La précision obtenue pour $\sin^2\theta_W^{\text{eff}}$ ne rivalise pas avec celle des mesures actuelles, et par conséquent, elle ne permet pas d'apporter des contraintes sur de potentiels nouveaux phénomènes physiques. Néanmoins, la polarisation mesurée est en adéquation avec la valeur prédite par le modèle standard, soit $A_\ell = 0.1468 \pm 0.0003$.

Table of Contents

List of Figures

Introduction

Un des enjeux majeurs du Grand collisionneur de hadrons (*Large Hadron Collider* - LHC) est de découvrir un signe de nouvelle physique, par des recherches directes mais également des mesures de précision du modèle standard (MS) de la physique des particules.

Au grand collisionneur électron-positon (*Large Electron Positron collider* - LEP), prédécesseur du LHC, de nombreuses mesures de précision de la théorie électrofaible ont été menées grâce à l'étude de la résonance Z^0. Avec la découverte du boson de Higgs, le LHC a sans doute mis en évidence le mécanisme de brisure de cette théorie électrofaible. Néanmoins de nombreuses mesures des paramètres du MS doivent être encore menées, ceci afin d'améliorer encore les précisions obtenues, et déceler d'éventuels signes de nouvelle physique.

La violation de la parité dans les courants neutres induit un couplage différent du boson Z aux fermions d'hélicité gauche et droite. De là découlent plusieurs asymétries, parmi lesquelles une asymétrie de polarisation des leptons taus. De cette asymétrie on peut mesurer l'angle électrofaible, un des 18 paramètres fondamentaux du MS. Les expériences du LEP ont mesuré la polarisation du lepton tau dans des collisions à la masse au pôle du boson Z, avec une précision de l'ordre de 10%. Plus récemment l'expérience ATLAS a mesuré cette polarisation à 8 TeV dans des collisions proton-proton avec une précision de l'ordre de 35% pour une luminosité intégrée de 20.2 fb^{-1} [10]. Cette thèse présente une nouvelle mesure de la polarisation des leptons taus dans des collisions proton-proton à 13 TeV collectées en 2016 pour une luminosité intégrée de 36.3 fb^{-1}. Elle étend l'usage de variables optimales [8] à tous les canaux de désintégrations hadroniques du lepton tau, jusqu'à présent utilisés au sein de l'expérience CMS uniquement dans le canal $Z \to \mu\tau_h\nu_\mu\nu_\tau \to \mu a_1\nu_\mu\nu_\tau$ [11, 12]. Elle permet également de donner une nouvelle mesure de l'angle électrofaible effectif, dont les mesures les plus précises datent de la mesure combinée du LEP et de l'expérience SLD, respectivement égales à 0.23221 ± 0.00029 [1, 13–16] et 0.23098 ± 0.00026 [17].

Le chapitre 1 présente une courte introduction au contexte expérimental de la phase de haute luminosité du LHC. Ceci afin d'introduire, dans le chapitre 2, les tests en faisceaux effectués à l'Institut Pluridisciplinaire Hubert Curien (IPHC) auprès du cyclotron CYRCé, dans le cadre des activités de jouvence du trajectographe pour la phase de haute luminosité du LHC dans lesquelles l'IPHC est impliqué. Le chapitre 3 présente l'analyse développée pour mesurer la polarisation des leptons taus. Le chapitre 4 dévoile les résultats obtenus sur les données réelles (*unblinding*). Finalement, le résultat de la mesure de l'angle électrofaible effectif est donné au chapitre 5.

Chapter 1

Experimental context

1.1 The CMS detector

The primary component of the Compact Muon Solenoid (CMS) apparatus is a 6 m internal diameter superconducting solenoid that produces a magnetic field of 3.8 T. Inside the volume of the superconducting solenoid are placed several detectors, including a silicon spixel and strip tracker, a lead tungsten crystal electromagnetic calorimeter (ECAL), and a brass and scintillator hadron calorimeter (HCAL), each consisting of a barrel and two endcap sections. Additionally, forward calorimeters extend the pseudorapidity coverage provided by the barrel and endcap detectors.

The silicon tracker measures charged particles within the pseudorapidity range $|\eta| < 2.5$. It consists of 1440 silicon pixel and 15 148 silicon strip detector modules. For non-isolated particles of $1 < p_{\mathrm{T}} < 10\,\mathrm{GeV}$ and $|\eta| < 1.4$, the track resolutions are typically 1.5% in p_{T} and 25–90 and 45–150) μm in the transverse and longitudinal impact parameter, respectively, [18]. The electron momentum is estimated by combining the energy measurement in the ECAL with the momentum measurement in the tracker. The momentum resolution for electrons with p_{T} around 45 GeV from $Z \to e^+e^-$ decays ranges from 1.7% for nonshowering electrons in the barrel region to 4.5% for showering electrons in the endcaps [19]. Muons are measured in the pseudorapidity range $|\eta| < 2.4$, with detection planes made using three technologies: drift tubes, cathode strip chambers, and resistive plate chambers. Matching these muons to tracks measured in the silicon tracker results in a relative transverse momentum resolution for muons with $20 < p_{\mathrm{T}} < 100\,\mathrm{GeV}$ of 1.3–2.0% in the barrel and better than 6% in the endcaps. The p_{T} resolution in the barrel is better than 10% for muons with p_{T} up to 1 TeV [20].

In the barrel section of the ECAL, an energy resolution of about 1% is achieved for unconverted or late-converting photons in the tens of GeV energy range. The remaining barrel photons have a resolution of better than 2.5% for $|\eta| < 1.4$. In the endcaps, the

resolution of unconverted or late-converting photons is about 2.5%, while the remaining endcap photons have a resolution between 3 and 4% [21].

The missing transverse momentum vector $\vec{p}_{\mathrm{T}}^{\,\mathrm{miss}}$ is defined as the projection on the plane perpendicular to the beams of the negative vector sum of the momenta of all reconstructed particles in an event. Its magnitude is referred to as $E_{\mathrm{T}}^{\mathrm{miss}}$.

The *Particle-Flow* algorithm [6] reconstructs and identifies each individual particle of an event with an optimized combination of information from the various elements of the CMS detector. The energy of photons is directly obtained from the ECAL measurement. The energy of electrons is determined from a combination of the electron momentum at the primary interaction vertex as determined by the tracker, the energy of the corresponding ECAL cluster, and the energy sum of all bremsstrahlung photons spatially compatible with originating from the electron track. The momentum of muons is obtained from the curvature of the corresponding track. The energy of charged hadrons is determined from a combination of their momentum measured in the tracker and the matching ECAL and HCAL energy deposits, corrected for zero-suppression effects and for the response function of the calorimeters to hadronic showers. Finally, the energy of neutral hadrons is obtained from the correspondingly corrected ECAL and HCAL energy deposits.

The first level, Level-1 (L1), of the CMS trigger system [22], composed of custom hardware processors, uses information from the calorimeters and muon detectors to select the most interesting events in a time interval of less than $4\,\mu$s. The High-Level trigger (HLT) processor farm further decreases the event rate from around 100 kHz to less than 1 kHz, before data storage.

A more detailed description of the CMS detector, together with a definition of the coordinate system used and the relevant kinematic variables, can be found in Ref. [23].

Many physics analyses performed with data from the LHC accelerator are statistically limited, especially analyses seeking to challenge the Standard Model. In order to increase the discovery potential and the precision of the measurements, the total luminosity delivered by the LHC will be increased by a factor of approximately 10.

This upgrade into a high-luminosity accelerator also involves upgrades of the different detectors in order not to degrade reconstruction performance in these extreme conditions.

The High-Luminosity LHC (HL-LHC) upgrade will be briefly presented in this section, followed by an overview of the main upgrades of the CMS detector, with a more detailed part on the Outer Tracker.

1.2 The High-Luminosity LHC

A machine upgrade is scheduled in order to exploit the full potential of this hadron collider. The target instantaneous luminosity value to be delivered is 5×10^{34} cm^{-2} s^{-1}, leading to an integrated luminosity of 250 fb^{-1} per year of operation, with the goal of 3000 fb^{-1} in about a dozen years after the upgrade, which represents an order of magnitude of the total integrated luminosity until now at the LHC [24]. A recent exemple of the timeline for this upgrade is presented in Fig. 1.1.

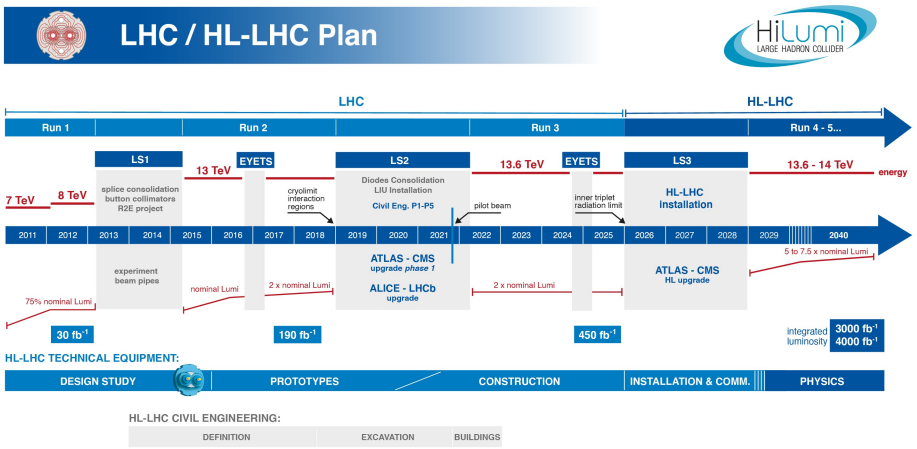

Figure 1.1: Timeline of the LHC upgrade to high-luminosity (January 2022).

1.3 The CMS Upgrade for the HL-LHC

The High-Luminosity Upgrade will bring more challenging conditions for the experiment and its data taking.

Firstly the higher instantaneous luminosity will lead to larger pile-up effects and therefore higher particle rate. It is required that the future detector have a higher granularity to reduce occupancy and improved Level-1 (L1) trigger and High-Level trigger (HLT) capabilities to continue to efficiently select the events of interest.

Finally the high integrated luminosity also implies an accumulation of radiation dose in the detector components. Majority of sub-detectors need to be replaced and designed for higher performence and radiation hardness.

The new CMS detector designs for the HL-LHC upgrade, also known as *Phase-2* upgrade, are well advanced and described in [25–33]. The electromagnetic and hadronic calorimeters will have to be replaced due to radiation damages. They will be replaced by the High Granularity calorimeter (HGCAL), that will allow three dimensional images of

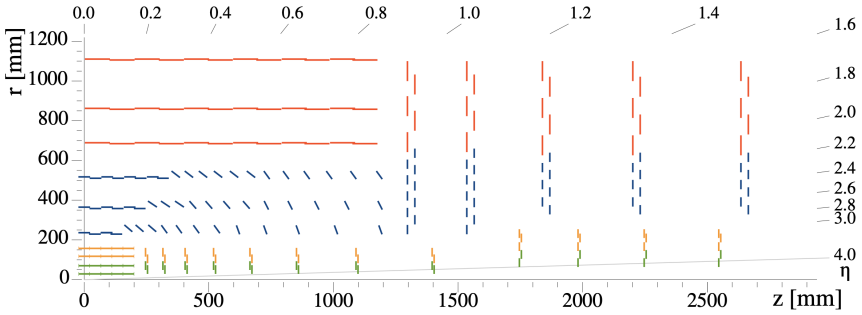

Figure 1.2: The overall layout of the new CMS tracker.

showers. Tungsten and copper plates interleaved with silicon sensors as the active material will form the electromagnetic part, followed by brass and copper plates interleaved with silicon sensors to form the hadronic part. Additional chambers that make use of new detector technologies with higher rate capability will be installed: two Gas Electron Multipliers (GEM) and Resistive Plate Chambers (RPC).

For this thesis the upgrade of the Tracking system is of particular interest: CMS will install a new silicon tracking detector with some major improvements: higher granularity, smaller material budget, improved radiation hardness, compatible with high particle rates and Level-1 trigger capability. The overall new layout of the tracker is shown in Fig. 1.2. Figure 1.3 shows the associated material budget.

The new tracker consists out of an Inner Tracker (IT) part composed of four barrel layers (TBPX) plus eight small disks (TFPX) and four large disks (TEPX) in each forward direction, and an Outer Tracker (OT) part, which will supply additional tracking information to the CMS Level-1 trigger system and will efficiently select events of interest. To achieve this, the future OT will be build with so-called p_{T}-modules consisting out of two closely spaced silicon sensors read out by the same Front-End (FE) integrated circuit. These FE chips are designed to discriminate tracks based on their transverse momentum (p_{T}) as illustrated in Fig. 1.4.

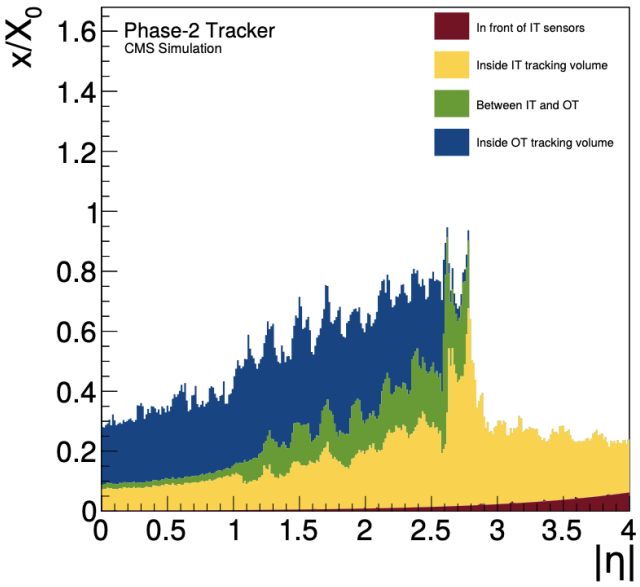

Figure 1.3: The material budget (radiation length) of the new CMS tracker.

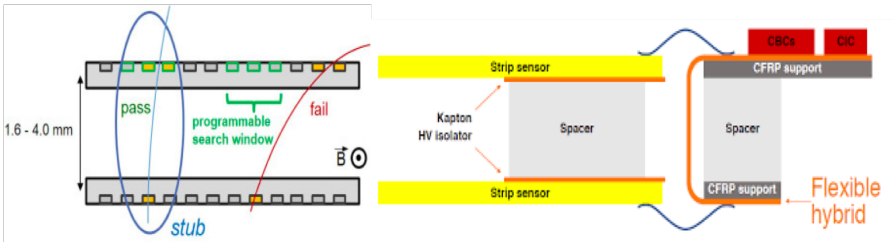

Figure 1.4: Schematic view of the 2S modules and their integrated circuit comparing the hits in the two layers of silicon strip detectors.

Conclusion

Afin d'augmenter le potentiel de découverte et la précision des mesures de l'accélérateur LHC, la luminosité totale fournie par le LHC sera augmentée d'un facteur d'environ 10, avec pour objectif 3000 fb^{-1} dans une douzaine d'années. La jouvence du LHC à haute luminosité impliquera également des améliorations des différents sous-détecteurs composant le détecteur CMS afin de ne pas dégrader les performances de reconstruction dans ces conditions extrêmes. Les nouveaux designs des sous-détecteur pour la jouvence du HL-LHC sont avancés et décrits en détail dans divers rapports techniques. L'une des jouvences les plus importantes est le remplacement des calorimètres électromagnétiques et hadroniques par le calorimètre à haute granularité (HGCAL). De plus, un nouveau trajectographe en silicium sera installé avec une granularité plus élevée, une meilleure résistance aux radiations et une capacité de déclenchement au niveau 1 pour continuer à sélectionner efficacement les événements d'intérêt malgré le taux élevé de particules.

Chapter 2

First measurement at the new test beam facility for CMS at the cyclotron CYRCé at the IPHC

Contents

2.1 Test beams for LHC availability

The prototyping phase of the new *Phase-2* OT modules started during the second long shutdown (LS2) period of the LHC. Test beams allow detectors to be characterised with particle beams and hence provide additional information to simulations and laboratory tests.

Tracking detectors for particle physics are usually tested in high energy beams of hadrons or leptons. However in particular during the long shutdown at CERN (2019-2022) after the *Run-2* period those beams were of limited availability.

Other facilities at low energy cyclotrons allow irradiations up to high doses and also high intensity tests of the tracking modules. However spatial resolution measurement are limited due to increased multiple scattering.

In this context the idea emerged to install such a test and radiation facility in Strasbourg.

The prototype modules, usually referred to as Devices Under Test (DUT), are operated under conditions close to those of their final deployment in the experiment, in particular under higher rates than using radioactive sources or cosmic rays.

The characterisation of DUT requires independent measurements of the beam particle tracks. These reference tracks are provided by a system called a beam telescope, composed of several planes of well-known detectors with suitable high spatial resolution in order to reconstruct with high accuracy particle tracks and measure the tracking efficiency of the DUT.

Beam test facilities have in most cases already beam telescope installed, however they do not allow to test protoypes with high rates, because of their too slow readout frequency. Existing Telescopes consist often out of Monolithic Active Pixel Sensor detectors (MIMOSA) as reference planes [34]. The integration time of theses sensor chips typically equals 115.2 μs i.e. a 8.68 Hz readout frequency. This frequency is 4600 times lower than that of *Phase-2* OT modules with an integration time of 25 ns, which corresponds to 40 MHz. The prototype modules therefore cannot be tested at the nominal rate with the existing telescopes used by the CMS collaboration.

With the aim of carrying out high rate performance and stress tests with CMS *Phase-2* Tracker prototypes, dedicated high-rate telescopes with CMS-standard hardware and software were developped and installed: firstly CHROMIE at CERN and nearly in parallel a smaller version called CHROMini at the CYRCé beam test facility located at IPHC.

2.2 Test beams at the CYRCé cyclotron

The IPHC of Strasbourg installed in 2013 a cyclotron named CYRCé (for *Cyclotron pour la recherche et l'enseignement*) which operates at energies from 16–25 MeV and up to very high intensities (current of up to 400 μA). The initial objective is to perform radiobiological experiments and the production of radioisotopes (^{18}F, ^{64}Cu and ^{89}Zr are the main radioelements produced). Later external beam lines (PRECy) were added to the cyclotron for further experimentation.

2.2.1 The CMS IPHC beamline

The CMS beamline [35] is specifically dedicated to irradiations and tests of tracking modules and their Data acquisition (DAQ) system scheduled for *Phase-2* of the LHC. The proton beam is pulsed and is accelerated to an energy of 25 MeV by the CYRCé cyclotron and delivered at a bunch frequency of 85 MHz, which is divided by two, i.e. 42.5 MHz using a high frequency electrostatic kicker allowing to operate the detectors and electronics at frequencies close to the nominal LHC rate of 40 MHz. Beam intensity ranges from 1 fA to 100 nA in these external beam lines. The maximum beam spot diameter is limited by the beam optics to 30 mm.

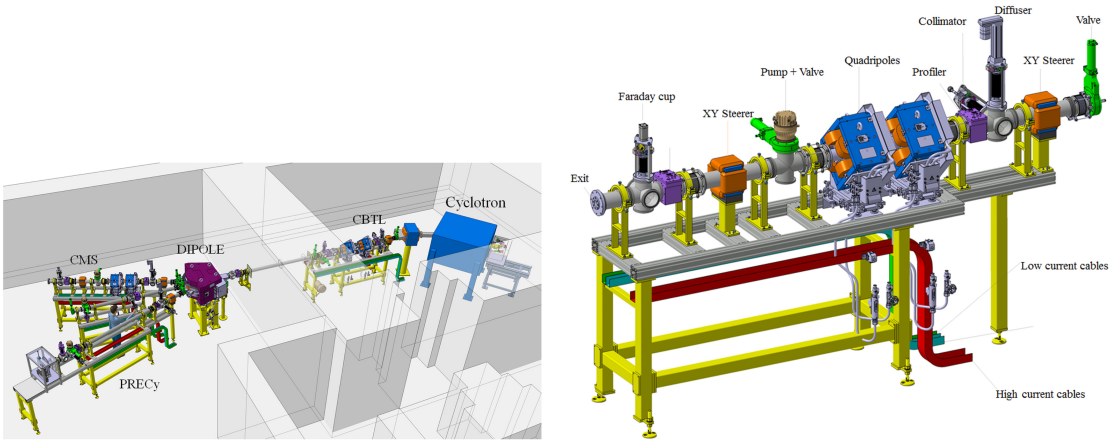

Figure 2.1: 3D schematic views of experimental area (left) and the dedicated CMS beamline (right).

Schematic views of the experimental area of the CYRCé platform with the CMS and PRECy beamlines are shown in Fig. 2.1. The PRECy beamline allows to perform radiobiological experiments. A photo of the CMS beamline is shown in Fig. 2.2.

2.3 Design of the mini-telescope CHROMini

In this section, the design, calibration, commissioning and testing of CHROMini is presented.

To test the *Phase-2* Tracker prototypes under the LHC nominal rate, a new mini-telescope named CHROMini was installed and commissioned at IPHC for test beams. Its design is inspired by the CHROMIE (CMS High-Rate telescOpe MachInE) telescope [36] installed at CERN.

2.3.1 Layout of the mini-telescope

The low energy of the beam requires an optimisation of all parts in order to reduce energy losses and multiple scattering by any materiel in the setup. A schematic view is shown in Fig. 2.3. The proton beam exits the vacuum chamber via a 100 μm thick Aluminum window and then hits two successive planes of CMS pixel planes. Behind the last plane a 2 mm thick scintillator provides a trigger signal. The two pixel planes define a reference track for the detector under test (DUT), which is situated between the two planes.

Each Pixel plane is composed of two standard CMS Layer-3 and Layer-4 Pixel modules, mounted with minimal overlap on both sides of a small Al-frame. The modules consist of 16 Pixel detectors with their corresponding Read Out Chip (ROC) electronics. The total area covered by each plane is about 65×32 mm^2, see the photo of Fig. 2.4, where

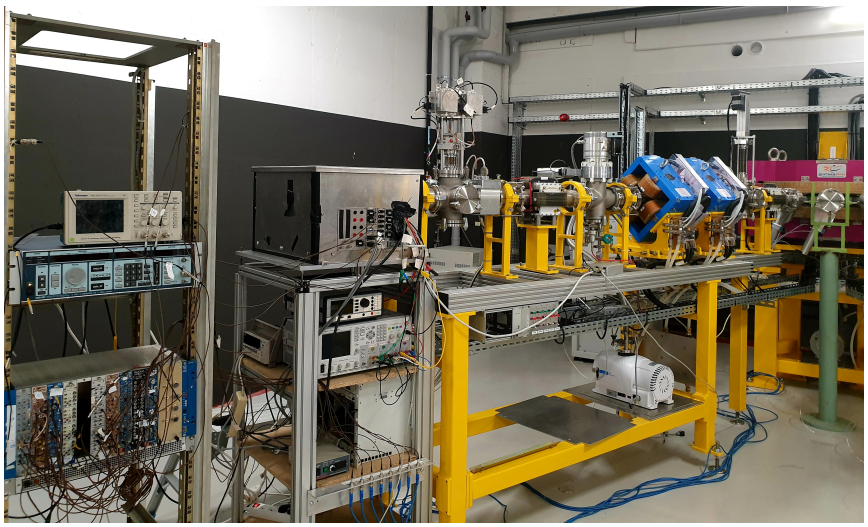

Figure 2.2: Picture of the CMS beamline with the experimental box containing the setup at the exit.

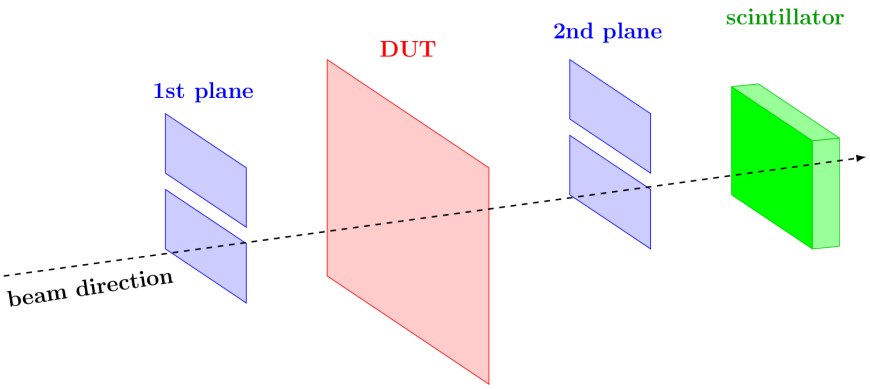

Figure 2.3: Schematic view of the setup, consisting out of two planes of Pixel detectors and a scintillator for triggering. The DUT is positioned between the two Pixel planes.

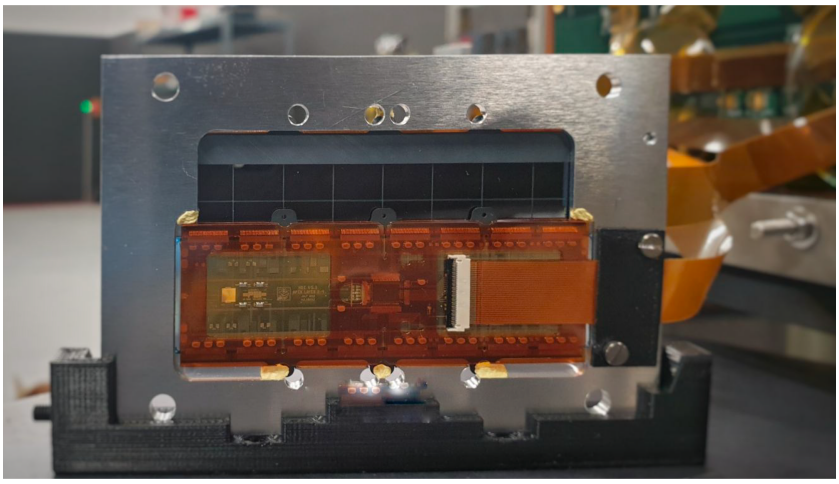

Figure 2.4: A Pixel plane composed of two standard CMS Layer-3 and Layer-4 Pixel modules, mounted on both sides of a small Al-frame with minimal overlap.

the Pixel detectors are clearly visible for the module mounted on the back side of the Al-frame, the front face displays the electronic hybrid carrying additional components.

Before assembling the Pixel planes, each Pixel module had to be tested and calibrated following the standard procedure of the CMS Pixel group.

2.4 Calibration of the mini-telescope

The first calibration steps are carried out in the laboratory to select modules and ensure that the modules composing the telescope are all in good working order before installing them. Modules are individually calibrated using a Digital Test Board (DTB) and `pXar` software following the procedure explained in Sect. 2.4.1.

2.4.1 Individual test of modules via DTB and `pXar`

The Digital Test Board (DTB) is the custom-designed readout electronics for laboratory tests during the production of the CMS *Phase-1* pixel detector chips and modules. This Data acquisition (DAQ) board provides all the components necessary to operate the detector, such as IO devices, high-voltage relay for the bias voltage and trigger modules. An Altera Cyclone® III FPGA controls the board and communications which are established via USB 2.0 and Ethernet ports. A block diagramm illustrating the main features of the DTB is available in the Appendix A. The test board is also capable of operating the detectors in beam test environments, by allowing the reception of triggers

and external clock signals.

The operation of the DTB is simplified by using the *pxarCore* library [37] which provides users with easy-to-use functions for high-level applications. All test procedures for module calibration and qualification are implemented in Pixel eXpert Analysis and Readout (`pXar`) software [38] interface which is the most commonly used.

The module calibration procedure is divided into three steps. First the basic functionalities of the components are checked and the operational Digital to Analog Converter (DAC) parameters for stable communication with the readout electronics of the module are adjusted (this procedure is called *pretest*). The following test (*fulltest*) checks the characteristics of ROCs and all Pixel Unit Cells (PUCs). The last advanced step is to calibrate the charge threshold of module and perform high-rate tests using X-rays. The final step was not carried out during this thesis. The first two procedures are described in more details in the following sections and illustrated with test results for the detector module with serial number *M3558* which was selected to compose the CHROMini telescope (upper module of the first Pixel plane).

2.4.1.1 *Pretest* procedure

Since ROCs are reset after power up, they must be programmed to be functional. The first concern is therefore to establish communication with the ROCs. The electrical integrity of the circuit for each chip is checked by scanning the VANA DAC parameter. The analog current I_{ana} drawn by the DTB should rise with increasing VANA. If this behaviour is correctly observed, the VANA is adjusted in order to reach the optimal analog current value $I_{ana} = 24\,\text{mA}$ for each ROC.

The next step is to establish communication with the Token Bit Manager (TBM) in order to receive pixel hit data from the module. Obtaining correct phase settings requires several internal delays to be adjusted: the phase of the TBM header and trailer, the data signals of each ROC and the token return signals. Finally to test the PUCs the calibration signals must be correctly synchronised with the triggered bunch crossing. For each ROC the delay of the signal can be adjusted via the CALDEL DAC setting. This parameter depends closely on the parameter of the threshold comparator voltage VCTH as illustrated in the Fig. 2.5. The optimal working point for CALDEL and VCTH is determined from a two-dimensional scan of these parameters, providing the so-called *tornado plot* in the Fig. 2.6.

After performing this set of tests and applying the settings, the module is functional and its performance can be quantified using the *fulltest* procedure on the PUCs.

2.4.1.2 *Fulltest* procedure

The *fulltest* module is used to characterise the performance of the detector module, the response and noise of the PUCs. The results of these tests determine whether the

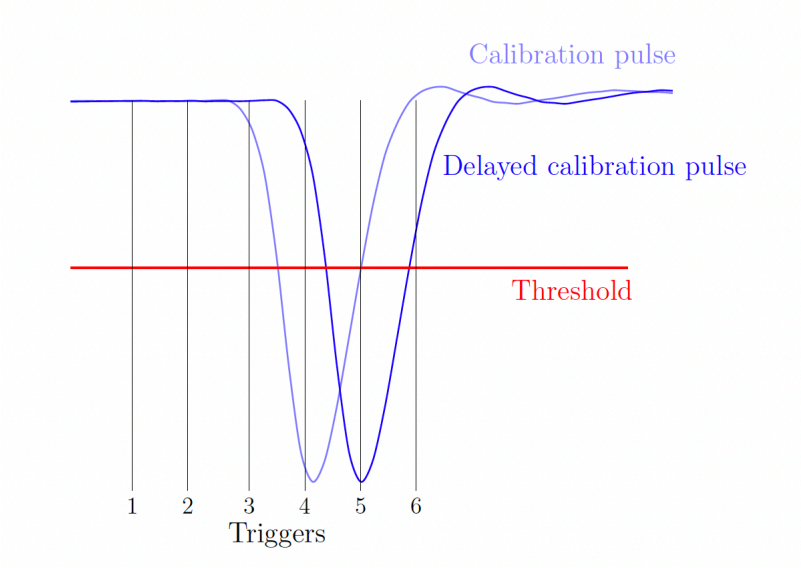

Figure 2.5: Illustration of the influence of the chosen threshold value and the calibration signal delay on triggering. The non-delayed calibration signal (light blue) is detected by triggers 4 and 5 while the delayed calibration signal (dark blue) is only detected with trigger 5.

module will integrate the telescope or leave as spare. The response efficiency of the PUCs is measured by injecting a calibration charge into each of the pixels.

2.4.2 Latency scan with a ^{90}Sr-source

After performing the initial calibration procedures, the Pixel modules can be operated stably and a scan of the trigger latency is carried out. The objective of this scan is to find the latency parameters allowing the modules to send data to the Front-End Driver (FED), used in the DAQ system of the CMS Phase-1 pixel detector, within the expected time frame. Pixel hits that are sent outside this configured trigger latency are not selected and the buffer cells are drained. Pixel ROCs associate the hits with a timestamp in bunch-crossing units. When trigger signals arrive, hits matching a pre-set timestamp are read-out. This adjustable timing to chose a certain bunch-crossing, working as a bunch-crossing pointer, is configured with the Write Bunch Crossing (WBC) register. This DAC parameter is counted at the edges of the LHC clock, one WBC unit corresponds to the time of one bunch-crossing i.e. to 25 ns. The WBC parameter counts the bunch crossings in an earlier time: an event with a larger WBC value happened before an event with a smaller WBC value. The results of the trigger latency scan carried out with a ^{90}Sr radioactive source are shown in the Fig. 2.7 representing the mean number of clusters per event in the two Pixel planes for three different values of WBC (64, 65 and 66).

The number of clusters per event is almost zero for a delay of 64 clock cycles,

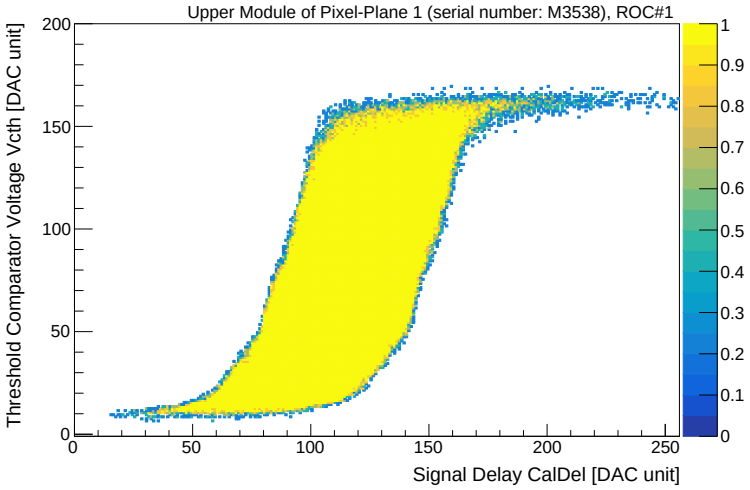

Figure 2.6: 2D-scan of the threshold comparator voltage VCTH and the signal delay CALDEL DAC settings for the ROC-1 of the upper module (serial number *M3558*) of the first Pixel plane.

and the trigger efficiencies are respectively 58.5% and 46.1% for values 65 and 66 clock cycles. These relatively high efficiency values for two different WBC values indicate that the trigger and clock delays are close to edge of a clock, the event is either read out within the N or N+1 clock cycle.

The timing is then more finely tuned by setting the GLOBALDELAY25 parameter that delays the signal in the Delay25 chip for the clock and data. The same delay is added in the FED so that the digitisation works independently of this global delay. The delay is adjustable in steps of 0.499 ns. The efficiencies measured by adjusting this parameter are also shown in the figure. An efficiency plateau beyond 96% is reached and the values of WBC=66 and GD=25=12.5 ns are chosen.

2.5 Beam tests of 2S silicon detector module together with the CHROMini mini-telescope

In this section, the results of the data taken during a test campaign in January 2022 at the CYRCé facility at IPHC are presented and discussed. The prototype 2S-module equipped with 16 CMS Binary Chips version 3 (CBC3) was operated as a DUT. This is the first campaign during which the CHROMini Pixel telescope and the DUT, each having its own DAQ system have been properly synchronised making it possible to study the correlations between the DUT and the CHROMini Pixel telescope.

Figure 2.8 shows a photo of a CMS 2S silicon detector (DUT) mounted on Al-

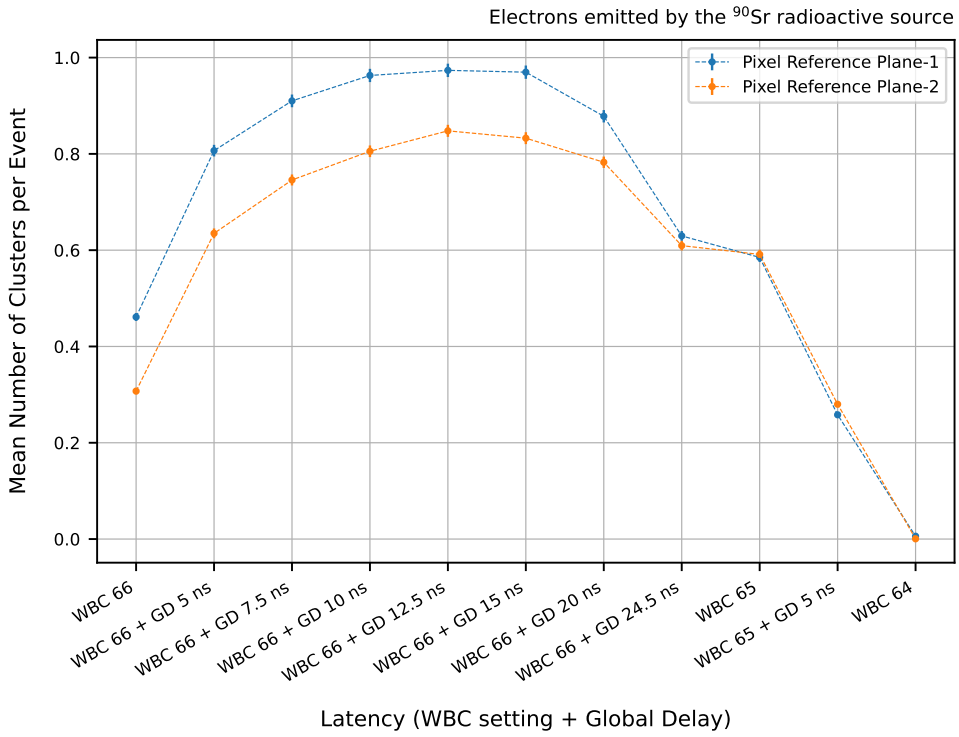

Figure 2.7: Latency scan obtained with a ^{90}Sr-source. First a corse scan is performed in steps of one bunch-crossing and then a second fine scan in steps of 2.5 ns around the suspected maximum.

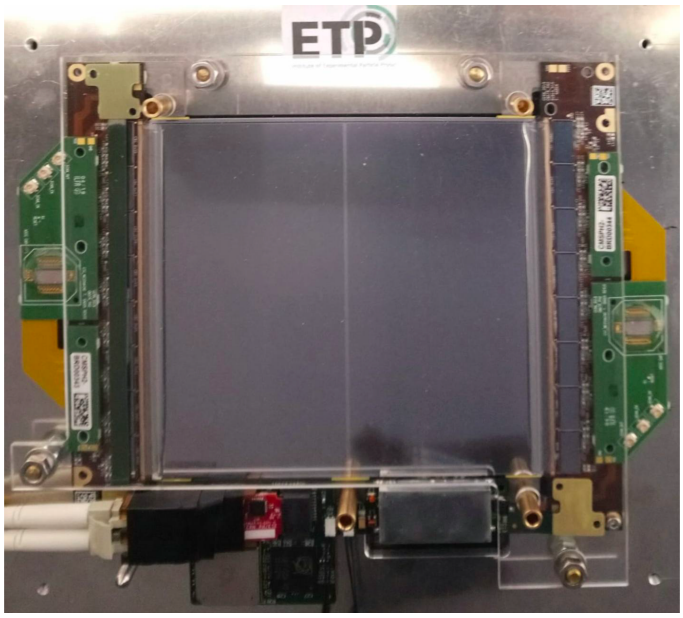

Figure 2.8: CMS 2S silicon detector (DUT) mounted on Al-carrier frame for beam tests.

carrier frame for beam tests.

The data analysis is performed in several successive steps which are discussed below in their respective subsections. First the local reconstruction of the raw data from the telescope and the DUT is carried out respectively with the CMS offline software (`CMSSW`) and the CMS Tracker *Phase-2* Acquisition and Control Framework (`Ph2_ACF`) middleware. Candidate clusters are then formed in each system. The reference tracks are built from the clusters of reference Pixel planes of the CHROMini mini-telescope. The misalignement between the two reference planes is corrected before finally comparing event-by-event the global positions of the tracks and the DUT.

2.5.1 Reconstruction and Clustering

2.5.1.1 CHROMini mini-telescope

The first step in this data analysis is the local reconstruction that provides information about the individual hits in the detector. The mini-telescope raw data are unpacked and interpreted in `CMSSW` to create *digis*: each *digi* represents a single pixel hit with a collected charge above the signal-over-noise threshold and contains information about the local row and column positions, the charge and the event timestamp.

The standard CMS algorithm for the reconstruction of pixel clusters is then applied. The algorithm is an explicit threshold-based and topological algorithm: the clustering process starts with seed pixels and continues by adding adjacent pixels above

the pixel threshold. Both side and corner adjacent pixels can be included in the cluster. The formed cluster has to have a total charge above a defined threshold. This procedure is repeated until all the pixels have been assigned to a seed.

An illustration of the clustering is shown in Fig. 2.9, with the cluster size on the right hand side.

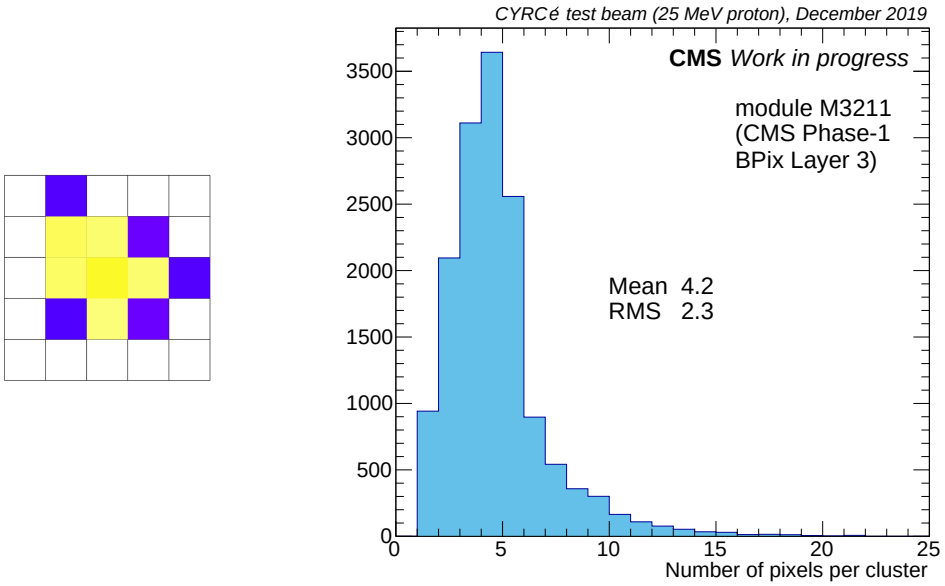

Figure 2.9: Typical Pixel cluster with a saturated pixel in the center. The image on the *left* displays a representative pixel cluster with a pixel that is saturated in the center. The cluster seed is the pixel with the highest pulse height and above 150 ADC counts. The distribution of the cluster size is shown on the *right*.

For 25 MeV protons the energy loss at minimum ionisation is at least eleven times greater than at relativistic energies as expected at the LHC, leading to charge saturation in the silicon modules (Pixels and DUT), which are of course designed for LHC conditions, namely minimum ionising particles. This saturation contributes to large cluster sizes but does however not deteriorate the overall resolution of the telescope, which is limited by multiple scattering.

For the Pixel detectors, which have a 8 bits analog read out of the pixel charge, the saturation of the electronics is clearly visible in the pulse height spectrum shown in the left part of Fig. 2.10: although the 8 bits would allow signals up to 255 Analog-to-Digital converter (ADC) counts, a saturation peak occurs already at around 160 caused by the analog electronic chain. The right part of Fig. 2.10 illustrates the large clusters due to saturation by two bit maps of the pixel plane with super imposed events. the bright yellow pixels are those already in saturation. These images were taken in a special

run early in the testing of the Pixels in the 25 MeV beam with a random trigger and read out by the DTB board described in Subsection 2.4.1. The results of these early results were presented at the 8th Beam Telescopes and Test Beams (BTTB) Workshop in 2020 [39].

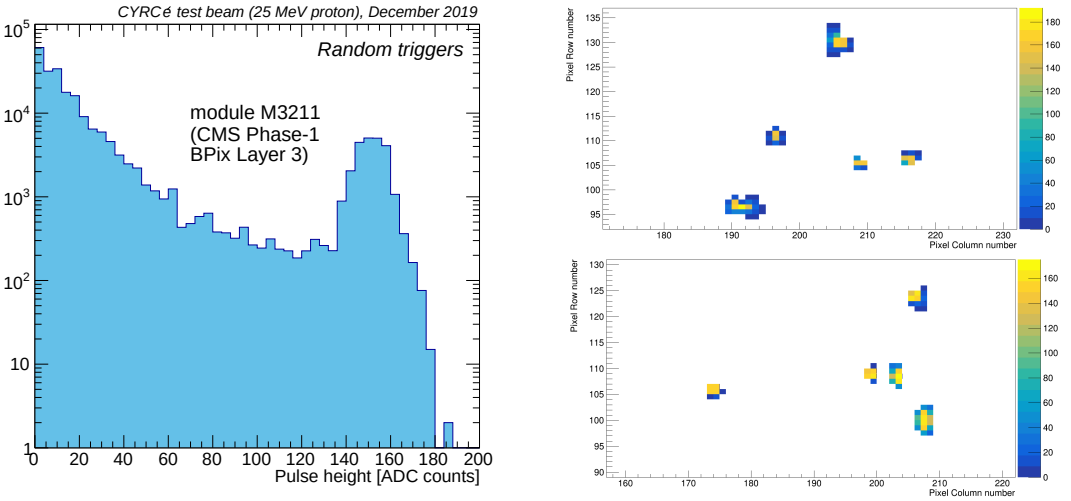

Figure 2.10: Saturation of Pixel analog electronic by the high ionisation of 25 MeV protons (*left*). Superimposed event displays (*right*) of Pixel planes for clusters with a highly saturated pixel seeds.

The size of the clusters characterise the mechanism of charge sharing which impacts on the spatial resolution. The Figure 2.11 shows the cluster size n_{px} which measures the number of pixels forming it. In addition, the projections of the cluster size on the column and row directions are shown in the Fig. 2.12.

For a given cluster the cluster local position x_c (similar for y_c) is calculated as:

$$x_c = p_x \frac{\sum_{k=0}^{n_{px}} q_k \cdot i_k}{\sum_{k=0}^{n_{px}} q_k} \quad , \tag{2.1}$$

where p_x is the pitch in x-direction, q_k is the pixel charge of a given pixel k forming the cluster, i_k is the row (column) index of the pixel k and n_{px} is the number of pixels in the cluster. This algorithm is usually referred to as position weighted centre-of-gravity algorithm. Within the scope of this study, the performances of other clustering algorithms have not been compared, the choice is based on the simplicity and robustness of the algorithm.

2.5.1.2 Beam profiles

In Figure 2.13 the measured profiles for a fairly focused beam in the two Pixel planes are presented. The beam is not totally uniform, in the first plane one can see a two

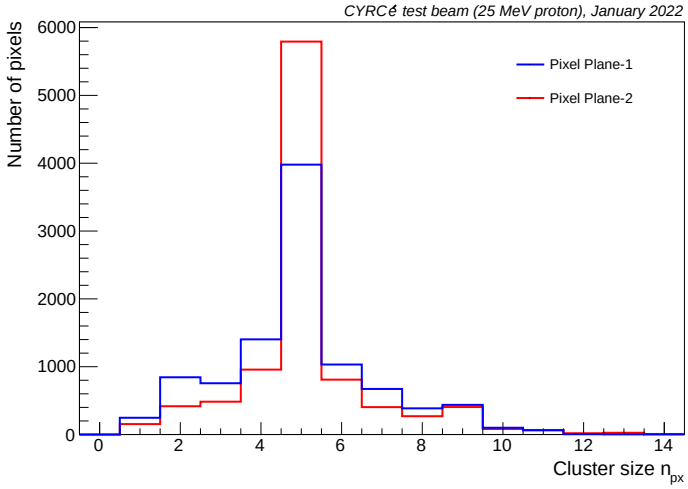

Figure 2.11: Cluster size n_{px} for the two reference Pixel planes of the CHROMini mini-telescope. The number of pixels depends on the applied threshold.

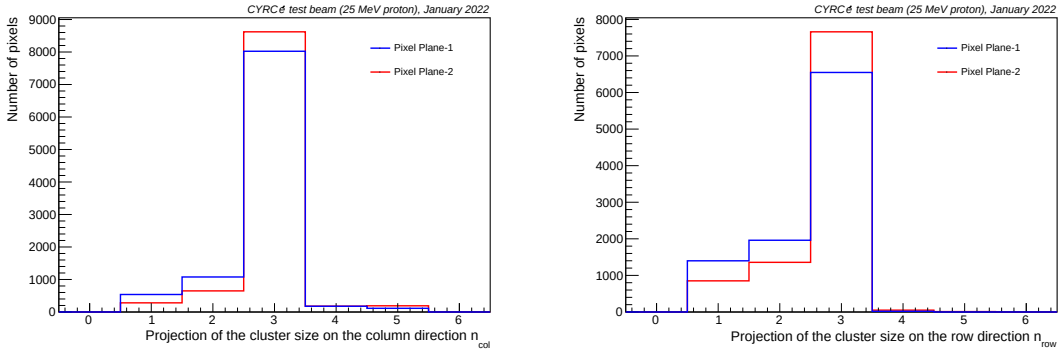

Figure 2.12: Projections n_{col} and n_{row} of the cluster size on the column (left) and row (right) directions for the two reference Pixel planes of the CHROMini mini-telescope.

component structure, which is also visible on the beam diagnostic instrumentation. It is at least partially due to protons scattered at the extraction point of the cyclotron.

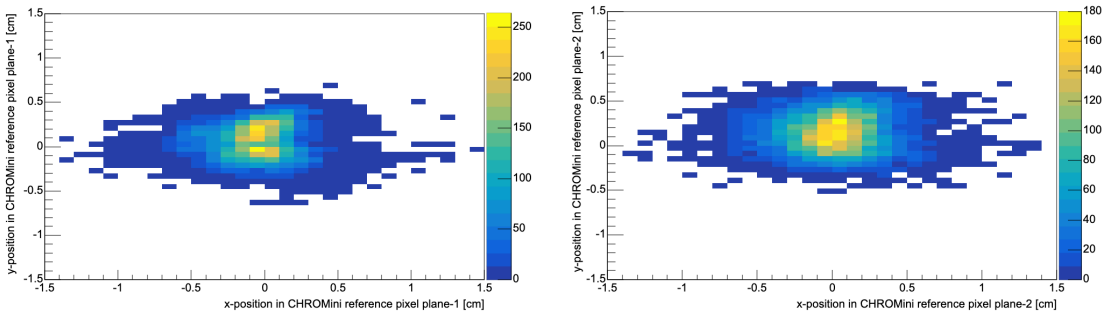

Figure 2.13: Measured profiles of the fairly focused beam in the two CHROMini reference Pixel planes, the first one on the *left* and the second one on the *right*.

2.5.2 Reference track reconstruction and Alignment

2.5.2.1 Alignement of Pixel planes

The cluster positions are calculated according to Eq. (2.1) in the local coordinates of each mini-telescope plane. The first step towards the reconstruction of the reference tracks is the transformation of local coordinates into global ones. The z-direction in the global coordinate system is parallel to the beam and the x- and y-directions as illustrated in the Fig. 2.3.

As a single cluster is reconstructed in each plane in the majority of events (see Fig. 2.14), only events with a single cluster in each plane are considered and the track is defined as a straight line between the two cluster positions in plane-1 (x_1, y_1) and in plane-2 (x_2, y_2). The mini-telescope residuals are defined as:

$$\Delta x_{tel} = x_1 - x_2 \quad \text{and} \quad \Delta y_{tel} = y_1 - y_2 \quad . \tag{2.2}$$

Figure 2.15 shows the position correlation in the vertical and horizontal direction between the two Pixel planes: one can clearly observe a small misalignment between the two planes and a large width, entirely dominated by multiple scattering widening the beam.

The precision of reference tracks depends also on the quality of the detector alignment. Alignment corrections are determined and applied at the software level. To align reference plane-1 with respect to reference plane-2 in x- and y-directions, Δx_{tel} and Δy_{tel} residual distributions are used. Such distributions are shown again in Fig. 2.16 for the misaligned and aligned case. Offset corrections in x- and y- directions are determined by fitting the (misaligned) distributions with a Gaussian function to estimate the peak position. The estimation of alignment parameters, $x^a_{tel} = 672 \pm 3\,\mu$m and $y^a_{tel} = 781 \pm$

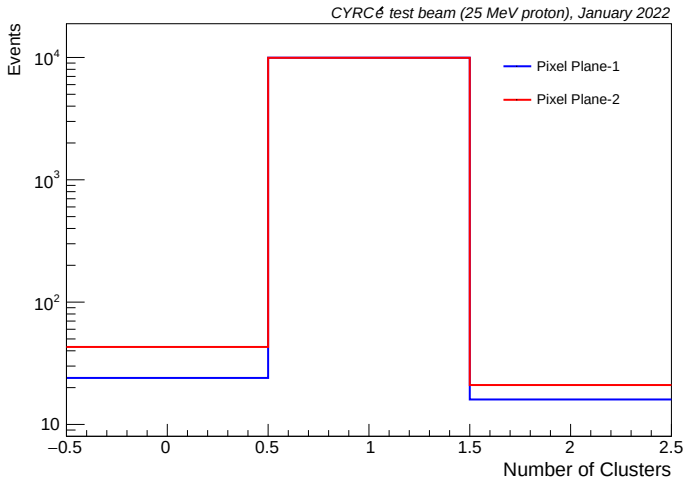

Figure 2.14: Number of clusters in the two reference Pixel planes of the CHROMini mini-telescope (logarithmic scale). Only one cluster is reconstructed for each plane for more than 99% of events.

3 μm, are based on direct measurement see Fig. 2.15 and on prior knowledge of previous runs. After this procedure, in the aligned case the peak is situated at zero by construction.

In Figures 2.17 the mean residual $\overline{\Delta x_{tel}}$ ($\overline{\Delta y_{tel}}$) are shown as a function of the y-coordinate (x-coordinate) plane-1 position of the corresponding reference track.
By fitting with a linear function, the estimated slope indicates that the mean of residuals is not only shifted but impacted by a rotation around the z-axis. Another alignment correction $\vec{\theta_z}$ corresponding to rotation angles can be determined from the slope of the linear fits.

2.5.2.2 DUT

The two 2S-sensors are each segmented in two columns of 1016 strips of 90 μm pitch (y-direction) and 5 cm in length (x-direction). Each column of strips will be read-out independently by 8 CBC chips, each connected to 127 strips.

The DUT data are decoded with the `Ph2_ACF` middleware. Given that there is no information on the charge provided, the clustering is based on the correlations between the two sensors.

The beam was hitting only the left side of the DUT as can be seen in the hit-map, Fig. 2.18.

The DUT also needs to be aligned with respect to the mini-telescope to evaluate the performance of this system.

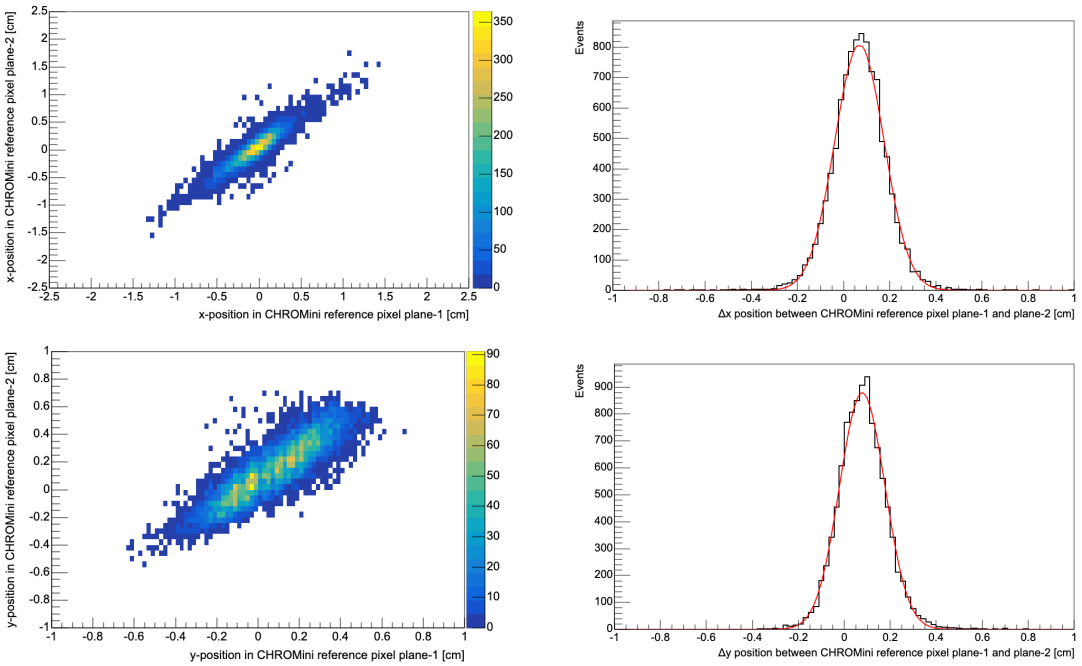

Figure 2.15: Correlation of hits in the two reference Pixel planes of the CHROMini mini-telescope. The x position is shown on the *top* and y position on the *bottom*. The mean value of the difference, Δx and Δy (on the *right*), between the two positions gives the relative misalignment between the planes, and the σ_x and σ_y values represent the width of the beam, broadened by multiple scattering. The values obtained after fitting with Gaussian functions (*red lines*) are: $\Delta x = 672 \pm 3\,\mu$m, $\sigma_x = 1074 \pm 9\,\mu$m, $\Delta y = 781 \pm 3\,\mu$m and $\sigma_y = 999 \pm 8\,\mu$m.

Similar to telescope plane alignment, DUT alignment is based on residual distribution. The first step towards this alignment is to calculate the intersection between the extrapolated reference tracks and the DUT plane, using z-positions of the planes measured with high precision on the setup. The next step is to convert the points of intersection into local DUT coordinates. The DUT rotations around x- and y-axis are not taken into account. The x- and y-axis are parallel to the columns and rows. The origin of the DUT reference frame is chosen arbitrarily for this step.

The alignment parameters x^a_{dut} and y^a_{dut} are estimated in the same procedure as describe above for the reference planes. The considered residuals are:

$$\Delta x_{dut} = x_{dut} - x_{ref} \quad \text{and} \quad \Delta y_{dut} = y_{dut} - y_{ref} \quad , \tag{2.3}$$

where (x_{dut}, y_{dut}) is the position of a DUT cluster and (x_{ref}, y_{ref}) the intersection of the mini-telescope track from reference planes and the DUT plane, however only the y-direction can be determined.

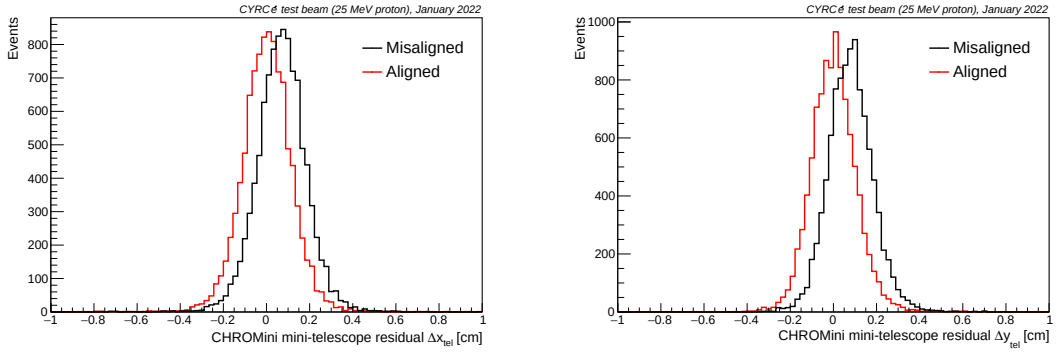

Figure 2.16: Residual distributions Δx_{tel} (left) and Δy_{tel} (right) before (black) and after (red) offline alignment.

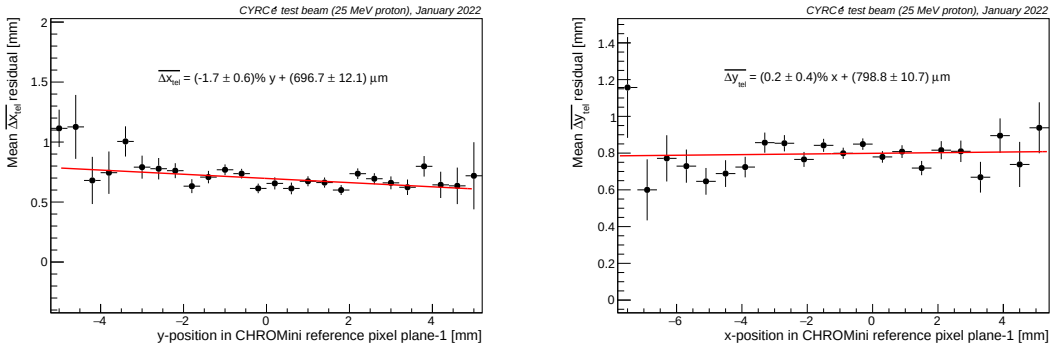

Figure 2.17: Mean residual distributions $\overline{\Delta x_{tel}}$ (left) and $\overline{\Delta y_{tel}}$ (right) as a function of the y- and x-coordinate plane-1 position respectively, in the misaligned case.

2.5.3 Characterisation of the DUT

2.5.3.1 Hit efficiency

The definition of the DUT hit efficiency is:

$$\epsilon_{dut} = \frac{N(\text{DUT hit associated with a reference track})}{N(\text{reference track})} \quad , \tag{2.4}$$

where $N(\text{reference track})$ is the number of selected reference tracks and $N(\text{DUT hit associated with a reference track})$ is the number of events with a DUT cluster hit associated with those tracks.

The criterion of association between the reference track and DUT hit is based on the distance between the reference track and the hit within a given window d:

$$d = |\Delta y_{dut}| \quad , \tag{2.5}$$

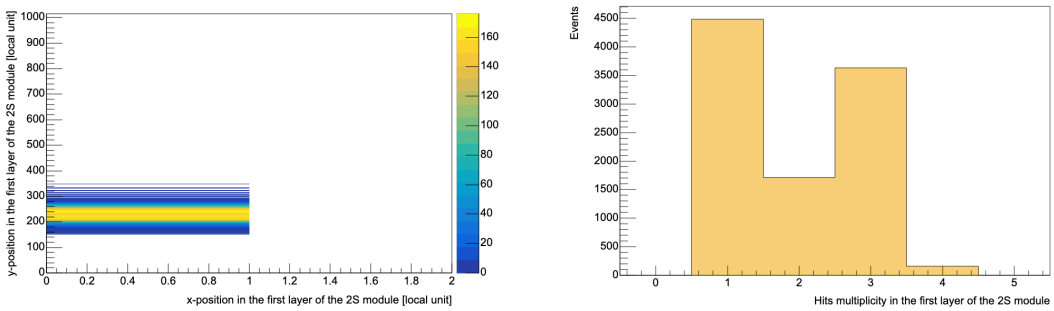

Figure 2.18: Beam profile (*left*) and hits multiplicity distribution (*right*) in the first plane of the 2S module (DUT). The beam was hitting only on the left side of the module consisting of two columns of strips in the x-direction.

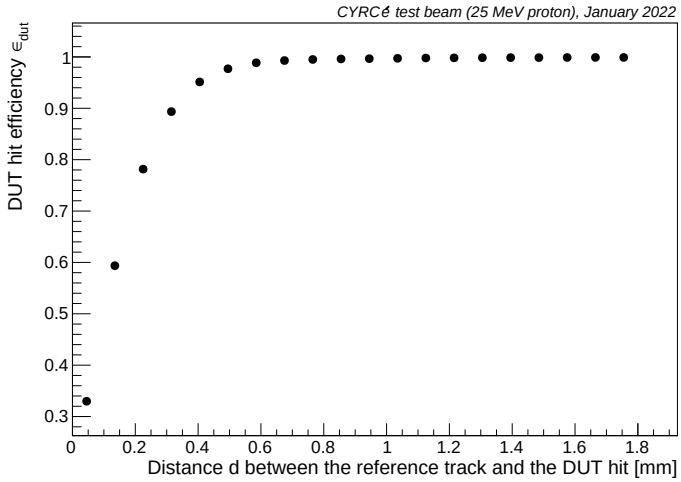

Figure 2.19: Hit efficiency as a function of the window width of acceptance.

with Δy_{dut} the previously defined y-residual.

The DUT hit efficiency is represented as a function of the distance d in the Fig. 2.19. The error on the hit efficiency is calculated according to the Bayesian method in Ref. [40], but are invisible on the figure due the large number of tracks (around 10 000 tracks). From Figure 2.19 a selection criterion on d is chosen, for example a conservative threshold of $d < 0.8\,\text{mm}$ (well after the rising efficiency slope) to include events with degraded resolutions.

2.5.3.2 Spatial correlations between DUT and reference track

The pointing resolution here refers to the uncertainty on the position of the track measured by the pixel planes and extrapolated to the plane of the investigated sensor module (DUT).

The width of the distributions in x- and y-direction is given by the width of the residuals distribution Δx_{dut} and Δy_{dut}. In this study, only the resolution in y-direction can be discussed.

The residual distributions between the telescope planes Δy_{tel} and between the extrapolated track position and the DUT hit position Δy_{dut} are shown in Fig. 2.20.

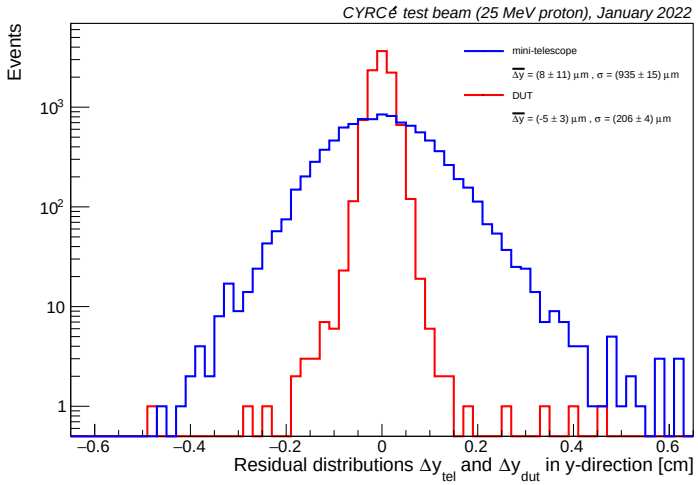

Figure 2.20: Distribution of residuals between hits of the two Pixel planes in *blue* and the distribution of dy_1, the deviation between extrapolated and real particle trajectory, in *red*.

The characterisation of the width of these distributions must take into account the non-Gaussian nature due to multiple Coulomb scattering (impacting the tails) and asymmetries caused by biases in the reconstruction of algorithms.

The wide distribution of Δy_{tel} is dominated by the multiple scattering in the first Pixel plane (nearly 1 mm equivalent of silicon) and the materiel of the DUT (two planes of 290 μm silicon) in between the two planes and measures the widening of the beam as already remarked above. The extrapolated track, a straight line, can deviate from the real particle trajectory due to the multiple scattering in the DUT, and only in the DUT, as becomes clear by the geometry shown in Fig. 2.21.

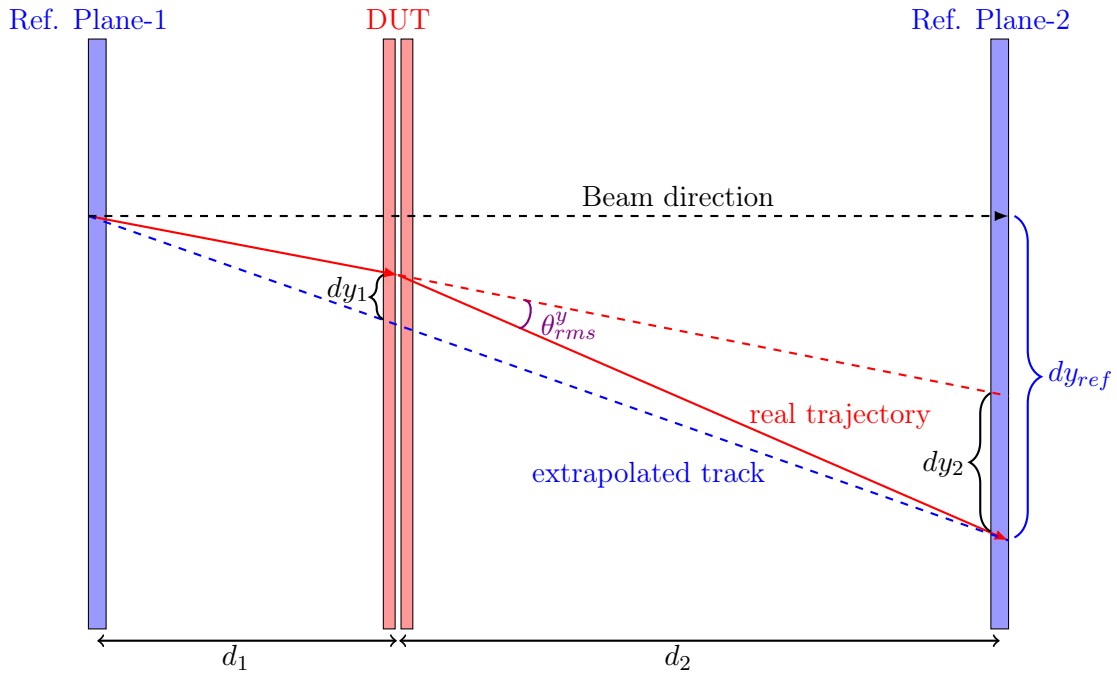

Figure 2.21: Schematic view of the geometry and the distances involved. dy_1 is the deviation between the real particle track (*red line*) and the extrapolated track position (*blue dashed line*). In the considered beam test setup, the distances d_1 and d_2 are 14 and 28 mm, respectively.

The total thickness of the two silicon planes of the DUT of about 600 microns of silicon corresponds to 0.0064 X_0 radiation length. Calculating the multiple scattering angular diffusion we find:

$$\theta^y_{rms} = \frac{13.6 MeV/c}{p \cdot \beta} Z \sqrt{\frac{x}{X_0}} \cdot \left[1 + 0.038 \cdot \ln\left(\frac{x}{X_0}\right)\right] \tag{2.6}$$

$$= \frac{13.6 MeV/c}{2E_{kin}} \sqrt{0.0064} = 22.5\,\text{mrad} \tag{2.7}$$

$$dy_2 = \theta^y_{rms} \cdot d_2 \tag{2.8}$$

$$dy_1 = dy_2 \cdot \frac{d_1}{d_1 + d_2} = 210\,\mu\text{m} \quad . \tag{2.9}$$

The value of dy_1, which should be compared to the RMS of the distribution

Δy_{dut}, is nearly 10 times larger than the intrinsic spacial resolution of the Si-module with a pitch of 90 μm giving about $\sigma_{dut} = \frac{90}{\sqrt{12}} = 26\,\mu$m for the intrinsic spatial resolution of the detector.

The observed residuals in Fig. 2.20, the red histogram, corresponds exactly to the expectation for multiple scattering.

2.6 Conclusion

The results presented in this chapter show the operation readiness of the test facility installed at the new beam line for tests and irradiations of CMS detectors at the CYRCé cyclotron at IPHC, Strasbourg. The reference telescope composed out of two planes of CMS Pixel detectors is operational and the performance is as expected, taking into account the large multiple scattering and energy deposition of the 25 MeV proton beam. This allows to make a first measurement on a 2S-CMS tracker module (DUT) and to measure its efficiency and to correlate hits in the DUT with tracks of the telescope. This correlation will allow in the future to measure the performance of the CMS detectors at locally high occupancy and high rate.

Conclusion

Les résultats présentés dans ce chapitre témoignent de la capacité opérationnelle de l'installation de test mise en place sur la nouvelle ligne de faisceau destinée aux tests et irradiations des détecteurs CMS au cyclotron CYRCé de l'IPHC à Strasbourg. Le télescope de référence composé de deux plans de détecteurs Pixel CMS fonctionne conformément aux attentes, malgré la forte diffusion multiple et le dépôt d'énergie du faisceau de protons de 25 MeV. Cela permet de réaliser une première mesure sur un module de trajectographie 2S (DUT) prévue pour la jouvence du détecteur CMS, de mesurer son efficacité et de corréler les coups dans le DUT avec les traces reconstruites avec le télescope. Cette corrélation permettra ultérieurement de mesurer les performances des détecteurs CMS à une occupation et un taux localement élevés.

Chapter 3

Measurement of the tau lepton polarisation in Z boson decays

Contents

3.1 Introduction

The difference of the neutral weak couplings to the right- and left-handed fermions results in the polarisation of fermion-antifermion pairs in the decay of the Z boson.

The τ lepton polarisation is defined as $P_\tau = \frac{\hat{\sigma}_+ - \hat{\sigma}_-}{\hat{\sigma}_+ + \hat{\sigma}_-}$, where $\hat{\sigma}_+$ and $\hat{\sigma}_-$ are the cross-sections of the production of the τ^- with positive and negative helicity, respectively.

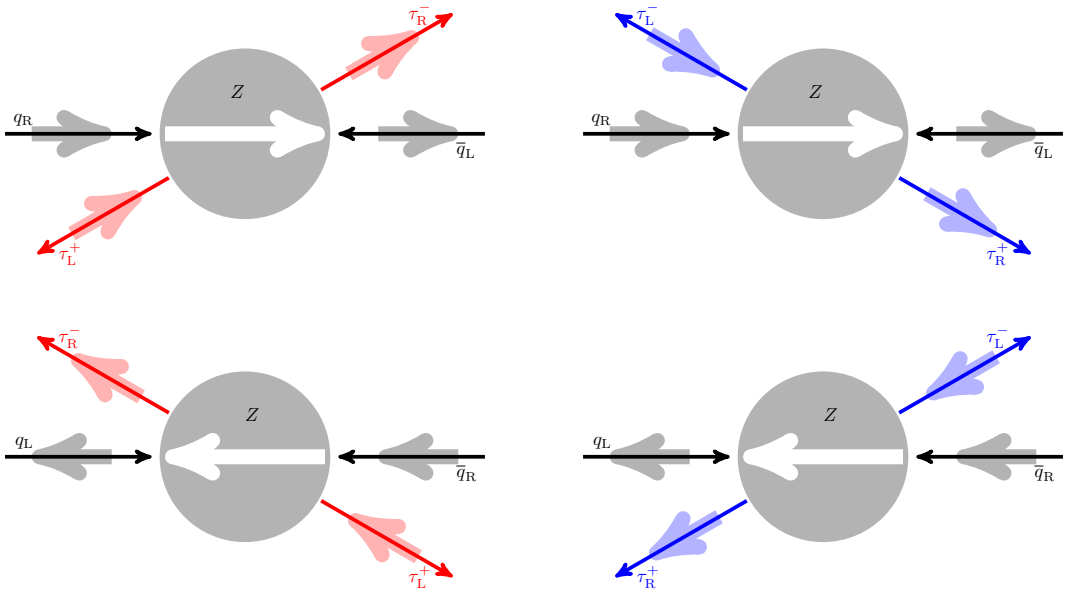

Figure 3.1: Four possible helicity states of incoming quarks and outgoing τ lepton. Thin arrows depict the direction of movement and the thick arrows show the helicity of particles. The angle θ_τ is the scattering angle of the τ^- with respect to the quark momentum in the rest frame of the Z boson.

The differential cross-section of the process $q\bar{q} \to \mathrm{Z} \to \tau^+\tau^-$ in the lowest order can be expressed as [41]:

$$\frac{d\hat{\sigma}}{d\cos\theta_\tau} = F_0(\hat{s})(1+\cos^2\theta_\tau)+2F_1(\hat{s})\cos\theta_\tau - h_\tau[F_2(\hat{s})(1+\cos^2\theta_\tau)+2F_3(\hat{s})\cos\theta_\tau] \ . \quad (3.1)$$

Here θ_τ is the scattering angle of the τ^- with respect to the direction of the incoming quark in the rest frame of the Z boson as illustrated in Fig. 3.1, h_τ the helicity of the τ^- and $\hat{s}$ the squared centre-of-mass energy of the $q\bar{q}$ system. The $F_i(\hat{s})$ are structure functions depending on the neutral current vector and axial-vector couplings of the initial quark flavour and the τ lepton. The total cross-section summed over τ helicity states reads:

$$\hat{\sigma} = \sum_{h_\tau} \int \frac{d\hat{\sigma}}{d\cos_{\theta_\tau}} d\cos\theta_\tau \quad . \quad (3.2)$$

From the cross-section (3.1) the following quantities are defined: the forward-backward asymmetry of the cross-section A^{FB}, the polarisation of the τ^- A_{pol}, and the forward-backward polarisation asymmetry A_{pol}^{FB}:

$$A^{FB} = \frac{1}{\hat{\sigma}}[\hat{\sigma}(\cos\theta_\tau > 0) - \hat{\sigma}(\theta_\tau < 0)] = \frac{3F_1(\hat{s})}{4F_0(\hat{s})} \quad , \tag{3.3}$$

$$A_{pol} = P_\tau = \frac{1}{\hat{\sigma}}[\hat{\sigma}(h_\tau = +1) - \hat{\sigma}(h_\tau = -1)] = -\frac{F_2(\hat{s})}{F_0(\hat{s})} \quad , \tag{3.4}$$

$$A^{FB}_{pol} = \frac{1}{\hat{\sigma}}[A_{pol}(\cos\theta_\tau > 0) - A_{pol}(\cos\theta_\tau < 0)] = -\frac{3F_3(\hat{s})}{4F_0(\hat{s})} \quad . \tag{3.5}$$

The cross sections include contributions from Z^0 exchange, photon exchange and photon-Z^0 interference. The contributions from the photon exchange cancel in the numerator of the asymmetries. If $\sqrt{\hat{s}}$ is equal to the mass of the Z-boson M_Z, the following holds:

$$\begin{aligned} A^{FB} &\approx \frac{3}{4}A_f A_\tau \quad , \\ A_{pol} &\approx -A_\tau \quad , \\ A^{FB}_{pol} &\approx \frac{3}{4}A_f \quad ; \end{aligned} \tag{3.6}$$

where $A_\tau = \frac{2v_\tau a_\tau}{v_\tau^2 + a_\tau^2}$ and v_τ and a_τ the effective neutral current vector and axial vector couplings of the τ lepton. The vector and axial vector couplings of the initial state fermions, v_f and a_f, define the quantity $A_f = \frac{2v_f a_f}{v_f^2 + a_f^2}$. The τ lepton couplings are defined as:

$$v_\tau = I^3_W - 2Q\sin^2\theta^\tau_{eff} \quad , \tag{3.7}$$

$$a_\tau = I^3_W \quad ; \tag{3.8}$$

where I^3_W is the third component of the weak isospin of the τ lepton and $Q = -1$ is the charge of the τ^-. Hence, a measurement of the polarisation P_τ provides a precise determination of $\sin\theta^\tau_{eff}$ from τ lepton couplings only. It is, in addition, a test of the hypothesis of lepton universality in the neutral current.

Since τ leptons decay inside the detector their polarisation is measured by analysing kinematic quantities depending on angles of the decay products with respect to the direction of flight of the τ lepton or unstable particles in the decay chain. In this chapter a measurement of the average τ lepton polarisation $P_\tau = A_{pol}$ is presented using $Z \to \tau\tau$ events with $\sqrt{\hat{s}}$ near the mass of the Z-boson. The data sample collected with the CMS detector in 2016 at 13 TeV centre-of-mass energy corresponding to an integrated luminosity of 36.3 fb^{-1} is used [42]. The measurement is performed using all possible τ lepton decays identified in the CMS detector. The polarisation is obtained from a fit to a channel specific observable calculated from the momenta of the τ lepton and their decay products or the momenta of both τ leptons in the event and their corresponding decay products. From P_τ, averaged over the mass range of the Z-boson, the weak mixing angle θ_W is determined taking into account photon-Z^0 interference and the ratio between u- and d-type quarks in the formation of the Z-boson.

Measurements of the τ polarisation have been performed previously in e^+ e^- annihilations in experiments at LEP at centre-of-mass energies near M_Z [1–4] and in the ATLAS experiment at LHC at $\sqrt{s} = 8$ TeV [5].

3.2 Datasets

This analysis is based on proton-proton collision data at a centre-of-mass energy of 13 TeV collected in 2016 with the CMS detector at the CERN LHC. The analysed data corresponds to an integrated luminosity of $36.3\,\text{fb}^{-1}$. A summary of the datasets and their associated run ranges and integrated luminosities is given in Table 3.1. Only data that is collected and fully certified by the CMS collaboration is used for this analysis.

The signal and background Monte Carlo (MC) samples in this analysis are listed in Table 3.2. The W+jets, and $Z \to \tau\tau$ samples are generated with MadGraph5 while the single top and $t\bar{t}$ samples are generated with Powheg. The diboson samples are generated either with MadGraph5 or Powheg. The Pythia8 generator, with the tune *CUETP8M1*, is used to model the parton shower and hadronization processes, as well as tau decays in all samples. The *NNPDF3.0* parton distribution functions are used. A problem was encountered using the official Drell-Yan(DY)+jets samples, which are produced with MadGraph5 and then processed by Pythia8. The tau polarisation flag is not transmitted to Pythia8. In the standard settings of Pythia8 steering cards, Pythia8 ignores the *Les Houches Event* (LHE) flag of MadGraph5 and proceeds with its own calculation of the most probable tau polarisation. The flag concerned in Pythia8 is TauDecays:externalMode, which has a default value = 2 but has to be set to TauDecays:externalMode = 0 in order to force the tau polarisation to the value generated by MadGraph5. The consequence is a inconsistency between the MadGraph5 generation and the Pythia8 processing: the MadGraph5 generation is performed using a leading-order (LO) weak mixing angle of $\sin^2\theta_W^{\text{eff}} = 0.222246$, whereas Pythia8 uses an effective weak mixing angle of $\sin^2\theta_W^{\text{eff}} = 0.2315$. (In fact in MadGraph5 it is the Fermi constant G_F which is specified and the W-mass and the weak mixing angle is calculated in LO from there). This inconsistency led to an uncontrolled bias in the comparison of *reconstructed* and *generated* polarisation. Therefore a special set of Drell-Yan simulated data was produced using the standard MadGraph5 parameters of the official production, but using the TauDecays:externalMode = 0 flag for the Pythia8 processing. A dataset of about 60 million events was produced in this way and also processed through the detector simulation and reconstruction chain. All MC samples used for the analysis can be found in Table 3.2.

3.3 Object reconstruction

The object reconstruction is based on the *particle flow* (PF) algorithm [6] which relies on the information from the different subdetectors to reconstruct muons, electrons and charged or neutral hadrons. These objects are combined to form more complex objects,

Channel	Dataset	Run range	Integrated Luminosity
$\tau_e\tau_\mu$	/MuonEG/Run2016B-17Jul2018-ver2-v1/MINIAOD	273158–275376	5.829 /fb
	/MuonEG/Run2016C-17Jul2018-v1/MINIAOD	275657–276283	2.618 /fb
	/MuonEG/Run2016D-17Jul2018-v1/MINIAOD	276315–276811	4.286 /fb
	/MuonEG/Run2016E-17Jul2018-v2/MINIAOD	276831–277420	4.066 /fb
	/MuonEG/Run2016F-17Jul2018-v1/MINIAOD	277981–278808	3.135 /fb
	/MuonEG/Run2016G-17Jul2018-v1/MINIAOD	278820–280385	7.653 /fb
	/MuonEG/Run2016H-17Jul2018-v1/MINIAOD	281613–284044	8.740 /fb
$\tau_\mu\tau_\mathrm{h}$	/SingleMuon/Run2016B-17Jul2018-ver2-v1/MINIAOD	273158–275376	5.829 /fb
	/SingleMuon/Run2016C-17Jul2018-v1/MINIAOD	275657–276283	2.618 /fb
	/SingleMuon/Run2016D-17Jul2018-v1/MINIAOD	276315–276811	4.286 /fb
	/SingleMuon/Run2016E-17Jul2018-v1/MINIAOD	276831–277420	4.066 /fb
	/SingleMuon/Run2016F-17Jul2018-v1/MINIAOD	277981–278808	3.135 /fb
	/SingleMuon/Run2016G-17Jul2018-v1/MINIAOD	278820–280385	7.653 /fb
	/SingleMuon/Run2016H-17Jul2018-v1/MINIAOD	281613–284044	8.740 /fb
$\tau_e\tau_\mathrm{h}$	/SingleElectron/Run2016B-17Jul2018-ver2-v1/MINIAOD	273158–275376	5.829 /fb
	/SingleElectron/Run2016C-17Jul2018-v1/MINIAOD	275657–276283	2.618 /fb
	/SingleElectron/Run2016D-17Jul2018-v1/MINIAOD	276315–276811	4.286 /fb
	/SingleElectron/Run2016E-17Jul2018-v1/MINIAOD	276831–277420	4.066 /fb
	/SingleElectron/Run2016F-17Jul2018-v1/MINIAOD	277981–278808	3.135 /fb
	/SingleElectron/Run2016G-17Jul2018-v1/MINIAOD	278820–280385	7.653 /fb
	/SingleElectron/Run2016H-17Jul2018-v1/MINIAOD	281613–284044	8.740 /fb
$\tau_\mathrm{h}\tau_\mathrm{h}$	/Tau/Run2016B-17Jul2018-ver2-v1/MINIAOD	273158–275376	5.829 /fb
	/Tau/Run2016C-17Jul2018-v1/MINIAOD	275657–276283	2.618 /fb
	/Tau/Run2016D-17Jul2018-v1/MINIAOD	276315–276811	4.286 /fb
	/Tau/Run2016E-17Jul2018-v1/MINIAOD	276831–277420	4.066 /fb
	/Tau/Run2016F-17Jul2018-v1/MINIAOD	277981–278808	3.135 /fb
	/Tau/Run2016G-17Jul2018-v1/MINIAOD	278820–280385	7.653 /fb
	/Tau/Run2016H-17Jul2018-v1/MINIAOD	281613–284044	8.740 /fb

Table 3.1: List of 2016 (referred to as *legacy* and processed with `CMSSW` version 94X) datasets included in the analysis. Mini Analysis Object Data (miniAOD) format is used for data.

like τ_h candidates or missing momentum $E_\mathrm{T}^\mathrm{miss}$. More details are given in the following sections about the objects used in this analysis.

3.3.1 Muon identification

Muons are required to satisfied the *medium* criteria for identification as recommended by the *Muon Physics Object group* [43]. These requirements are:

Process	Dataset name	Cross-section [pb]
Signal		
$Z \to \tau\tau$	/DYJetsToTauTau_M-50_TuneCUETP8M1_13TeV-madgraphMLM-pythia8[9,10]	2025.74 (NNLO)
Background		
$Z \to LL(L = e, \mu)$	/DYJetsToLL_M-50_TuneCUETP8M1_13TeV-madgraphMLM-pythia8[7]	6077.22 (NNLO)
Z + 1jet	/DY1JetsToLL_M-50_TuneCUETP8M1_13TeV-madgraphMLM-pythia8[1]	1012.5 (LO)
Z + 2jets	/DY2JetsToLL_M-50_TuneCUETP8M1_13TeV-madgraphMLM-pythia8[5]	332.8 (LO)
Z + 3jets	/DY3JetsToLL_M-50_TuneCUETP8M1_13TeV-madgraphMLM-pythia8[5]	101.8 (LO)
Z + 4jets	/DY4JetsToLL_M-50_TuneCUETP8M1_13TeV-madgraphMLM-pythia8[5]	54.8 (LO)
Low mass $Z \to LL$	/DYJetsToLL_M-10to50_TuneCUETP8M1_13TeV-madgraphMLM-pythia8[5]	18610.0 (LO)
W+jets	/WJetsToLNu_TuneCUETP8M1_13TeV-madgraphMLM-pythia8[5,7]	61526.7 (NNLO)
W + 1jet	/W1JetsToLNu_TuneCUETP8M1_13TeV-madgraphMLM-pythia8[1]	9644.5 (LO)
W + 2jets	/W2JetsToLNu_TuneCUETP8M1_13TeV-madgraphMLM-pythia8[5,6]	3144.5 (LO)
W + 3jets	/W3JetsToLNu_TuneCUETP8M1_13TeV-madgraphMLM-pythia8[5,6]	954.8 (LO)
W + 4jets	/W4JetsToLNu_TuneCUETP8M1_13TeV-madgraphMLM-pythia8[3,5,6]	485.6 (LO)
EWK W^- + 2jets	/EWKWMinus2Jets_WToLNu_M-50_13TeV-madgraph-pythia8[5,6,7]	20.25
EWK W^+ + 2jets	/EWKWPlus2Jets_WToLNu_M-50_13TeV-madgraph-pythia8[5,6,7]	25.62
EWK Z + 2jets	/EWKZ2Jets_ZToLL_M-50_13TeV-madgraph-pythia8[6,7,8]	3.987
	/EWKZ2Jets_ZToNuNu_13TeV-madgraph-pythia8[5,6,7]	10.01
$t\bar{t}$	/TT_TuneCUETP8M2T4_13TeV-powheg-pythia8[1]	831.76
Single top	/ST_t-channel_antitop_4f_inclusiveDecays_13TeV-powhegV2-madspin-pythia8_TuneCUETP8M1[1]	80.95
	/ST_t-channel_top_4f_inclusiveDecays_13TeV-powhegV2-madspin-pythia8_TuneCUETP8M1[1]	136.02
	/ST_tW_antitop_5f_inclusiveDecays_13TeV-powheg-pythia8_TuneCUETP8M1[2]	35.6
	/ST_tW_top_5f_inclusiveDecays_13TeV-powheg-pythia8_TuneCUETP8M1[2]	35.6
VV	/VVTo2L2Nu_13TeV_amcatnloFXFX_madspin_pythia8[5,6]	11.95
$W\gamma$	/WGToLNuG_01J_5f_TuneCUETP8M1_13TeV-amcatnloFXFX-pythia8[1,2]	178.4
	/WGToLNuG_TuneCUETP8M1_13TeV-amcatnloFXFX-pythia8[2,3,4]	489.0
$W\gamma^*$	/WGstarToLNuEE_012Jets_13TeV-madgraph[1]	3.526
	/WGstarToLNuMuMu_012Jets_13TeV-madgraph[1]	2.793
WW	/WWTo1L1Nu2Q_13TeV_amcatnloFXFX_madspin_pythia8[5]	49.997
WZ	/WZJToLLLNu_TuneCUETP8M1_13TeV-amcnlo-pythia8[1]	4.708
	/WZTo1L1Nu2Q_13TeV_amcatnloFXFX_madspin_pythia8[5]	10.71
	/WZTo1L3Nu_13TeV_amcatnloFXFX_madspin_pythia8[5]	3.05
	/WZTo2L2Q_13TeV_amcatnloFXFX_madspin_pythia8[5]	5.595
ZZ	/ZZTo2L2Q_13TeV_amcatnloFXFX_madspin_pythia8[1]	3.22
	/ZZTo4L_13TeV-amcatnloFXFX-pythia8[6]	1.212

[1] /RunIISummer16MiniAODv3-PUMoriond17_94X_mcRun2_asymptotic_v3-v1/MINIAODSIM
[2] /RunIISummer16MiniAODv3-PUMoriond17_94X_mcRun2_asymptotic_v3-ext1-v1/MINIAODSIM
[3] /RunIISummer16MiniAODv3-PUMoriond17_94X_mcRun2_asymptotic_v3-ext2-v1/MINIAODSIM
[4] /RunIISummer16MiniAODv3-PUMoriond17_94X_mcRun2_asymptotic_v3-ext3-v1/MINIAODSIM
[5] /RunIISummer16MiniAODv3-PUMoriond17_94X_mcRun2_asymptotic_v3-v2/MINIAODSIM
[6] /RunIISummer16MiniAODv3-PUMoriond17_94X_mcRun2_asymptotic_v3-ext1-v2/MINIAODSIM
[7] /RunIISummer16MiniAODv3-PUMoriond17_94X_mcRun2_asymptotic_v3-ext2-v2/MINIAODSIM
[8] /RunIISummer16MiniAODv3-PUMoriond17_94X_mcRun2_asymptotic_v3-v3/MINIAODSIM
[9] /cgrimaul-RunIISummer16MiniAODv3-PUMoriond17_94X_mcRun2_asymptotic_v3_ext1-bd3e7bcff6c9bcad356ea4ed7e4f08b4/USER
[10] /cgrimaul-RunIISummer16MiniAODv3-PUMoriond17_94X_mcRun2_asymptotic_v3_ext2-bd3e7bcff6c9bcad356ea4ed7e4f08b4/USER

Table 3.2: MC signal and background (referred to as *legacy* and processed with CMSSW version 94X) samples included in the analysis. All samples are generated for p–p collisions at a centre-of-mass energy of 13 TeV. Samples used in this analysis are reconstructed and stored in miniAOD format. When available, all sample extensions are used.

- The muon is identified as a muon by the *Particle Flow* and is either a *Global* or *Tracker* muon.
- The impact parameters d_{xy} and d_z between the muon track and the primary vertex are restricted as $d_{xy} < 0.045\,\text{cm}$ and $d_z < 0.2\,\text{cm}$ to ensure that the muon is associated with the primary vertex.
- The muon must have a high fraction (at least 80%) of valid tracker hits.

In addition, one of the following two sets of criteria must be satisfied:
Good *Global* muon

- The muon is reconstructed as a *Global* muon;
- The χ^2 /ndof of the global track fit is smaller than 3;
- The χ^2 of the tracker-standalone position match is smaller than 12;
- The χ^2 of the track kink finder is less than 20;
- The muon segment compatibility is > 0.303.

or **Tight segment compatibility**

- The muon segment compatibility is > 0.451.

In this analysis, muons are selected with $p_{\mathrm{T}} > 10\,\mathrm{GeV}$ and $|\eta| < 2.4$.

3.3.2 Electron identification

Electrons are required to be identified as electron by the `PF` algorithm. In addition, electrons must pass identification working points provided by a multivariate analysis (MVA) [44] based on a Boosted Decision Tree (BDT) which uses track quality, shower shapes and kinematic quantities as input.

For electrons selected in this analysis we require the electron to pass the 90% efficiency working point of the training that does not include isolation variables. In this analysis, electrons are selected with $p_{\mathrm{T}} > 10\,\mathrm{GeV}$ and $|\eta| < 2.5$.

3.3.3 Lepton isolation

Leptonic τ lepton decays, labelled τ_e and τ_μ in the following, are identified as isolated electrons and muons. The relative isolation $I_{rel}(\ell)$ is defined differently depending on the lepton ℓ (e, μ).

3.3.3.1 Muon isolation

The isolation is based on photon and neutral and charged hadron particle-flow candidates within a cone size of $\Delta R < 0.4$ centered on the lepton direction where $\Delta R = \sqrt{(\Delta\eta)^2 + (\Delta\phi)^2}$ refers to the distance from the muon to a given charged particles. A relative combined isolation variable is defined as:

$$I_{rel}(\mu) = \frac{\sum\limits_{\text{ch. hadr.}} p_{\mathrm{T}} + \max\left(0, \sum\limits_{\text{n. hadr.}} p_{\mathrm{T}} + \sum\limits_{\gamma} p_{\mathrm{T}} - 0.5 \sum\limits_{PU} p_{\mathrm{T}}\right)}{p_{\mathrm{T}}^{\mu}} \quad , \tag{3.9}$$

where $\sum_{\text{ch. hadr.}} p_{\text{T}}$ is the scalar sum of the transverse momenta of all charged hadronic particles originating from the primary vertex. The sum $\sum_{\text{n. hadr.}} p_{\text{T}} + \sum_{\gamma} p_{\text{T}}$ represents a similar quantity for all photon and neutral hadron candidates. The contribution of photons and neutral hadrons originating from pileup vertices is estimated from the scalar sum of the transverse momenta of charged hadrons in the cone originating from pileup vertices, $\sum_{PU}$. This sum is multiplied by a factor of 1/2, which corresponds approximately to the ratio of neutral to charged hadron production in the hadronisation process of inelastic pp collisions, as estimated from simulation.

3.3.3.2 Electron isolation

The isolation is based on photon and neutral and charged hadron particle-flow candidates within a cone size of $\Delta R < 0.3$ centered on the lepton direction but used a different method to estimate the neutral particles due to pileup, namely the rho-effective-area method.

The pileup in this method is estimated as PU $= \rho \cdot EA$, where ρ is the event-specific average pile-up energy density per unit area in the $\phi - \eta$ plane and the EA is the effective area specific to the given type of isolation. The rho-effective-area subtracted relative combined isolation variable is defined as:

$$I_{rel}(e) = \frac{\sum_{\text{ch. hadr.}} p_{\text{T}} + \max\left(0, \sum_{\text{n. hadr.}} p_{\text{T}} + \sum_{\gamma} p_{\text{T}} - \rho \cdot EA\right)}{p_{\text{T}}^{e}} \quad , \tag{3.10}$$

where the EA is measured in bins of η.

3.3.4 Tau reconstruction

The reconstruction of the momentum of the decay products of the τ lepton in hadronic decays τ_{h}, hereafter referred to as visible momentum of the τ lepton, and the decay channel identification is performed by the *Hadron-Plus-Strips* algorithm (`HPS`) [7]. This algorithm is intended to reconstruct individual τ lepton decay modes exploiting the excellent performance of the Particle Flow algorithm [6]. Combining the information from all CMS sub-detectors the Particle Flow algorithm reconstructs individual charged hadrons, neutral hadrons, electrons, photons and muons.

3.3.4.1 Tau decay mode reconstruction

Jets are reconstructed from particle-flow constituents with the anti-k_{T} algorithm [45] with a distance parameter $R = 0.4$. Jets are considered as τ_{h} candidates if they comprise one or three charged hadrons with a net charge of $\pm$1e, and up to two neutral pions. Dedicated attention is given to photons originating from $\pi^0 \to \gamma\gamma$ decays likely to convert to e^+e^- pairs, by collecting the energy of the photon and electron constituents, called strips, in an

area of the pseudorapidity η and the azimuthal angle ϕ around the jet direction. The size of the strip is allowed to vary dynamically in order to account for low p_{T} electrons and photons produced by interactions with the tracker material and multiple bremsstrahlung and conversions. The strips should represent the decay products of π^0s. Depending on the number of charged particles and strips, the reconstructed decays are labeled with a number defined as $\mathrm{DM} = 5 \cdot (N_{h^\pm} - 1) + N_{\mathrm{strips}}$ where $N_{h^\pm}$ is the number of charged particles and N_{strips} the number of strips.

Considering the number of reconstructed strips and charged particles, the following decay modes are reconstructed:

- *onePronqZeroPizero* (DM=0): one charged particle without any strip;
- *onePronqOnePizero* (DM=1): one charged particle and one strip with reconstructed τ_{h} mass $0.3 < m_\tau < 1.3 \cdot \sqrt{p_T/100}$ GeV compatible with the $\rho(770)$ resonance;
- *threeProngZeroPizero* (DM=10): three charged particles without any strip. The τ_{h} mass should be $0.8 < m_\tau < 1.5$ GeV compatible with the $a_1(1260)$ resonance;
- *threeProngOnePizero* (DM=11): three charged particles and one strip.

The visible four-momentum of the τ_h candidate is computed as the sum of the four-momenta of particles identified as τ-lepton decay products.

3.3.4.2 Tau decay mode identification with BDT

In this analysis, since the decay channels of τ_{h} have different polarisation sensitivity, it is fundamental to identify these channels correctly. As explained in the previous paragraph, the reconstruction and the resulting identification of decay modes is currently performed by the *Hadron-Plus-Strips* algorithm.

In order to increase the purity of the reconstructed decay channels, a multi-class Multivariate Analysis (MVA) with a Boosted Decision Tree (BDT) algorithm (using XGBoost library) is used [46] on top of the `HPS` algorithm. The `MVA-DM` was developed for Higgs CP analysis which faced a similar problem of reduced CP sensitivity due to migrations between reconstructed decay modes.

3.3.4.3 MVA training

The input data for the `MVA-DM` training are $H \to \tau\tau$ events (ggH and VFB processes generated with POWHEG in experimental conditions of 2017). The `MVA-DM` is trained on τ_{h} from $\tau_{\mathrm{h}}\tau_{\mathrm{h}}$ or $\tau_\mu\tau_{\mathrm{h}}$ channels with $p_{\mathrm{T}} > 20\,\mathrm{GeV}$. The training is independent of the production process (can also be applied to $\mathrm{Z} \to \tau\tau$ events) and is valid for all three years of the *Run-2*.

3.3.4.4 Performance comparison

In order to compare the MVA decay mode (`MVA-DM`) with the `HPS` algorithm performances, two quantities are introduced (depending on the generated decay mode [DM] g and the reconstructed decay mode r):

$$\text{purity(gen DM = g, reco DM = r)} = \frac{N_{\text{events}}\text{(gen DM = g, reco DM = r)}}{\sum_{g'} N_{\text{events}}\text{(gen DM = g', reco DM = r)}} \quad (3.11)$$

and

$$\text{efficiency(gen DM = g, reco DM = r)} = \frac{N_{\text{events}}\text{(gen DM = g, reco DM = r)}}{\sum_{r'} N_{\text{events}}\text{(gen DM = g, reco DM = r')}} \quad . \quad (3.12)$$

The purity is used to compare the fraction of events generated in a given reconstructed mode, and the efficiency, the fraction of events correctly reconstructed in a given generated mode. These two quantities are measured in $\tau_\mu\tau_\text{h}$ and $\tau_e\tau_\text{h}$ channels after all kinematic selections listed in 3.5 have been applied and are presented in the form of matrices of migrations between τ_h decay modes in Figs. 3.2 and 3.3 for $\tau_\mu\tau_\text{h}$ channel and $\tau_e\tau_\text{h}$ channel, respectively. The total number of events studied to compare the `HPS` and the `MVA-DM` algorithms is identical: the `MVA-DM` is applied on top of the `HPS` and offers a new classification (that is why term predicted is used instead of reconstructed for the MVA decay modes).

In fact, only the diagonal elements of the matrix (for which the reconstructed decay mode matches the generated decay mode) give the purities of the reconstructed modes, the off-diagonal elements give the relative contamination by a different decay mode.

The main 1-prong decays of τ_h are $\tau \to \pi\nu$, $\tau \to \rho\nu \to \pi\pi^0\nu$ and $\tau \to a_1\nu \to \pi 2\pi^0\nu$. Almost all of the $\tau \to a_1\nu \to \pi 2\pi^0\nu$ events (91.7% based on efficiency matrix) are wrongly reconstructed in *onePronqOnePizero* (DM=1) since the `HPS` algorithm cannot efficiently distinguish between two π^0s and only one. In fact, the ECAL deposits from the individual π^0s are very close to each other in the detector and often clustered into a single `PF` gamma candidate. Even in cases of multiple `PF` gamma candidates are reconstructed, it is unpractical to allocate the `PF` gamma to the individual π^0s. Therefore, the `HPS` algorithm tends to group them all into a single strip.

This limitation of the `HPS` algorithm leads to significant contamination in the *onePronqOnePizero* decay mode (DM=1) by these $\tau \to a_1\nu \to \pi 2\pi^0\nu$ events, 32.8% as shown in purity matrix, which have been reduced to 19.6% by the `MVA-DM` algorithm. Other important contaminations in the decay modes used in this analysis are: $\tau \to \pi\pi^0\nu$ events wrongly reconstructed as *onePronqZeroPizero* (DM=0) and $\tau \to 3\pi\pi^0\nu$ events as *threePronqZeroPizero* (DM=10), leading to contaminations of 29.7% and 12.5% of the relevant decay mode respectively, improved to 16.5% and 9.3% respectively.

Figure 3.4 summarises the purity and efficiency for the reconstructed decay modes. Only three decay modes are used in this analysis (more details in Sect. 3.5.4).

3.3.4.5 Background rejection

The `deepTau` discriminator [47] is used in this analysis in order to distinguish τ_{h} from quark and gluon jets, electrons and muons. In fact the `deepTau2017v2p1` discriminator is a deep neural network (DNN) algorithm that returns three outputs: tau against jets, tau against electrons and tau against muons scores providing reduction in jet $\rightarrow \tau_h$, $e \rightarrow \tau_h$ and $\mu \rightarrow \tau_h$ fake rates respectively. The working points for these discriminators used in this analysis are listed in Sect. 3.5.3.

3.3.5 Jets and b-tagging

Jets are clustered from all particle-flow candidates using the anti-k_{T} algorithm [45] with a distance parameter $R = 0.4$. The *slimmedJets* collection from miniAOD dataformat is used and the jet energy is corrected (JEC) from the global tags:
94X_mcRun2_asymptotic_v3 (MC) and *94X_dataRun2_v10* (data).

The `deepCSV` [48] algorithm is used to determine information about the b-tagging status of the jets. Jets with $p_T > 20$ GeV and $|\eta| < 2.4$ are considered b-tagged, if their `deepCSV` discriminator value is larger than 0.6321, corresponding to the medium working point for 2016 data provided by the *b-tag Physics Object group* [49].

This analysis is not sensitive to jets (unlike most $H \rightarrow \tau\tau$ analyses, there is no event classification by number of jets in this analysis).

3.3.6 Missing transverse energy

The missing transverse energy in the event is reconstructed using the PileUp Per Particle Identification (`PUPPI`) algorithm [50] which is more robust against pileup than `PF` MET. The `PUPPI` algorithm assigns weights to `PF` candidates based on the probability that they come from pileup or the primary vertex. Type-I corrections are applied to correct the MET due to inefficiencies in the detector. These corrections propagate the Jet Energy Corrections (JEC) to the MET as:

$$\vec{E}_{\mathrm{T}}^{\mathrm{miss,corr}} = \vec{E}_{\mathrm{T}}^{\mathrm{miss}} - \sum_{\mathrm{jets}} (\vec{p}_{\mathrm{T}}^{\mathrm{corr}} - \vec{p}_{\mathrm{T}}) \quad . \tag{3.13}$$

3.4 Triggers and Filters

The data samples are collected using the triger paths summarised in this section. In addition to the event firing the trigger path, the selected reconstructed leptons of the $\tau\tau$ pair must match the corresponding High-Level trigger (HLT) objects listed in Tables 3.3

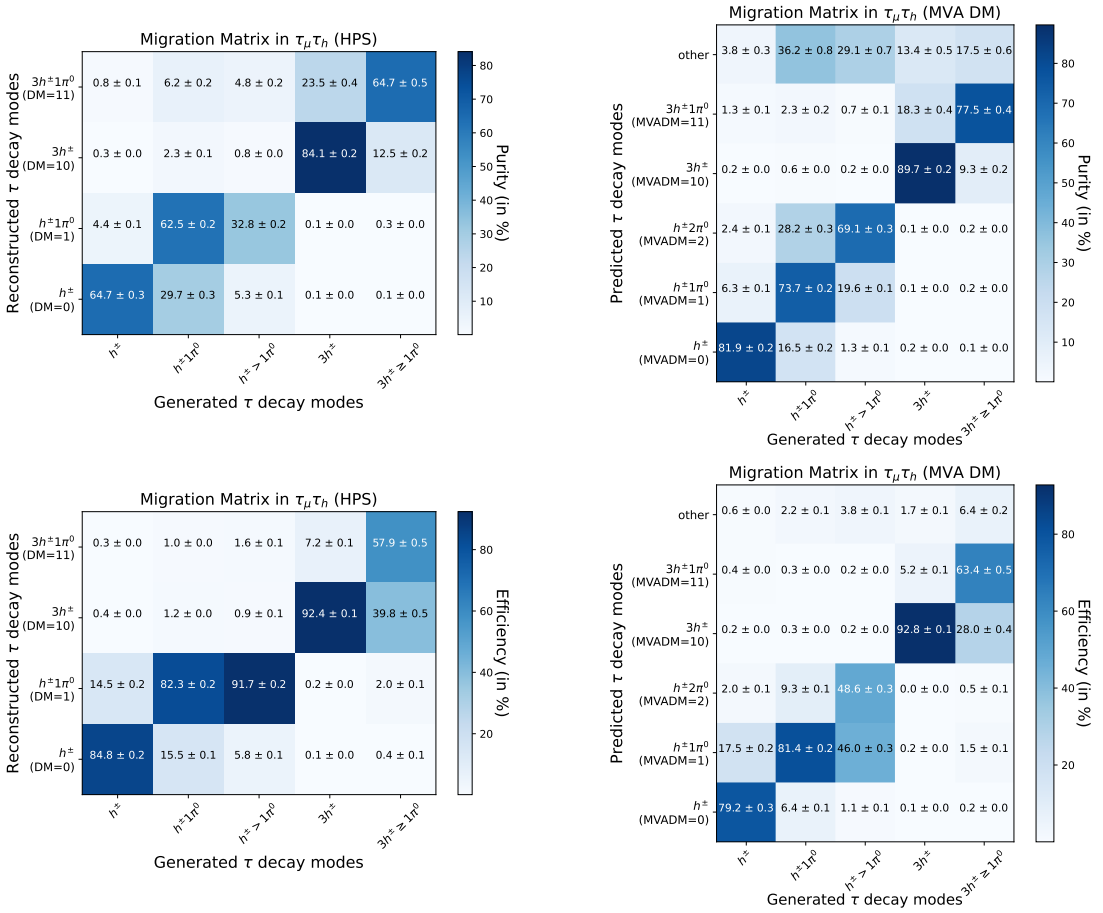

Figure 3.2: Migration matrices for τ_h decay modes in $\tau_\mu\tau_\mathrm{h}$ channel (final selections). Upper part: The purity of the decay mode identification for the `HPS` and the `MVA-DM` algorithms on the left and on the right, respectively. In fact only the diagonal elements of the matrix (generated decay mode matches reconstructed decay mode) give the purities of the reconstructed decay mode, the off-diagonal elements give the relative contaminations by a different decay mode. Lower part: On the diagonal (generated decay mode matches reconstructed decay mode) the efficiencies for reconstructing a given generated decay mode as exactly that decay mode. The probabilities of wrongly reconstruct a decay modes are the off-diagonal for the `HPS` and the `MVA-DM` algorithms on the left and on the right, respectively.

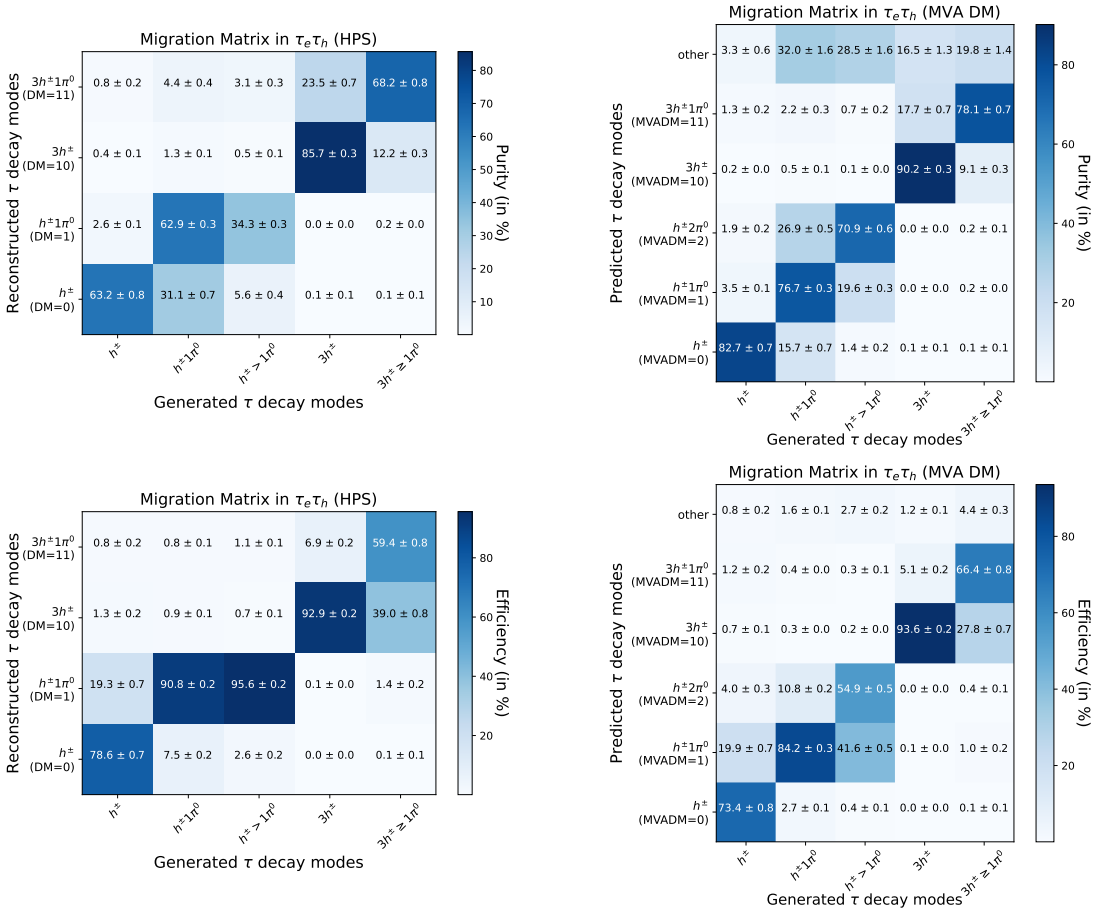

Figure 3.3: Migration matrices for τ_h decay modes in $\tau_e\tau_\mathrm{h}$ channel (final selections). Upper part: The purity of the decay mode identification for the `HPS` and the `MVA-DM` algorithms on the left and on the right, respectively. In fact only the diagonal elements of the matrix (generated decay mode matches reconstructed decay mode) give the purities of the reconstructed decay mode, the off-diagonal elements give the relative contaminations by a different decay mode. Lower part: On the diagonal (generated decay mode matches reconstructed decay mode) the efficiencies for reconstructing a given generated decay mode as exactly that decay mode. The probabilities of wrongly reconstruct a decay modes are the off-diagonal for the `HPS` and the `MVA-DM` algorithms on the left and on the right, respectively.

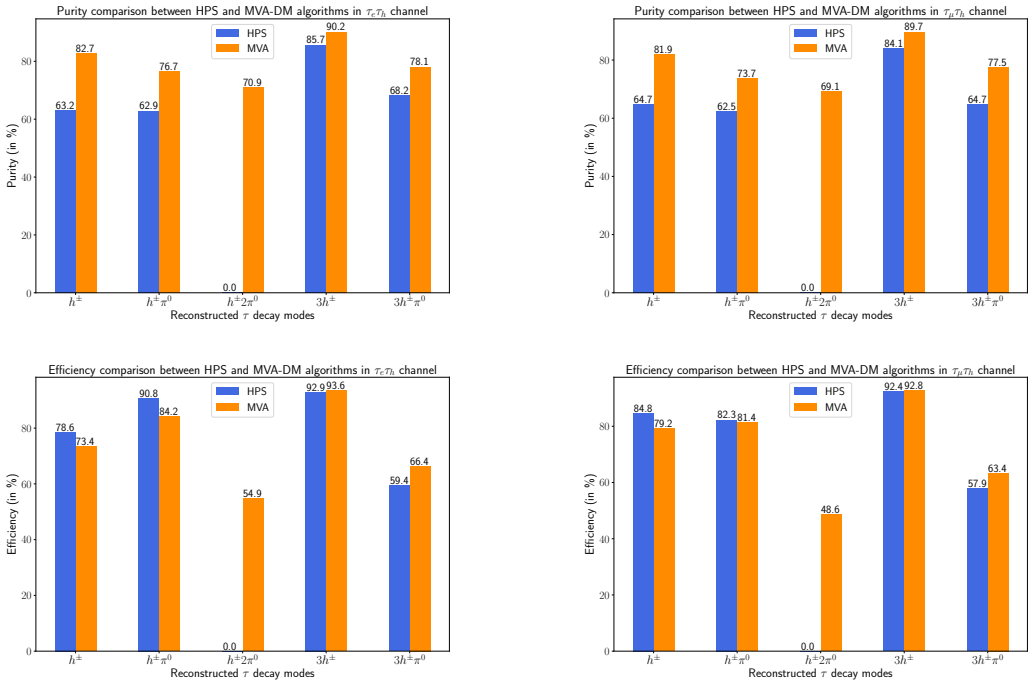

Figure 3.4: Comparison of the decay mode identification efficiency and purity of τ_h. Improved purity (top) and efficiency (bottom) performances, measured with `HPS` and `MVA-DM` algorithms in $\tau_e\tau_\mathrm{h}$ (left) and $\tau_\mu\tau_\mathrm{h}$ (right) channels.

to 3.6 withing a distance $\Delta R = 0.5$ ($\Delta R = 0.4$ for the $\tau_e\tau_\mu$ channel). These trigger paths are applied consistently to data and simulated samples.

3.4.1 $\tau_h\tau_h$ channel

Both τ_h candidates have to be matched to the HLT objects from Table 3.3. The τ_h candidates are only considered as matched to the HLT objects if the offline p_T of the p_T-leading(trailing) τ_h candidate is 10(5) GeV higher than the corresponding HLT path threshold: $p_T(\tau_h^1) > 45\,\text{GeV}$ and $p_T(\tau_h^2) > 40\,\text{GeV}$.

3.4.2 $\tau_\mu\tau_h$ channel

The muon or τ_h candidate in the selected pair must pass a combination of HLT paths from Table 3.4: a logical `OR` combination of single lepton HLT paths and cross-HLT paths is considered. The muon is only considered as matched to the HLT object if its offline p_T is 1 GeV higher than the corresponding HLT path threshold: $p_T > 23$ GeV for the *SingleMuon* HLT path and $p_T > 20$ GeV for the *MuTau* cross-HLT path.

3.4.3 $\tau_e\tau_h$ channel

The electron in the selected pair has to match the corresponding *SingleElectron* HLT path (Table 3.5) and its offline p_T is 5 GeV higher ($p_T > 30$ GeV) than the HLT path threshold.

3.4.4 $\tau_e\tau_\mu$ channel

Both the electron and the muon in the selected pair must pass a combination of HLT paths from Table 3.6. The transverse momentum of either the electron or the muon matched to the high-p_T leg of the HLT path has to exceed 24 GeV to ensure that the HLT path selection is fully efficient.

3.5 Event selection

The $\tau\tau$ final states are categorised according to the number of identified electrons and muons in the event. Events containing a muon and an electron are assigned to the $\tau_e\tau_\mu$ category. If at least a muon and a τ_h candidate is found, but no electron, the event is assigned the $\tau_\mu\tau_h$ final state, similarly it is assigned the $\tau_e\tau_h$ final state if it contains at least one electron candidate, but no muon. If nor electron nor muon is found but two τ_h candidates, the event is assigned to the $\tau_h\tau_h$ final state.

As four different final states are considered, it is needed to make sure each event is selected in a maximum of one of the final states. This is achieved by requiring extra lepton (described in 3.5.1.2) and di-lepton (described in 3.5.1.3) vetoes as the final stage of pair selection for all 4 final state channels. These vetoes require the absence of additional electrons and muons on top of those already part of the selected pair.

HLT path	Tau filter to match
Runs B-C-D-E-F-G	
HLT_DoubleMediumIsoPFTau35_Trk1_eta2p1_Reg	hltDoublePFTau35TrackPt1MediumIsolationDz02Reg
Run H	
HLT_DoubleMediumCombinedIsoPFTau35_Trk1_eta2p1_Reg	hltDoublePFTau35TrackPt1MediumCombinedIsolationDz02Reg

Table 3.3: Triggers used to collect the 2016 data samples for the $\tau_h\tau_h$ channel.

HLT path	Filter(s) to match
	Muon filter
HLT_IsoMu22	hltL3crIsoL1sMu20L1f0L2f10QL3f22QL3trkIsoFiltered0p09
HLT_IsoTkMu22	hltL3fL1sMu20L1f0Tkf22QL3trkIsoFiltered0p09
HLT_IsoMu22_eta2p1	hltL3crIsoL1sSingleMu20erL1f0L2f10QL3f22QL3trkIsoFiltered0p09
HLT_IsoTkMu22_eta2p1	hltL3fL1sMu20erL1f0Tkf22QL3trkIsoFiltered0p09
HLT_IsoMu19_eta2p1_LooseIsoPFTau20	Muon filters
	hltL3crIsoL1sMu18erTauJet20erL1f0L2f10QL3f19QL3trkIsoFiltered0p09
	hltOverlapFilterIsoMu19LooseIsoPFTau20
	Tau filters
	hltPFTau20TrackLooseIsoAgainstMuon
	hltOverlapFilterIsoMu19LooseIsoPFTau20
HLT_IsoMu19_eta2p1_LooseIsoPFTau20_SingleL1	Muon filters
	hltL3crIsoL1sSingleMu18erIorSingleMu20erL1f0L2f10QL3f19QL3trkIsoFiltered0p09
	hltOverlapFilterSingleIsoMu19LooseIsoPFTau20
	Tau filters
	hltPFTau20TrackLooseIsoAgainstMuon
	hltOverlapFilterSingleIsoMu19LooseIsoPFTau20

Table 3.4: Triggers used to collect the 2016 data samples for the $\tau_\mu \tau_h$ channel.

HLT path	Electron filter to match
HLT_Ele25_eta2p1_WPTight_Gsf	hltEle25erWPTightGsfTrackIsoFilter

Table 3.5: Triggers used to collect the 2016 data samples for the $\tau_e\tau_h$ channel.

The kinematic, identification and isolation requirements on these additional leptons are at least as loose as the loosest cuts required for signal electron or muon of the final states. This ensures that the four final states are mutually exclusive and of very good purity.

3.5.1 General event criteria

3.5.1.1 MET filters

Events are required to pass the following $E_{\mathrm{T}}^{\mathrm{miss}}$ filters recommended by the *JetMET Physics Object group* [51]:

- primary vertex filter (Data and MC);
- beam halo filter (Data and MC);
- HBHE noise filter (Data and MC);
- HBHEiso noise filter (Data and MC);
- ECAL TP filter (Data and MC);
- Bad `PF` Muon filter (Data and MC);
- ee badSC noise filter (Data).

3.5.1.2 Extra lepton veto

The events are rejected if they contain a third lepton (loosely selected) that passes the following selection criteria.
Electron:

- $p_T > 10\,\mathrm{GeV}$ and $|\eta| < 2.5$;
- $d_{xy} < 0.045\,\mathrm{cm}$ and $d_z < 0.2\,\mathrm{cm}$;
- pass the 90% efficiency working point of the electron MVA ID (*Fall17-V2*) without isolation variables in the MVA ID training;
- I_e (cone size 0.3) $< 0.3\,p_T^e$.

HLT path	Filters to match
Runs B-C-D-E-F	
HLT_Mu8_TrkIsoVVL_Ele23_CaloIdL_TrackIdL_IsoVL	Electron filter
	hltMu8TrkIsoVVLEle23CaloIdLTrackIdLIsoVLElectronlegTrackIsoFilter
	Muon filter
	hltMu8TrkIsoVVLEle23CaloIdLTrackIdLIsoVLMuonlegL3IsoFiltered8
HLT_Mu23_TrkIsoVVL_Ele12_CaloIdL_TrackIdL_IsoVL	Electron filter
	hltMu23TrkIsoVVLEle12CaloIdLTrackIdLIsoVLElectronlegTrackIsoFilter
	Muon filter
	hltMu23TrkIsoVVLEle12CaloIdLTrackIdLIsoVLMuonlegL3IsoFiltered23
Runs G-H	
HLT_Mu8_TrkIsoVVL_Ele23_CaloIdL_TrackIdL_IsoVL_DZ	Electron filters
	hltMu8TrkIsoVVLEle23CaloIdLTrackIdLIsoVLElectronlegTrackIsoFilter
	hltMu8TrkIsoVVLEle23CaloIdLTrackIdLIsoVLDZFilter
	Muon filters
	hltMu8TrkIsoVVLEle23CaloIdLTrackIdLIsoVLMuonlegL3IsoFiltered8
	hltMu8TrkIsoVVLEle23CaloIdLTrackIdLIsoVLDZFilter
HLT_Mu23_TrkIsoVVL_Ele12_CaloIdL_TrackIdL_IsoVL_DZ	Electron filters
	hltMu23TrkIsoVVLEle12CaloIdLTrackIdLIsoVLElectronlegTrackIsoFilter
	hltMu23TrkIsoVVLEle12CaloIdLTrackIdLIsoVLDZFilter
	Muon filters
	hltMu23TrkIsoVVLEle12CaloIdLTrackIdLIsoVLMuonlegL3IsoFiltered23
	hltMu23TrkIsoVVLEle12CaloIdLTrackIdLIsoVLDZFilter

Table 3.6: Triggers used to collect the 2016 data samples for the $\tau_e\tau_\mu$ channel.

Muon:

- $p_T > 10\,\text{GeV}$ and $|\eta| < 2.4$;
- $d_{xy} < 0.045\,\text{cm}$ and $d_z < 0.2\,\text{cm}$;
- pass the *medium* muon ID;
- I_μ (cone size 0.4) $< 0.3\,p_T^\mu$.

3.5.1.3 Di-lepton veto

A veto on events containing di-lepton pairs is applied. The opposite-sign leptons must be separated by $\Delta R > 0.15$ and pass the following loose selections:
Di-electrons:

- $p_T > 15\,\text{GeV}$ and $|\eta| < 2.5$;
- $d_{xy} < 0.045\,\text{cm}$ and $d_z < 0.2\,\text{cm}$;
- pass the electron cut based ID (*Fall17-V2*) veto;
- I_e (cone size 0.3) $< 0.3\,p_T^e$.

Di-muons:

- $p_T > 15\,\text{GeV}$ and $|\eta| < 2.4$;
- $d_{xy} < 0.045\,\text{cm}$ and $d_z < 0.2\,\text{cm}$;
- pass the *loose* muon ID;
- I_μ (cone size 0.4) $< 0.3\,p_T^\mu$.

3.5.2 Pair selection algorithm

There can be more than one possible $\tau\tau$ pair candidate after requiring trigger, identification and kinematic cuts. In this case a single pair is chosen as follows:

- prefer the pair with the most isolated candidate 1 (muon in the $\tau_\mu\tau_\text{h}$ and in the $\tau_e\tau_\mu$, electron in the $\tau_e\tau_\text{h}$ and either τ_h candidate in the $\tau_\text{h}\tau_\text{h}$). For muons and electrons this means the object with the smallest relative isolation value is retained, for τ_h the object with raw `deepTau` neural network against jets (*byDeepTau2017v2p1VSjetraw*) highest value;
- if the isolation of candidate 1 is the same in both pairs, prefer the pair with highest candidate 1 p_T;

- if the p_{T} of candidate 1 is the same in both pairs, prefer the pair with most isolated candidate 2 (the other τ_{h} candidate in the $\tau_{\mathrm{h}}\tau_{\mathrm{h}}$, the τ_{h} candidate in the $\tau_\mu\tau_{\mathrm{h}}$ and $\tau_e\tau_{\mathrm{h}}$ and the electron in the $\tau_e\tau_\mu$);
- if the isolation of candidate 2 is the same in both pairs, prefer the pair with highest candidate 2 p_{T}.

3.5.3 Offline selections

Oppositely charged τ lepton candidates (OS) are selected for signal extraction, and same sign (SS) are used to estimate the background, as detailed in Sect. 3.5.6. In the $\tau_\ell\tau_h$ ($\ell = e, \mu$) channels, the transverse mass m_T is defined using the transverse momentum of the lepton, p_{T}^{ℓ}, and transverse missing energy:

$$m_T = \sqrt{2p_{\mathrm{T}}^{\ell}E_{\mathrm{T}}^{\mathrm{miss}}(1 - cos(\Delta\phi(\ell, \vec{p}_{\mathrm{T}}^{\mathrm{miss}})))} \quad . \tag{3.14}$$

High values of m_T are expected for events containing a W boson, hence a cut on m_T is applied to reduce this background.

3.5.3.1 $\tau_{\mathrm{h}}\tau_{\mathrm{h}}$ final state

Events in the $\tau_{\mathrm{h}}\tau_{\mathrm{h}}$ final state are selected by requiring:

- τ_{h} candidates must have opposite sign (OS) electric charges;
- τ_{h} candidates are separated by $\Delta R > 0.5$;
- the event to pass the relevant $E_{\mathrm{T}}^{\mathrm{miss}}$ filters listed in 3.5.1.1;
- each τ_h candidates to satisfy the following selection criteria:
  - $p_T(\tau_h) > 40\,\mathrm{GeV}$ and $|\eta(\tau_h)| < 2.1$,
  - pass the *medium* working point of the `deepTau` neural network against jets,
  - pass the *very very loose* working point of the `deepTau` neural network against electrons,
  - pass the *very loose* working point of the `deepTau` neural network against muons,
  - $d_z < 0.2\,\mathrm{cm}$ between leading charged track and first primary vertex,
  - identify as one of the following decay modes: *onePronZeroPizero* (MVADM=0), *onePronOnePizero* (MVADM=1) or *threeProngZeroPizero* (MVADM=10).
- extra muon and electron vetoes are applied as described in 3.5.1.2;

- the event has no b-tagged jets (to reject top-pair and single-top backgrounds);
- the visible mass of τ_h candidates is required to satisfy $40 < m_\mathrm{vis} < 85\,\mathrm{GeV}$;
- if more than one possible $\tau_\mathrm{h}\tau_\mathrm{h}$ pair exists in the event, the most isolated pair is selected as described in 3.5.2.

3.5.3.2 $\tau_\mu\tau_\mathrm{h}$ final state

Events in the $\tau_\mu\tau_\mathrm{h}$ final state are selected by requiring:

- the muon and τ_h must have opposite sign (OS) electric charges;
- the muon and τ_h candidate are separated by $\Delta R > 0.5$;
- the event to pass the relevant $E_\mathrm{T}^\mathrm{miss}$ filters listed in 3.5.1.1;
- a muon to satisfy the following selection criteria:
  - $p_T^\mu > 20\,\mathrm{GeV}$ and $|\eta^\mu| < 2.1$,
  - $I_\mu < 0.15\,p_T^\mu$,
  - $d_z < 0.2\,\mathrm{cm}$ and $d_{xy} < 0.045\,\mathrm{cm}$
- a τ_h candidate to satisfy the following selection criteria:
  - $p_T(\tau_h) > 30\,\mathrm{GeV}$ and $|\eta(\tau_h)| < 2.3$,
  - pass the *medium* working point of the `deepTau` neural network against jets,
  - pass the *very very loose* working point of the `deepTau` neural network against electrons,
  - pass the *tight* working point of the `deepTau` neural network against muons,
  - $d_z < 0.2\,\mathrm{cm}$ between leading charged track and first primary vertex,
  - identify as one of the following decay modes: *onePronZeroPizero* (MVADM=0), *onePronOnePizero* (MVADM=1) or *threePronZeroPizero* (MVADM=10).
- the transverse mass m_T of the muon plus missing transverse energy $E_\mathrm{T}^\mathrm{miss}$ is required to satisfy $m_T < 50\,\mathrm{GeV}$ in order to reject W+jets background;
- extra muon and electron vetoes are applied as described in 3.5.1.2;
- di-lepton veto is applied as described in 3.5.1.3;
- the event has no b-tagged jets (to reject $\mathrm{t\bar{t}}$ and single-top backgrounds);

- the visible mass of the muon plus the τ_{h} candidate is required to satisfy $40 < m_{\mathrm{vis}} < 85\,\mathrm{GeV}$;
- if more than one possible $\tau_\mu\tau_{\mathrm{h}}$ pair exists in the event, the most isolated pair is selected as described in 3.5.2.

3.5.3.3 $\tau_e\tau_{\mathrm{h}}$ final state

Events in the $\tau_e\tau_{\mathrm{h}}$ final state are selected by requiring:

- the electron and τ_{h} must have opposite sign (OS) electric charges;
- the electron and τ_{h} candidate are separated by $\Delta R > 0.5$;
- the event to pass the relevant $E_{\mathrm{T}}^{\mathrm{miss}}$ filters listed in 3.5.1.1;
- an electron to satisfy the following selection criteria:
  - $p_T^e > 30\,\mathrm{GeV}$ and $|\eta^e| < 2.1$,
  - $I_e < 0.15\,p_T^e$,
  - $d_z < 0.2\,\mathrm{cm}$ and $d_{xy} < 0.045\,\mathrm{cm}$
- a τ_h candidate to satisfy the following selection criteria:
  - $p_T(\tau_h) > 30\,\mathrm{GeV}$ and $|\eta(\tau_h)| < 2.3$,
  - pass the *medium* working point of the `deepTau` neural network against jets,
  - pass the *tight* working point of the `deepTau` neural network against electrons,
  - pass the *loose* working point of the `deepTau` neural network against muons,
  - $d_z < 0.2$ cm between leading charged track and first primary vertex,
  - identify as one of the following decay modes: *onePronZeroPizero* (MVADM=0), *onePronOnePizero* (MVADM=1) or *threeProngZeroPizero* (MVADM=10).
- the transverse mass m_T of the electron plus missing transverse energy $E_{\mathrm{T}}^{\mathrm{miss}}$ is required to satisfy $m_T < 50\,\mathrm{GeV}$ in order to reject W+jets background;
- extra muon and electron vetoes are applied as described in 3.5.1.2;
- di-lepton veto is applied as described in 3.5.1.3;
- the event has no b-tagged jets (to reject $\mathrm{t\bar{t}}$ and single-top backgrounds);

- the visible mass of the electron plus the τ_{h} candidate is required to satisfy $40 < m_{\mathrm{vis}} < 85\,\mathrm{GeV}$;
- if more than one possible $\tau_e\tau_{\mathrm{h}}$ pair exists in the event, the most isolated pair is selected as described in 3.5.2.

3.5.3.4 $\tau_e\tau_\mu$ final state

Events in the $\tau_e\tau_\mu$ final state are selected by requiring:

- the electron and the muon must have opposite sign (OS) electric charges;
- the electron and the muon are separated by $\Delta R > 0.3$;
- the event to pass the relevant $E_{\mathrm{T}}^{\mathrm{miss}}$ filters listed in 3.5.1.1;
- an electron to satisfy the following selection criteria:
  - $p_T^e > 15\,\mathrm{GeV}$ and $|\eta^e| < 2.4$,
  - $I_e < 0.15\,p_T^e$,
  - $d_z < 0.2\,\mathrm{cm}$ and $d_{xy} < 0.045\,\mathrm{cm}$
- a muon to satisfy the following selection criteria:
  - $p_T^\mu > 15\,\mathrm{GeV}$ and $|\eta^\mu| < 2.4$,
  - $I_\mu < 0.20\,p_T^\mu$,
  - $d_z < 0.2\,\mathrm{cm}$ and $d_{xy} < 0.045\,\mathrm{cm}$
- $m_T(E_{\mathrm{T}}^{\mathrm{miss}}, e\mu) < 60\,\mathrm{GeV}$ to remove di-boson events for which the transverse mass of the $E_{\mathrm{T}}^{\mathrm{miss}}$ and the system of the electron and muon is above 60 GeV;
- To reduce $\mathrm{t\bar{t}}$ background, the variable D_ζ was introduced [52] as:

$$D_\zeta = p_\zeta^{\mathrm{miss}} - 0.85 p_\zeta^{\mathrm{vis}} \quad , \quad p_\zeta^{\mathrm{miss}} = \vec{p}_{\mathrm{T}}^{\,\mathrm{miss}} \cdot \hat{\zeta} \quad , \quad p_\zeta^{\mathrm{vis}} = (\vec{p}_{\mathrm{T}}^{\,e} + \vec{p}_{\mathrm{T}}^{\,\mu}) \cdot \hat{\zeta} \quad ; \qquad (3.15)$$

  where $\vec{p}_{\mathrm{T}}^{\,e,\mu}$ corresponds to the transverse momentum vector of the electron (muon) lepton and $\hat{\zeta}$ to the bisectional direction between the two leptons in the transverse plane. The selected pair has the additional requirement of $D_\zeta > -35\,\mathrm{GeV}$.
- extra muon and electron vetoes are applied as described in 3.5.1.2;
- the event has no b-tagged jets (to reject $\mathrm{t\bar{t}}$ and single-top backgrounds);

- the visible mass of the electron plus the muon is required to satisfy $40 < m_{\text{vis}} < 85\,\text{GeV}$;
- if more than one possible $\tau_e\tau_\mu$ pair exists in the event, the most isolated pair is selected as described in 3.5.2.

Table 3.7 summarises the technical aspects of the analysis, including the exact identification variables and kinematic cuts used. It is worthwhile to note that the third lepton veto and τ_h identification criteria are applied after the pair selection algorithm. Table 3.8 gives a reminder of the considered triggers.

3.5.4 Event categorisation

After the event selection described above, events are categorised according to the `MVA-DM` predicted decay mode (MVADM) on the top of `HPS` reconstruction of the hadronically decaying τ leptons. In Section 3.6 is outlined, that the performance of the kinematic reconstruction of τ lepton decays strongly depends on the decay mode. This justifies the separate treatment of each decay mode and results in 1, 3, 3 or 4 categories in the $\tau_e\tau_\mu$, $\tau_e\tau_h$, $\tau_\mu\tau_h$ and $\tau_h\tau_h$ channels, respectively, as summarised in Table 3.9. Note, that the fully hadronic channel would result in six different combinations of decay modes of the hadronically decaying τ lepton, but the three combinations containing $\tau \to \rho\nu$ events are combined into one category because of the possibility of a better discriminator choice in this category (see Sect. 3.10). The decay modes *oneProngZeroPizero* (MVADM=0), *oneProngOnePizero* (MVADM=1) and *threeProngZeroPizero* (MVADM=10) are dominated by $\tau \to \pi\nu$, $\tau \to \rho\nu$ and $\tau \to a_1\nu$ decays, respectively.

3.5.5 Corrections applied to Monte Carlo samples

The corrections applied to MC events to improve the description of the data follow closely those used for the analysis of the Higgs CP state in τ decays [53]. The corrections dedicated to the use of the `MVA-DM` for τ_h decay mode identification are:

- Hadronic tau ID scale factors in bins of MVADM (instead of DM from `HPS`) and in two p_T bins ($p_T < 40$ GeV and $p_T > 40$ GeV). The measurement of these scale factors are described in [53].
- Hadronic tau trigger scale factor in bins of MVADM (instead of DM from `HPS`) and in p_T bins. The measurement of these scale factors are described in Ref. [53].
- Residual corrections for $\mu \to \tau_h$ fake rate in the same p_T and MVADM bins as the tau ID scale factors.

These corrections were endorsed by the *Tau Physics Object group*. Other corrections applied to the MC are:

- pileup reweighting (identical for all the MC samples);

Table 3.7: Selection cuts used in the analysis.

Final state	$\boldsymbol{\tau_\mu\tau_h}$	$\boldsymbol{\tau_e\tau_h}$	$\boldsymbol{\tau_h\tau_h}$	$\boldsymbol{\tau_e\tau_\mu}$
e/μ kinematic cuts	$p_T(\mu) > 20\,\text{GeV}$, $\lvert\eta(\mu)\rvert < 2.1$ $d_{xy} < 0.045\,\text{cm}$, $d_z < 0.2\,\text{cm}$	$p_T(e) > 30\,\text{GeV}$, $\lvert\eta(e)\rvert < 2.1$ $d_{xy} < 0.045\,\text{cm}$, $d_z < 0.2\,\text{cm}$		$p_T(e) > 15\,\text{GeV}$, $\lvert\eta(e)\rvert < 2.4$ $d_{xy} < 0.045\,\text{cm}$, $d_z < 0.2\,\text{cm}$ $p_T(\mu) > 15\,\text{GeV}$, $\lvert\eta(\mu)\rvert < 2.4$ $d_{xy} < 0.045\,\text{cm}$, $d_z < 0.2\,\text{cm}$ $p_T > 24\,\text{GeV}$ for the lepton firing the trigger
e/μ identification	$I_{rel}(\mu) < 0.15$ Medium ID for μ	$I_{rel}(e) < 0.15$ 90% efficiency WP for e conversion veto for e less than two missing hits for e		$I_{rel}(e) < 0.15$, $I_{rel}(\mu) < 0.20$ Medium ID for μ 90% efficiency WP for e conversion veto for e less than two missing hits for e
τ_h identification	DM finding, $dz < 0.2\,\text{cm}$ Medium deepTau iso VVLoose deepTau anti-e Tight deepTau anti-μ	DM finding, $dz < 0.2\,\text{cm}$ Medium deepTau iso Tight deepTau anti-e Loose deepTau anti-μ	DM finding, $dz < 0.2\,\text{cm}$ Medium deepTau iso VVLoose deepTau anti-e VLoose deepTau anti-μ	

Table 3.8: Triggers used in the analysis

Final state	Trigger	Lepton selection	Additional selection	
$\tau_h\tau_h$	$\tau_h(35)\tau_h(35)$	$p_T^{\tau_h} > 45(40)$ GeV, $\lvert\eta^{\tau_h}\rvert < 2.1$	Medium deepTau iso	
$\tau_\mu\tau_h$	$\mu(22)$	$p_T^{\mu} > 20$ GeV, $\lvert\eta^{\mu}\rvert < 2.1$	$I_{rel}(\mu) < 0.15$	$M_T^{\mu} < 50$ GeV
	or $\mu(19)\tau_h(20)$	$p_T^{\tau_h} > 30$ GeV, $\lvert\eta^{\tau_h}\rvert < 2.3$	Medium deepTau iso	
$\tau_e\tau_h$	$e(25)$	$p_T^{e} > 30$ GeV, $\lvert\eta^{e}\rvert < 2.1$	$I_{rel}(e) < 0.15$	$M_T^{e} < 50$ GeV
		$p_T^{\tau_h} > 30$ GeV, $\lvert\eta^{\tau_h}\rvert < 2.3$	Medium deepTau iso	
$\tau_e\tau_\mu$	$\mu(8)$e(23)	$p_T^{e} > 15$ GeV, $\lvert\eta^{e}\rvert < 2.4$	$I_{rel}(e) < 0.15$	
	or $\mu(23)$e(12)	$p_T^{\mu} > 15$ GeV, $\lvert\eta^{\mu}\rvert < 2.4$	$I_{rel}(\mu) < 0.20$	
		$p_T^{\ell} > 24$ GeV for the lead. trigger leg		

- missing d_z filter in $\tau_e\tau_\mu$ simulation: in 2016, the d_z filter of the HLT paths employed for the $\tau_e\tau_\mu$ channel in runs G and H is not modelled in simulation (only applied in data). The simulation is corrected by the efficiency of the filter in data, which amouts to 97.9%;
- electron tracking scale factors (p_T and η dependent) provided by the *EGamma Physics Object group*;
- electron trigger and ID-isolation scale factors (p_T and η dependent);
- electron smear and scale corrections (from *EGamma Physics Object group*);
- muon tracking scale factor (η dependent) provided by the *Muon Physics Object group*;
- muon (single and cross-) trigger and ID-isolation scale factor (p_T and η dependent);
- $\ell \to \tau_h(\ell = e, \mu)$ fake rate corrections (η dependent) provided by the *Tau Physics Object group*;
- hadronic tau energy scale corrections (for genuine tau and $\ell \to \tau_h$ fakes) provided by the *Tau Physics Object group*. The MET should be corrected accordingly;
- MET recoil corrections (for Z, W and electroweak [EWK] samples);
- prefiring;
- partons reweighting;
- Z p_T-mass reweighting (for DY+jets MC);

Table 3.9: The event categories in the four channels. $\tau_{\mathrm{h},1/2}$ refers to the leading and trailing leg in the fully hadronic channel. The categorisation does not depend on whether a leg is leading or trailing in p_{T}.

Channel	**Category**	**Criteria**
$\tau_e\tau_\mu$	$e+\mu$	–
$\tau_e\tau_\mathrm{h}$	$e+a_1$	$\mathrm{MVADM}(\tau_\mathrm{h})=10$
	$e+\rho$	$\mathrm{MVADM}(\tau_\mathrm{h})=1$
	$e+\pi$	$\mathrm{MVADM}(\tau_\mathrm{h})=0$
$\tau_\mu\tau_\mathrm{h}$	$\mu+a_1$	$\mathrm{MVADM}(\tau_\mathrm{h})=10$
	$\mu+\rho$	$\mathrm{MVADM}(\tau_\mathrm{h})=1$
	$\mu+\pi$	$\mathrm{MVADM}(\tau_\mathrm{h})=0$
$\tau_\mathrm{h}\tau_\mathrm{h}$	a_1+a_1	$\mathrm{MVADM}(\tau_{\mathrm{h},1})=10$ AND $\mathrm{MVADM}(\tau_{\mathrm{h},2})=10$
	$a_1+\pi$	$\mathrm{MVADM}(\tau_{\mathrm{h},1/2})=10$ AND $\mathrm{MVADM}(\tau_{\mathrm{h},2/1})=0$
	$\rho+\tau_\mathrm{h}$	$\mathrm{MVADM}(\tau_{\mathrm{h},1})=1$ OR $\mathrm{MVADM}(\tau_{\mathrm{h},2})=1$
	$\pi+\pi$	$\mathrm{MVADM}(\tau_{\mathrm{h},1})=0$ AND $\mathrm{MVADM}(\tau_{\mathrm{h},2})=0$

- top p_{T} reweighting (for $\mathrm{t\bar{t}}$ MC).

3.5.5.1 Lepton trigger efficiencies

Trigger efficiencies have been measured in data using well known *tag and probe* techniques in Z events as described in Ref. [54]. For the $e+\mu$ cross trigger efficiencies are determined separately for each trigger leg with the help of di-muon and di-electron monitoring triggers with identical legs. The values are determined in bins of p_{T} and η.

In the $\tau_\mu\tau_\mathrm{h}$ channel an event is selected if it passes the *single muon trigger* OR *muon+tau cross-trigger*. To account for differences in the trigger efficiencies between data and simulated events, a weight is applied for each event as:

$$w_{\mathrm{trig}} = \frac{\epsilon_{\mathrm{trig}}^{\mathrm{data}}}{\epsilon_{\mathrm{trig}}^{\mathrm{MC}}} \quad , \tag{3.16}$$

where $\epsilon_{\mathrm{trig}}^{\mathrm{data}}$ is the efficiency of event to pass the *single muon trigger* OR the *muon+tau cross-trigger* as measured for data events, and $\epsilon_{\mathrm{trig}}^{\mathrm{MC}}$ is the efficiency of event to pass the *single muon trigger* OR the *muon+tau cross-trigger* as determined in the simulated events. The HLT filter of the *single muon triggers* differs from the muon filter of the *muon+tau cross-trigger* only by the online p_{T} threshold. The threshold for the muon filter of the *muon+tau cross-trigger* is lower. Therefore the efficiency to fire the *single*

muon trigger OR the *muon+tau cross-trigger* can be computed as:

$$\epsilon_{\text{trig}} = \epsilon_L + (\epsilon_\ell - \epsilon_L)\epsilon_\tau \quad , \tag{3.17}$$

where ϵ_L is the efficiency of the *single muon trigger*, ϵ_ℓ efficiency of the muon filter of the *muon+tau cross-trigger* and ϵ_τ efficiency of the tau filter of the *muon+tau cross-trigger*. The measurement of the efficiencies ϵ_L and ϵ_ℓ is documented in Ref. [55]. The measurement of the efficiency ϵ_τ is described in Ref. [53].

In the $\tau_e\tau_\mu$ channel, the scale factor to correct the simulation is applied as formula (3.16) where $\epsilon_{\text{trig}}^{\text{data/MC}}$ calculation is based on the following combination of efficiencies for the trigger legs:

$$\epsilon_{\text{trig}} = \epsilon_{\text{trig}}(\text{Mu23})\epsilon_{\text{trig}}(\text{Ele12}) + \epsilon_{\text{trig}}(\text{Mu8})\epsilon_{\text{trig}}(\text{Ele23}) - \epsilon_{\text{trig}}(\text{Mu23})\epsilon_{\text{trig}}(\text{Ele23})\,. \tag{3.18}$$

3.5.5.2 Tau energy scale

The energy scale correction is computed for each decay mode using either the visible mass of both τ leptons or the invariant mass distributions of the $\pi^\pm\pi^0$, $\pi^\pm\pi^0\pi^0$ and $\pi^+\pi^-\pi^\pm$ systems. The correction factors are chosen such that either the visible mass distributions of both τ leptons of the MC events match the data distribution, or the invariant mass distributions of the $\pi^\pm\pi^0$, $\pi^\pm\pi^0\pi^0$ and $\pi^+\pi^-\pi^\pm$ systems match the parameters of the ρ and a_1 resonances.

3.5.5.3 Muon/electron momentum scale, isolation and efficiency

Lepton isolations and efficiencies are measured via *tag and probe* methods in Z to leptons events for differents lepton p_{T} and η bins and recorded by single lepton triggers. More details can be found in Ref. [54].

3.5.5.4 Transverse missing energy corrections

In order to account for mismodeling of $E_{\text{T}}^{\text{miss}}$ in the simulated samples of Drell-Yan, W+jets and EWK production ($W^\pm+2$ jets and $Z+2$ jets), recoil corrections are applied using the quantity $\vec{U}$:

$$\vec{U} = \vec{p}_{\text{T}}^{\text{miss}} - \vec{p}_{T,\nu} \quad , \tag{3.19}$$

where $\vec{p}_{\text{T}}^{\text{miss}}$ is the missing transverse momentum of the simulated event and $\vec{p}_{T,\nu}$ the sum of the transverse momenta of neutrinos originating from subsequant decays in Drell-Yan, W+jets and EWK production.

For leptonically decaying bosons this quantity can be expressed as:

$$\vec{U} = -\vec{p}_{T,B} - \vec{H}_T \quad , \tag{3.20}$$

where $\vec{H}_T$ is the transverse momentum of the hadronic recoil, and $\vec{p}_{T,B}$ the transverse momentum of leptonically decaying Z or W boson. The vector $\vec{U}$ is measured in $Z \to \mu\mu$

events. Corrections are applied parallel and orthogonal to the boson transverse momentum. These corrections are computed for different values of the Z-boson transverse momentum and jet multiplicities. More details can be found in Ref. [54].

3.5.6 Background estimation

The largest background comes from multijet events where one of the jets is misidentified as a τ_h. It represents respectively about 84%, 20% and 16% of the expected background in the $\tau_h\tau_h$, $\tau_\mu\tau_h$ and $\tau_e\tau_h$ channels. Drell-Yan events in $\ell\ell(\ell = e, \mu)$ final states may contribute if either a lepton is identified as a τ_h or an additional jet is misidentified as τ_h. These contributions are suppressed by rejecting events containing di-leptons with same flavour and opposite electric charge as well as by the anti-electron and anti-muon discriminants being applied to the τ_h candidates. While control samples are used in data to evaluate the multijet background, other contributions as $t\bar{t}$ and electroweak processes (single-top quark, Z+jets and di-bosons) rely on simulation. The W+jets background is significant in the $\tau_\mu\tau_h$ and $\tau_e\tau_h$ final state (respectively about 31% and 27% of the expected background) and is evaluated from data.

3.5.6.1 $\tau_\mu\tau_h$ and $\tau_e\tau_h$ final states

The QCD and W+jets estimates are obtained from so-called *ABCD* regions, delimited by the lepton (e, μ) isolation and lepton-τ_h pair charges (opposite (OS) or same sign (SS) pairs). The signal region A is defined by $I_\ell < 0.15$ and an OS pair; B by $I_\ell < 0.15$ and a SS pair; C by $I_\ell > 0.15$ and an OS pair; D by $I_\ell > 0.15$ and a SS pair. These regions receive significant contributions from W+jets events, that must be evaluated simultaneously to the multijet background. Therefore, two samples are defined in which the *ABCD* methods will be used: one follows the signal selection criteria for which the transverse mass verifies $m_T < 50$ GeV and one is enriched in W+jets events and verifies $m_T > 70$ GeV. These samples are called *Low* and *High* in what follows. The *High* region enriched by W+jets is used to evaluate the W+jets background in the $I_\ell < 0.15$ isolation regions and the ratio between *High* and *Low* is then used to translate it to the $I_\ell > 0.15$ region.

The number of multijet events (QCD) in the signal region is given by:

$$QCD^A_{Low} = QCD^B_{Low} \times f^{OS/SS} \quad . \tag{3.21}$$

$f^{OS/SS}$ is defined as the ratio of events in data in the C and D regions from which non-QCD events have been subtracted.

QCD^B_{Low} is defined by the number of events observed in region B (N^B_{Low}), from which backgrounds have been subtracted: $QCD^B_{Low} = N^B_{Low} - EWK^B_{Low} - W^B_{Low}$.

W^B_{Low} is obtained from the *High* region: $W^B_{Low} = W^B_{High} \times f^{SS}_{Low/High}$. The high transverse mass region is expected to be enriched in W+jets events, EWK ($W^\pm$ +

2 jets) estimates from simulation are nevertheless subtracted. $f^{SS}_{Low/High}$ is obtained from simulated W+jets events.

Similarly the W+jets yield in the signal region A is given by: $W^{A}_{Low} = W^{A}_{High} \times f^{OS}_{Low/High}$. To avoid statistical fluctuation relaxed criteria on the muon and τ_h isolations ($I_\ell < 0.5$ and *very very very loose* working point of the `deepTau` neural network against jets for τ_h) are used to obtain $f^{OS}_{Low/High}$.

3.5.6.2 $\tau_h\tau_h$ final state

The multijet background estimation differs for the $\tau_h\tau_h$ final state as the W+jets background is negligible for this final state. A sideband region is defined from which the yields and shapes are defined. This sideband region is the same as the signal region except that the isolation of the two τ_h are relaxed. The purpose of relaxing the criteria for both taus and not only for one is to gain in statistics. One τ_h is required to be of *medium* isolation and the second one to be *loose* (without being allowed to be *tight*). The extrapolation from the sideband region to the signal region is obtained by applying a so called *loose-to-tight isolation scale factor*, denoted $f^{tight/loose}$:

$$QCD = f^{tight/loose} N^{OS}_{loose} \quad . \tag{3.22}$$

The *loose-to-tight isolation scale factor* is computed in same sign events, $f^{tight/loose} = N^{SS}_{tight}/N^{SS}_{loose}$. The numbers of events measured in these three side-band regions, namely N^{OS}_{loose}, N^{SS}_{tight} and N^{SS}_{loose} have been estimated by removing the residual backgrounds estimated using MC simulation.

Three systematic uncertainties affect this measurement, one related to the shape compatibility, one to the yields obtained in the three side-band regions and one to the method itself. The relative associated uncertainties are described in Sect. 3.9.

The Appendix B contains a wide range of control plots that compare the most important variables in data and simulation. The excellent agreement observed is indicative of the successful application of all corrections described earlier. The grey uncertainty band displayed in these plots includes only the statistical uncertainty.

3.6 Tau spin observables

3.6.1 Angular analysis

The spin of τ lepton is transformed into the total angular momentum of its decay products and therefore it reveals through the angular distributions of the decay products relative to each other and to the flight direction of the τ lepton.

The first angle to consider is the angle θ between the direction of flight of the τ lepton and the direction of the hadron or the direction of the lepton in case of the

leptonic τ lepton decay) as it is seen from the τ lepton rest frame, see also Fig. 3.5:

$$\cos\theta = \boldsymbol{n_\tau} \cdot \boldsymbol{p} \quad , \tag{3.23}$$

where $\boldsymbol{n_\tau}$ is the vector pointing along the τ direction and $\boldsymbol{p}$ is a unit vector pointing along the momentum of the hadron in the τ lepton rest frame. Considering the decay $\tau^- \to \pi^-\nu$, there is no angular momentum in the two-body τ decay and since the pion carries no spin the angular momentum conservation requires the neutrino to adopt the spin of τ lepton. Since the neutrino is always left-handed the π^- is preferably emitted in the direction of the τ lepton spin direction, so in the case of a τ lepton with right-handed helicity the pion is emitted preferentially in the direction of flight of the τ lepton. In the τ lepton rest frame neutrino and pion are emitted back-to-back and therefore in the decay of τ_R the angle θ prefers small values and large values in the case of the τ lepton is left-handed. In this case of $\tau^- \to \pi^-\nu$ the angle θ carries all spin information. Boosting the pion into the laboratory frame gives the following relation:

$$\cos\theta = 2 \cdot \frac{E_\pi}{E_\tau} - 1 \quad , \tag{3.24}$$

where E_π and E_τ are, respectively, the energies of the pion and the tau lepton.

The decay into a spin-one resonance, ρ or a_1, ρ $(J^P = 1^-)$ also offers the kinematic simplicity of a two-body decay, like the $\tau^- \to \pi^-\nu$, but with a more complicated dynamics since the resonances ρ and a_1 can have longitudinal and transverse spin states. Conservation of angular momentum allows for the ρ and a_1 resonances helicities $\lambda_V = 0$ or -1. The angle θ for τ decays $\tau \to \pi, \rho, \nu$ and the possible ρ-meson helicities are shown in Fig. 3.5. As it is evident from the Fig. 3.5 the angle θ can be large or small for the same polarisation of the τ^- depending on whether the V-resonance is in a longitudinal $(\lambda_\rho = 0)$ polarisation state or in the transversal polarisation state $(\lambda_\rho = -1)$. The two ρ polarisation states can be distinguished by the angular distribution of its decay products. In the case of a longitudinal $(\lambda_\rho = 0)$ polarisation the pions will have in most cases an asymmetric energy distribution depending on the emission angle w.r.t. the movement of the ρ. However in the case of a transversal polarisation state $(\lambda_\rho = -1)$ the plane in which the two pions are emitted will be perpendicular to the spin of the ρ and its movement, consequentially the energy will be shared more symmetrically between the two pions.

For the negative helicity state of the τ lepton the ρ will be boosted more in its transversal polarisation state, whereas in the case of positive tau helicity it will be the longitudinal polarisation of the ρ, which will be boosted more, therefore the pion energy difference compared to the energy of the tau lepton can be used as a τ polarisation analyser.

If the τ lepton is in the right-handed state the V ($V = \rho$, a_1) resonance tends to be in longitudinally polarised state (λ_V =0) and oppositely if τ is left-handed the V

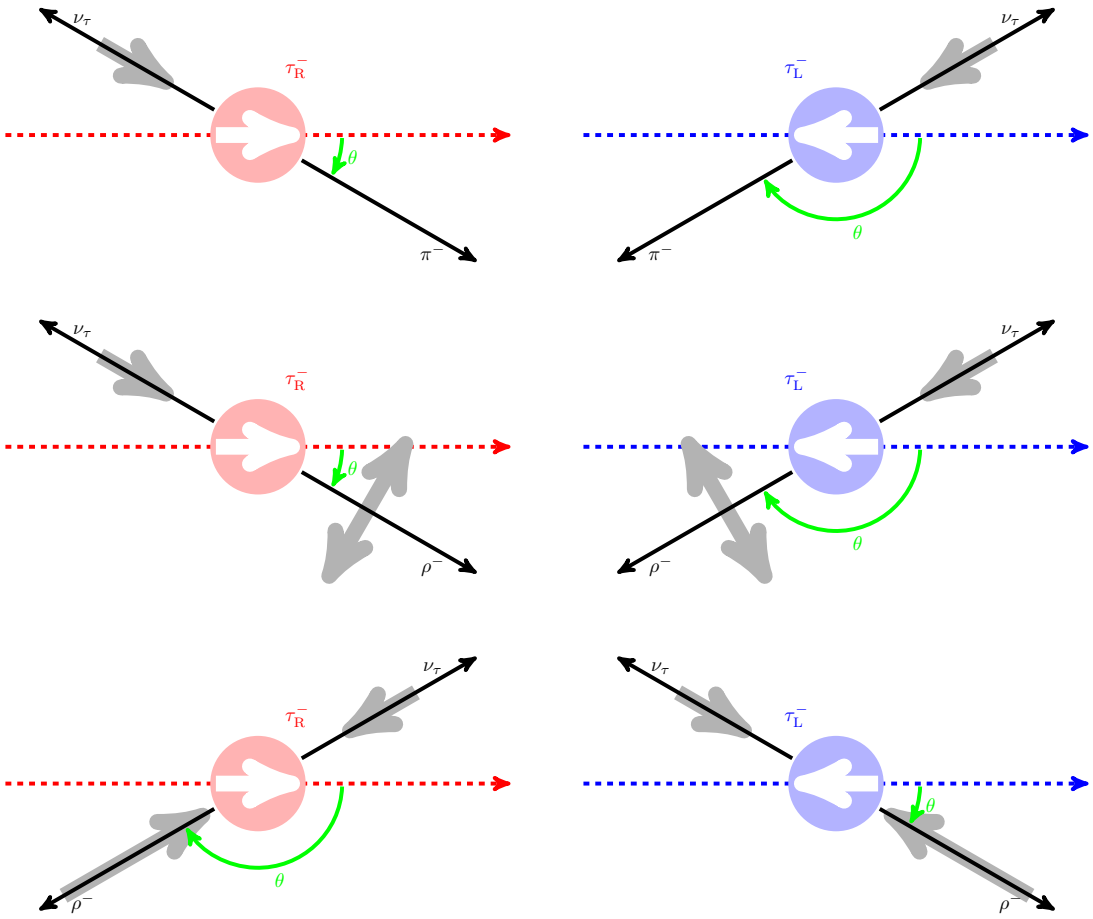

Figure 3.5: Definition of angle θ in the decays $\tau \to h\nu\,(h = \pi,\, \rho,\, a_1)$ and $\tau \to e/\mu\nu\bar{\nu}$. *Left column* for τ_R, *Right Column* for τ_L.

is preferably transversely polarised (λ_V = -1). Combining the spin amplitudes for all possible configuration of V resonance and τ helicities, one gets [56] [57]:

$$\frac{1}{\Gamma}\frac{d\Gamma}{d\cos\theta} \propto 1 + \alpha_V h_\tau \cos\theta \quad , \tag{3.25}$$

where the dilution factor $\alpha_V = \frac{|M_L|^2-|M_T|^2}{|M_T|^2+|M_L|^2} = \frac{m_\tau^2-2m_V^2}{m_\tau^2+2m_V^2}$ is a result of the presence of the transverse V resonance spin amplitude. The value of the factor α characterises the sensitivity of the $\cos\theta$ observable. For comparison, in the τ lepton decay to a_1, $\alpha_{a_1} = 0.021$, to ρ, $\alpha_\rho = 0.46$ to pion decay $\alpha_\pi = 1$. Consequently, the sensitivity to the τ lepton helicity in the decay $\tau \to V\nu$ is strongly reduced if only the $\cos\theta$ angle is analysed. The loss of sensitivity due to factor α_V can be compensated if the helicity state of the V resonance can be determined.

The spin of V is transformed into the total angular momentum of the decay products and thus can be retrieved by analysing the subsequent V decay.

There are two additional angles in the decay $\tau \to \rho\nu\,(\rho \to \pi\pi)$: β denotes the angle between the direction of charged pion and the direction of the ρ as seen in the ρ rest frame:

$$\cos\beta = \boldsymbol{q}\cdot\boldsymbol{n_\rho} = \frac{m_\rho}{\sqrt{m_\rho^2 - 4m_\pi^2}} \cdot \frac{E_{\pi^-} - E_{\pi^0}}{|p_{\pi^-} - p_{\pi^0}|} \quad , \tag{3.26}$$

where $\boldsymbol{q}$ is a unit vector along direction of charged pion in the ρ rest frame and $\boldsymbol{n_\rho}$ is the direction of the movement of the ρ projected into its rest frame. In the analysis m_ρ is replaced by the invariant mass of the two pions as observed event by event. The rotation plane of two pions is aligned correspondingly to the helicity of the ρ resonance. In case of $\lambda_\rho = 0$ the angle β tends to small values and to large values if $\lambda_\rho = -1$. The angle β is sketched in Fig. 3.6b (*centre*).

The second angle α is defined by the two planes spanned by vectors $(\boldsymbol{n_\rho}, \boldsymbol{n_\tau})$ and $(\boldsymbol{n_\rho}, \boldsymbol{q})$ respectively:

$$\cos\alpha = \frac{(\boldsymbol{n_\rho}\times\boldsymbol{n_\tau})\cdot(\boldsymbol{n_\rho}\times\boldsymbol{q})}{|\boldsymbol{n_\rho}\times\boldsymbol{n_\tau}|\cdot|\boldsymbol{n_\rho}\times\boldsymbol{q}|} \quad , \tag{3.27}$$

where $\boldsymbol{n_\tau}$ is the direction of τ lepton, $\boldsymbol{n_\rho}$ is the direction of the movement of the ρ projected into its rest frame and $\boldsymbol{q}$ is the direction of the charged pion. All vectors are defined in the ρ rest frame. The angle α describes the correlation between the helicity of τ lepton and decay products of the ρ meson.

In the decay $\tau^- \to a_1\nu$ there are three angles in addition to angle θ. All three angles are described in the a_1 rest frame. An angle β is defined as the angle between the normal to the 3π decay plane and the a_1 flight direction. This is analogous but not

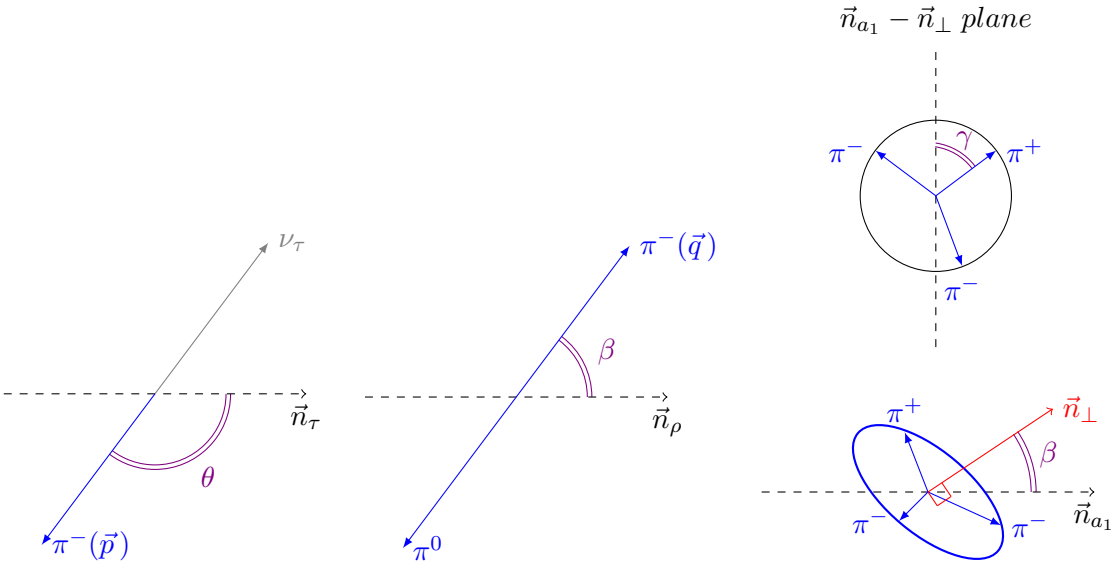

(a) $\tau^- \to \pi^-\nu_\tau$ (b) $\tau^- \to \rho^-\nu_\tau \to \pi^-\pi^0\nu_\tau$ (c) $\tau^- \to a_1^-\nu_\tau \to \pi^-\pi^+\pi^-\nu_\tau$

Figure 3.6: Definitions of angles θ, β, α and γ in $\tau^- \to \pi^-\nu_\tau$ (*left*, [a]), $\tau^- \to \rho^-\nu_\tau$ (*centre*, [b]) and $\tau^- \to a_1^-\nu_\tau$ (*right*, [c]).

identical to the angle β in the $\tau \to \rho\nu$ decay channel. The angle γ describes the relative orientation of the pions in their decay plane. The angles are shown in Fig. 3.6c (*right*) for an illustration.

The method of combining the angles described above into one quantity, which carries the full analysing power is described in the next section.

3.6.2 Optimal observable

In the general case the differential widths of any decay of a polarised τ lepton has the form [58, 59]:

$$d\Gamma = \frac{|\bar{M}|^2}{2m_\tau}(1 - h_\mu s^\mu) d\text{Lips} \quad , \tag{3.28}$$

where $|\bar{M}|^2$ is the spin averaged squared matrix element, s is the four-vector of the spin of the τ lepton, h_μ is the polarimetric 4-vector and Lips is the Lorentz-invariant phase-space. In the rest frame of the τ lepton, s_0 =0, the choice for h_0 is therefore arbitrary. Assuming that the τ lepton spin is aligned to the τ lepton flight direction (all transverse τ spin components are zero) the decay distribution transforms in this case to:

$$\frac{d\Gamma}{d\cos\theta_h} \propto \frac{1}{2}(1 + P_\tau \cos\theta_h) \quad , \tag{3.29}$$

where P_τ is the τ lepton polarisation or a helicity state for a given τ lepton decay, $\cos\theta_h$ is the angle between the polarimetric vector $\vec{h}$ and the direction of the τ lepton $\vec{n}_\tau$ as seen from the τ rest frame.

In the case of $\tau \to \pi\nu$ the polarimetric vector is aligned along the direction of π meson:

$$\vec{h} = \vec{n}_\pi \quad , \tag{3.30}$$

where $\vec{n}_\pi$ is a unit vector pointing along the direction of flight of the pion.

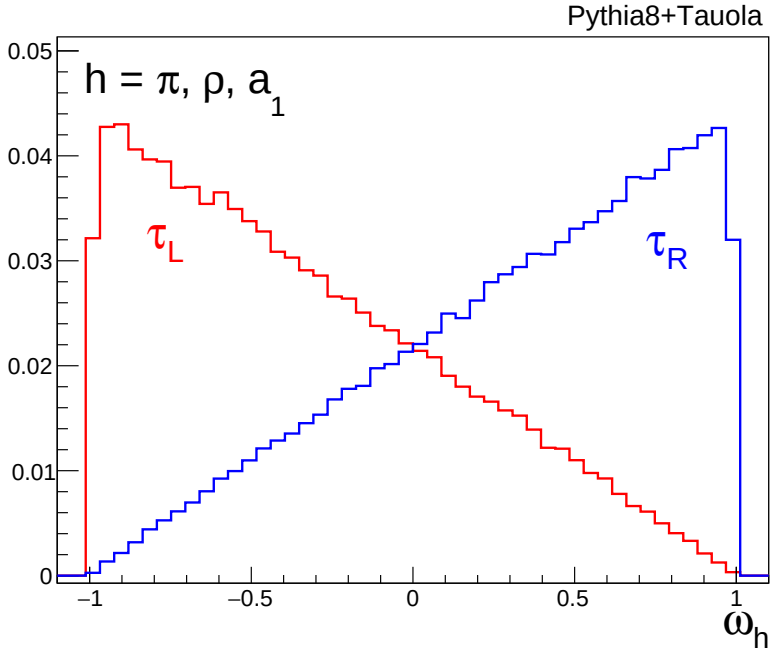

Figure 3.7: The distribution of $\cos\theta_h$ for negative (*red*) and positive (*blue*) τ helicity. The distribution is identical for the τ decays to: $\tau \to \pi\nu$, $\tau \to \rho\nu$, $\tau \to a_1\nu$.

The situation in $\tau \to \rho\nu$ and $\tau \to 3\pi\nu$ decays is slightly more complicated due to the complexity of the resonance structure. The general expressions for polarimetric vector in decays $\tau \to \rho\nu$ and $\tau \to a_1\nu$ can be found in Ref. [12]. For the hadronic form factor in $\tau \to a_1\nu$ decay we use the parametrization provided by the CLEO Collaboration [60], which includes in total seven resonances that describes the intermediate states of the $a_1 \to \pi\pi\pi$ decay. The CLEO parametrization for this decay mode is also used in TAUOLA [59] and PYTHIA8 [61] Monte Carlo generators.

Further in the text the **optimal observable** is denoted for a single τ decay as ω_h which is defined as:

$$\omega_h = \cos\theta_h \quad . \tag{3.31}$$

The distribution for the variable ω_h at generator level is shown in Fig. 3.7. Events of $e^-e^+ \to Z/\gamma \to \tau^-\tau^+$ process are generated using PYTHIA8 [61] supplemented with the TAUOLA [59] program for τ lepton decays. The distribution for ω_h is the same for all τ lepton decay channels considered. The gaps in the first and last bins are caused by the finite mass of the hadron system.

3.6.3 Helicity correlation

The helicities of two τ leptons in the $Z \to \tau^-\tau^+$ decay are 100% anti-correlated (in the limit $E_\tau \gg m_\tau$). Therefore, the helicity state separation and consequently the sensitivity to the polarisation measurement can gain by exploiting this correlation. The method proposed in Ref. [8] consists in defining a new optimal observable using both tau leptons in the decay. Denoting ω_1 and ω_2 to be the observables for τ^- and τ^+, from the joint decay distribution one can define:

$$\Omega = \frac{\omega_1 + \omega_2}{1 + \omega_1\omega_2} \quad . \tag{3.32}$$

The distribution of Ω is shown at the generator level in Fig. 3.8 with both τ leptons decaying into hadrons (*left*) and with one of the τ lepton decaying to hadron and other to a lepton (*right*). The separation between left-handed tau (τ_L^-) and right-handed tau (τ_R^-) is clearly improved comparing to distribution of ω_h.

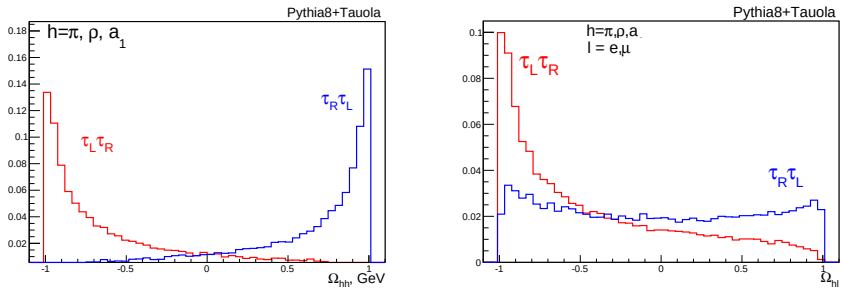

Figure 3.8: The distribution of Ω for negative (*red*) and positive (*blue*) τ^- helicity. This variable can be defined for any combination of hadronic and leptonic decays $\tau_h\tau_h$, $\tau_h\tau_\ell$ or $\tau_\ell\tau_\ell$ ($h = \pi$, ρ, a_1 and $\ell = e, \mu$), and is selected in $a_1 + \pi$ category in this analysis.

It has been shown [62] that the energies of the decay products of the τ leptons and the acollinearity angle between the decay products in the laboratory frame carry information about the helicity states of τ leptons. A suitable observable which includes both quantities is the invariant mass of the visible decay products of both τ leptons:

$$m_{\text{vis}} = \sqrt{2\,E_1E_2(1 - \cos\delta)} \quad , \tag{3.33}$$

where $E_{1,2}$ is the energy of the lepton in the leptonic τ lepton decay or the energy of the hadrons in the case of a hadronic τ lepton decay and δ is the acollinearity angle.

It should be noted that the reconstruction of the optimal observable ω_h requires the knowledge of the rest frame of the τ lepton (both τ leptons for Ω), which is usually not a simple task. In cases the flight direction of τ leptons cannot be measured, the `SVfit` algorithm [9] for the reconstruction of the τ lepton decay is used in this analysis. Since its performance is limited in some event categories the better sensitivity is obtained from observables, which are measured directly in the detector, e.g. the angle β in ρ decays and the angles β and γ in the decay of $\tau \to a_1\nu$). These quantities are denoted hereafter in the text as visible observables ω_{vis} or Ω_{vis}. The summary of the observables used in each category is given in Table 3.15. In Figure 3.9 the distributions of the observables used in the categories $\rho\pi$, $\pi\pi$, μa_1, $e\mu$, $\rho\rho$, $\mu\rho$ are shown at the generator level.

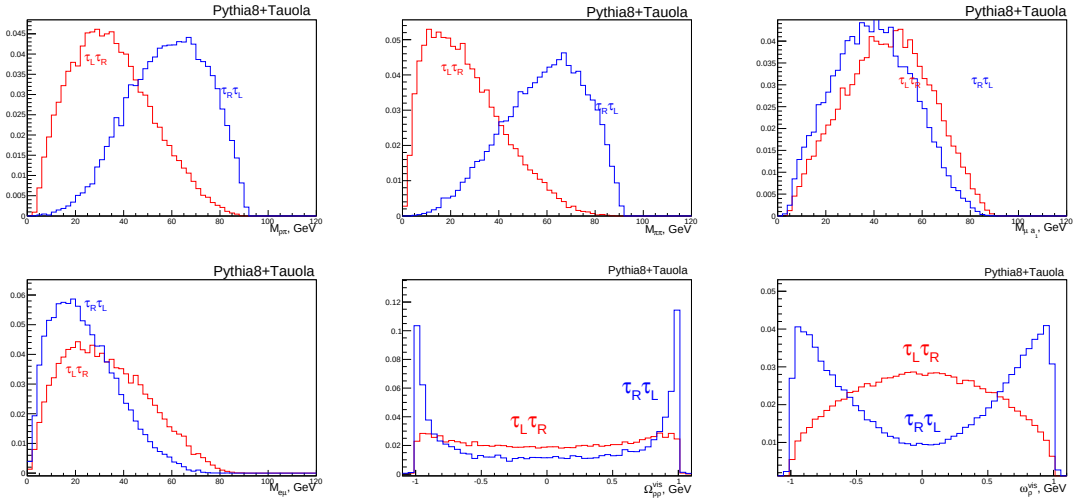

Figure 3.9: Distributions for τ polarisation observables in different categories. *Upper row*: $m_{\text{vis}}(\rho\pi)$, $m_{\text{vis}}(\pi\pi)$, $m_{\text{vis}}(\mu a_1)$ and *Bottom row*: $m_{\text{vis}}(e\mu)$, $\Omega_{\text{vis}}(\rho\rho)$, $\omega_{\text{vis}}(\rho)$. The labels LR and RL denote the helicity states of the τ^- and τ^+.

3.7 Tau helicity state in CMS Monte Carlo sample

3.7.1 `TauSpinner` applied to official CMS Drell-Yan samples

The `TauSpinner` [63] algorithm allows to assign the most probable helicity to τ leptons in every simulated $Z \to \tau\tau$ decay. For input `TauSpinner` requires the generated four-momenta of both τ leptons and their decay products. It then calculates the polarimetric vectors for both τ leptons, $\mathbf{h}^-$, $\mathbf{h}^+$ that determine the spin-dependent part of the $Z \to \tau\tau$ matrix element:

$$w = \frac{1}{4} \sum_{i,j=0,4}^{4} h_i^+ h_j^- R_{ij} \quad , \tag{3.34}$$

where R_{ij} describes the spin orientation of τ leptons with respect to each other. Neglecting the transverse spin components of the τ leptons in case of $Z \to \tau\tau$ it has the

form:

$$R_{ij} = \begin{pmatrix} 1 & 0 & 0 & -P_\tau \\ 0 & 0 & 0 & 0 \\ 0 & 0 & 0 & 0 \\ -P_\tau & 0 & 0 & 1 \end{pmatrix} \quad . \tag{3.35}$$

Then the probability of that the τ^- is produced in the right-handed state is calculated as:

$$P_R = \frac{\frac{d\hat{\sigma}}{d\cos\theta'}(\hat{s}, \cos\theta', P_\tau = +1)}{\frac{d\hat{\sigma}}{d\cos\theta'}(\hat{s}, \cos\theta', P_\tau = +1) + \frac{d\hat{\sigma}}{d\cos\theta'}(\hat{s}, \cos\theta', P_\tau = -1)} \quad , \tag{3.36}$$

where $\hat{s}$ is the squared centre-of-mass energy of the τ lepton pair and $\cos\theta$' the scattering angle of the τ^- with respect to the incoming quark.

The probability (calculated as 3.36) is then compared to the random value r $(0 < r < 1)$, if $P_R > r$ the event is assigned to be $\tau_R^- \tau_L^+$ and $\tau_L^- \tau_R^+$ otherwise.

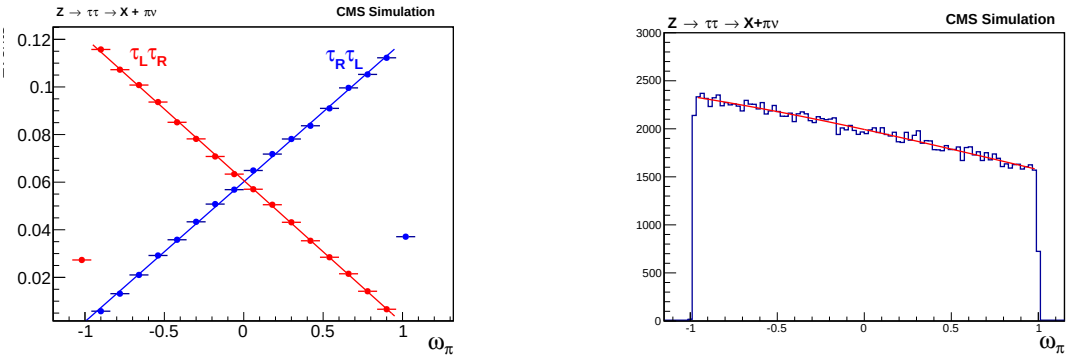

Figure 3.10: Distributions of generated ω_π in the decays $Z \to \tau\tau \to X + \pi\nu$ with selected helicity states (*left*) and with the nominal mixture of τ_L and τ_R states as observed in official CMS DY Monte Carlo sample (*right*).

In Figure 3.10 the distribution of ω_π is shown with selected helicities obtained from `TauSpinner` (*left*) and without separating τ helicity states (*right*). The slope on the *right* distribution is about -16% roughly corresponding to a combination of the SM weak couplings used in PYTHIA8 for the decay of the tau leptons and the different value in the MADGRAPH5 generator.

3.7.2 MADGRAPH5 LHE helicity flag and Dedicated MC simulation

Unfortunately it tuned out that the method of determining the original helicity of the tau lepton using the `TauSpinner` algorithm only works on average but does not work on an event by event basis, which is necessary to construct templates for a given helicity

of the tau lepton. This is because MadGraph5 calculates leading-order (LO) matrix elements using values of (M_Z, G_F, α_{elm}) leading to a LO value for $\sin^2\theta_W^{\text{eff}} = 0.22224$ very different than the effective value used by Pythia8, $\sin^2\theta_W^{\text{eff}} = 0.2315$, resulting in different couplings and average polarisations.

Consequently, it was necessary to produce and process a dedicated DY sample, using Pythia8 configuration that properly transfers the LHE value for the tau-lepton helicity from MadGraph5 to Pythia8. This approach guarantees that the tau helicities are accurately accounted for an event-by-event basis, thereby enabling the generation of left- and right-handed templates. More details on this dedicated production were already given in Sect. 3.2.

3.8 The average τ lepton polarisation and Unpolarisation procedure of Monte Carlo sample

The average τ lepton polarisation, $\langle P_\tau \rangle$, reads:

$$\langle P_\tau \rangle = \frac{N(Z \to \tau_R^- \tau_L^+) - N(Z \to \tau_L^- \tau_R^+)}{N(Z \to \tau_R^- \tau_L^+) + N(Z \to \tau_L^- \tau_R^+)} \quad , \tag{3.37}$$

where $\mathrm{N}(Z \to \tau_R^- \tau_L^+)$ and $\mathrm{N}(Z \to \tau_L^- \tau_R^+)$ are the numbers of events with positive and negative τ^- helicity in the event sample.

The MC generator MadGraph5 is used to generate $Z \to \tau\tau$ events. The events are fully simulated in the CMS detector, and reconstructed with the same software as used for data. Then trigger, τ lepton identification and event selection criteria are applied. The number of events matching these criteria, $N_{\text{reco}}(Z \to \tau\tau)$ are split into event samples containing either $Z \to \tau_R^- \tau_L^+$ or $Z \to \tau_L^- \tau_R^+$ decays, using the LHE helicity flag. The corresponding event numbers are $N_{\text{reco}}(Z \to \tau_R^- \tau_L^+)$ and $N_{\text{reco}}(Z \to \tau_L^- \tau_R^+)$, respectively. The total number of events $N_{\text{reco}}(Z \to \tau\tau)$ reads then as a function of the integrated luminosity:

$$\begin{aligned} N_{\text{reco}}(Z \to \tau\tau) &= \sigma(Z \to \tau\tau) \cdot \mathcal{L}_{\text{int}} \cdot \epsilon_{\text{av}} && (3.38)\\ &= \sigma(Z \to \tau\tau) \cdot \mathcal{L}_{\text{int}} \cdot \left[\epsilon(Z \to \tau_R^- \tau_L^+) \cdot \frac{1 + \langle P_\tau \rangle^{\text{MC}}}{2} \right. && (3.39)\\ &\quad \left. + \epsilon(Z \to \tau_L^- \tau_R^+) \cdot \frac{1 - \langle P_\tau \rangle^{\text{MC}}}{2} \right] && (3.40)\\ &= N_{\text{reco}}(Z \to \tau_R^- \tau_L^+) + N_{\text{reco}}(Z \to \tau_L^- \tau_R^+) \quad . && (3.41) \end{aligned}$$

The total Z production cross-section times branching fraction in τ-leptons is denoted as $\sigma(Z \to \tau\tau)$ and the average acceptance by ϵ_{av}. $\epsilon(Z \to \tau_R^- \tau_L^+)$, $\epsilon(Z \to \tau_L^- \tau_R^+)$ are the acceptances for the two different helicity states of the τ-leptons and $\langle P_\tau \rangle^{\text{MC}}$ is the average polarisation in the Monte Carlo generator.

The average polarisation in the Monte Carlo at the generator level depends strongly on the mass range over which the average is taken. In Figure 3.11 the mass distributions for the two polarisation state of the tau pair and the resulting polarisation as a function of mass are shown for different values of $\sin^2\theta_W^{\text{eff}}$. A mass window of **75 to 120 GeV** is chosen based on the criteria of maximizing the cross-section and maintaining an average polarization value that is very close to the Z-peak value. The latter is important for the extraction of the polarisation and its interpretation in terms of the effective electro-weak mixing angle as discussed in Chapter 5 and Fig. 5.1.

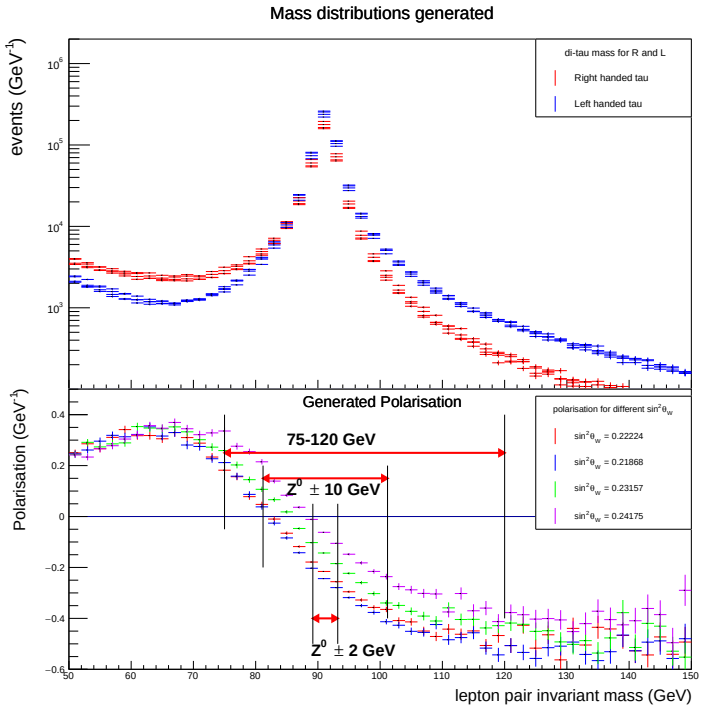

Figure 3.11: Generated di-tau mass distributions for left- and right-handed tau leptons and the resulting tau-polarisation in the upper and lower part of the figure, respectively. The curves are for four different values of the electro-weak mixing angle.

The red line in Fig. 3.12 shows the average polarisation at generator level after a mass window of 75 to 120 GeV is applied on the generated mass for different event categories. This line corresponds to the polarisation implemented in the MC generator. After applying the τ-lepton identification and event selection described in Sect. 3.5, the fraction of the two different helicity states is shown by the black dots, changing the value of the average polarisation in the sample due to different acceptances $\epsilon(Z \to \tau_R^- \tau_L^+)$ and $\epsilon(Z \to \tau_L^- \tau_R^+)$. This change depends further on the decay modes of the τ leptons as shown in the Fig. 3.12.

To create templates corresponding to zero polarisation for the measurement of the average τ-lepton polarisation in $Z \to \tau\tau$ events in data, the Monte Carlo sample has been unpolarised by re-weighting the events to achieve $\langle P_\tau \rangle^{\mathrm{MC}} = 0$.

An unpolarised Monte Carlo sample is obtained by applying a scale factor $s_{LR/RL}$ (LR/RL denotes here the helicity configuration of the $\tau^-\tau^+$ pair) using the number of events of different helicities in the generated event sample:

$$\frac{s_{RL} \cdot N_{\mathrm{gen}}(Z \to \tau_R^- \tau_L^+) - s_{LR} \cdot N_{\mathrm{gen}}(Z \to \tau_L^- \tau_R^+)}{s_{RL} \cdot N_{\mathrm{gen}}(Z \to \tau_R^- \tau_L^+) + s_{LR} \cdot N_{\mathrm{gen}}(Z \to \tau_L^- \tau_R^+)} \triangleq 0 \tag{3.42}$$

$$\Rightarrow s_{RL/LR} = \frac{1}{N_{\mathrm{gen}}(Z \to \tau_{L/R}^- \tau_{R/L}^+)} \quad . \tag{3.43}$$

In this way the difference of the selection efficiency in samples of different helicity and decay modes are considered in the measurement of the polarisation. The result is shown in Fig. 3.13. There is no remaining polarisation in the generated sample, but the differences in the acceptance of the samples with different helicities become visible.

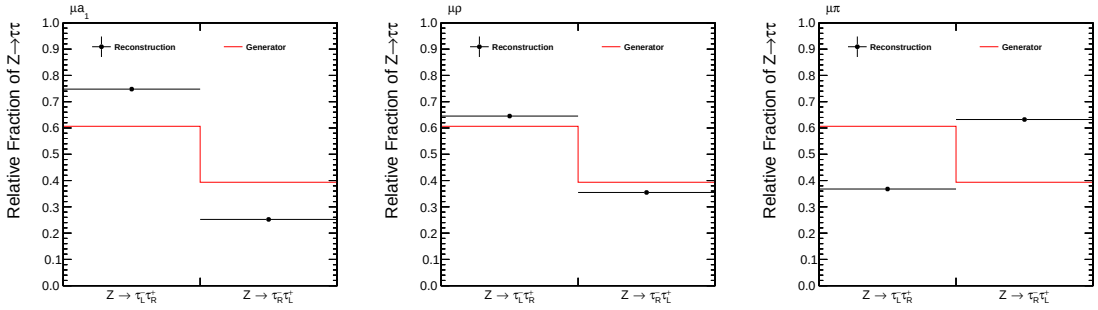

Figure 3.12: Number of events with positive ($Z \to \tau_R^- \tau_L^+$) and negative ($Z \to \tau_L^- \tau_R^+$) τ^- helicity before any event selection (*red line*) and after applying τ-lepton identification and event selection (*black dot*). A mass window of 75 to 120 GeV is applied on the generated mass. Three different hadronic τ-lepton decay modes in the $\tau_\mu \tau_{\mathrm{h}}$ channel are compared: $\tau \to a_1 \nu$ (*left*), $\tau \to \rho\nu$ (*centre*) and $\tau \to \pi\nu$ (*right*). The fractions of events correspond to the values obtained before applying the scale factors $s_{LR/RL}$ and s_{integral} (i.e. before *unpolarisation* procedure).

The scale factors $s_{LR/RL}$ from Eq. (3.42) modify the normalisation of the signal. A common scale factor s_{integral} is applied to the samples of both helicity states in order to preserve the signal yield at $\langle P_\tau \rangle = \langle P_\tau \rangle^{\mathrm{MC}}$. It is obtained from:

$$N_{\mathrm{reco}}(Z \to \tau\tau) \triangleq s_{\mathrm{integral}} \cdot \left[s_{RL} \cdot N_{\mathrm{reco}}(Z \to \tau_R^- \tau_L^+) \cdot \frac{1 + \langle P_\tau \rangle^{\mathrm{MC}}}{2} + s_{LR} \cdot N_{\mathrm{reco}}(Z \to \tau_L^- \tau_R^+) \cdot \frac{1 - \langle P_\tau \rangle^{\mathrm{MC}}}{2} \right] \tag{3.44}$$

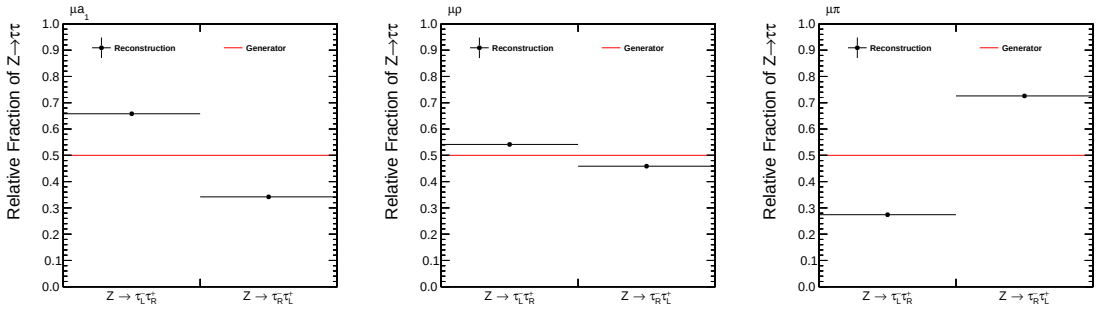

Figure 3.13: Number of events with positive ($Z \to \tau_R^- \tau_L^+$) and negative ($Z \to \tau_L^- \tau_R^+$) τ^- helicity before any event selection (*red line*) and after applying τ-lepton identification and event selection (*black dot*). A mass window of 75 to 120 GeV is applied on the generated mass. Three different hadronic τ-lepton decay modes in the $\tau_\mu \tau_\mathrm{h}$ channel are compared: $\tau \to a_1 \nu$ (*left*), $\tau \to \rho\nu$ (*centre*) and $\tau \to \pi\nu$ (*right*). The fractions of events correspond to the values obtained after applying the scale factors $s_{LR/RL}$ and s_integral (i.e. after *unpolarisation* procedure).

and

$$\langle P_\tau \rangle^\mathrm{MC} = \frac{N_\mathrm{gen}(Z \to \tau_R^- \tau_L^+) - N_\mathrm{gen}(Z \to \tau_L^- \tau_R^+)}{N_\mathrm{gen}(Z \to \tau_R^- \tau_L^+) + N_\mathrm{gen}(Z \to \tau_L^- \tau_R^+)} \quad . \tag{3.45}$$

Therefore:

$$s_\mathrm{integral} = N_\mathrm{gen}(Z \to \tau_R^- \tau_L^+) + N_\mathrm{gen}(Z \to \tau_L^- \tau_R^+) \quad . \tag{3.46}$$

The samples for the construction of the templates for the two different helicity states used for the measurement of the polarisation in data are then obtained as:

$$N_\mathrm{fit}(Z \to \tau_{L/R}^- \tau_{R/L}^+) = s_\mathrm{integral} \cdot s_{RL/LR} \cdot N_\mathrm{reco}(Z \to \tau_{L/R}^- \tau_{R/L}^+) \quad , \tag{3.47}$$

with the scale factors defined in Eqs. 3.46 and 3.42. As the selection efficiency depends on the average tau polarisation, the inclusive normalisation is only preserved for the polarisation implemented in the MC generator.

The average tau polarisation is obtained in data from a fit to the distributions of optimal observables, introduced in Sect. 3.6, using templates for signal and background.

$$\mathcal{T}(\mathrm{data}) \overset{\mathrm{fit}}{=} \mathcal{T}(\mathrm{sig.}, \langle P_\tau \rangle, r) + \mathcal{T}(\mathrm{bkg.}) \quad . \tag{3.48}$$

The signal template $\mathcal{T}(\mathrm{sig.}, \langle P_\tau \rangle, r)$ is split into two parts, $\mathcal{T}(Z \to \tau_R^- \tau_L^+)$ and $\mathcal{T}(Z \to \tau_L^- \tau_R^+)$, and depends on two parameters of interest, the average tau polarisation, $\langle P_\tau \rangle$, and an overall signal strength modifier, r, as given in the following formula:

$$\mathcal{T}(\mathrm{sig.}, \langle P_\tau \rangle, r) = r \cdot \left[\frac{1 + \langle P_\tau \rangle}{2} \cdot \mathcal{T}(Z \to \tau_R^- \tau_L^+) + \frac{1 - \langle P_\tau \rangle}{2} \cdot \mathcal{T}(Z \to \tau_L^- \tau_R^+) \right] . \tag{3.49}$$

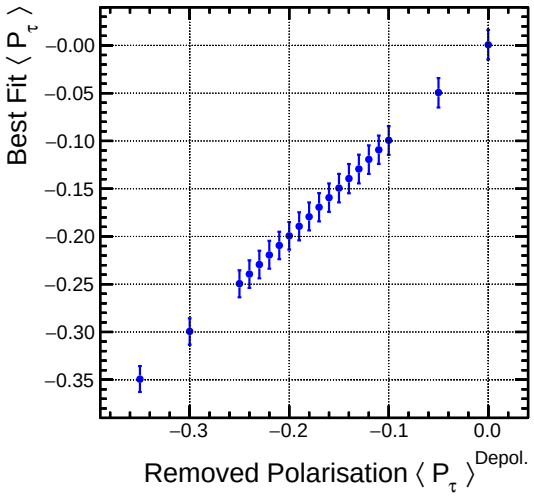

Figure 3.14: Linearity check for the polarisation fit, proving the one-to-one relation between the average τ lepton polarisation that is removed in the *unpolarisation* procedure from the signal templates and the fitted average polarisation.

In order to be able to directly retrieve the average τ lepton polarisation from the fit, the signal templates using for the fit must be rescaled such that they correspond to an unpolarised sample of $Z \to \tau\tau$ events. This is achieved by scaling the integrals of the templates $\mathcal{T}(Z \to \tau^-_{L/R}\tau^+_{R/L})$ to the number of events $N_{\text{fit}}(Z \to \tau^-_{L/R}\tau^+_{R/L})$. After this scaling of the signal, the expected values for the average polarisation as well as for the signal strength modifier do not depend any more on the final state and the tau decay mode, respectively, and can therefore be easily combined in a global fit.

It has been checked that the polarisation fit is able to find back the polarisation, that was taken out in this re-weighting/unpolarisation step in an *Asimov* dataset [64]. An *Asimov* dataset is generated for a particular set of model parameters, here $(r, \langle P_\tau \rangle)$, such that the maximum likelihood best-fit value of all those parameters are equal to their generated values.

Maximum likelihood fits (as described in Sect. 3.11) have been performed with an *Asimov* dataset. The single difference between all these fits is the variation of the parameter $\langle P_\tau \rangle^{\text{unpol.}} = \langle P_\tau \rangle^{\text{MC}}$ in the range from -35% to 0% in steps of 1-5%.

Figure 3.14 shows the *measured* average polarisation as a function of this so-called *removed* polarisation. There is a one-to-one relation between input and output of these fits. This proves that the fit is able to find back the polarisation that was removed in the *unpolarisation* step. It also shows, that the measured polarisation strongly depends on the knowledge and the mass interval of the polarisation in the MC sample.

3.9 Systematic uncertainties

In this section, the various sources of systematic uncertainties that impact the measurement of the tau-lepton polarisation are briefly described. These systematics are divided into two categories depending on whether they affect the normalisation or the shape of the fit templates. The name of the individual nuisance parameter corresponding to the systematic is indicated in parentheses and their impact on the total error are presented in Fig. 4.6 following these designation. The systematic uncertainties follow closely the studies documented in Ref. [53].

3.9.1 Normalisation uncertainties

Systematics affecting only the normalisation of templates are described in this section and summarised in Table 3.10.

- **Luminosity (*lumi_13TeV*)**
  The luminosity uncertainty is 1.2% on the data collected in 2016 [65]. This uncertainty is applied to all backgrounds and signal processes where the yield is estimated from MC.

- **Muon identification efficiency (*CMS_eff_m*)**
  The uncertainty on the muon identification efficiency is treated as correlated bewteen channels with muons (2% for $\tau_\mu\tau_\mathrm{h}$ and $\tau_e\tau_\mu$).

- **Electron identification efficiency (*CMS_eff_e*)**
  The uncertainty on the electron identification efficiency is treated as correlated bewteen channels with electrons (2% for $\tau_e\tau_\mathrm{h}$ and $\tau_e\tau_\mu$).

- **Electron tracking efficiency (*CMS_eff_e_trk*)**
  The uncertainty on the electron tracking efficiency is treated as correlated bewteen channels with electrons (1% for $\tau_e\tau_\mathrm{h}$ and $\tau_e\tau_\mu$).

- **Signal normalisation uncertainty (*CMS_htt_dyXsec_13TeV*)**
  The uncertainty on the Drell-Yan normalisation include the 2% cross-section uncertainty and uncertainties due to variations from PDF, α_s and QCD scales (see Sect. 3.9.5).

- **QCD estimation in the $\tau_\mathrm{h}\tau_\mathrm{h}$ channel (*CMS_htt_QCD_tt_13TeV*)**
  A 3% uncertainty on the QCD yield in $\tau_\mathrm{h}\tau_\mathrm{h}$.

- **QCD estimation in the $\tau_e\tau_\mu$ channel (*CMS_htt_QCD_em_13TeV*)**
  A 10% uncertainty on the QCD yield in $\tau_e\tau_\mu$.

- **QCD extrapolation between anti-isolated and isolated regions (*QCD_Extrap_Iso_nonIso_[mt,et]*)**

Extrapolation uncertainty from the anti-isolated control region to the signal region, 20% uncertainty on the QCD yield in $\tau_\mu\tau_\mathrm{h}$ and $\tau_e\tau_\mathrm{h}$ channels.

- **W+jets cross-section (*CMS_htt_wjXsec*)**
  A 4% uncertainty is applied to the W+jets process in $\tau_\mathrm{h}\tau_\mathrm{h}$ and $\tau_e\tau_\mu$ channels for the uncertainty on the cross-section.

- **W+jets high to low m_T extrapolation (*WHighMTtoLowMT_13TeV*)**
  Extrapolation uncertainty from the high to low m_T region, 10% uncertainty on the W+jets yield in $\tau_\mu\tau_\mathrm{h}$ and $\tau_e\tau_\mathrm{h}$ channels.

- **W+jets normalisation (*CMS_htt_jetFakeLep_13TeV*)**
  Additional 20% normalisation uncertainty in the $\tau_e\tau_\mu$ channel where W+jets normalisation is based from MC.

- **$\mathrm{t\bar{t}}$ cross-section (*CMS_htt_ttXsec_13TeV*)**
  A 4.2% uncertainty is applied to the $\mathrm{t\bar{t}}$ process for the uncertainty on the cross-section.

- **Di-boson and single top cross sections (*CMS_htt_vvXsec_13TeV*)**
  A 5% uncertainty is applied to the di-boson and single-top processes for the the uncertainties on the production cross-sections.

- **EWK cross-section (*CMS_htt_ewkzXsec_13TeV*)**
  A 4% uncertainty is applied to the EWKZ process for the uncertainty on the cross-section.

Table 3.10: Systematic uncertainties affecting the normalisation of templates only.

Source of uncertainty	**Prefit uncertainty per channel**			
	$\boldsymbol{\tau_\mathrm{h}\tau_\mathrm{h}}$	$\boldsymbol{\tau_\mu\tau_\mathrm{h}}$	$\boldsymbol{\tau_e\tau_\mathrm{h}}$	$\boldsymbol{\tau_e\tau_\mu}$
Integrated luminosity	1.2%	1.2%	1.2%	1.2%
μ identification efficiency (correlated)	–	2%	–	2%
e identification efficiency (correlated)	–	–	2%	2%
e tracking efficiency (correlated)	–	–	1%	1%
DY cross-section	5.6%	5.6%	5.6%	5.6%
$\mathrm{t\bar{t}}$ cross-section	4.2%	4.2%	4.2%	4.2%
Di-boson cross-section	5%	5%	5%	5%
EWK cross-section	4%	4%	4%	4%
W+jets cross-section & normalisation	4%	10%	10%	20%
QCD normalisation	3%	20%	20%	10%

3.9.2 Shape uncertainties

Systematics affecting the shape of templates are described in this section and summarised in Table 3.13. Some of these may affect only a specific event categories and are therefore included as a mixture of shape and normalisation uncertainties.

- $e \to \tau_h$ **fake rate (*CMS_ eFakeTau_ [tt,mt,et]_ 13TeV*)**
  For τ_h candidates matched to electrons at the generated level, uncertainties in the scale factors that depend on detector region are provided by the *Tau Physics Object group* (fully uncorrelated between tau decay mode).

- $\mu \to \tau_h$ **fake rate (*CMS_ muFakeTau_ [tt,mt,et]_ 13TeV* and *CMS_ muFakeTau_ mt_ MVADM[0,1,10]_ 13TeV*)**
  For τ_h candidates matched to muons at the generated level, uncertainties in the scale factors that depend on detector region are provided by the *Tau Physics Object group* (fully uncorrelated between tau decay mode). In addition to this uncertainty on the identification of τ_h fakes (related to the `deepTau` neural network against muons), three independent uncertainties depending on the `MVA-DM` of the $\mu \to \tau_h$ candidate are included to account for the uncertainty on residual corrections for $\tau_\mu\tau_\mathrm{h}$ (specific to the use of `MVA-DM`).

- jet $\to \tau_h$ **fake rate (*CMS_ htt_ jetToTauFake_ 13TeV*)**
  The uncertainty for the probability for a jet to fake a hadronic tau depends on the p_T of the jet associated to the fake τ_h. The uncertainty amounts to $20\% \times p_\mathrm{T}^\mathrm{jet}$ / 100 GeV. Due to the lack of statistics, the correction for all events with $p_\mathrm{T} > 200$ GeV is taken as 40%. It is applied as a shape uncertainty to processes with a jet faking a hadronic tau.

- **Tau identification efficiency (*CMS_ eff_ t_ pT[low,high]_ MVADM[0,1,10]_ 13TeV*)**
  For τ_h candidates matched to genuine τ_h, the ID scale factors are computed in two p_T bins ($p_\mathrm{T} < 40$ GeV and $p_\mathrm{T} > 40$ GeV) and in three MVADM bins (MVADM $\in$ [0,1,10]). The uncertainties come from the ID scale factor fits described in Ref. [53] and are fully correlated between the $\tau_\mathrm{h}\tau_\mathrm{h}$, $\tau_e\tau_\mathrm{h}$, $\tau_\mu\tau_\mathrm{h}$ channels because the same working point of the deepTau neural network against jets is used.

- **Tau trigger efficiency (*CMS_ eff_ t_ trg_ MVADM[0,1,10]_ 13TeV* and *CMS_ eff_ Xtrigger_ mt_ MVADM[0,1,10]_ 13TeV*)**
  For triggers with τ_h legs, the uncertainties are p_T and MVADM dependent and come from the fits described in Ref. [53]. The τ_h trigger uncertainties are treated as uncorrelated between MVADM bins and channels ($\tau_\mathrm{h}\tau_\mathrm{h}$ and $\tau_\mu\tau_\mathrm{h}$ channels). Since only the single electron trigger is used in $\tau_e\tau_\mathrm{h}$, the cross-trigger efficiency is not applied.

- **Electron and muon trigger efficiencies**
  (*CMS_eff_trigger_[et,mt,em]_13TeV*)
  The uncertainty on the trigger efficiencies amounts to 2% per lepton in the $\tau_e\tau_h$, $\tau_\mu\tau_h$ and $\tau_e\tau_\mu$ channels. They are basically normalisation uncertainties but implemented as shape uncertainties as they only affect the events triggered by the corresponding cross-trigger or single lepton trigger. These uncertainties are uncorrelated between channels as different triggers are used for each channel.

- **Hadronic tau energy scale**
  (*CMS_scale_t_[1prong,1prong1pizero,3prong]_13TeV*)
  The energy of genuine τ_h is corrected by decay mode. Uncertainties on this correction depend on the decay mode and are provided by the *Tau Physics Object group*.

- **Energy resolution of the charged and neutral hadrons**
  (*CMS_res_[charged,neutral]Hadrons_13TeV*)
  These uncorrelated nuisance parameters aims to take into account different reconstruction energy resolution of the charged hadrons VS neutral hadrons. A 2% shift on the charged (neutral) hadron energy is applied, this magnitude is based on the typical uncertainty associated with tracks (ECAL clusters).

- **Muon energy scale (*CMS_scale_mu_13TeV*)**
  The energy scale of muons is not corrected with Rochester corrections because the analysis does not need to describe precisely the mass of any narrow dimuon resonance. The uncertainty in the muon energy scale corresponds to the *Muon Physics Object group* recommendation in the case where no such correction is applied. The uncertainty depends on the muon pseudorapidity, and varies between 0.4-2.7% (summarised in Table 3.11). Three separate nuisance parameters are used, one for each pseudorapidity region.

Table 3.11: Uncertainty in the muon energy scale

Detector region	$\lvert\eta\rvert < 1.2$	$1.2 < \lvert\eta\rvert < 2.1$	$\lvert\eta\rvert > 2.1$
Uncertainty	0.4%	0.9%	2.7%

- **Muon to tau fake energy scale**
  (*CMS_ZLShape_mt_[1prong,1prong1pizero]_13TeV*)
  Two uncorrelated uncertainties that affect the *oneProng* and *oneProngOnePizeros* tau decay modes are applied to the $Z \to \ell\ell$ process in the $\tau_\mu\tau_h$ channel. The uncertainties shift the p_T^μ by 1% for both the *oneProng* and *oneProngOnePizeros* decay modes. These shifts are also propagated to the E_T^{miss}.

- **Electron energy scale (*CMS_scale_e_13TeV*)**
  Uncertainties on the electron energy scale are provided by the *EGamma Physics*

Object group.

- **Electron to tau fake energy scale**
  (*CMS_ZLShape_et_[1prong,1prong1pizero]_[etalt1p5,etagt1p5]_13TeV*)
  For electrons to τ_h fakes, four uncorrelated uncertainties that affect the *oneProng* and *onePronOnePizeros* tau decay modes and also depending on detector region ($|\eta^e| < 1.5$ or $|\eta^e| > 1.5$) are applied to the $Z \to \ell\ell$ process in the $\tau_e\tau_h$ channel. To shift the p_T^e specific values (between 0.8% to 6.6%, summarised in Table 3.12) depending on the detector region are provided by the *Tau Physics Object group*.

Table 3.12: Uncertainty in the electron to tau fake energy scale

	Detector region	
	$\|\eta\| < 1.5$	$\|\eta\| > 1.5$
$1h^{\pm}$	$^{+0.806\%}_{-0.982\%}$	$^{+1.808\%}_{-1.102\%}$
$1h^{\pm}1\pi^0$	$^{+1.168\%}_{-2.475\%}$	$^{+6.570\%}_{-5.694\%}$

- **τ_h decay mode migration uncertainty**
  (*CMS_recoTauDecayModeFake_[pi,rho,a1]_13TeV*)
  The uncertainties on a possible over- or under-estimation of the main migrations between τ_h decay modes in the data compared to Monte-Carlo predictions are derived from the fits described in the Sect. 3.9.4.

- **Drell-Yan MC re-weighting (*CMS_htt_dyShape_13TeV*)**
  The uncertainty on the re-weighting applied to $Z \to \ell\ell$ process in all channels varies between no and twice the correction.

- **Top p_T re-weighting (*CMS_htt_ttbarShape_13TeV*)**
  The uncertainty on the re-weighting applied to $\bar{t}t$ process in all channels varies between no and twice the correction.

- **MC comparison for signal (*CMS_dy_mcComp_13TeV*)**
  Theoretical uncertainty for the $Z \to \tau\tau$ signal, based on different partons distribution observed with dedicated and official (from CMS collaboration) Drell-Yan samples. In this analysis the DY signal is only based on an inclusive sample (in number of jets) replacing the official exclusive and inclusive samples. The data/MC agreement in the distributions related to jets is improved by matching the number of partons at generated level between dedicated and official samples (magnitude of corrections between 3.9% and 12.3%). The uncertainty on this parton re-weighting varies between no and twice the correction.

- **MET unclustered energy (*CMS_scale_met_unclustered_13TeV*)**
  The MET unclustered energy uncertainty is applied to all MC processes that do not have recoil corrections applied, namely $\bar{t}t$ and di-boson processes, as recommended

by the *JetMET Physics Object group*.

- **MET recoil correction (*CMS_htt_boson_[reso,scale]_met_13TeV*)**
  For all MC processes that have recoil correction (Z+jets, W+jets and EWK processes) the hadronic response and its resolution are varied within the uncertainties determined during the computation of the recoil corrections.

- **B-tag efficiency (*CMS_eff_b_13TeV*)**
  The b-tagging scale factors are provided with uncertainties by the *b-tag Physics Object group*. These are applied per jet to MC simulation. The uncertainties are treated only in $t\bar{t}$ and di-boson processes.

- **Bin-by-bin uncertainties (*prop_bin[mt,et,em,tt]_*_bin[0-99]**)**
  Statistical shape uncertainties due to the use of templates derived from Monte-Carlo with limited number of events are taken into account via `Combine` framework functionality.

3.9.3 Tau decay model systematics

Systematic uncertainties on the τ lepton polarisation measurement related to the decay model of τ lepton decays are discussed in this section. As it was pointed out in Sect. 3.6.2 the polarimetric vector in the decays $\tau \to \pi\nu$ and $\tau \to \rho\nu$ is determined purely by the Lorentz structure of these decays and thus contains no QCD dynamics. For the same reason the categories where m_{vis} is used as an observable no model dependence is expected.

Only the decay $\tau \to a_1\nu$ has non zero uncertainty due to the model used to describe the decay chain. The τ decay to three pions and a neutrino is dominated by the $a_1(1260)$ ($J^{PG} = 1^{+-}$). It decays through the intermediate state of $\rho\pi$, with mostly $\rho(770)$ and an admixture of $\rho(1450)$ at higher masses, followed by $\rho \to \pi\pi$ decay. One expects the two charge combinations $\tau^- \to \pi^+\pi^-\pi^-\nu_\tau$ and $\tau^- \to \pi^-\pi^0\pi^0\nu_\tau$ to have a similar structure.

The theoretical systematic uncertainty originates from the imperfect knowledge of the decay $a_1 \to 3\pi$. The procedure used to estimate the uncertainty is the following. Distributions of the $\cos\theta_h$ for a positive and negative τ lepton helicity have been produced with the TAUOLA Monte Carlo program using the nominal values for the parameters and relative contribution of the resonances listed in Table 3.14. Further these distributions will be referred to as $\cos\theta_h^R$ and $\cos\theta_h^L$. Then, a linear combination of $\cos\theta_h^R$ and $\cos\theta_h^L$ is produced with a fixed value of the τ lepton polarisation ($P_\tau^0 = -0.15$). Two additional samples of $\tau \to 3\pi\nu_\tau$ decay have been generated with a modified version of TAUOLA corresponding to *up* and *down* variation of the resonance parameters and their relative contribution. Parameters were varied within their uncertainties published by the CLEO collaboration.

Table 3.13: Systematic uncertainties affecting the shapes of templates. The uncertainty magnitudes listed in the Table refer to modifications of the relevant quantity.

Source of uncertainty	**Prefit uncertainty per channel**			
	$\boldsymbol{\tau_h\tau_h}$	$\boldsymbol{\tau_\mu\tau_h}$	$\boldsymbol{\tau_e\tau_h}$	$\boldsymbol{\tau_e\tau_\mu}$
$e \to \tau_h$ fake rate	η dependent	η dependent	η dependent	-
$\mu \to \tau_h$ fake rate	p_T/MVADM dependent	p_T/MVADM dependent	p_T/MVADM dependent	-
jet $\to \tau_h$ fake rate	p_T dependent	p_T dependent	p_T dependent	p_T dependent
Tau identification efficiency	p_T/MVADM dependent	p_T/MVADM dependent	p_T/MVADM dependent	-
Tau trigger efficiency	p_T/MVADM dependent	p_T/MVADM dependent	p_T/MVADM dependent	-
Electron trigger efficiency	-	-	p_T/η dependent	p_T/η dependent
Muon trigger efficiency	-	p_T/η dependent	-	p_T/η dependent
Hadronic tau energy scale	DM dependent	DM dependent	DM dependent	
Muon energy scale	-	0.4–2.7%	-	0.4–2.7 %
Muon to tau fake energy scale	-	1%	-	-
Electron energy scale	-	-	Event-dependent	Event-dependent
Electron to tau fake energy scale	-	-	0.8–6.6%	-
Misidentified $\tau_h \to h^\pm$	2.8%	2.8%	2.8%	-
Misidentified $\tau_h \to h^\pm\pi^0$	3.2%	3.2%	3.2%	-
Misidentified $\tau_h \to h^\pm h^\pm h^\pm$	3.7%	3.7%	3.7%	-
Drell-Yan MC re-weighting	100%	100%	100%	100%
Top p_T re-weighting	100%	100%	100%	100%
MC comparison for signal	100%	100%	100%	100%
MET unclustered energy	Event-dependent	Event-dependent	Event-dependent	Event-dependent
MET recoil correction	Event-dependent	Event-dependent	Event-dependent	Event-dependent
B-tag efficiency	Event-dependent	Event-dependent	Event-dependent	Event-dependent
Limited MC statistics	per bin	per bin	per bin	per bin

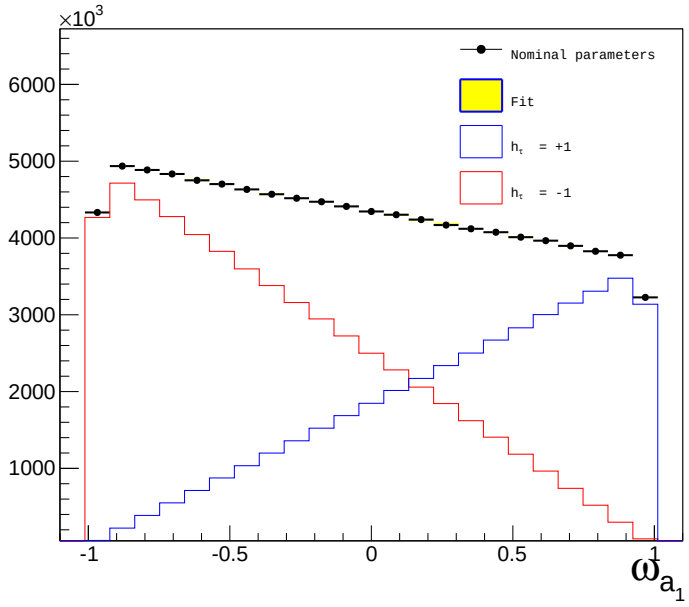

Figure 3.15: Fit of the templates for ω_{a_1} produced with *up* variation of the resonance parameters to pseudo-data generated with nominal parameters values.

Two fits of the templates for $\cos\theta_h^R$ and $\cos\theta_h^L$ taken from the samples produced with varied parameters to the sample with nominal parameters values have been performed. The half difference of the value for P_τ^0 extracted from both fits is taken as an estimate of the uncertainty. An example of the fit to the *up* variation of the resonance parameters is shown in Fig. 3.15. The obtained variation is $(\Delta P_\tau)_{model} = (1.41 \pm 1.37) \times 10^{-4}$. The error on this uncertainty comes from the Monte Carlo statistics used to perform the fits. This value is far below of any currently reached experimental precision on the τ lepton polarisation measurement.

3.9.4 Tau decay mode migrations

The reconstruction of decay modes of hadronically decaying τ leptons from `HPS` is imperfect. In CMS, τ lepton decay modes (DM) are conventionally denoted by the following definition, where $N_{h^\pm}$ is the number of charged particles (also called *prong*) and N_{strips} the number of strips (that should represent the number of π^0s decay products) in the τ_h candidate.

$$\text{DM} = 5\,(N_{h^\pm} - 1) + N_{\text{strips}} \tag{3.50}$$

Figures 3.2 and 3.3 in Section 3.3.4.1 show the performance of the τ lepton decay mode (DM) reconstruction from `HPS` and improved by the `MVA-DM` algorithm obtained in simulated $Z \to \tau\tau \to \ell\tau_\text{h}$ events for the τ_h side. One- and three-prong decays can be

Table 3.14: Result of a fit of the a_1 including different intermediate resonances to the decay $\tau^- \to \pi^-\pi^0\pi^0\nu_\tau$ be the CLEO collaboration. The first column gives the intermediate state, the second specifies the relative angular momentum between two particles, the third is the significance of the amplitude in the standard deviations and the last column is the fraction of the events.

Resonance	L	Significance	Fraction, %
$\rho(770)\pi$	S	-	68.11
$\rho(1450)\pi$	S	1.4σ	0.30 ± 0.66
$\rho(770)\pi$	D	5.0σ	0.36 ± 0.18
$\rho(1450)\pi$	D	3.1σ	0.43 ± 0.29
$f_2(1270)\pi$	P	4.2σ	0.14 ± 0.06
$\sigma\pi$	P	8.2σ	16.18 ± 4.06
$f_0(1370)\pi$	P	5.4σ	4.29 ± 2.40

well separated, but within these groups migrations between decay modes amount for up to 20% even after the improvements by the `MVA-DM`.

Systematic uncertainties result from possible differences between the migration matrices in Figs. 3.2 and 3.3 and their counterparts in data. However, it is challenging to measure these matrices in data where the true decay mode is not known. The analysis discussed in this note is affected in two ways by these decay mode migrations. Firstly, events are categorised by the τ lepton decay mode. Migrations lead to effects on the normalisation of signal with respect to data and therefore potentially to tensions between categories. Secondly, the final disciminators are (in most categories) optimised on a certain τ lepton decay mode. Evaluating a given disciminator on events with misidentified decay mode might lead to a shape altering effect worsening the agreement of data with simulation in individual categories.

The second effect is special to this analysis and has been studied in detail. Simulated templates are fitted to data in the $\tau_\mu\tau_\mathrm{h}$ channel were small variations of the relative contamination of a given reconstructed decay mode DM are treated as parameters of interest. The templates are defined in bins of the visible $\tau_\mu\tau_\mathrm{h}$ mass, m_vis for single pion and in bins of the visible τ_h mass, m_{τ_h}, in reconstructed ρ and 3-prong events.

Contaminations of a reconstructed decay mode are the horizontal off-diagonal elements in the upper parts of Figs. 3.2 and 3.3 defined by the formula (3.11).

The possible variation δ in data with respect to the estimated contamination for

a given reconstructed decay mode r by other generated decay mode g' ($g' \neq r$) is:

$$\delta_{r,g'} = \text{contamination}(r \leftarrow g')^{\text{data}}_{r \neq g'} - \text{contamination}(r \leftarrow g')^{\text{simulation}}_{r \neq g'} \tag{3.51}$$

$$\equiv x^{\text{reco}}(r \leftarrow g')_{r \neq g'} \quad . \tag{3.52}$$

$\delta = 0$ means perfect agreement between the estimated contaminations and data and no corrections are necessary. Only the three most important migrations are considered:

$$x^{\text{reco}}_0 \equiv x^{\text{reco}}(0 \leftarrow 1) = x^{\text{reco}}(h^{\pm} \leftarrow h^{\pm}\pi^0) \tag{3.53}$$

$$x^{\text{reco}}_1 \equiv x^{\text{reco}}(1 \leftarrow 2,3,4) = x^{\text{reco}}(h^{\pm}\pi^0 \leftarrow h^{\pm}\pi^0, h^{\pm}\pi^0\pi^0, h^{\pm}\pi^0\pi^0\pi^0) \tag{3.54}$$

$$x^{\text{reco}}_{10} \equiv x^{\text{reco}}(10 \leftarrow 11,12) = x^{\text{reco}}(h^{\pm}h^{\pm}h^{\pm} \leftarrow h^{\pm}h^{\pm}h^{\pm}\pi^0, h^{\pm}h^{\pm}h^{\pm}\pi^0\pi^0) \tag{3.55}$$

The variables x^{reco}_r parametrise the change in the comparison of data and simulation of the fraction of all events reconstructed as decay mode r, that migrated from the other matching generated decay modes g' to the reconstructed decay mode r. The relative normalisations are adjusted in the fit to conserve the total number of events.

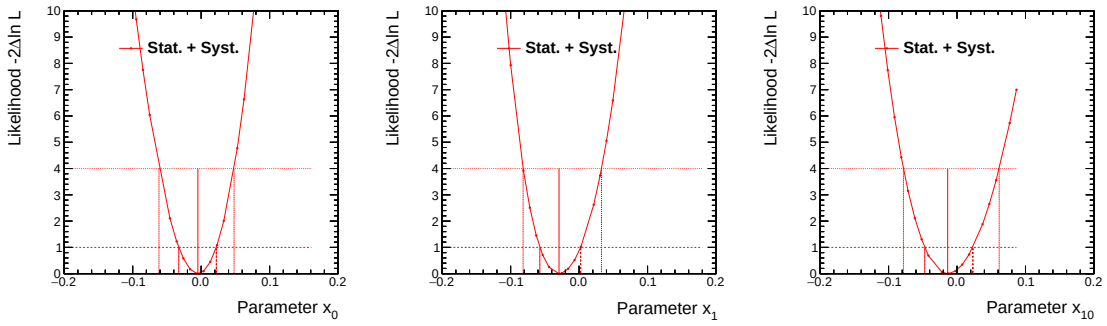

Figure 3.16: Likelihood scans of the parameters x^{reco}_r parametrising possible migrations within reconstructed decay modes. The best fit values indicate agreement between data and simulation at a level of 1 to 2σ. The black points from the likelihood scan are fitted with parabolas shown as red curves. From these, the best fit values and uncertainties are extracted.

The parameters x^{reco}_r are measured simultaneously in the same combined fit in all three categories of the $\tau_\mu\tau_{\text{h}}$ channel. Distributions before (*pre-fit*) and after (*post-fit*) this fit are shown in Fig. 3.17.

Systematic uncertainties are the same as in the final polarisation fit except for decay mode migration uncertainties. The agreement between data and simulation improves slightly when going from pre-fit to post-fit distributions. The corresponding likelihood scans for single scaling parameters x^{reco}_r are depicted in Fig. 3.16.

The black dots are fitted with parabolas (red curves), where the position to the minimum is fixed to the value retrieved from global fit. The fit range is restricted to a small region around the minimum. The parameters are measured as follows:

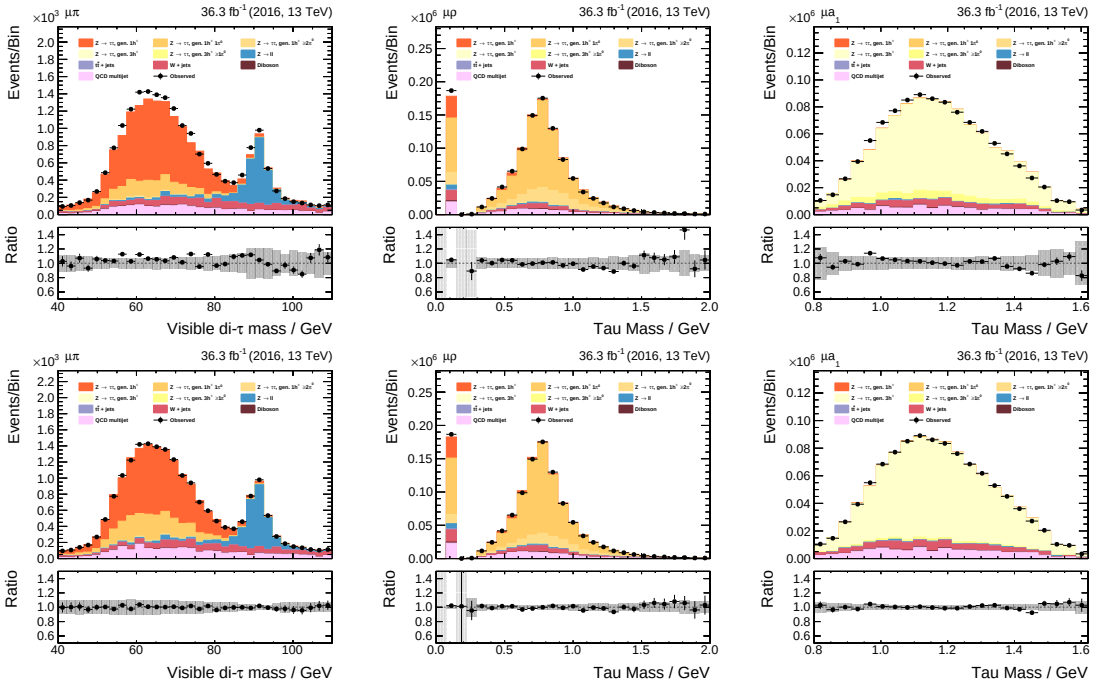

Figure 3.17: Distributions before (*top*) and after (*bottom*) the combined fit in the three categories, $\mu + \pi$ (*left*), $\mu + \rho$ (*centre*), $\mu + a_1$ (*right*), of the $\tau_\mu \tau_\mathrm{h}$ channel. The $Z \to \tau\tau$ signal is splitted in the five components according to the generated hadronic decay mode. After the fit with respect to the decay mode migrations within reconstructed decay modes, x_r^reco, there is a good agreement between data and simulation.

$$
\begin{aligned}
x_0^\mathrm{reco} &= -0.005^{+0.027}_{-0.028} \\
x_1^\mathrm{reco} &= -0.029^{+0.032}_{-0.028} \\
x_{10}^\mathrm{reco} &= -0.014^{+0.037}_{-0.034}
\end{aligned}
$$

The measured shifts in data with respect to simulation are all compatible with zero within $1\,\sigma$. These small corrections are applied for events in all three reconstructed decay modes. Together with the normalisation factors, these measurements can be translated in systematic uncertainties for the polarisation measurement.

3.9.5 Theoretical uncertainties

Uncertainties on the signal yield related to the QCD scales like the factorisation scale and the renormalisation scale, to the value of the strong coupling constant, α_s, and to the choice of the Parton Distribution Functions (PDF) sets used in the MC simulation have been studied as outlined in Ref. [66]. The QCD scales have been varied up and down by a factor of 2. The strong coupling constant has been varied by ± 0.0015. The maximum effect of these variations in both directions does not indicate any shape dependence on the final discriminators nor any difference for the two helicity states. For the study of effects related to the PDF choice weights for 100 different PDF sets from NNPDF collaboration have been applied and the mean of the change with respect to the nominal shapes has been studied. Again no shape or helicity dependence has been found. The weights for reweighting to the different PDF sets do not contain any information about the helicities of the τ leptons. Therefore the differences related to these weights are (almost) 100% correlated among the two helicity states.

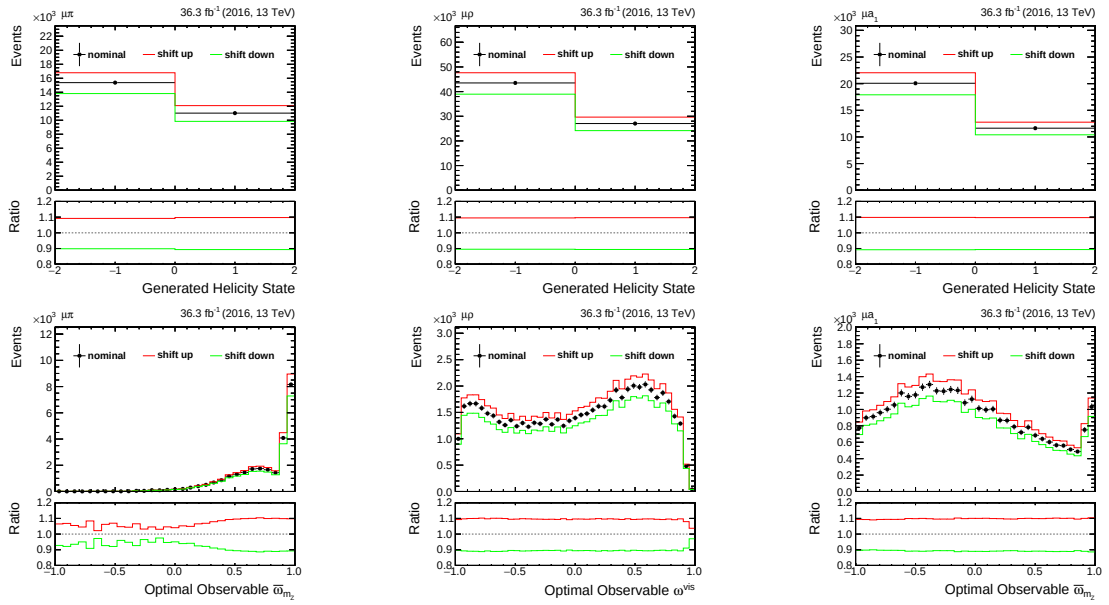

Figure 3.18: Effect of QCD scale variations (factorisation and renormalisation scales) on the two helicity states (*top*) and the final discriminators (*bottom*), $\omega(\pi)$ [*left*], $cos\beta(\rho)$ [*centre*] and $\omega(a_1)$ [*right*], for the three categories of the $\tau_\mu\tau_h$ channel. No significant impact on the shape of the final discriminator is observed.

Figures 3.18, 3.19, 3.20 and 3.21 depict details of this study for the $\tau_\mu\tau_h$ channel, which is the most sensitive channel, for QCD scale, α_s and PDF choice variations, respectively. The three columns contain plots for the $\mu + \pi$, $\mu + \rho$ and $\mu + a_1$ categories, respectively. The first row of each figure shows the dependence of these variations on the generated helicity state, whereas the second row shows the impact on the final discriminator for each category in the $\tau_\mu\tau_h$ channel. The ratio subplots compare the 1σ shift

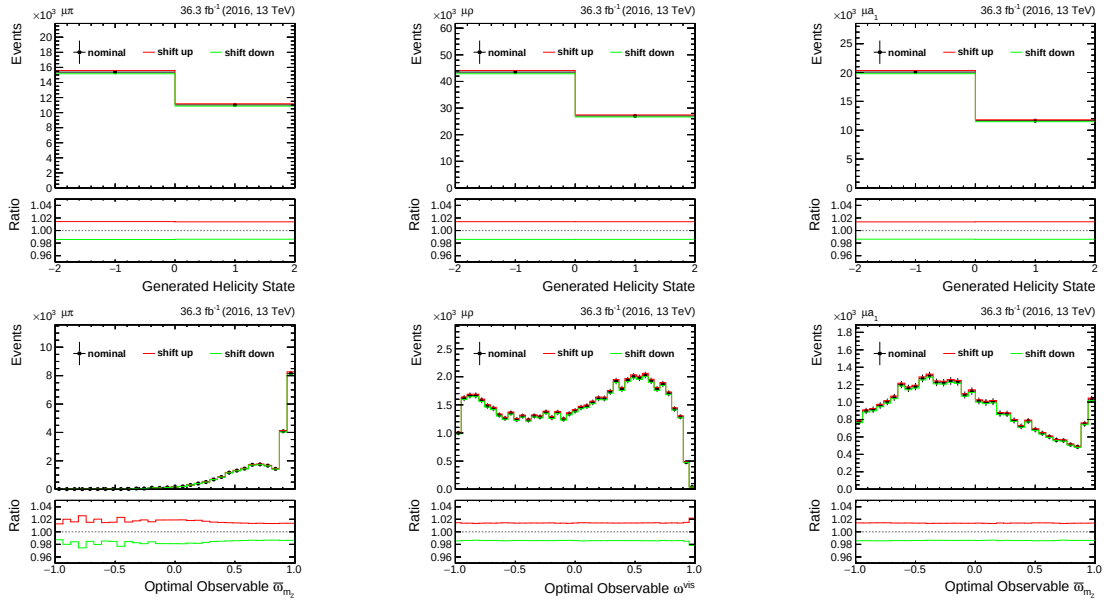

Figure 3.19: Effect of α_s variations on the two helicity states (*top*) and the final discriminators (*bottom*), $\omega(\pi)$ [*left*], $cos\beta(\rho)$ [*centre*] and $\omega(a_1)$ [*right*], for the three categories of the $\tau_\mu\tau_\mathrm{h}$ channel. No significant impact on the shape of the final discriminator is observed.

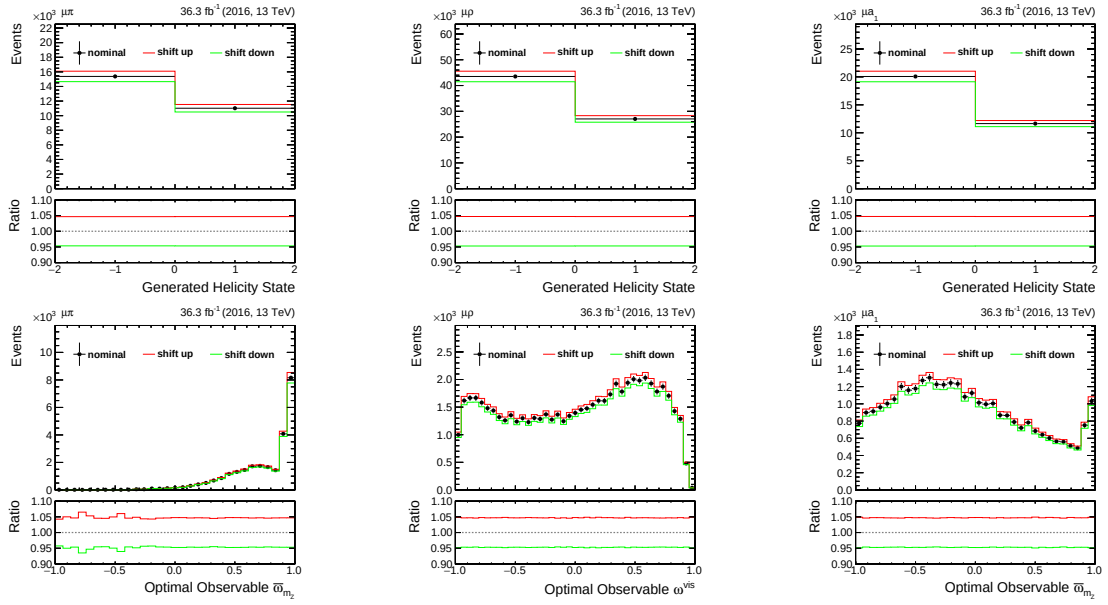

Figure 3.20: Effect of PDF choice variations (factorisation and renormalisation scales) on the two helicity states (*top*) and the final discriminators (*bottom*), $\omega(\pi)$ [*left*], $cos\beta(\rho)$ [*centre*] and $\omega(a_1)$ [*right*], for the three categories of the $\tau_\mu\tau_\mathrm{h}$ channel. No significant impact on the shape of the final discriminator is observed.

up/down uncertainties with the nominal histograms and are mostly flat.

Deviations from the flat characteristic of the ratios are observed only in regions with low statistics and mainly in the $\mu + \pi$ category, which has the lowest influence on the combined sensitivity.

Figure 3.21 shows the correlations of PDF set variations between different bins of histograms. In reasonably populated bins, they are all 100% correlated. The deterioration of the correlations in the $\mu + \pi$ category is explained by low statistics in the region from -1.0 to 0.0 of the final discriminator.

As a consequence it is concluded, that it is sufficient to apply normalisation uncertainties to cover these effects. Since the normalisation of the signal is anyway left freely floating in the final fits, it is sufficient to simply combine this normalisation uncertainty with the signal cross-section uncertainty.

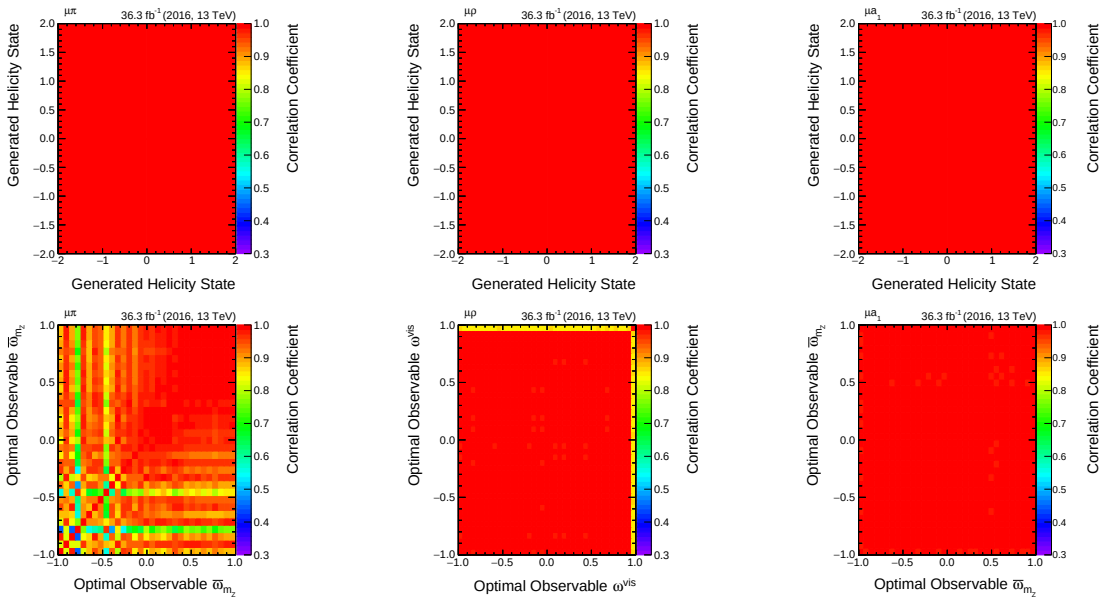

Figure 3.21: Correlations of variations of PDF sets between different bins of histograms. All variations are 100% correlated in well populated regions (low statistics in $\mu + \pi$ category). No dependence on the PDF choice is observed.

3.10 Choice of the final discriminator

As explained in Section 3.6, the following observables are studied with respect to their sensitivity to separate between the two helicity states, $Z \to \tau_R^- \tau_L^+$ and $Z \to \tau_L^- \tau_R^+$:

- Mass of the visible decay products, m_{vis},
- Optimal observable for single τ legs, $\omega(h = \pi, \rho, a_1)$,
- Combined optimal observable for both τ legs, Ω.

Whereas the mass of the visible decay products is uniquely defined, there are different options to reconstruct the optimal observables:

- Consider only angles that can be measured directly from visible decay products, ω_{vis} or Ω_{vis},
- Consider the full angular description of the τ lepton decay using `SVfit` or `FastMTT` algorithms without mass constraint for the reconstruction of the τ lepton four-momenta (labelled $\overline{\omega}_{\text{SVfit/FastMTT}}$ or $\overline{\Omega}_{\text{SVfit/FastMTT}}$ in Figs. 3.23 and 3.24),
- Consider the full angular description of the τ lepton decay using `SVfit` algorithm including a Z boson mass constraint for the reconstruction of the τ lepton four-momenta (labelled $\overline{\omega}_{\text{SVfit,m}_\text{Z}}$ or $\overline{\Omega}_{\text{SVfit,m}_\text{Z}}$ in Figs. 3.23 and 3.24).

The resolution $\frac{\text{reco}-\text{gen}}{\text{gen}}$ of reconstructed optimal observables determined from particles on generator level, that are matching with the reconstructed particles is depicted in Fig. 3.22 for the three event categories in the $\tau_\mu \tau_\text{h}$ channel: $\mu + a_1$ (*left*), $\mu + \rho$ (*centre*) and $\mu + \pi$ (*right*). The *top* row shows the single-τ lepton observables and the *bottom* row the combined di-τ observables. The cases without mass constraint with `SVfit` (*black*) and `FastMTT` (*green*) algorithms are compared with the case including a Z boson mass constraint with `SVfit` during the reconstruction of the original τ four-momenta (*red*). The events shown in these distributions include the full $Z \to \tau\tau$ MC sample. In the Appendix C one finds the same distributions split into the two helicity states, $Z \to \tau_R^- \tau_L^+$ in Fig. C.1 and $Z \to \tau_L^- \tau_R^+$ in Fig. C.2. Other channels are also shown in Appendix C.

The full likelihood function including statistical and systematic uncertainties, which is minimized to obtain the best fit value for the average polarisation, is scanned as a function of the average polarisation in order to compare the performance of the various discriminators. In the following two scans are presented for each discriminator in a given event category. Firstly, a scan including the full systematic uncertainties, whose nuisances parameters are optimised for each value of the parameter of interest, $\langle P_\tau \rangle$, is performed. This scan yields the expected total (statistical plus systematic) uncertainty on the average polarisation. A second fit is performed for obtaining the statistical uncertainty on the parameter of interest. In this fit, the nuisance parameters have been fixed to the best fit values obtained in the first fit. In both fits, the signal

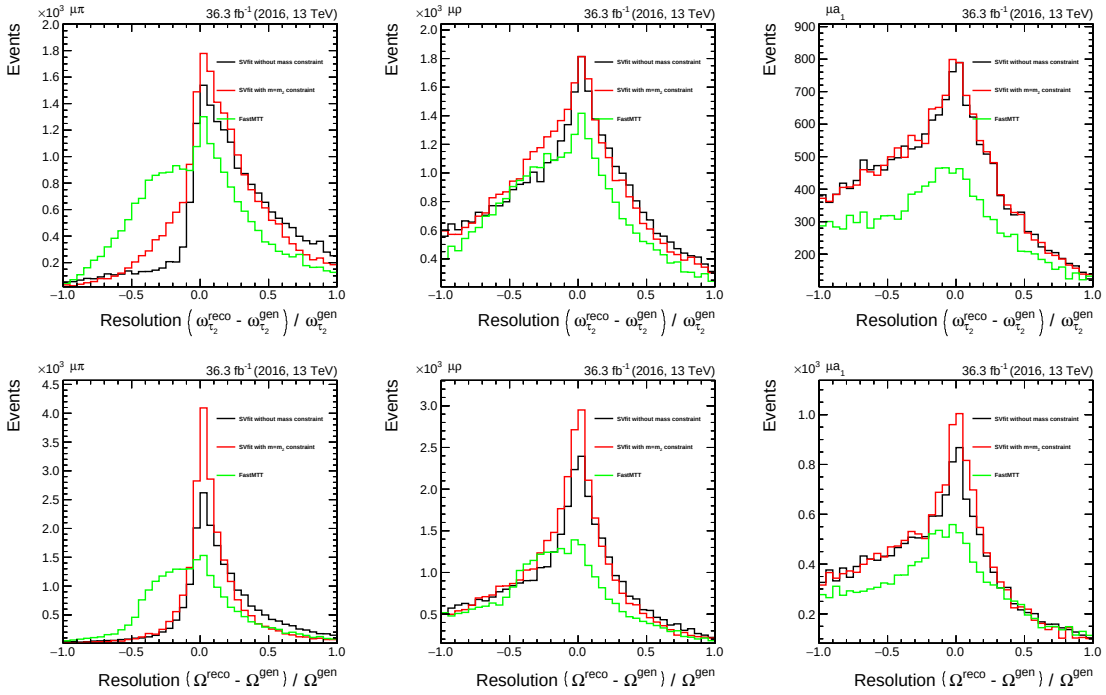

Figure 3.22: Reconstruction resolution for optimal observables obtained based on $Z \to \tau\tau$ events in the $\tau_\mu\tau_\mathrm{h}$ channel ($\mu+\pi$ events left, $\mu+\rho$ events in the middle and $\mu+a_1$ events right).

strength parameter, r is kept as a freely floating parameter.

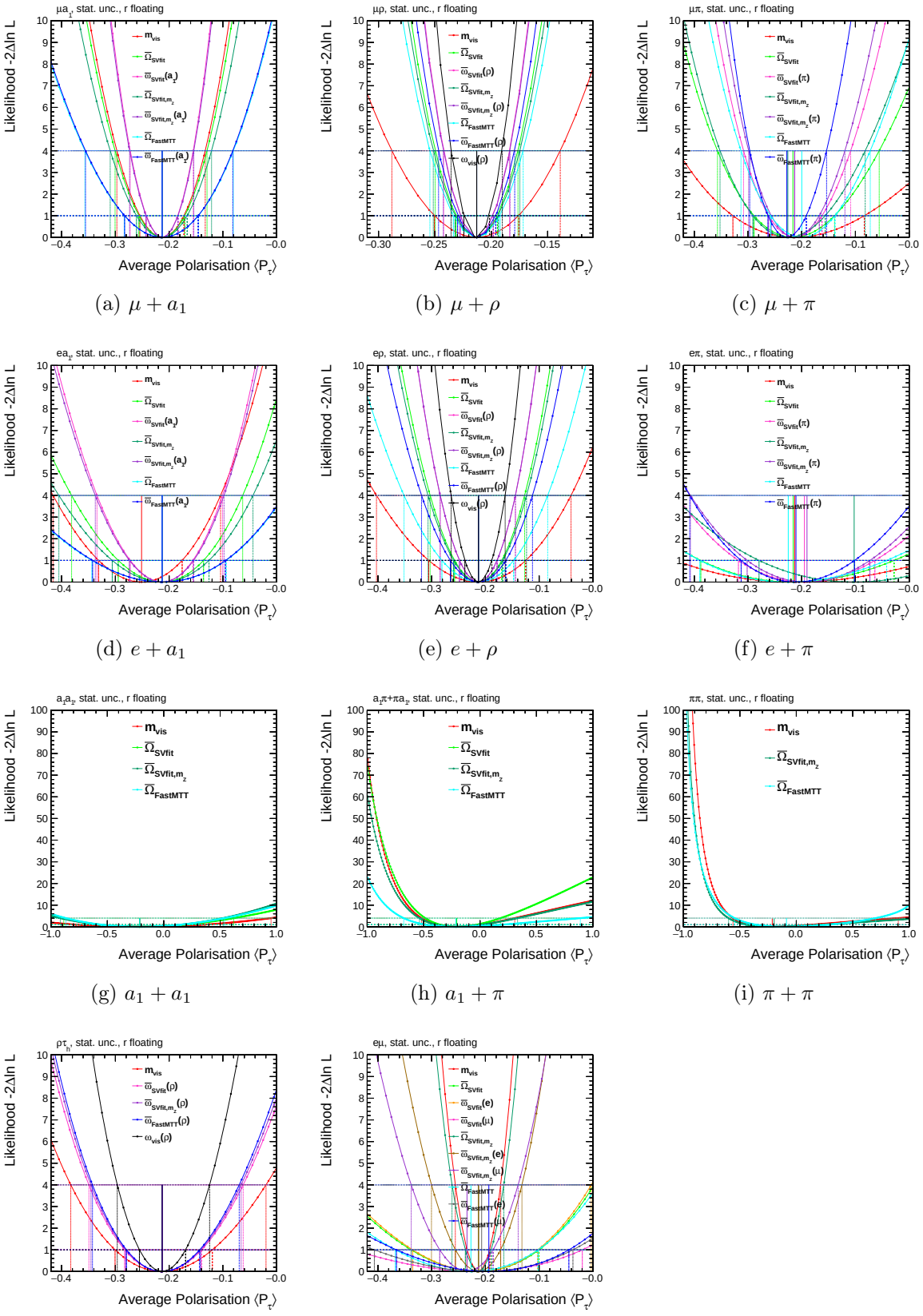

(a) $\mu + a_1$ (b) $\mu + \rho$ (c) $\mu + \pi$

(d) $e + a_1$ (e) $e + \rho$ (f) $e + \pi$

(g) $a_1 + a_1$ (h) $a_1 + \pi$ (i) $\pi + \pi$

(j) $\rho + \tau_h$ (k) $e + \mu$

Figure 3.23: Likelihood scans as a function of the average polarisation in all categories of the $\tau_\mu\tau_h$, $\tau_e\tau_h$, $\tau_h\tau_h$ and $\tau_e\tau_\mu$ channels. The results include only statistical uncertainties. Results with total uncertainties are shown in Fig. 3.24. Note the axis ranges, which are increased in the $\tau_h\tau_h$ channel, which is the least sensitive channel.

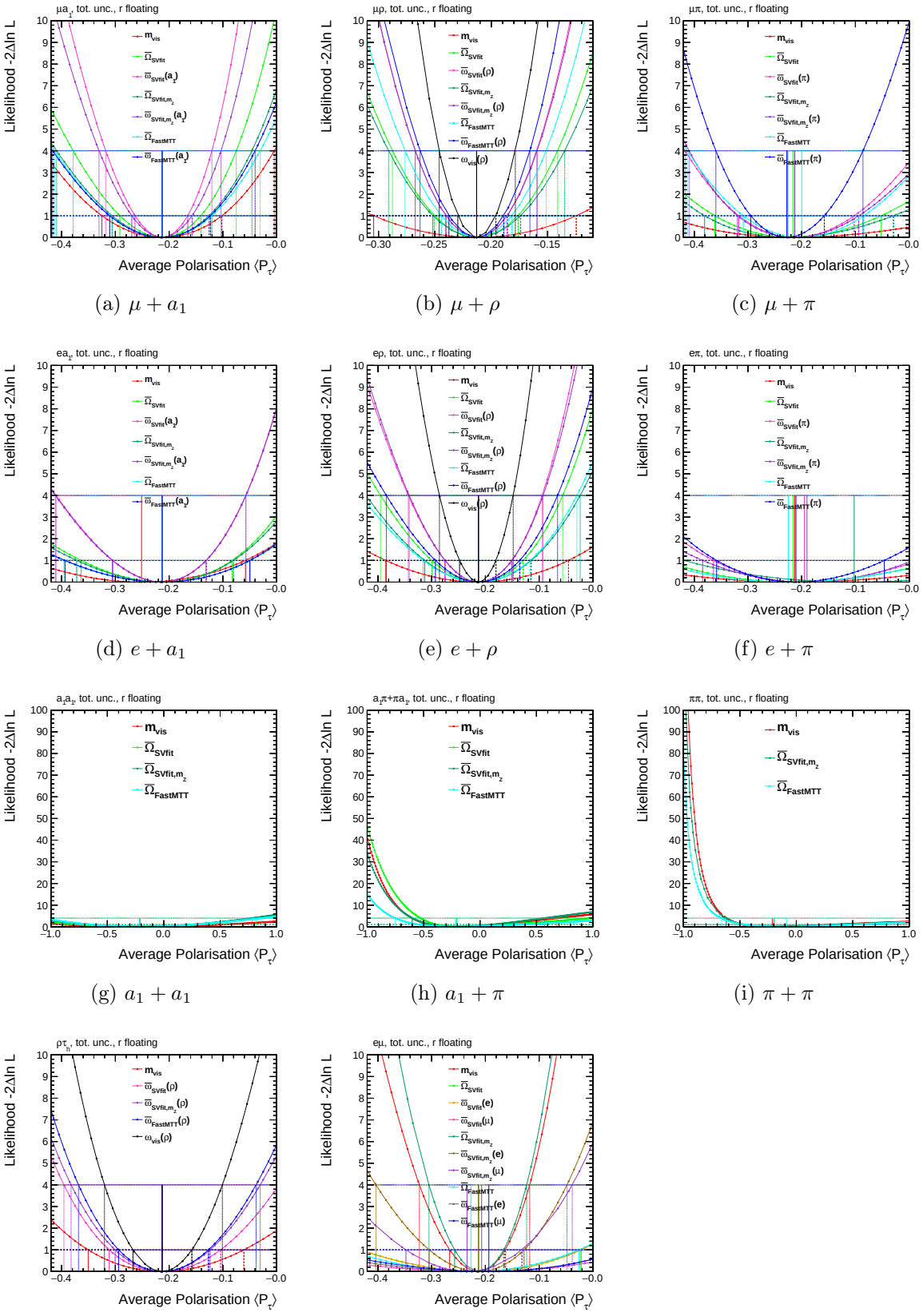

(a) $\mu + a_1$ (b) $\mu + \rho$ (c) $\mu + \pi$

(d) $e + a_1$ (e) $e + \rho$ (f) $e + \pi$

(g) $a_1 + a_1$ (h) $a_1 + \pi$ (i) $\pi + \pi$

(j) $\rho + \tau_h$ (k) $e + \mu$

Figure 3.24: Likelihood scans as a function of the average polarisation in all categories of the $\tau_\mu\tau_h$, $\tau_e\tau_h$, $\tau_h\tau_h$ and $\tau_e\tau_\mu$ channels. The results include the full systematic and statistical uncertainties. Results with only statistical uncertainties are shown in Fig. 3.23. Note the axis ranges, which are increased in the $\tau_h\tau_h$ channel, which is the least sensitive channel.

Figure 3.23 in the all categories of the $\tau_\mu\tau_\mathrm{h}$, $\tau_e\tau_\mathrm{h}$, $\tau_\mathrm{h}\tau_\mathrm{h}$ and $\tau_e\tau_\mu$ channels for statistical uncertainties only, whereas the full statistical plus systematic uncertainties are included in the scans shown in Fig. 3.24.

Figures 3.23a to 3.23c and 3.24a to 3.24c show scans in the three categories of the $\tau_\mu\tau_\mathrm{h}$ channel, respectively, for statistical uncertainties and total uncertainties. As a conclusion, the optimal observable using `SVfit` is selected in the $\mu + a_1$ category, the optimal observable based on visible decay products of the ρ decay in the $\mu + \rho$ category and the optimal observable using `SVfit` in the $\mu + \pi$. The chosen variables are based on this conducted sensitivity study. Figures 3.23d to 3.23f and 3.24d to 3.24f, respectively, show exactly the same for the $\tau_e\tau_\mathrm{h}$ channel, where the conclusion is the same. The conclusions are summarised in Table 3.15.

In the fully hadronic channel, four categories with three to five discriminators each have to be compared. Figures 3.23g to 3.23j show the results of the sensitivity study for the statistical uncertainties and Figs. 3.24g to 3.24j complete the picture with the total uncertainties. Again, the best choice is listed in Table 3.15.

Finally, Figures 3.23k and 3.24k compare the performance of ten different discriminators in the $\tau_e\tau_\mu$ channel. The mass of the visible decay products is chosen.

Table 3.15: Final choice of discriminators in the different event categories

Channel	**Category**	**Discriminator**		
$\tau_e\tau_\mu$	$e + \mu$	$m_\mathrm{vis}(e, \mu)$	visible mass	Eq. (3.33)
$\tau_e\tau_\mathrm{h}$	$e + a_1$	$\omega(a_1)$	optimal observable with `SVfit`	Eq. (3.31)
	$e + \rho$	$\cos\beta(\rho)$	visible optimal observable	Eq. (3.26)
	$e + \pi$	$\omega(\pi)$	optimal observable with `SVfit`	Eq. (3.24)
$\tau_\mu\tau_\mathrm{h}$	$\mu + a_1$	$\omega(a_1)$	optimal observable with `SVfit`	Eq. (3.31)
	$\mu + \rho$	$\cos\beta(\rho)$	visible optimal observable	Eq. (3.26)
	$\mu + \pi$	$\omega(\pi)$	optimal observable with `SVfit`	Eq. (3.24)
$\tau_\mathrm{h}\tau_\mathrm{h}$	$a_1 + a_1$	$m_\mathrm{vis}(a_1, a_1)$	visible mass	Eq. (3.33)
	$a_1 + \pi$	$\Omega(a_1, \pi)$	combined optimal observable with `SVfit`	Eq. (3.32)
	$\rho + \tau_\mathrm{h}$	$\cos\beta(\rho)$	visible optimal observable (for leading ρ)	Eq. (3.26)
	$\pi + \pi$	$m_\mathrm{vis}(\pi, \pi)$	visible mass	Eq. (3.33)

Figure 3.25 shows the distributions of these final disciminators in all 11 categories of the four channels. The black markers (*upper part*) show an *Asimov* dataset corresponding to the sum of signal and background expectations from MC. After performing the fit to estimate the average τ lepton polarisation, the *post-fit* distributions look like depicted in Fig. 3.26. The uncertainty bands include both statistical and systematic uncertainties, which decrease as a result of constraints imposed on the fit nuisance parameter.

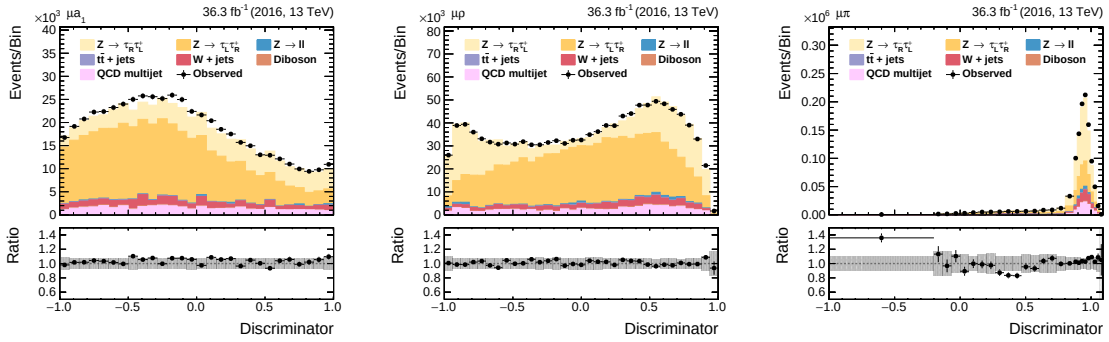

(a) $\mu + a_1$

(b) $\mu + \rho$

(c) $\mu + \pi$

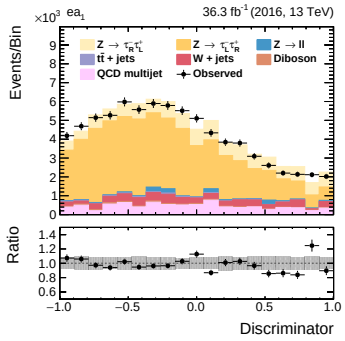

(d) $e + a_1$

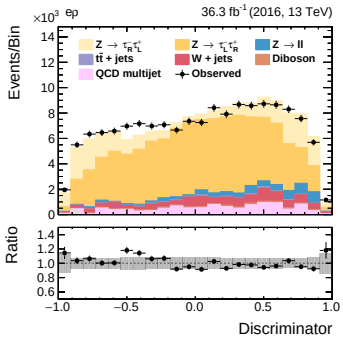

(e) $e + \rho$

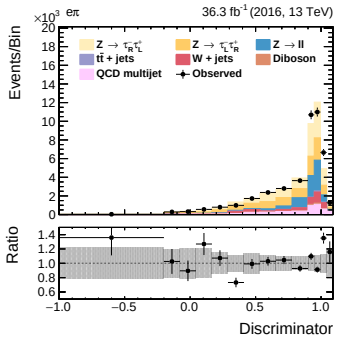

(f) $e + \pi$

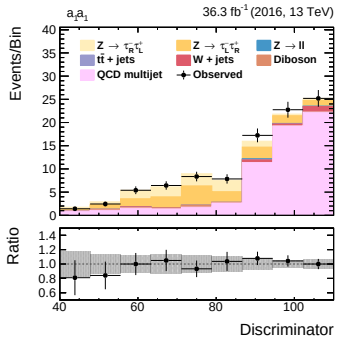

(g) $a_1 + a_1$

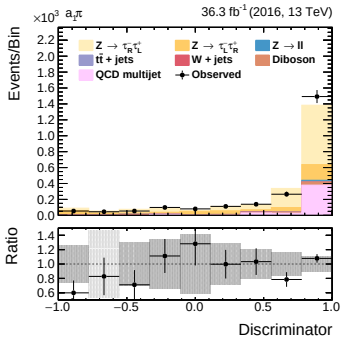

(h) $a_1 + \pi$

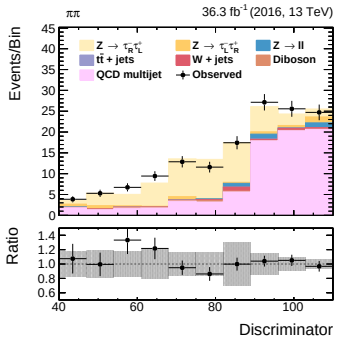

(i) $\pi + \pi$

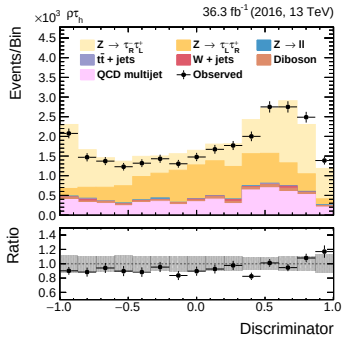

(j) $\rho + \tau_{\mathrm{h}}$

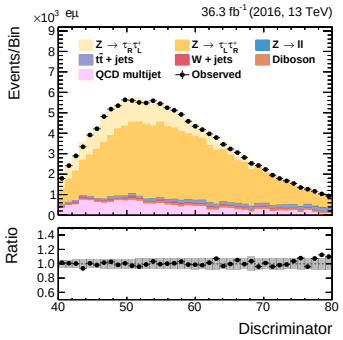

(k) $e + \mu$

Figure 3.25: *Pre-fit* distributions (with an *Asimov* dataset) of the final discriminators exploited in the 11 event categories in the four channels.

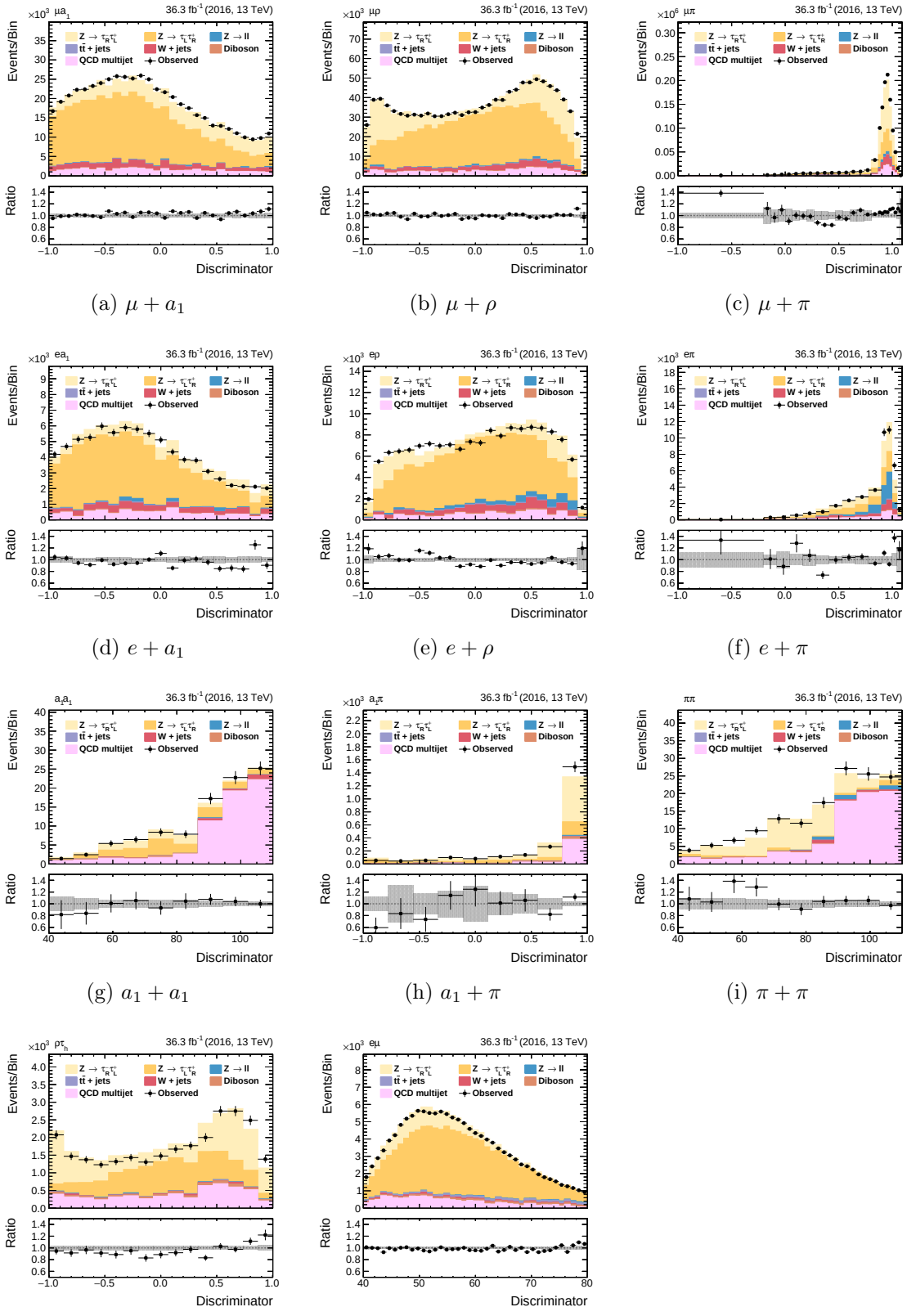

(a) $\mu + a_1$ (b) $\mu + \rho$ (c) $\mu + \pi$

(d) $e + a_1$ (e) $e + \rho$ (f) $e + \pi$

(g) $a_1 + a_1$ (h) $a_1 + \pi$ (i) $\pi + \pi$

(j) $\rho + \tau_h$ (k) $e + \mu$

Figure 3.26: *Post-fit* distributions (of fits with an *Asimov* dataset) of the final discriminators exploited in the 11 event categories in the four channels. The black markers in the subset of the distribution should not be considered as they do not indicate agreement between the simulated data and the *Asimov* dataset. Indeed, they are identical to those in the *pre-fit* distribution and indicate agreement between the simulation and the *data* prior to the fitting process.

3.11 Expected sensitivity and Closure of extraction procedure

In order to estimate the sensitivity, templates for observed data are replaced by an *Asimov* dataset following the signal plus background hypothesis, see Eq. (3.48). The signal is taken from the complete inclusive $Z \to \tau\tau$ MC in order to extract the polarisation configured in the MC generator ($\langle P_\tau \rangle^{MC} = -21.3\%$ in generated mass window of 75 to 120 GeV). A scan of the likelihood $-2\Delta \ln \mathcal{L}$ is performed as a function of the average τ lepton polarisation, where the signal strength, r, is treated as a freely floating parameter. The fits are performed by the *Higgs* `Combine` tool in each event category separately (see Sect. 3.10), in each channel combined and in a combination of all channels and categories.

Figure 3.27 shows these scans in the four channels for statistical uncertainties and Figure 3.28 the same but for the total uncertainties. Curves in colors show the scan for the best performing discriminator in individual categories and the black line depicts the combination of all categories per channel. In Figure 3.29 the four channels are then combined to retrieve the final sensitivity. The left plot shows the scan with statistical uncertainties only, whereas the right plot shows the effect of the total uncertainties. The final expected uncertainty (resulting 1σ intervals i.e. the crossings of $-2\Delta \ln \mathcal{L} = 1$) yields 1.5%.

3.12 Resulting systematic errors on the average polarisation

The impact of individual systematic uncertainties on the expected sensitivity of the polarisation measurement has been studied. Figure 3.31 displays the list of 30 systematic uncertainties which have the largest impact on the final result. The association of parameter labels (*left column*) with the source of the systematic uncertainties can be found in Sect. 3.9.

The final fit results at this stage of the analysis are shown in Fig. 3.30. The red error bars depict the statistical uncertaities whereas the total (statistical plus systematic) uncertainties are shown by the black error bars. The highest precision is observed in the $\mu + \rho$ category, benefiting from a proficient selection efficiency and an accurate reconstruction of the optimal observable, $\omega_{\text{vis}}(\rho) = \cos\beta(\rho)$. The least sensitivity is found in the fully hadronic decay channel, which suffers from high trigger thresholds and resulting poor selection efficiency. The combined best-fit value for the average τ lepton polarisation yields:

$$\langle P_\tau \rangle = -0.213 \pm 0.015 = -0.213 \pm 0.006\,(\text{stat.}) \pm 0.014\,(\text{syst.}) \text{ on } \textit{Asimov} \text{ dataset}\,.$$

It has been checked that the polarisation fit is able to find back the polarisation, that was used to construct the *Asimov* dataset. For this, multiple Maximum Likelihood fits have been performed with different *Asimov* datasets. Both signal and background expectations remained the same in all fits and correspond to the nominal fits. The single difference between all these fits is the variation of the parameter $\langle P_\tau \rangle$ in the range from -35% to 0% in steps of 1-5% for the construction of the signal contribution to the *Asimov* dataset. For this purpose, the reweighted/unpolarised signal templates have been scaled according to Eq. (3.49) with a given value for $\langle P_\tau \rangle$ before adding them to the background estimation to form the *Asimov* dataset.

Figure 3.32 shows the fitted average polarisation as a function of this so-called *Asimov* polarisation, $\langle P_\tau \rangle^{\text{Asimov}}$. There is a one-to-one relation between input and output of these fits. This proves that the fit is able to find back the polarisation implemented in the *Asimov* dataset.

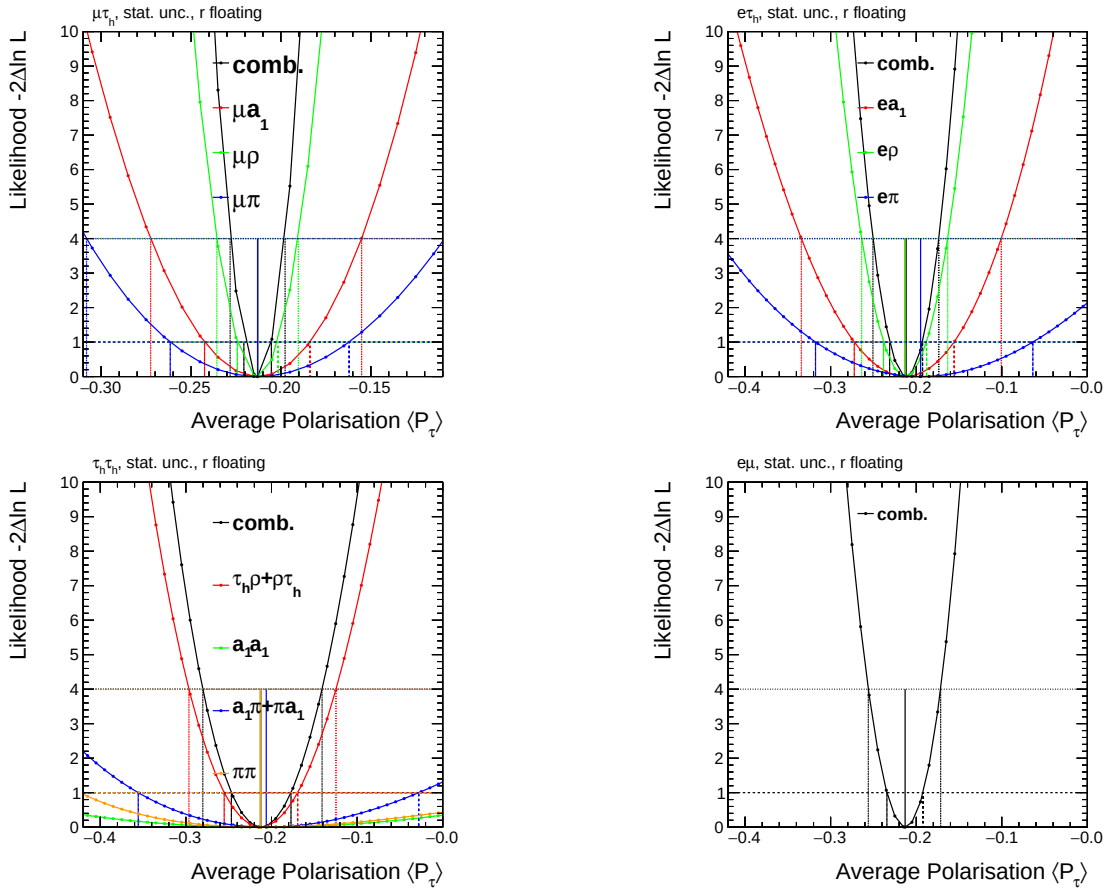

Figure 3.27: Likelihood scan as a function of the average polarisation in the three categories of the $\tau_\mu\tau_\mathrm{h}$ channel (*top left*), in the three categories of the $\tau_e\tau_\mathrm{h}$ channel (*top right*), in the four categories of the $\tau_\mathrm{h}\tau_\mathrm{h}$ channel (*bottom left*) and in the sole category of the $\tau_e\tau_\mu$ channel (*bottom right*). The black line shows the combination of all categories in a given channel. The scans show the effect of only statistical uncertainties.

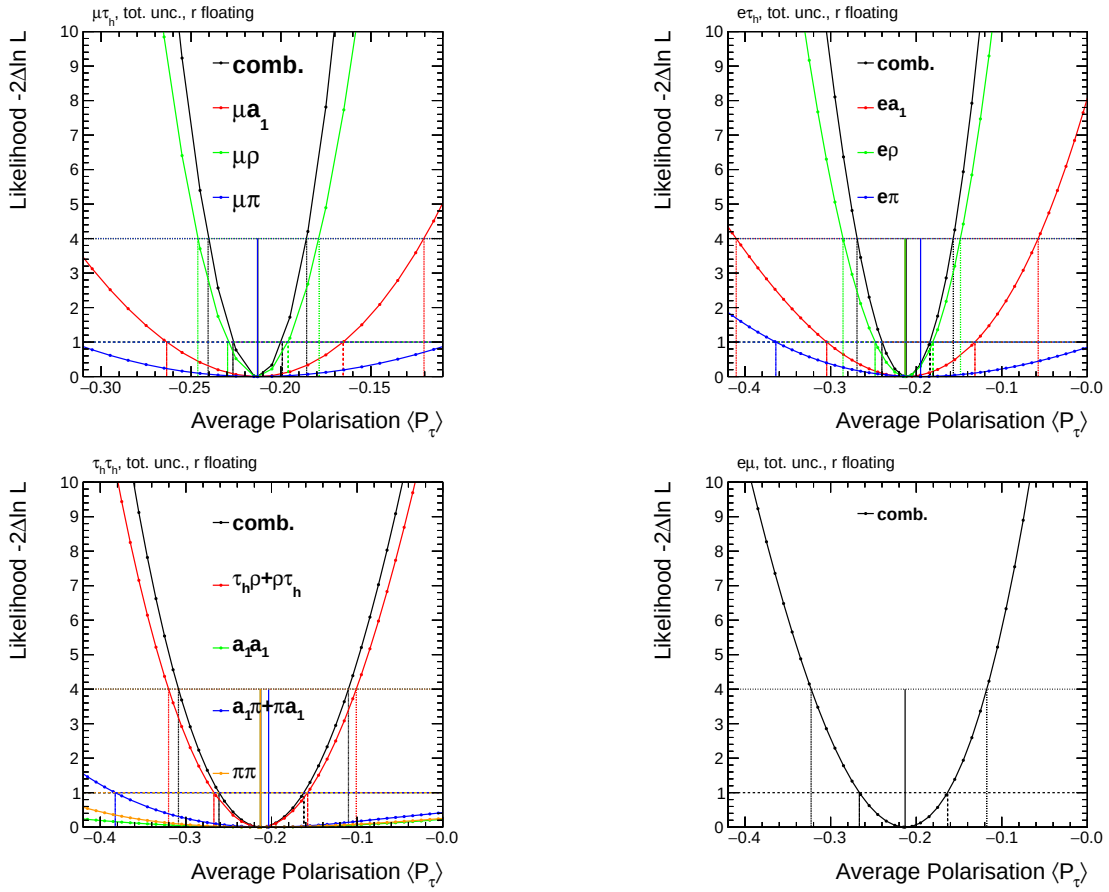

Figure 3.28: Likelihood scan as a function of the average polarisation in the three categories of the $\tau_\mu\tau_\mathrm{h}$ channel (*top left*), in the three categories of the $\tau_e\tau_\mathrm{h}$ channel (*top right*), in the four categories of the $\tau_\mathrm{h}\tau_\mathrm{h}$ channel (*bottom left*) and in the sole category of the $\tau_e\tau_\mu$ channel (*bottom right*). The black line shows the combination of all categories in a given channel. The scans show the effect of total (statistical plus systematic) uncertainties.

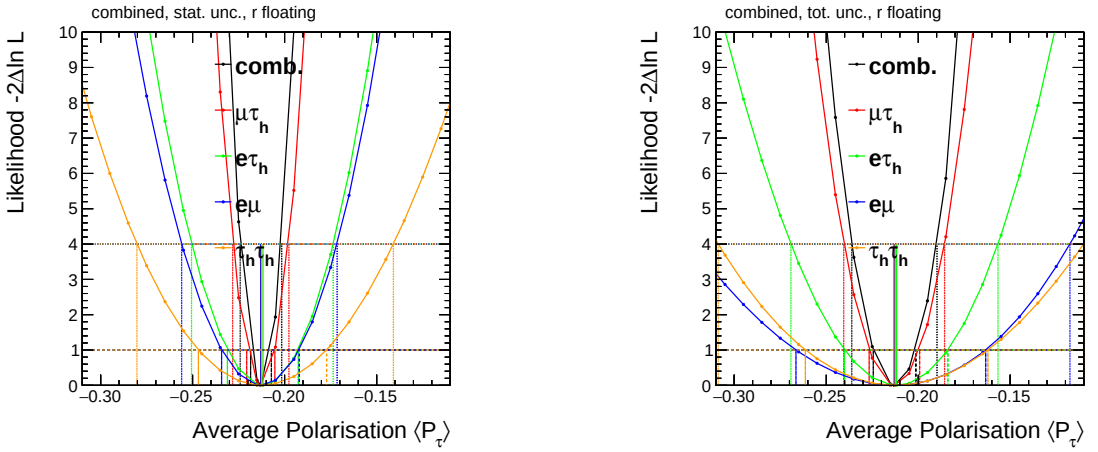

Figure 3.29: Likelihood scan as a function of the average polarisation in the four τ decay channels and their combination. Only statistical uncertainties on the *left* and statistical plus systematic uncertainties on the *right*. The black line shows the combination of all decay modes. The scans show the dominance of systematic uncertainties.

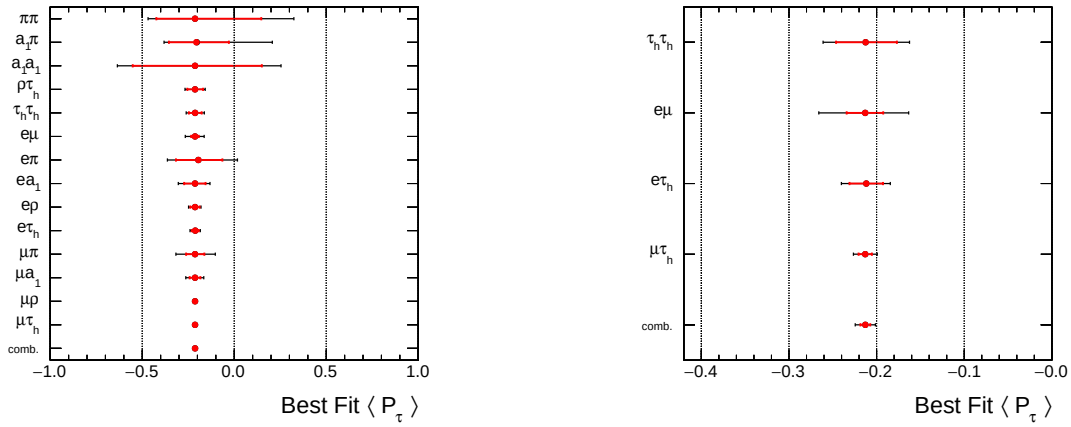

Figure 3.30: Fit results for the average τ lepton polarisation for the 11 event categories (*left*) and for the 4 channels separately and the combined fit to all channels and categories (*right*).

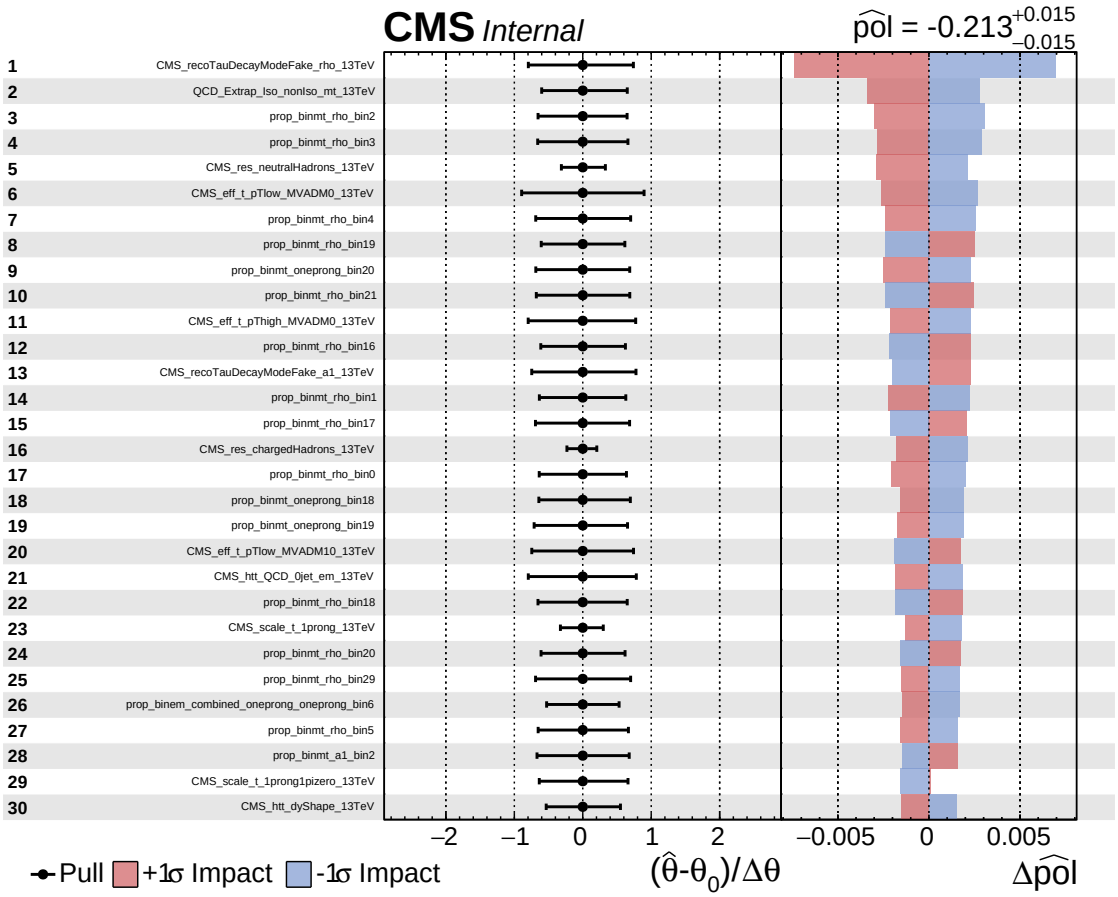

Figure 3.31: List of nuisance parameters and their impact on the combined maximum likelihood fit to an *Asimov* dataset. Only the 30 systematic uncertainties with the largest impact on the final sensitivity are shown here. The most dominant uncertainties raise from possible migrations between different generated and reconstructed τ lepton decay modes.

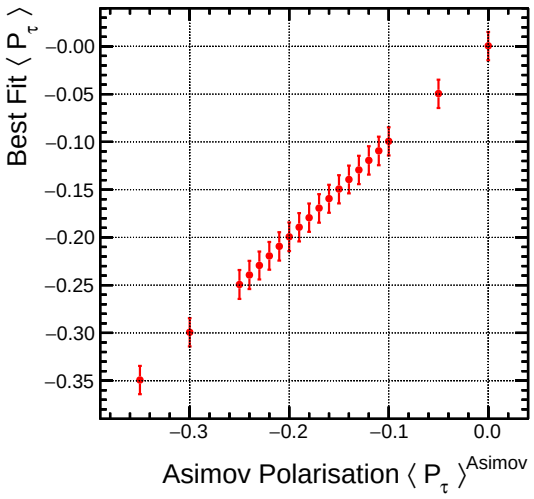

Figure 3.32: Linearity check for the polarisation fit, proving the one-to-one relation between the average τ lepton polarisation configured in the *Asimov* dataset and the *measured* average polarisation.

3.13 Further statistical tests

This section presents statistical studies demonstrating the validity of our fitting model.

3.13.1 Likelihood formalism

To extract the average tau polarisation, $\langle \mathcal{P}_\tau \rangle$, a simultaneous fit to the data is performed using the likelihood function, $\mathcal{L}(r, \langle \mathcal{P}_\tau \rangle, \vec{\theta})$ depending on the signal strength r, the average polarisation $\langle \mathcal{P}_\tau \rangle$ and the nuisance parameters $\vec{\theta}$ which account for the systematic uncertainties.

The likelihood function is defined as a product of conditional probabilities P over binned distributions of the optimal observables previously defined in each event category j,

$$\mathcal{L}(r, \langle \mathcal{P}_\tau \rangle, \vec{\theta}) = \prod_{j}^{N_{cat}} \prod_{i}^{N_{bin}} P(n_{i,j} | r \cdot s_{i,j}(\langle \mathcal{P}_\tau \rangle, \vec{\theta}) + b_{i,j}(\vec{\theta})) \times \prod_{k}^{N_{NP}} c_k(\vec{\theta}) \quad , \tag{3.56}$$

with $n_{i,j}$ corresponding to the observed data in each bin i of the optimal variable, $s_{i,j}$ and $b_{i,j}$ the signal and background predictions. Constraints on the nuisance parameters (NP) corresponding to systematic uncertainties described in Sect. 3.9 are represented by the functions $c_k(\vec{\theta})$. This fit is performed using the *Higgs* `Combine` framework.

Both parameter of interest, $\vec{\mu} = (r, \langle \mathcal{P}_\tau \rangle)$, are left freely floating in the fit as nuisance parameters.

The test statistic value used to analyse results is based on a profile negative log-likelihood ratio:

$$-2 \ln \mathcal{L} = -2 \ln \frac{\mathcal{L}(\vec{\mu}, \hat{\vec{\theta}}_\mu)}{\mathcal{L}(\hat{\vec{\mu}}, \hat{\vec{\theta}})} \text{ with } 0 < r < 5 \text{ and } -1 < \langle \mathcal{P}_\tau \rangle < 1 \quad . \tag{3.57}$$

In the numerator, the signal strength and the average polarisation are fixed while the nuisance parameters are allowed to float to the values that maximize the likelihood. Whereas in the denominator, the parameters of interest $\vec{\mu}$ and the nuisance parameters can all float to maximize the likelihood.

From the distribution of the test statistic the best-fit and uncertainties (68 % confidence intervals for $-2 \ln \mathcal{L} = 1$) are extracted for the parameters of interest.

3.13.2 *Goodness-of-fit*: saturated model

Goodness-of-fit (GOF) tests [67] are performed using the saturated model method to quantify the agreement between the expected processes and the observed data. The saturated model test is the negative log-likelihood ratio of the model to the saturated

model. In so-called saturated models the model prediction is matching exactly the observed data in each bin of the distribution and corresponds to a likelihood $\mathcal{L}_{sat}(\vec{n}|\vec{n})$ for a given dataset $\vec{n}$. The test statistic in a saturated GOF test is given by:

$$q_{sat} = -2\ln\frac{\mathcal{L}(\vec{n}|r\cdot\vec{s}(\langle\mathcal{P}_\tau\rangle,\vec{\theta})+\vec{b}(\vec{\theta}))}{\mathcal{L}_{sat}(\vec{n}|\vec{n})} \quad . \tag{3.58}$$

For histograms with independent Poisson-distributed bin contents,

$$q_{sat} = -2\ln\left[\prod_{i=1}^{N}\left(\frac{r\cdot s_i(\langle\mathcal{P}_\tau\rangle,\vec{\theta})+b_i(\vec{\theta})}{n_i}\right)^{n_i}\exp(-(r\cdot s_i(\langle\mathcal{P}_\tau\rangle,\vec{\theta})+b_i(\vec{\theta}))+n_i)\right], \tag{3.59}$$

and after simplification:

$$q_{sat} = 2\sum_{i=1}^{N} n_i\cdot\ln\left(\frac{n_i}{r\cdot s_i(\langle\mathcal{P}_\tau\rangle,\vec{\theta})+b_i(\vec{\theta})}\right)+(r\cdot s_i(\langle\mathcal{P}_\tau\rangle,\vec{\theta})+b_i(\vec{\theta}))-n_i \quad . \tag{3.60}$$

where n_i is the i^{th} measured data point, s_i and b_i are the signal and background model predictions with a signal strength r, an average polarisation $\langle\mathcal{P}_\tau\rangle$ and nuisance parameters $\vec{\theta}$ fitted to the dataset $\vec{n}$.

The observed value of the test statistic q_{obs} is obtained by minimizing q_{sat}.

3.13.3 *Goodness-of-fit*: results

Toy MC pseudo-datasets are generated according to the signal-plus-background hypothesis to test if the observed test statistic q_{obs} is compatible with the signal-plus-background predictions. For each pseudo-dataset a minimal test statistic is obtained, q_{toy} and the observed q_{obs} is compared to the distribution of all the q_{toy}. A p-value is then calculated from these results which quantify the agreement between the observation and the model predictions.

In Figure 3.33 the summary of all *Goodnes-of-Fit* results are shown. The obtained p-value for each category is presented. For more details, Figure 3.34 shows the individual toy distributions of the saturated GOF test. The blue arrow points to the q_{obs} value.

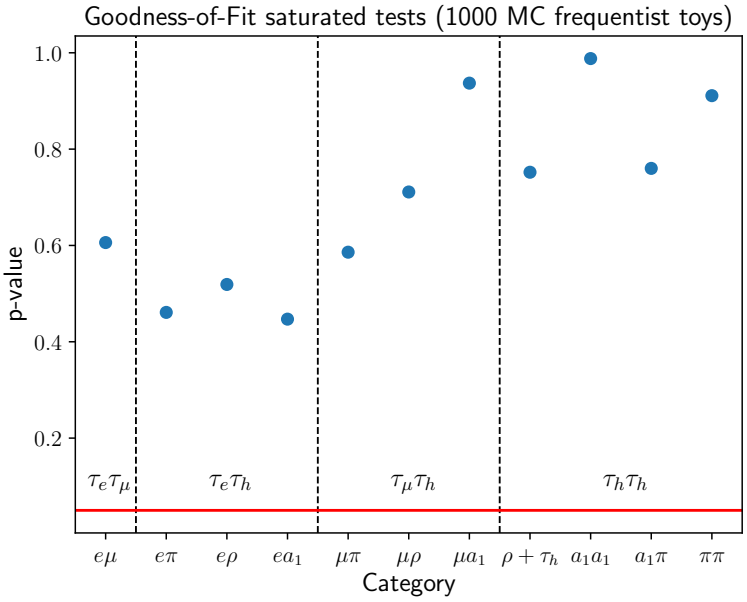

Figure 3.33: Summary of all *Goodnes-of-Fit* results, plotted is the obtained p-value for each category. The red line represents the minimum p-value threshold (0.05) to exceed for the statistical test to be considered conclusive.

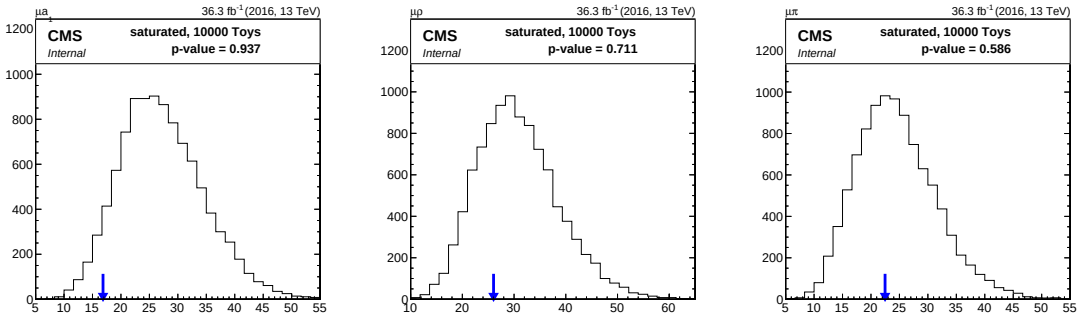

(a) $\mu + a_1$

(b) $\mu + \rho$

(c) $\mu + \pi$

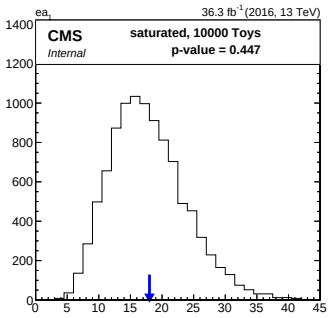

(d) $e + a_1$

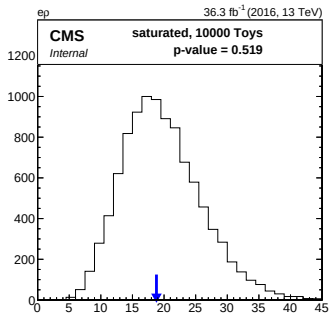

(e) $e + \rho$

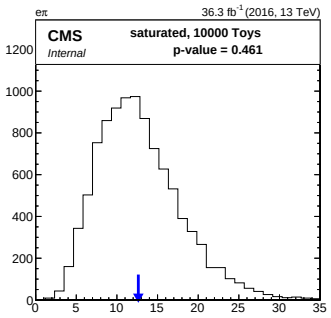

(f) $e + \pi$

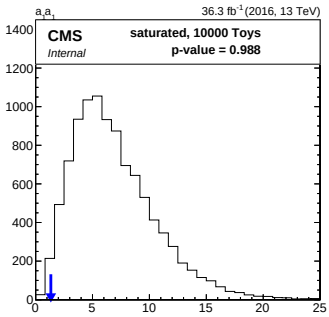

(g) $a_1 + a_1$

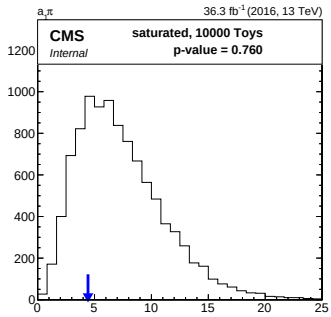

(h) $a_1 + \pi$

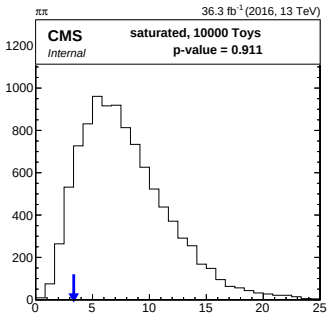

(i) $\pi + \pi$

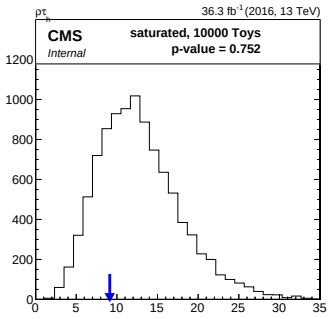

(j) $\rho + \tau_{\mathrm{h}}$

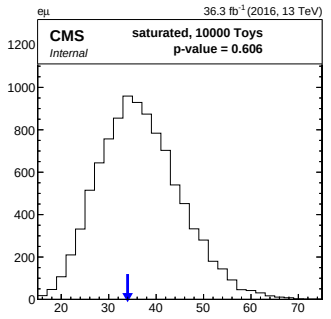

(k) $e + \mu$

Figure 3.34: Individual toy distributions of the saturated GOF test for the 11 categories. The blue arrow points at the q_{obs} value.

3.14 Final expected sensitivity and Closure test

The final sensitivity in different channels and categories after the statistical tests described above is shown in Fig. 3.35. Figure 3.36 verifies further that the extracted average polarisation does not depend on the (pseudo-)rapidity of the Z-boson, an important test because of the possible high-sensitivity on the angular acceptance of the tau-leptons.

Figure 3.30 also represents a closure test of the procedure as the extracted polarisation corresponds exactly to the nominal value of the generated Monte Carlo sample.

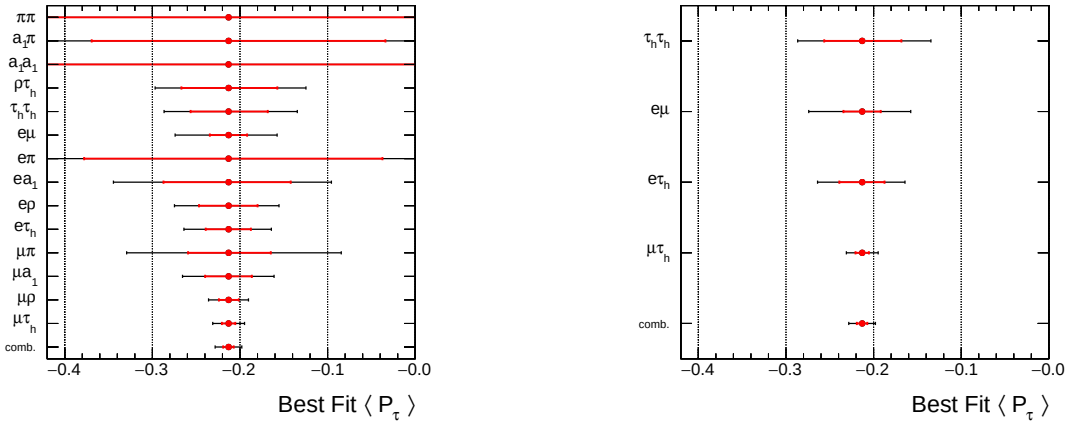

Figure 3.35: Final sensitivity in different channels and categories.

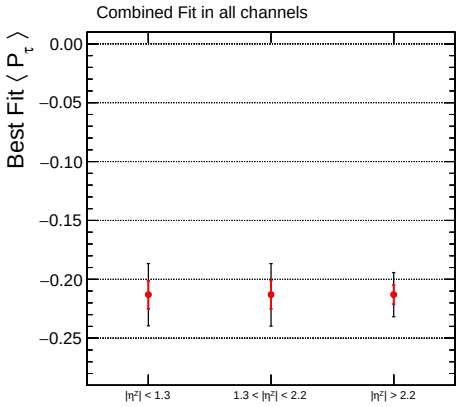

Figure 3.36: Final sensitivity in three different bins of the Z-boson pseudo-rapidity: $|\eta^Z| \leq 1.3$, $1.3 < |\eta^Z| \leq 2.2$ and $|\eta^Z| > 2.2$ for the combined fit in all categories and channels.

Conclusion

Ce chapitre décrit les méthodes de sélection des événements d'intérêt, à savoir les événements comportant une paire de leptons tau émanant de la désintégration d'un boson Z. Une méthode pour mesurer la polarisation moyenne de ces leptons tau est également présentée, qui consiste à étudier les angles entre les produits de désintégration du tau et à les condenser en une seule variable optimale, ω. Différents algorithmes ont été testés pour reconstruire l'impulsion totale du tau si nécessaire et pour déterminer la variable la plus sensible pour discriminer les deux états d'hélicité du tau. Une incertitude systématique a été étudiée pour prendre en compte la modélisation des migrations entre les modes de désintégration du tau, étant donné que la définition des variables optimales diffère selon le mode.

Chapter 4

Unblinding and results

4.1 Pre-fit and Post-fit distributions

In this section, the distributions before and after the fit, referred to as *pre-fit* and *post-fit*, respectively, are shown for the 2016 data, the so-called *unblinding* of the data. The variables selected for the best discrimination between $Z \to \tau_L^- \tau_R^+$ and $Z \to \tau_R^- \tau_L^+$ are listed in Table 3.15 (with a note on the algorithm used for total tau momentum reconstruction if needed).

4.1.1 $\tau_\mu\tau_h$ channel

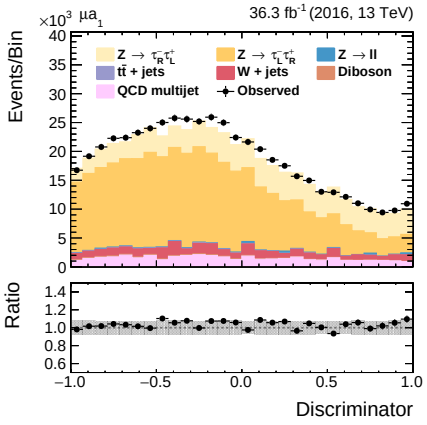

(a) *Pre-fit* in $\mu + a_1$ category: $\omega(a_1)$

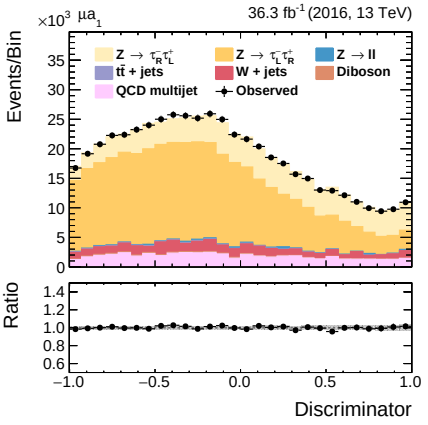

(b) *Post-fit* in $\mu + a_1$ category: $\omega(a_1)$

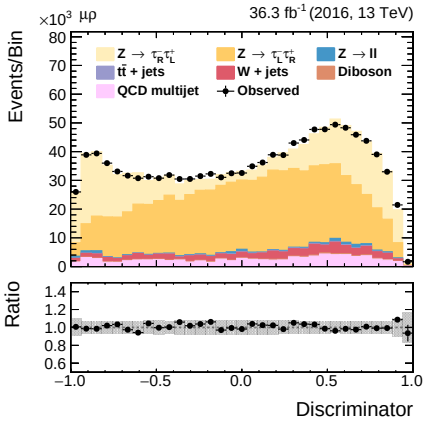

(c) *Pre-fit* in $\mu + \rho$ category: $\cos\beta(\rho)$

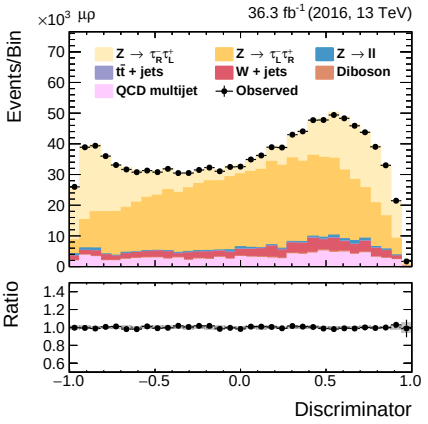

(d) *Post-fit* in $\mu + \rho$ category: $\cos\beta(\rho)$

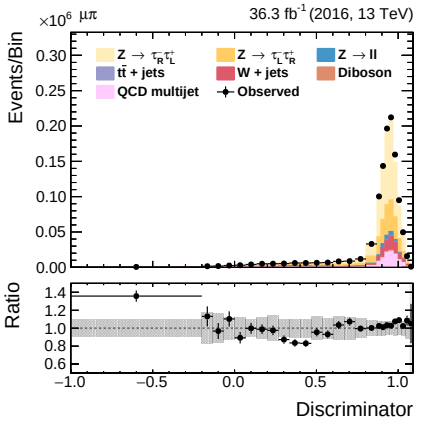

(e) *Pre-fit* in $\mu + \pi$ category: $\omega(\pi)$

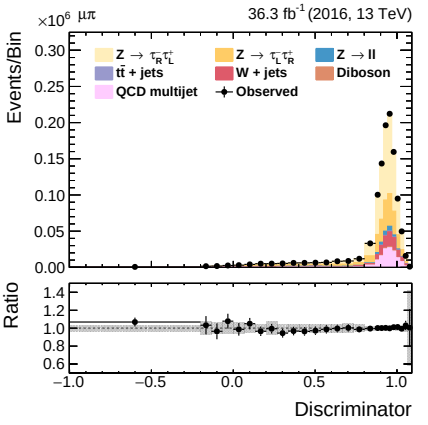

(f) *Post-fit* in $\mu + \pi$ category: $\omega(\pi)$

4.1.2 $\tau_e\tau_h$ channel

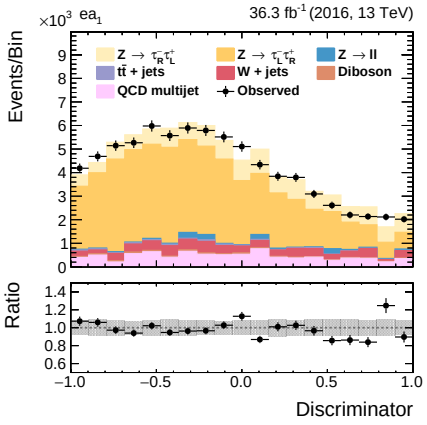

(a) *Pre-fit* in $e + a_1$ category: $\omega(a_1)$

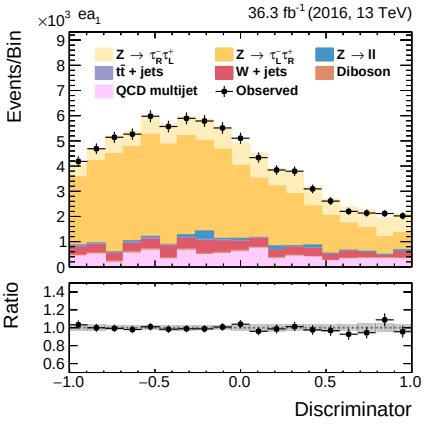

(b) *Post-fit* in $e + a_1$ category: $\omega(a_1)$

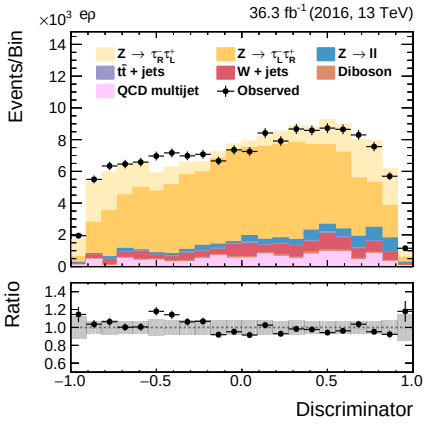

(c) *Pre-fit* in $e + \rho$ category: $\cos\beta(\rho)$

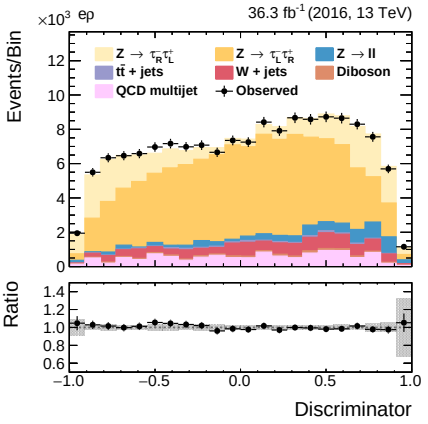

(d) *Post-fit* in $e + \rho$ category: $\cos\beta(\rho)$

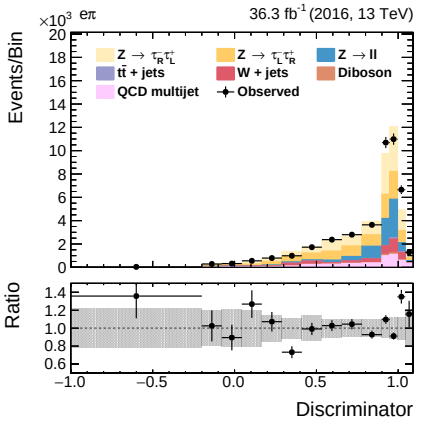

(e) *Pre-fit* in $e + \pi$ category: $\omega(\pi)$

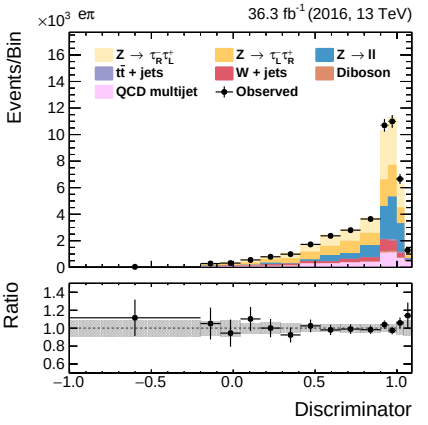

(f) *Post-fit* in $e + \pi$ category: $\omega(\pi)$

4.1.3 $\tau_e\tau_\mu$ channel

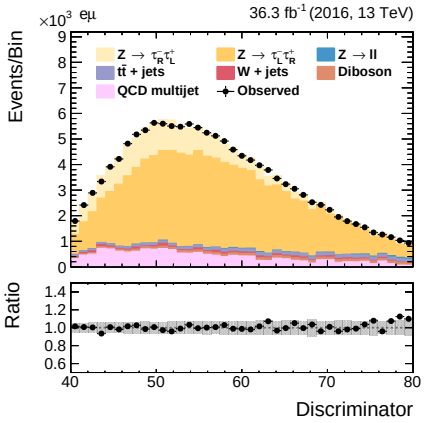

(a) *Pre-fit* in $e + \mu$ category: $m_{\text{vis}}(e, \mu)$

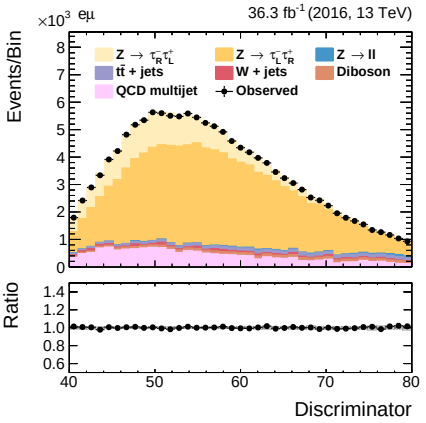

(b) *Post-fit* in $e + \mu$ category: $m_{\text{vis}}(e, \mu)$

4.1.4 $\tau_{\text{h}}\tau_{\text{h}}$ channel

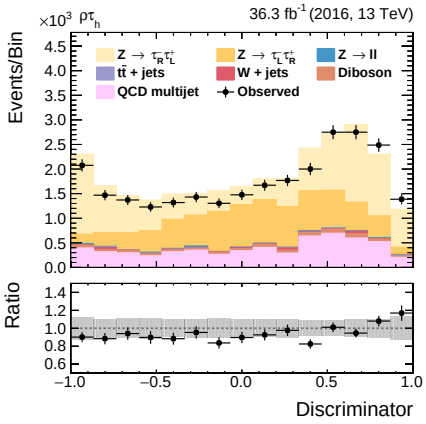

(a) *Pre-fit* in $\rho + \tau_{\text{h}}$ category: $\cos\beta(\rho)$

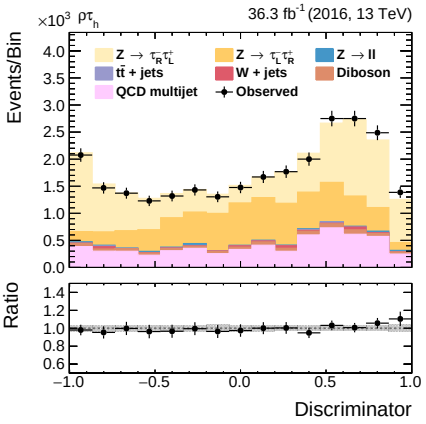

(b) *Post-fit* in $\rho + \tau_{\text{h}}$ category: $\cos\beta(\rho)$

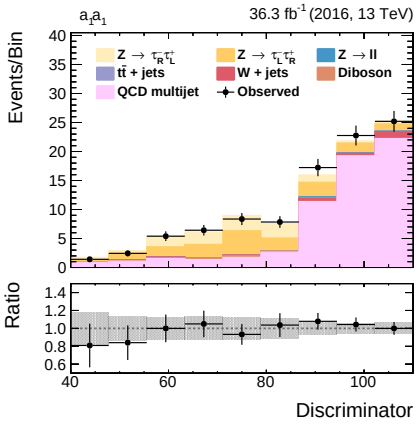

(a) *Pre-fit* in $a_1 + a_1$ category: $m_{\text{vis}}(a_1, a_1)$

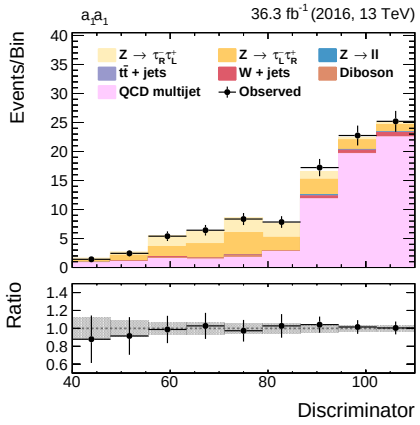

(b) *Post-fit* in $a_1 + a_1$ category: $m_{\text{vis}}(a_1, a_1)$

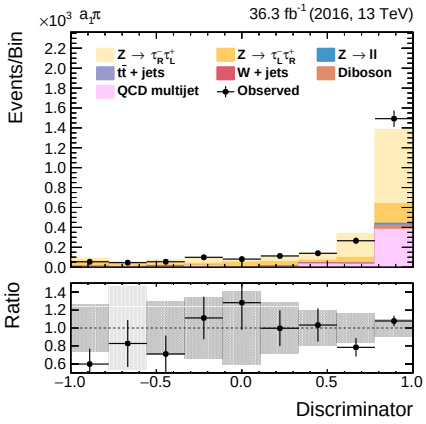

(c) *Pre-fit* in $a_1 + \pi$ category: $\Omega(a_1, \pi)$

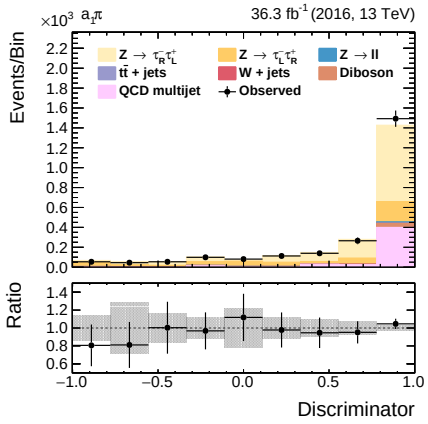

(d) *Post-fit* in $a_1 + \pi$ category: $\Omega(a_1, \pi)$

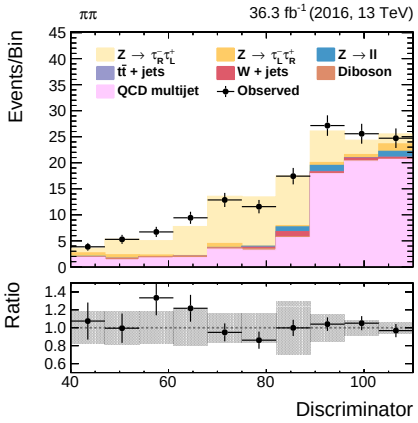

(e) *Pre-fit* in $\pi + \pi$ category: $m_{\text{vis}}(\pi, \pi)$

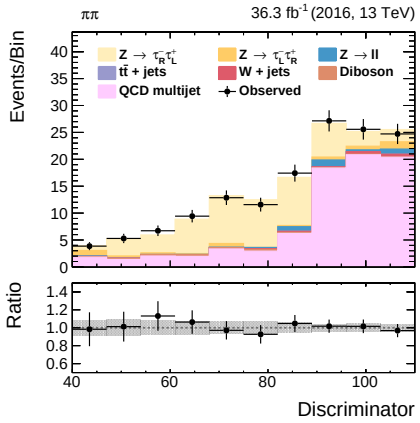

(f) *Post-fit* in $\pi + \pi$ category: $m_{\text{vis}}(\pi, \pi)$

4.2 Uncertainty on the measurement of τ lepton polarisation

4.2.1 Nuisance parameters of the fit

The impact of individual systematic uncertainties on the polarisation measurement has been studied. Figure 4.6 displays the list of 30 systematic uncertainties which have the largest impact on the final result.

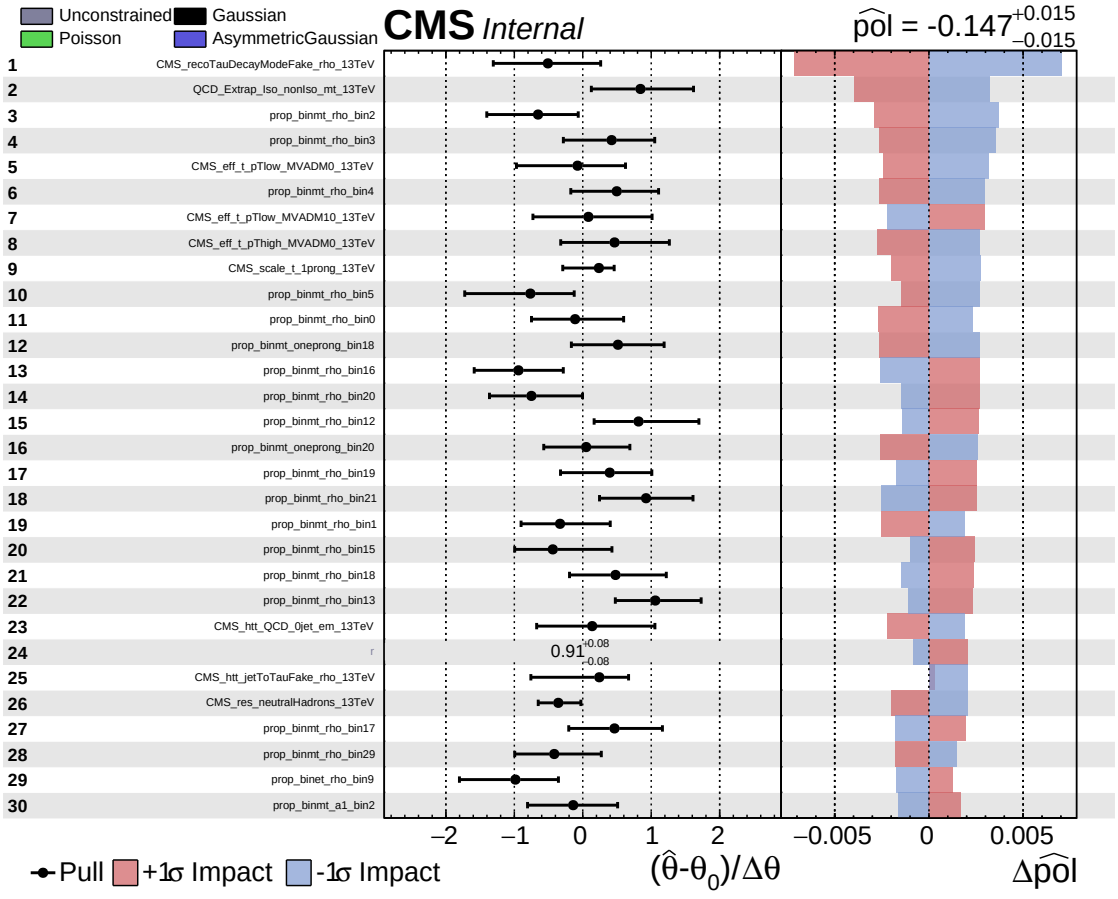

Figure 4.6: List of nuisance parameters and their impact on the combined maximum likelihood fit to data. Only the 30 systematic uncertainties with the largest impact on the final result are shown here.

4.2.2 Uncertainty breakdown

Table 4.1 summarises the impact of different sources of uncertainty on the measurement of polarisation in the final combined fit. The magnitudes of these sources of uncertainties are obtained by performing several maximum likelihood fits in Fig. 4.7 where the groups

of uncertainties are individually fixed, allowing the quadratic evaluation of their impact. The limited statistics (bin-by-bin) effects in the Monte Carlo datasets have the strongest impact. The uncertainty in modeling migrations between tau decay modes (particularly in $\tau \to \rho\nu$ categories) remains a significant source of error, despite the use of `MVA-DM` improving mode identification performance. The remaining significant sources of uncertainty are related to tau lepton identification and energy scale, as well as modeling of the QCD background. Finally, overall normalisation uncertainties (such as cross sections or luminosity) have no impact on the final result.

Table 4.1: Breakdown into subgroups of uncertainties for the total error on the measurement of the average τ polarisation $\langle P_\tau \rangle$.

Source of uncertainty	**Uncertainty magnitude** $\sigma_{\langle P_\tau \rangle}$
MC limited statistics	$^{+0.011}_{-0.010}$
τ_h decay mode migration	$^{+0.006}_{-0.007}$
τ_h identification and energy scale	0.004
QCD estimate	0.003
Jet faking τ_h rate	0.001
Other	0.005
Total systematic uncertainty	0.015
Statistical uncertainty	0.006

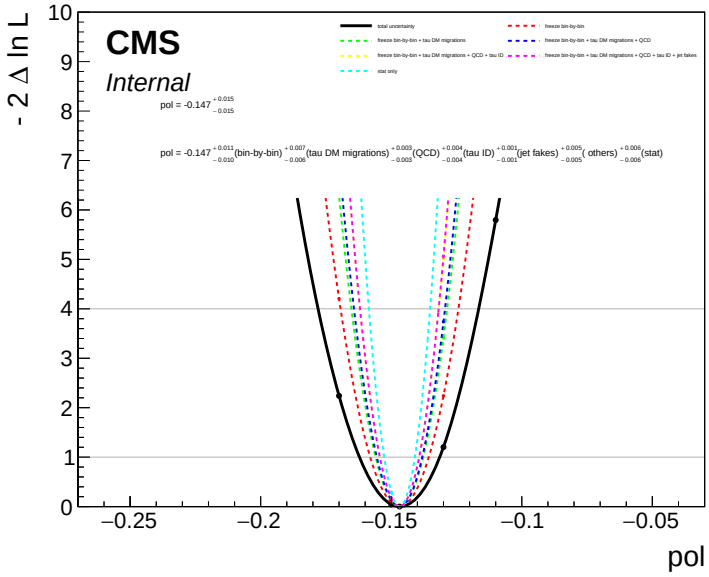

Figure 4.7: Likelihood scan as a function of the average polarisation where the main uncertainty groups (listed in Table 4.1) are successively fixed.

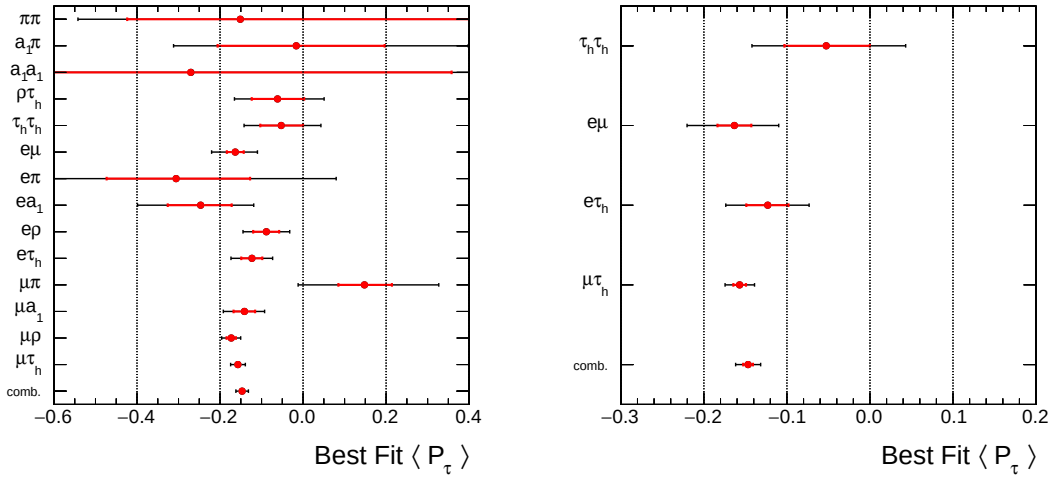

Figure 4.8: Final result on the average τ polarisation in different channels and categories.

4.3 Result of the average τ polarisation

The final result on the average τ polarisation in different channels and categories is shown in Fig. 4.8. Further Figure 4.9 verifies that the extracted average polarisation does not depend on the (pseudo-)rapidity of the Z-boson, with the result being included in the measurement error. Statistics are limited for high rapidity values.

The average τ polarisation measured for the interval of 75-120 GeV in di-tau mass yields:

$$\langle P_\tau \rangle = -0.147 \pm 0.015 = -0.147 \pm 0.006\,(\text{stat.}) \pm 0.014\,(\text{syst.}) \quad . \tag{4.1}$$

In order to directly compare to other LEP measurements the measured average polarisation $\langle \mathcal{P}_\tau \rangle$ is propagated to the polarisation value at the Z pole as shown in Fig. 4.10. The obtained value is:

$$\langle P_\tau \rangle = -0.152 \pm 0.015 = -0.152 \pm 0.006\,(\text{stat.}) \pm 0.014\,(\text{syst.}) \quad . \tag{4.2}$$

Figure 4.11 compares the measured and corrected τ polarisation at the Z pole of this measurement with the published results of previous τ lepton polarisation measurements, the ones of the four LEP experiments and SLD, the combination of LEP and SLD [68] and of ATLAS [5]. It has to be noted, that this analysis is significantly more precise than the one of ATLAS, slightly better than the one of SLD and almost reaches the precision of the individual LEP experiments. The combination of LEP and SLD results results in a precision that is better by a factor of 3 compared to this single LHC experiment measurement.

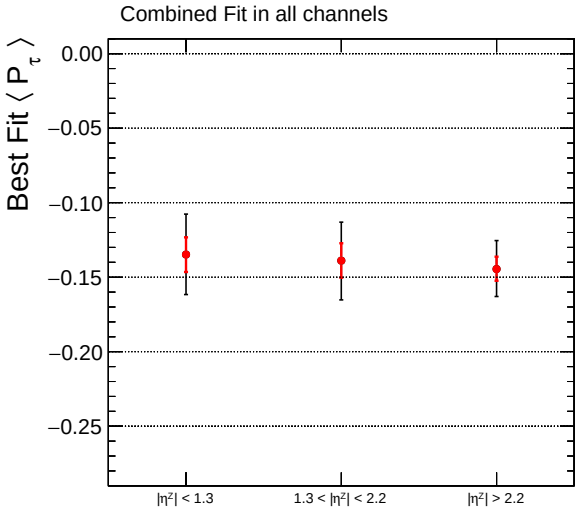

Figure 4.9: Final result on the average τ polarisation in different bins of the Z-boson rapidity.

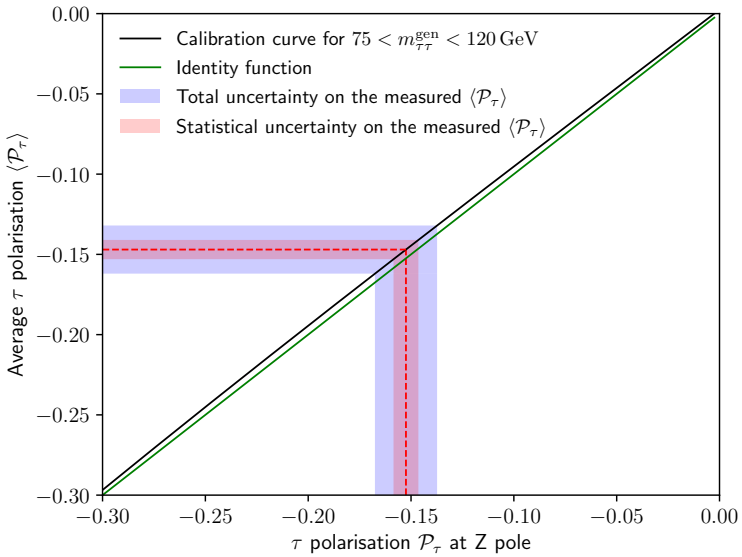

Figure 4.10: Average τ polarisation $\langle \mathcal{P}_\tau \rangle$ as a function of the τ polarisation at the Z pole. The value of the measured polarisation $\langle \mathcal{P}_\tau \rangle$ as well as its total and statistical uncertainties is propagated to the value of the polarisation at the Z pole using a calibration curve built with MADGRAPH5 for the considered mass range.

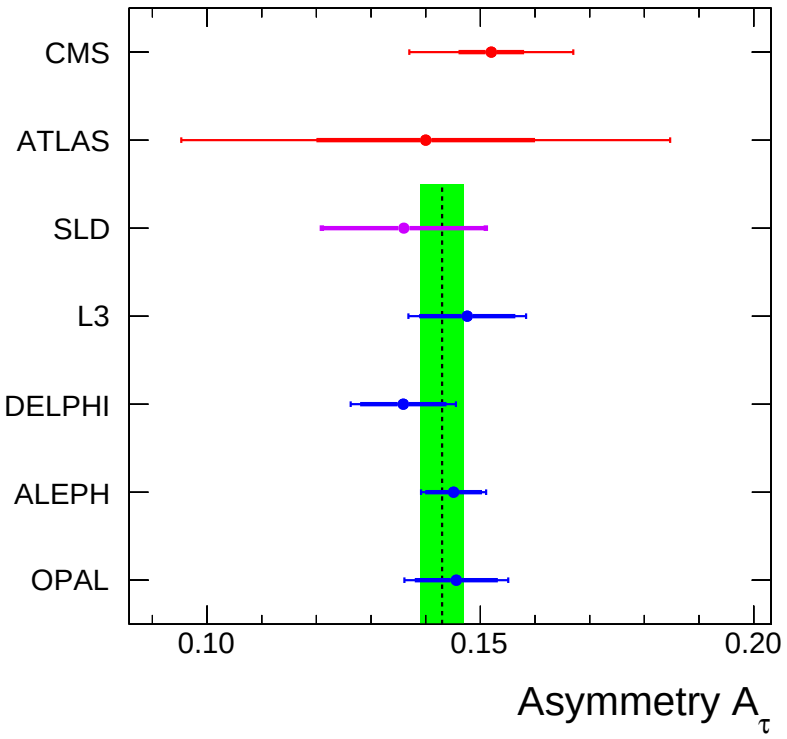

Figure 4.11: A comparison of the τ asymmetry, A_τ measured from τ polarisation at CMS in this thesis and other experiments, [4, 5, 69–71]. The combined LEP and SLD measurement, [72], is indicated by the green band.

Conclusion

Ce chapitre présente les résultats finaux de l'analyse mesurant la polarisation des leptons tau produits dans la désintégration du boson Z dans l'expérience CMS. Les résultats indiquent que les principales sources d'incertitude sont la statistique limitée dans les données de simulation Monte Carlo et la modélisation des migrations entre les modes de désintégration du tau, en particulier pour les catégories $\tau \to \rho\nu$. Les autres sources significatives d'incertitude sont liées à l'identification et à la correction de l'énergie du lepton tau, ainsi qu'à la modélisation du bruit de fond QCD. Les incertitudes de normalisation globale (telles que les sections efficaces ou la luminosité) n'ont pas d'impact sur les résultats finaux. L'analyse aboutit à une valeur pour la polarisation moyenne du tau de -0.147 ± 0.015 sur un intervalle de masse $M_{\tau\tau} \in [75, 120]\,\text{GeV}$, qui est ensuite propagée à la polarisation attendue au pôle du boson Z avec une valeur de -0.152 ± 0.015.

Chapter 5

Discussion of the measured polarisation with respect to the effective weak mixing angle

Contents

5.1 The polarisation and the weak vector- and axial-vector couplings

As already introduced above, the polarisation of τ leptons decaying from Z bosons is a direct consequence of the structure of the weak interaction, namely the mixing of the B^0 and the W^0 fields, which is parametrised by the effective mixing angle, $\sin^2\theta_W^{\mathrm{eff}}$. In the analysis it is not possible to distinguish between $Z \to \tau\tau$ and $\gamma \to \tau\tau$, as they produce exactly the same final state. The $\gamma \to \tau\tau$ process results in unpolarised τ leptons. As the relative fraction of $Z/\gamma \to \tau\tau$ events changes as a function of the quark-antiquark energy, $\hat{s}$, also the polarisation has to be considered as a function of this mass, the effective mixing

angle and the quark type, q, specifying whether the Z has been produced via a pair of up- or down-type quarks:

$$P_\tau = P_\tau\left(\sin^2\theta_W^{\text{eff}}, \hat{s}, q\right) \quad . \tag{5.1}$$

At tree level from the Eq. (3.3) the τ polarisation asymmetry A_{pol} reads, denoting $\hat{s} = m^2_{q\overline{q}}$:

$$P_\tau\left(\sin^2\theta_W^{\text{eff}}, \hat{s}, q\right) = -\frac{2Re\chi(\hat{s})q_q q_\tau v_q a_\tau + |\chi(\hat{s})|^2(v_q^2+a_q^2)2v_\tau a_\tau}{q_q^2 q_\tau^2 + 2Re\chi(\hat{s})q_q q_\tau v_q v_\tau + |\chi(\hat{s})|^2(v_q^2+a_q^2)(v_\tau^2+a_\tau^2)} \quad , \tag{5.2}$$

where q_τ, v_τ, a_τ and q_q, v_q, a_q are the electromagnetic charge, weak vector- and axial-vector couplings of τ lepton and the initial quark of type q. The function $\chi(\hat{s})$ describes the lineshape of the Z^0:

$$\chi(\hat{s}) = \frac{1}{4\sin^2\theta_W\cos^2\theta_W}\,\frac{\hat{s}}{\hat{s} - M_Z^2 + i\hat{s}\frac{\Gamma_Z}{M_Z}} \quad . \tag{5.3}$$

At the Z-pole ($\hat{s} = M_Z^2$) the τ polarisation does not depend on the initial quark flavour, neglecting the small electromagnetic term $q_q^2 q_\tau^2$ one obtains:

$$P_\tau\left(\sin^2\theta_W^{\text{eff}}, M_Z^2\right) = -\frac{|\chi(M_Z^2)|^2(v_q^2+a_q^2)2v_\tau a_\tau}{|\chi(M_Z^2)|^2(v_q^2+a_q^2)(v_\tau^2+a_\tau^2)} = -2\frac{v_\tau a_\tau}{v_\tau^2+a_\tau^2} \quad , \tag{5.4}$$

In $v_\tau \ll a_\tau$ limit one gets the approximate equation:

$$P_\tau\left(\sin^2\theta_W^{\text{eff}}, M_Z^2\right) \approx -2\frac{v_\tau}{a_\tau} \quad . \tag{5.5}$$

5.2 Average polarisation

The true quark-antiquark energy, $\hat{s}$, is not accessible in the analysis due to the presence of neutrinos in the τ decays. Instead, the measured τ lepton polarisation is a weighted average over a wider mass range. In the same way, the polarisation is averaged over the quark flavours, q:

$$\left\langle P_\tau(\sin^2\theta_W^{\text{eff}})\right\rangle = \frac{\sum\limits_{q=u,d}\int \mathrm{d}\hat{s}\; P_\tau\left(\sin^2\theta_W^{\text{eff}}, \hat{s}, q\right)\cdot w\left(\sin^2\theta_W^{\text{eff}}, \hat{s}, q\right)}{\sum\limits_{q=u,d}\int \mathrm{d}\hat{s}\, w\left(\sin^2\theta_W^{\text{eff}}, \hat{s}, q\right)} \quad . \tag{5.6}$$

Here, $w\left(\sin^2\theta_W^{\text{eff}}, \hat{s}, q\right)$ denote the weights used for averaging. They cover two effects: firstly the dependence of the cross section, σ, on the quark-antiquark mass, $\hat{s}$, and the quark type, q for a given value of the mixing angle, $\sin^2\theta_W^{\text{eff}}$, and secondly on the acceptance of the detector and on the selection efficiency in the analysis, ϵ, which depends on $\hat{s}$ and q, as well.

5.3 The relation between average polarisation at generator level and the weak mixing angle evaluated with MadGraph5

As explained in Sect. 3.8 the efficiencies for right- and left-handed τ leptons are different and also depend on the decay mode. Hence, a methodology has been adopted where templates for right- and left-handed τ leptons are utilised to account for these effects These templates are normalised in such a way that they correspond to zero polarisation for a given range ([75,120] GeV) of $\hat{s}$ at the generator level. The extracted polarisation by the fit of these templates to the distribution of the optimal observables corresponds then to the average polarisation within this mass range of $\hat{s}$ and this average value of the polarisation will be related to the weak mixing angle. If the fit is done to an *Asimov* dataset based on our leading-order (LO) MadGraph5 Drell-Yan (DY) dataset, the extracted polarisation will be the polarisation of that mass interval. This is a *closure test* of this procedure. For the fit to real data the extracted polarisation will be different, because it is determined by the effective mixing angle very different to the LO value in the simulated DY dataset. Calibration curves are necessary to convert different polarisation values to an effective mixing angle.

To generate such a calibration curve, four MadGraph5 samples of DY events are generated, at LO electroweak level, with varied value for the mixing angle. The values are shown in Table 5.1. Technically, because the mixing angle is not an input parameter for the MadGraph5 simulation, this was done by changing the value of the Fermi constant, which changes subsequentionaly the onshell mass value of M_W and thus the value of $\sin^2\theta_W$(MC) of the MadGraph5 run according the relation:

$$M_W^2 = \frac{M_Z^2}{2} + \sqrt{\left(\frac{M_Z^2}{2}\right)^2 - \frac{\alpha_{elm}\pi M_Z^2}{\sqrt{2}G_F}} \quad ; \tag{5.7}$$

and the mixing angle is then calculated according to:

$$\sin^2\theta_W = 1 - \frac{M_W^2}{M_Z^2} \quad . \tag{5.8}$$

The LHE content of the event record is utilised to count the number of left- and right-handed tau leptons within various $\hat{s}$ intervals at the generator level for each of the one million generated event samples. In this way, the average polarisation is calculated according to its definition, Eq. (3.3), in each interval of $\hat{s}$.

The numerical values for the average polarisations obtained in the four cited mass intervals are listed in Table 5.1, while the square solid symbols in Fig. 5.1 display the results.

The two open square symbols in Fig. 5.1 represent two MadGraph5 runs where additional QCD jets were included. Due to the increased computational time, only two

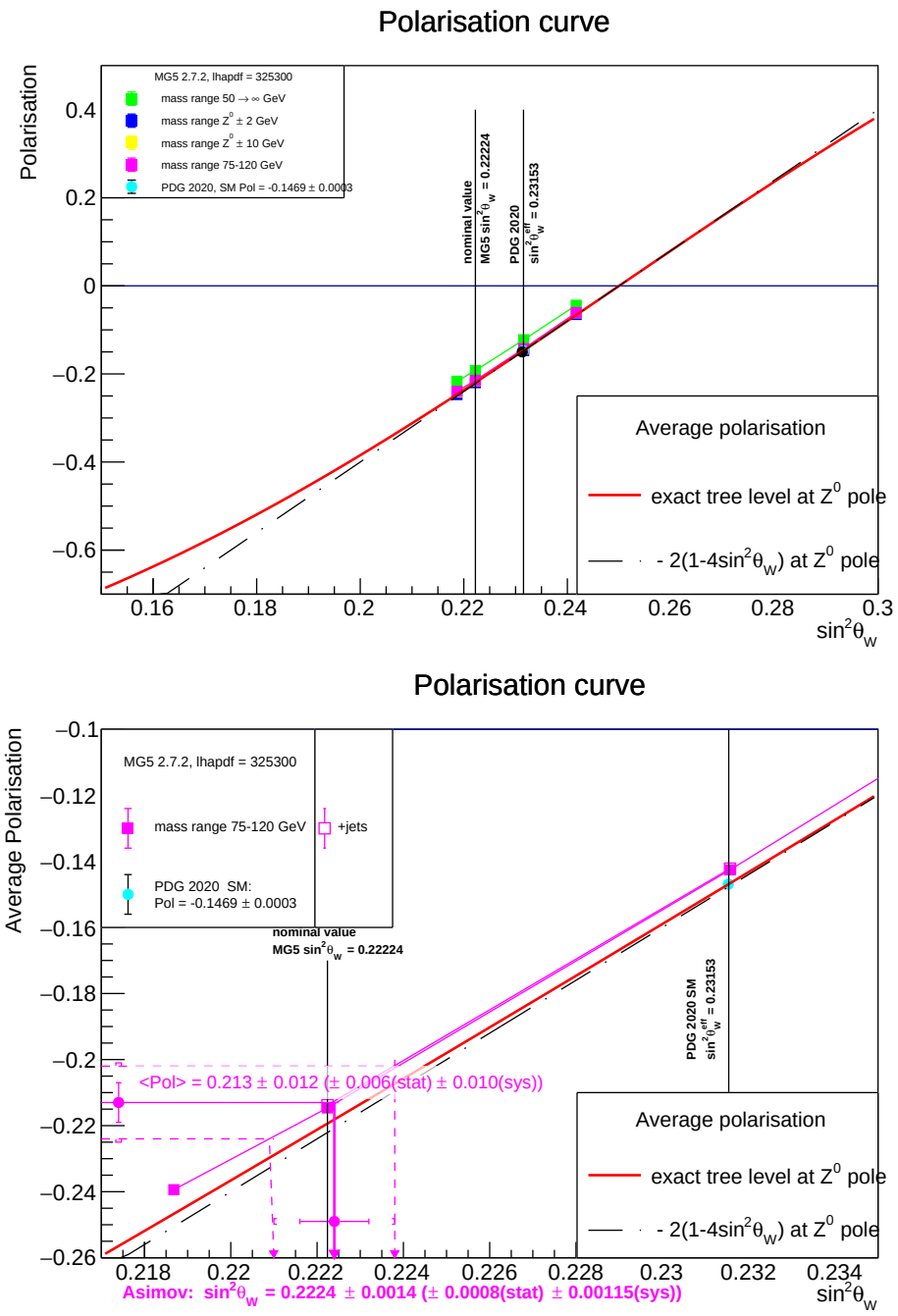

Figure 5.1: Average polarisation for different mass intervals derived from MadGraph5 samples with varied G_F as function of the corresponding weak mixing angle. The expected polarisation at tree-level at the Z^0 peak is shown as well. The upper graph shows a wider range of the weak mixing angle, the lower graph zooms into the interval of the MadGraph5 value and the SM effective mixing angle.

Table 5.1: Values of G_F, $\sin^2\theta$ used in generated samples and obtained average polarisation.

Run	G_F ($10^{-5}\,\mathrm{GeV}^{-2}$)	$\sin^2\theta_W$	$\langle\mathcal{P}_\tau\rangle$ in a given range of $\hat{s}$ (GeV): $[M_Z \pm 2]$	$[M_Z \pm 10]$	[75,120]	[50,250]
#1	1.1000	0.24171	-0.065	-0.061	-0.061	-0.044
#2	1.1330	0.23157	-0.147	-0.143	-0.143	-0.122
#3	1.1664	0.22225	-0.220	-0.216	-0.215	-0.192
#4	1.1800	0.21868	-0.247	-0.241	-0.240	-0.217
#2+jets	1.1330	0.23157	-0.147	-0.142	-0.142	-0.126
#3+jets	1.1664	0.22225	-0.219	-0.214	-0.214	-0.196

values were simulated. The impact on the average polarisation is minimal, especially when the mass interval is more centered around the Z^0-pole. The connecting lines between the symbols serve as simple interpolations, allowing for the retrieval of the effective mixing angle in the following way: when using templates at the generator level referring to a particular mass interval to extract polarization values from data, the corresponding interpolating line can be employed to determine the weak mixing angle that would produce the measured average polarization value in a LO simulation. This weak mixing angle corresponds to an effective mixing angle $\sin^2\theta_W^{\mathrm{eff},\tau}$. In this study, the interval between 75 and 120 GeV was selected to retain the majority of the statistics when creating the templates.

By performing a toy measurement on an *Asimov* dataset using the dedicated DY sample outlined in Table 3.2, and propagating the *measured* average value of τ polarisation of $\langle\mathcal{P}_\tau\rangle = -0.213 \pm 0.012$ over the Z-lineshape, we can derive the value of the weak mixing angle, which is:

$$\sin^2\theta_W\ (\text{MC toy}) = 0.22240 \pm 0.0014 \quad .$$

The obtained value is well consistent with $\sin^2\theta_W(\text{MC}) = 0.22224$ which is the LO value of MadGraph5.

To obtain the value of the average polarization at the Z^0 pole, only a small shift of 0.005 is required, which is the difference between the purple ($\hat{s} \in [75, 120]$ GeV) and red (tree level, $\hat{s} = M_Z$) lines in Fig. 5.1. This would return the nominal LO value of $\langle\mathcal{P}_\tau\rangle(\hat{s} \in [M_Z \pm 2]\,\mathrm{GeV}) = -0.219$ for the polarisation obtained through MadGraph5.

Whether one utilises the calibration curve or simply the shift of 0.005 between the average polarisation and the polarisation at the Z-pole is inconsequential, as the two lines in the figure are parallel to each other.

Propagating the measured polarisation (4.2) presented in this thesis to the value of the effective mixing angle yields:

$$\sin\theta_W^{\text{eff}} = 0.2308 \pm 0.0019 = 0.2308 \pm 0.0008\,(\text{stat.}) \pm 0.0018\,(\text{syst.}) \quad . \tag{5.9}$$

The precision of this value for $\sin^2\theta_W^{\text{eff}}$ is not competitive with the precision of existing measurements, and therefore cannot be used to constrain new physics. However, the measured polarisation is highly compatible with the Standard Model value of $A_\ell = 0.1468 \pm 0.0003$.

Conclusion

En utilisant la valeur de polarisation mesurée précédemment, la valeur de l'angle de mélange électrofaible effectif est calculée par interpolation de ces valeurs avec des courbes d'étalonnage produites avec le générateur d'événements MADGRAPH5. Cela conduit à $\sin\theta_W^{\text{eff}} = 0.2308 \pm 0.0019 = 0.2308 \pm 0.0008\,(\text{stat.}) \pm 0.0018\,(\text{syst.})$. Bien que cette précision ne soit pas suffisante pour contraindre une nouvelle physique, la polarisation mesurée est compatible avec la valeur du Modèle Standard de $A_\ell = 0.1468 \pm 0.0003$

Conclusion

La thèse présentée dans ce document propose une nouvelle mesure de la polarisation des leptons taus issus de la désintégration de bosons Z, produits en collisions proton-proton à 13 TeV par l'expérience CMS en 2016.

Un lot de données correspondant à une luminosité intégrée de 36.3 fb^{-1} a été étudié. La polarisation mesurée au pôle du Z est égale à $-0.152 \pm 0.015 = -0.152 \pm 0.006\,(\text{stat.}) \pm 0.014\,(\text{syst.})$. L'incertitude obtenue est comparable à celle obtenue par chaque expérience du LEP, supérieure d'un facteur 1.1 à 1.2, et plus faible d'un facteur 3.7 par rapport à la mesure effectuée par la collaboration ATLAS à 8 TeV.

De cette mesure une valeur de l'angle de mélange électrofaible égale à $\sin^2\theta_W^{\text{eff}} = 0.2308 \pm 0.0019 = 0.2308 \pm 0.0008\,(\text{stat.}) \pm 0.0018\,(\text{syst.})$ est dérivée. Celle-ci est obtenue en calibrant la moyenne de la polarisation mesurée sur l'intervalle de masse $M_{\tau\tau} \in [75, 120]$ GeV avec le générateur MADGRAPH5. La valeur mesurée est compatible avec la valeur attendue du modèle standard de la physique des particules. Elle offre l'avantage de proposer une méthode alternative à celle utilisant traditionnellement les asymétries avant-arrière. Elle démontre la faisabilité de l'emploi de variables optimales pour caractériser les états d'hélicité des leptons taus dans l'expérience CMS auprès du LHC, et ce pour tous les canaux hadroniques.

Une partie significative du travail de thèse, présentée en première partie du document, a été dévolue à la mise en fonctionnement du dispositif de tests des modules 2S du futur trajectographe de la phase de haute luminosité du LHC, auprès de la ligne CMS du cyclotron CYRCé de l'IPHC. Ces travaux permettent désormais d'effectuer des tests à haut taux d'acquisition et d'occupation des modules 2S sur cette ligne de faisceau.

Appendices

Appendix A

Appendix upgrades

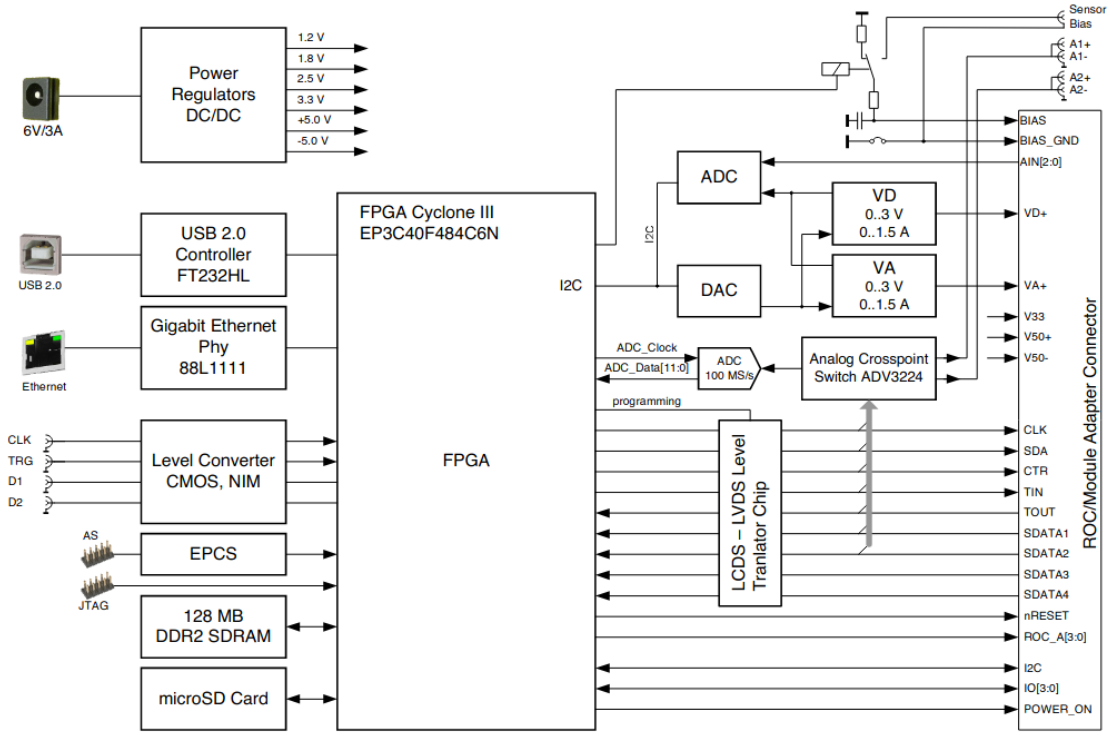

Figure A.1: Block diagram of essential features of the Digital Test Board (DTB) from DTB manual [73].

Appendix B

Control plots

B.1 $\tau_h\tau_h$ final state

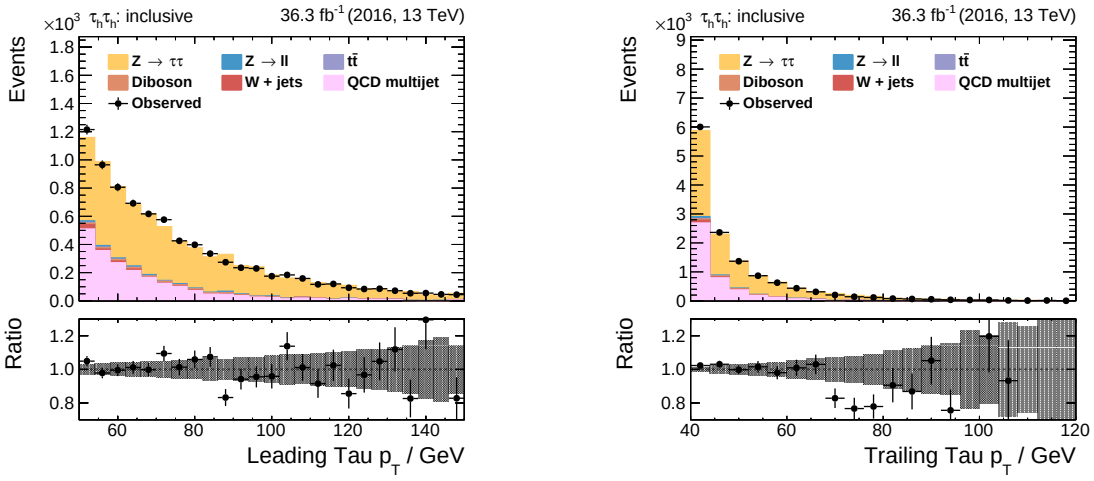

Figure B.1: Distributions of the leading (*left*) and the trailing (*right*) τ_h transverse momenta in $\tau_h\tau_h$ channel.

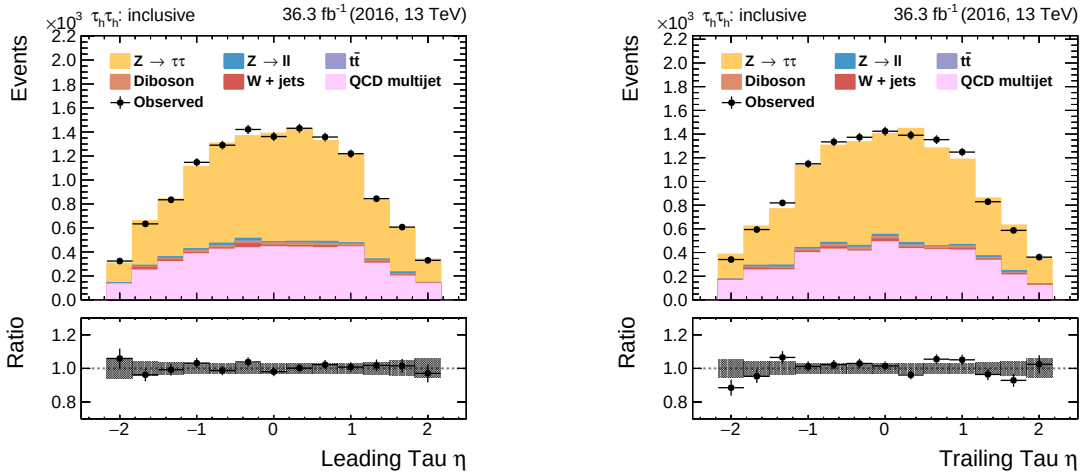

Figure B.2: Distributions of the leading (*left*) and the trailing (*right*) τ_h pseudo-rapidities in $\tau_h\tau_h$ channel.

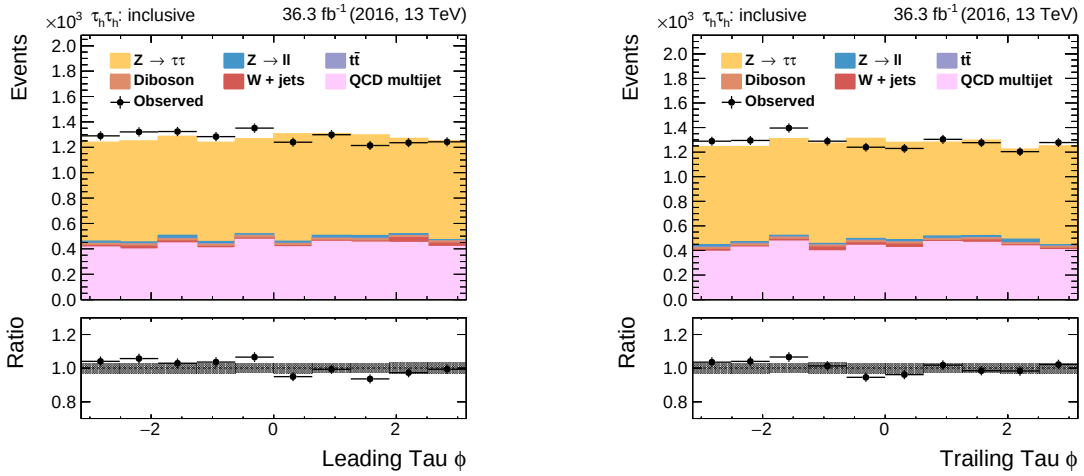

Figure B.3: Distributions of the leading (*left*) and the trailing (*right*) τ_h azimuthal angles in $\tau_h\tau_h$ channel.

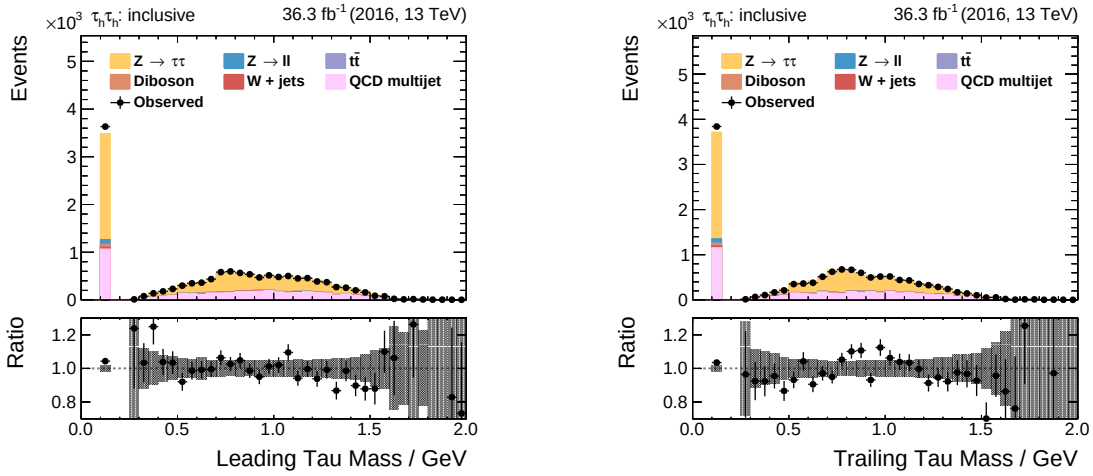

Figure B.4: Distributions of the leading (*left*) and the trailing (*right*) τ_h visible masses in $\tau_h\tau_h$ channel.

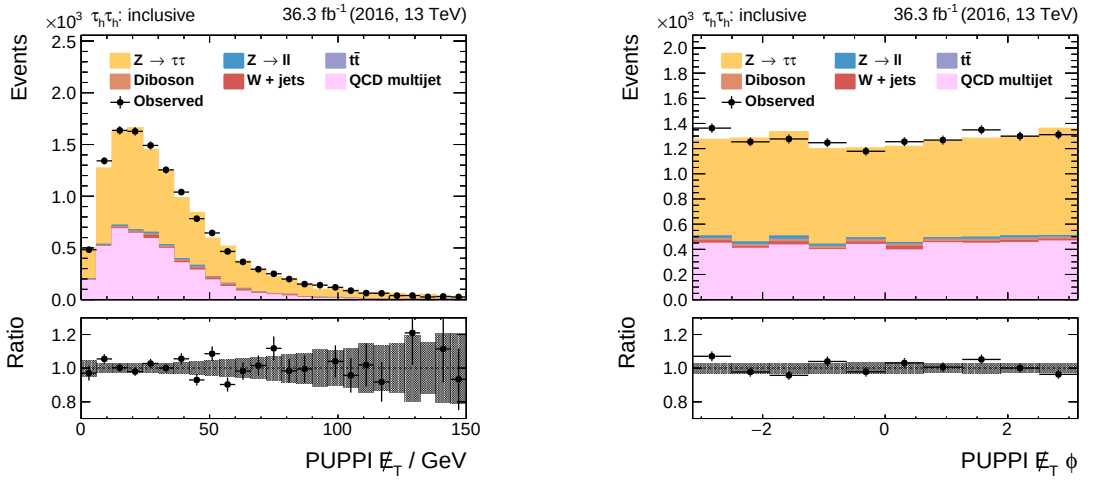

Figure B.5: Distributions of the transverse missing energy (*left*) and azimuthal angle (*right*) of the transverse missing momentum in $\tau_h\tau_h$ channel.

B.2 $\tau_\mu\tau_\mathrm{h}$ final state

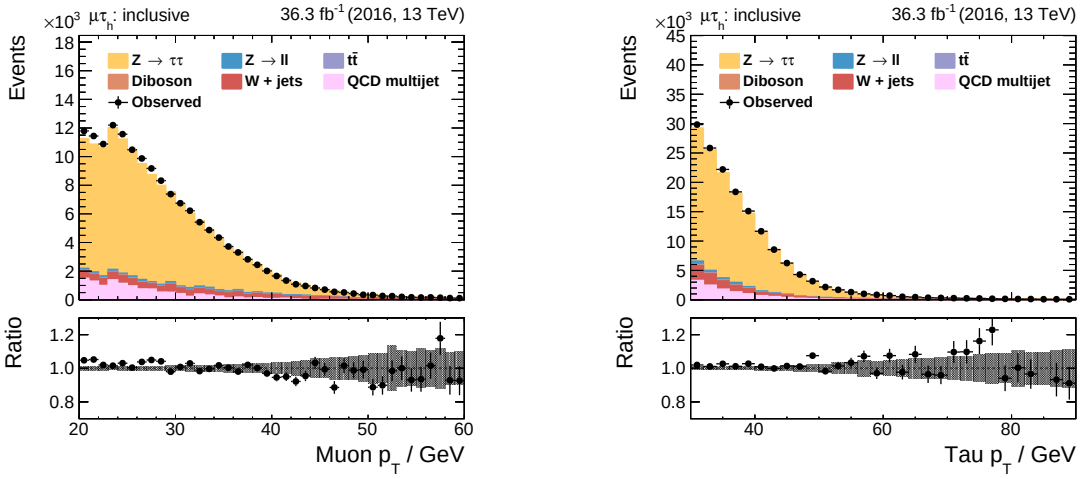

Figure B.6: Distributions of the muon (*left*) and the τ_h candidate (*right*) transverse momenta in $\tau_\mu\tau_\mathrm{h}$ channel.

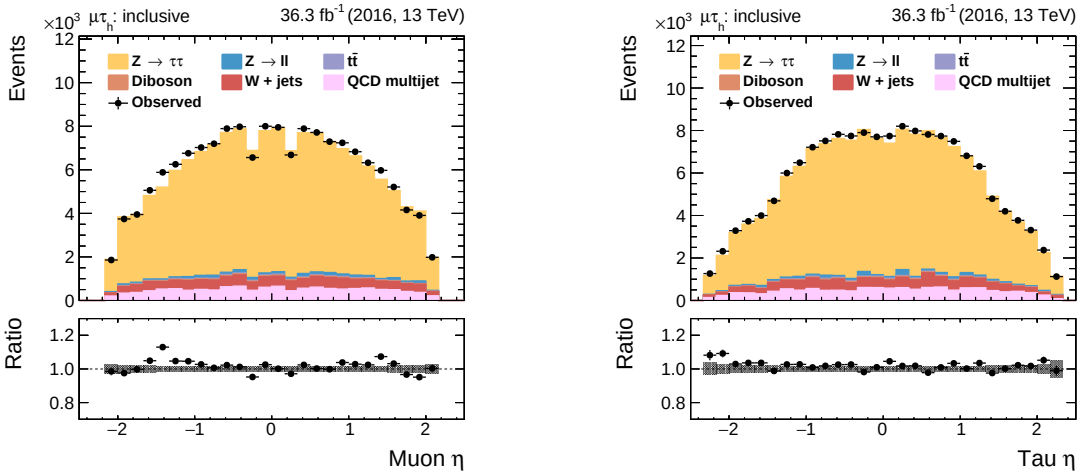

Figure B.7: Distributions of the muon (*left*) and the τ_h candidate (*right*) pseudo-rapidities in $\tau_\mu\tau_\mathrm{h}$ channel.

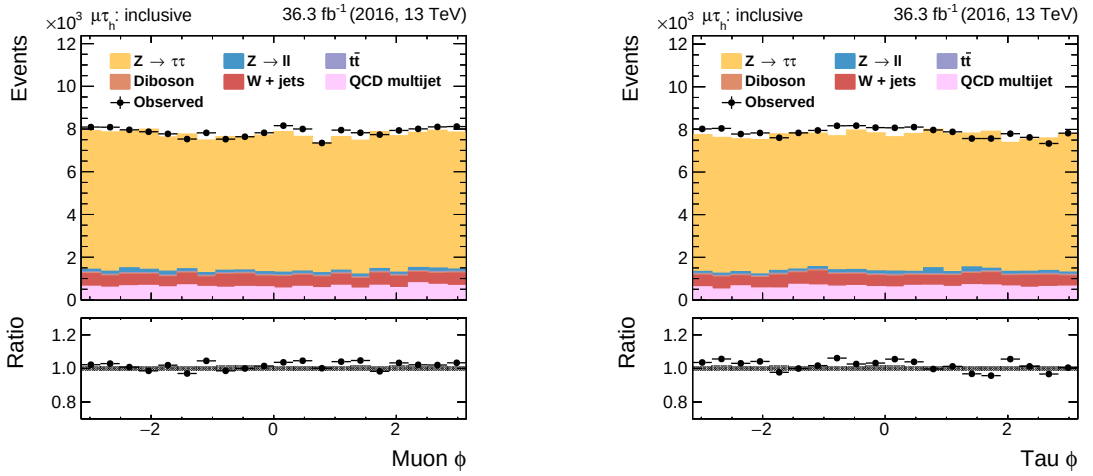

Figure B.8: Distributions of the muon (*left*) and the τ_h candidate (*right*) azimuthal angles in $\tau_\mu\tau_\mathrm{h}$ channel.

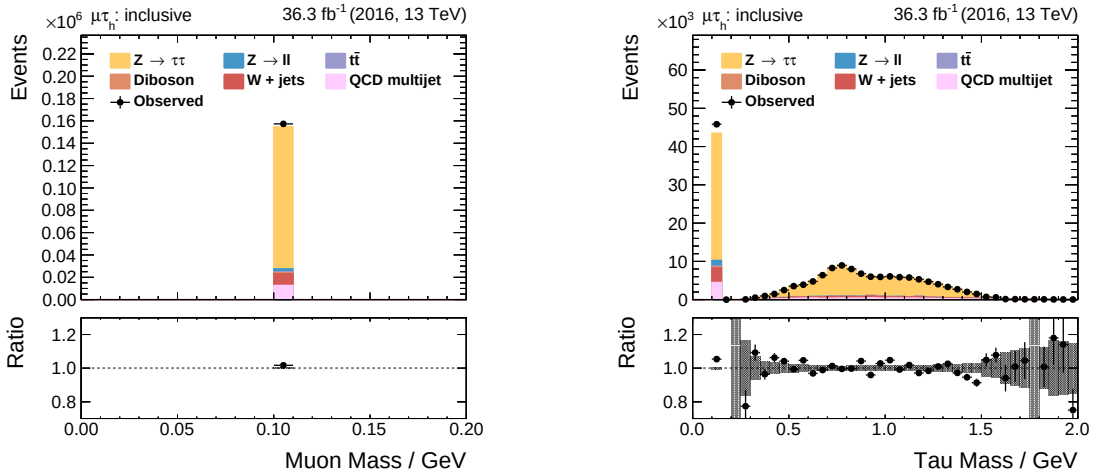

Figure B.9: Distributions of the muon (*left*) and the τ_h candidate (*right*) visible masses in $\tau_\mu\tau_\mathrm{h}$ channel.

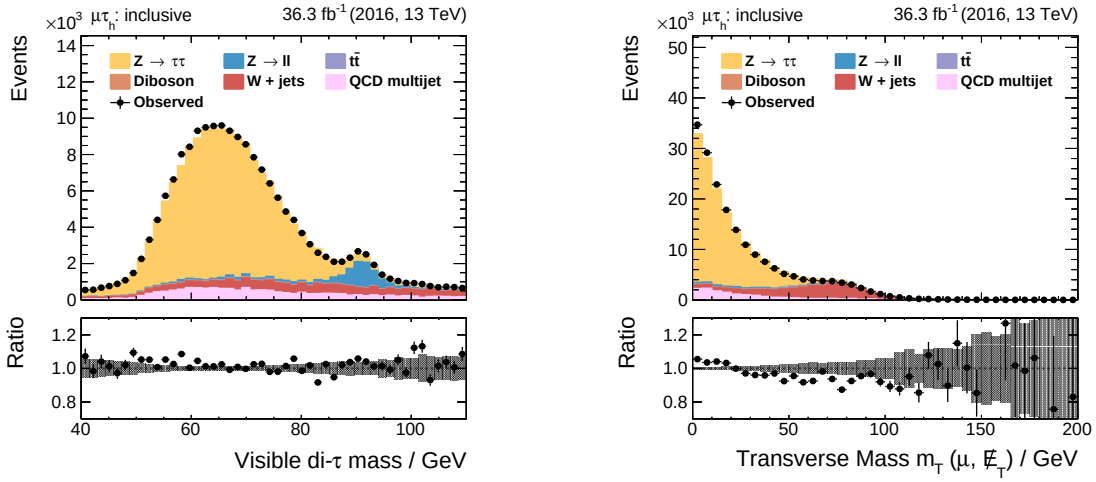

Figure B.10: Distributions of visible invariant mass $m_{\text{vis}}(\mu,\tau_h)$ (*left*) and transverse mass $m_T(E_T^{\text{miss}},\mu)$ (*right*), defined in Eq. (3.14), in $\tau_\mu\tau_h$ channel.

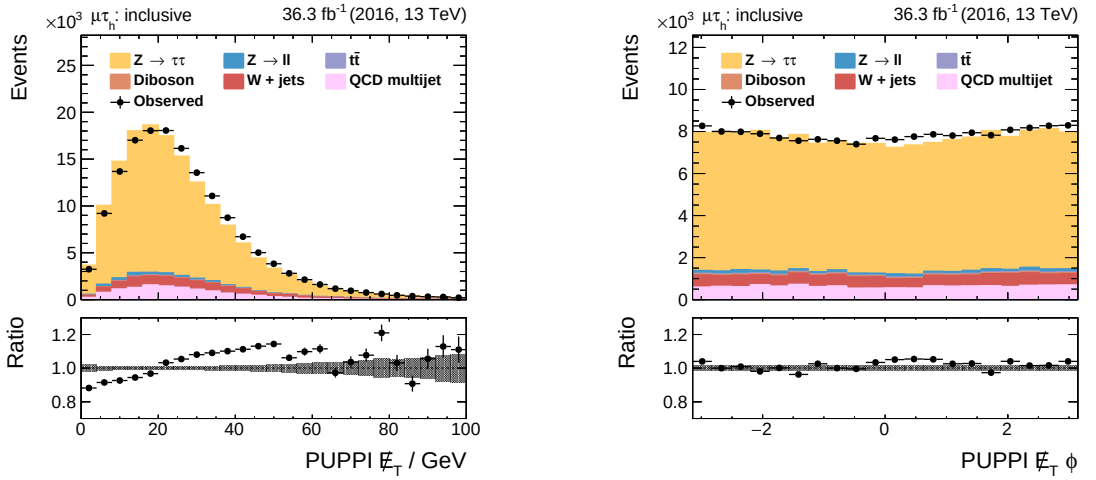

Figure B.11: Distributions of the transverse missing energy (*left*) and azimuthal angle of the transverse missing momentum (*right*) in $\tau_\mu\tau_h$ channel.

B.3 $\tau_e\tau_h$ final state

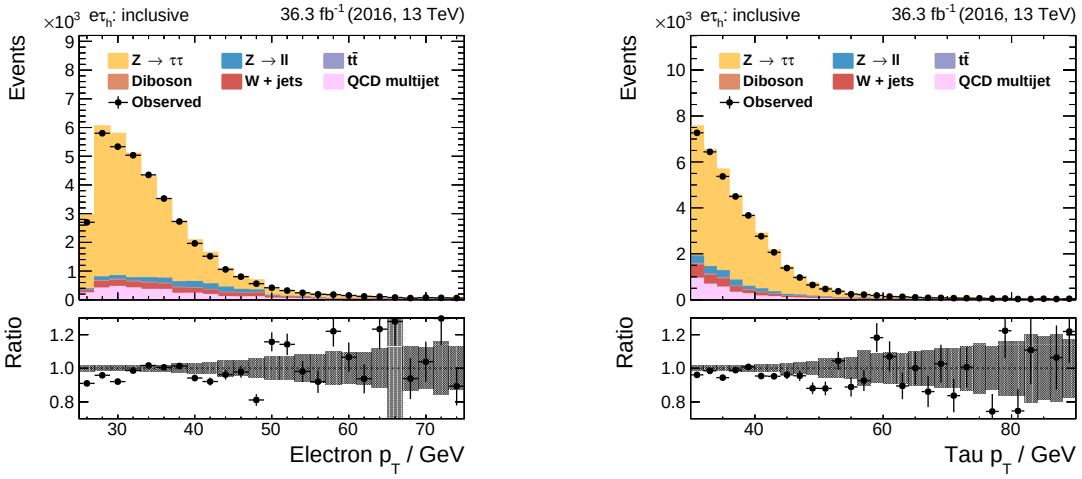

Figure B.12: Distributions of the electron (*left*) and the τ_h candidate (*right*) transverse momenta in $\tau_e\tau_h$ channel.

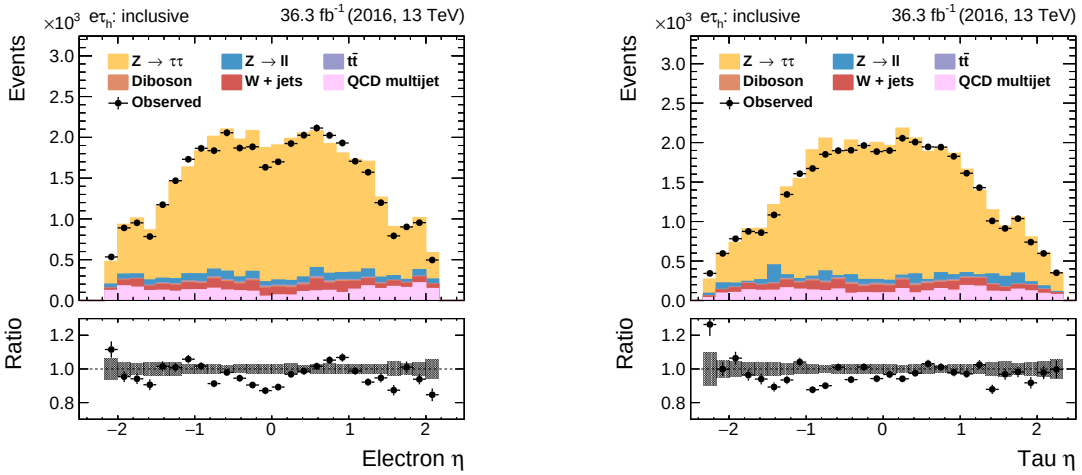

Figure B.13: Distributions of the electron (*left*) and the τ_h candidate (*right*) pseudo-rapidities in $\tau_e\tau_h$ channel.

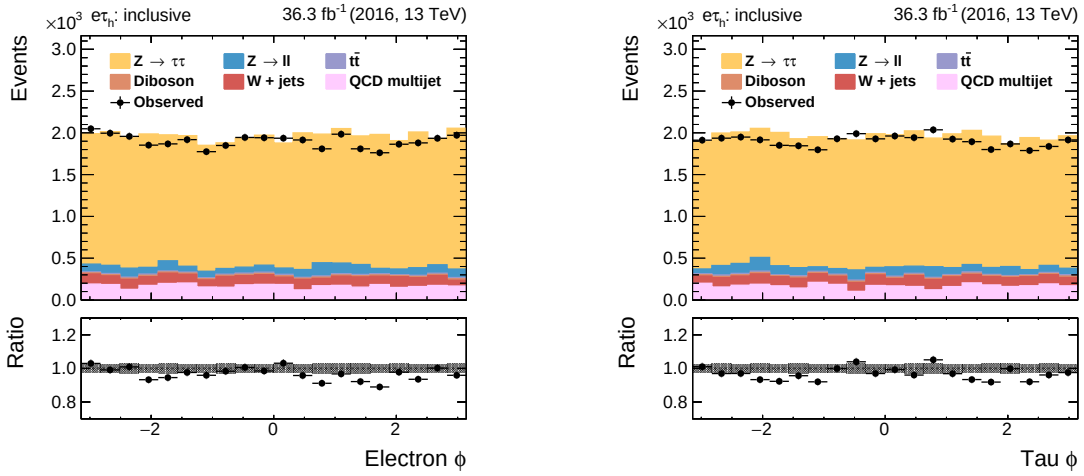

Figure B.14: Distributions of the electron (*left*) and the τ_h candidate (*right*) azimuthal angles in $\tau_\mu\tau_h$ channel.

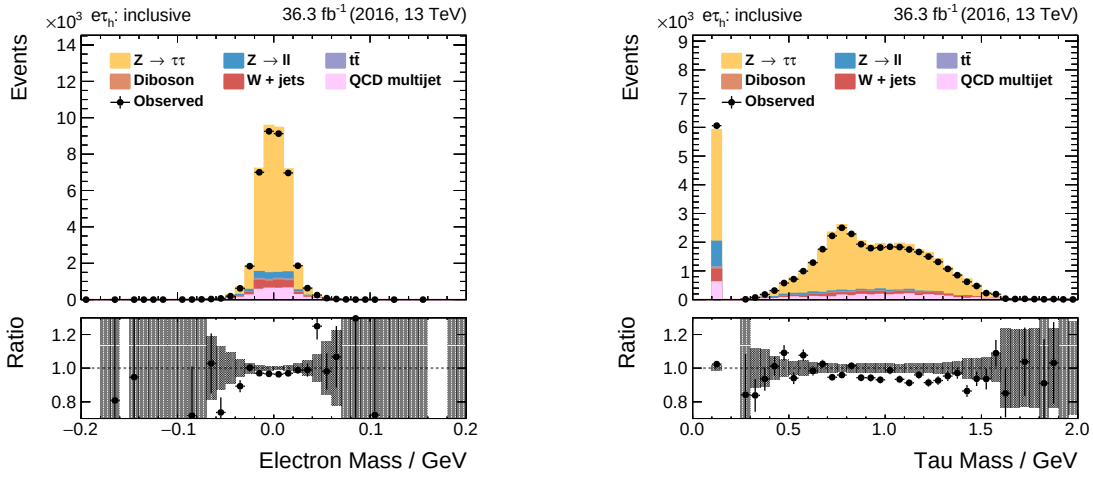

Figure B.15: Distributions of the electron (*left*) and the τ_h candidate (*right*) visible masses in $\tau_e\tau_h$ channel.

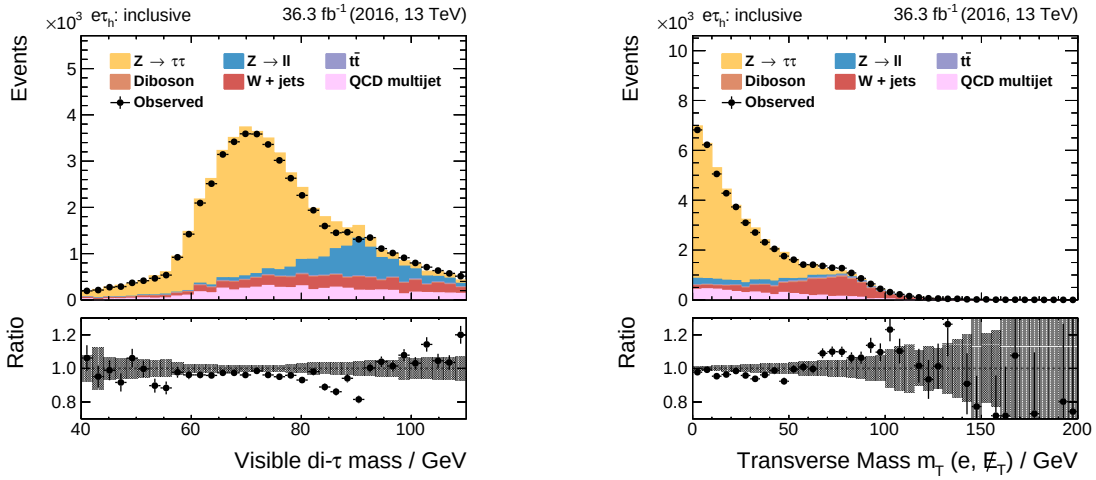

Figure B.16: Distributions of visible invariant mass $m_{\text{vis}}(\text{e},\tau_\text{h})$ (*left*) and transverse mass $m_\text{T}(E_\text{T}^\text{miss}, e)$ (*right*), defined in Eq. (3.14), in $\tau_e\tau_\text{h}$ channel.

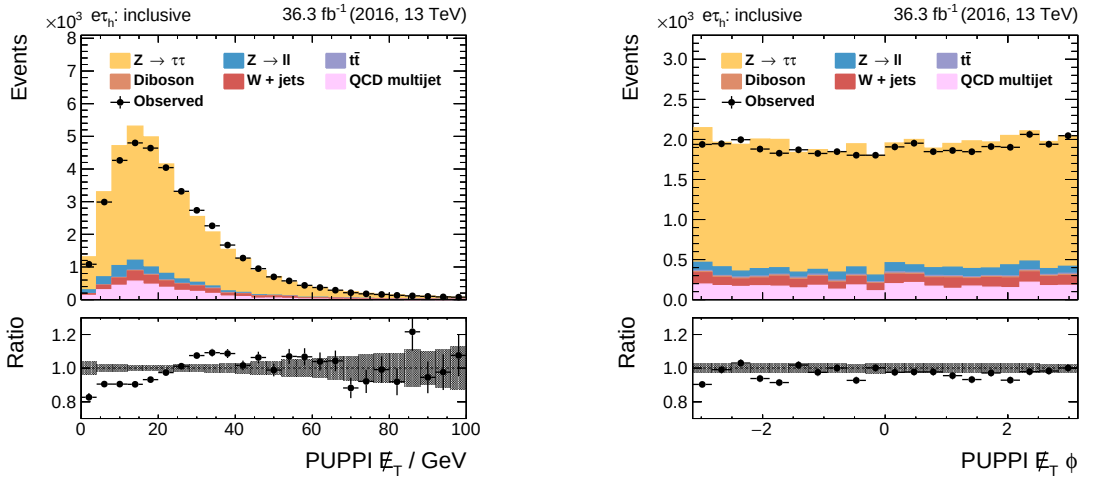

Figure B.17: Distributions of the transverse missing energy (*left*) and azimuthal angle of the transverse missing momentum (*right*) in $\tau_e\tau_\text{h}$ channel.

B.4 $\tau_e\tau_\mu$ final state

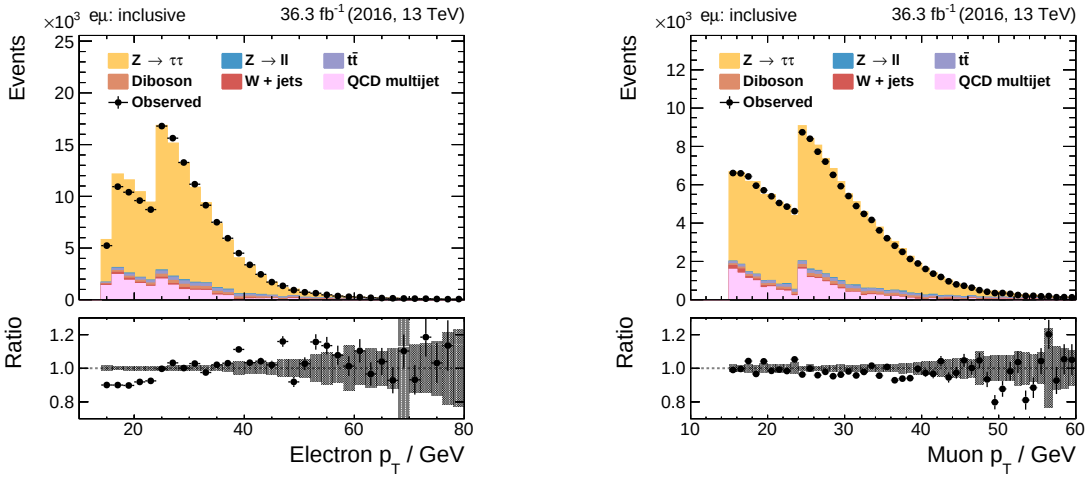

Figure B.18: Distributions of the electron (*left*) and the muon (*right*) transverse momenta in $\tau_e\tau_\mu$ channel.

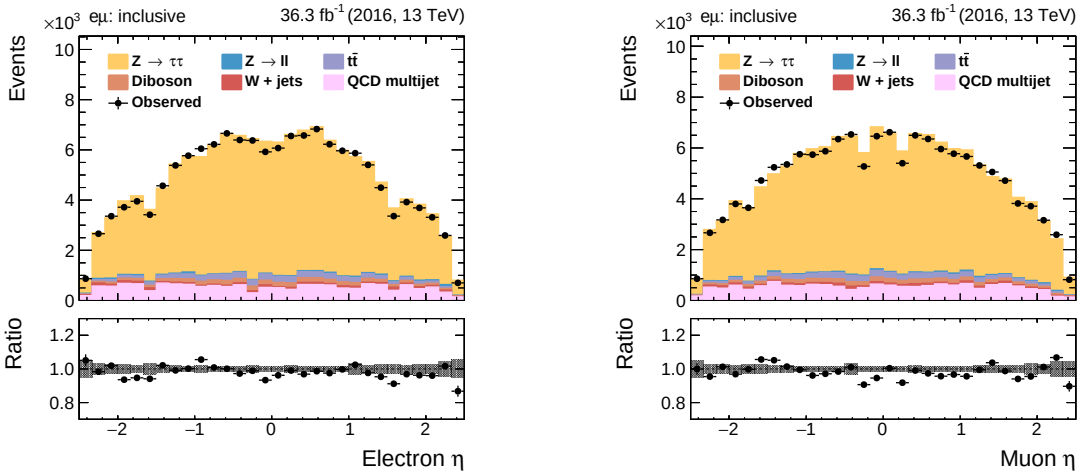

Figure B.19: Distributions of the electron (*left*) and the muon (*right*) pseudo-rapidities in $\tau_e\tau_\mu$ channel.

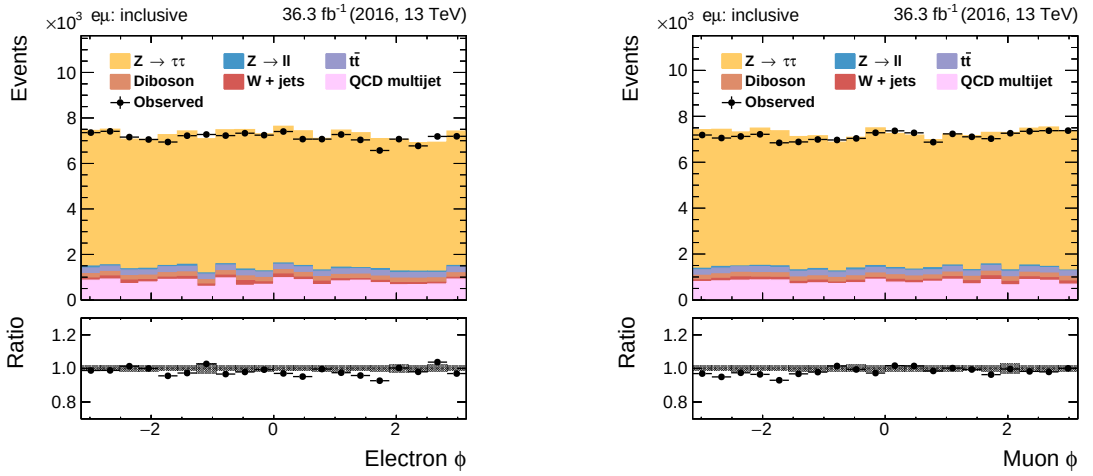

Figure B.20: Distributions of the electron (*left*) and the muon (*right*) azimuthal angles in $\tau_e\tau_\mu$ channel.

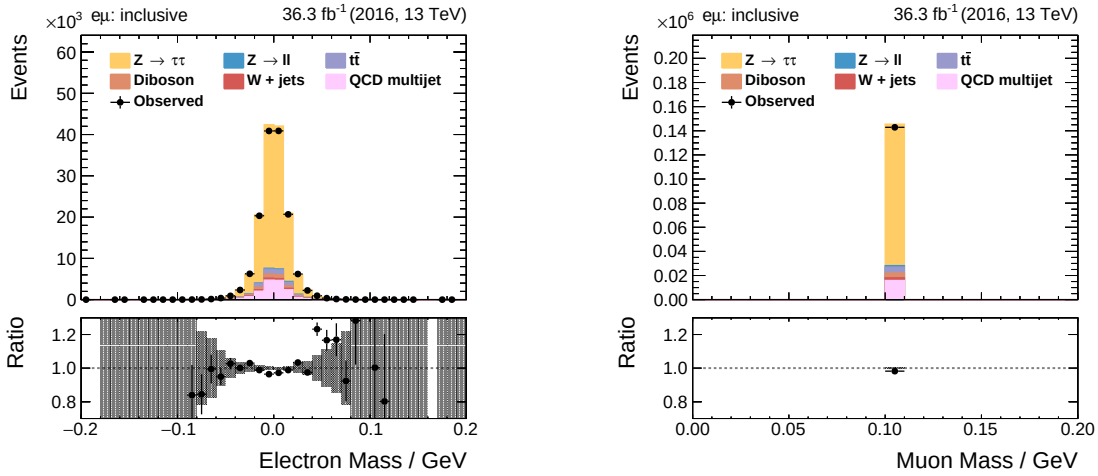

Figure B.21: Distributions of the electron (*left*) and the muon (*right*) visible masses in $\tau_e\tau_\mu$ channel.

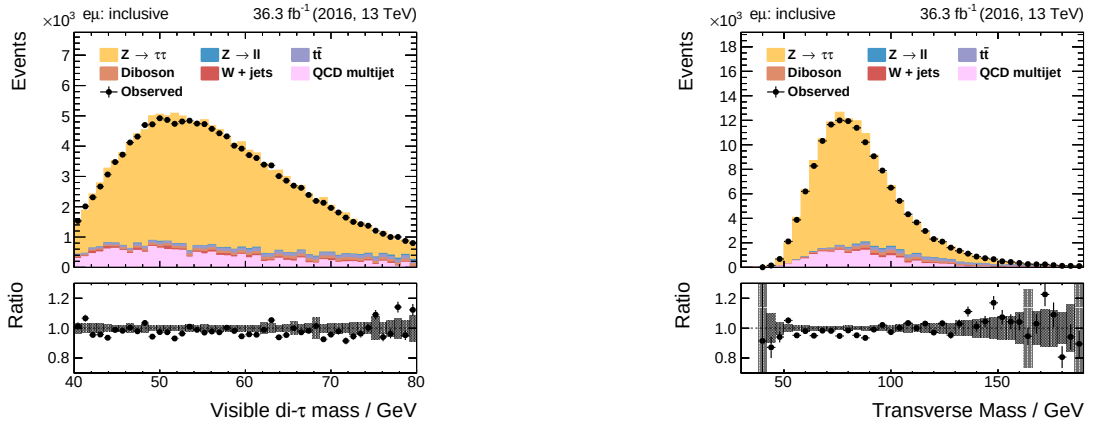

Figure B.22: Distributions of visible invariant mass $m_{\text{vis}}(\text{e},\mu)$ (*left*) and transverse mass $m_{\text{T}}(E_{\text{T}}^{\text{miss}}, e\mu)$ (*right*), defined in Eq. (3.14), in $\tau_e\tau_\mu$ channel.

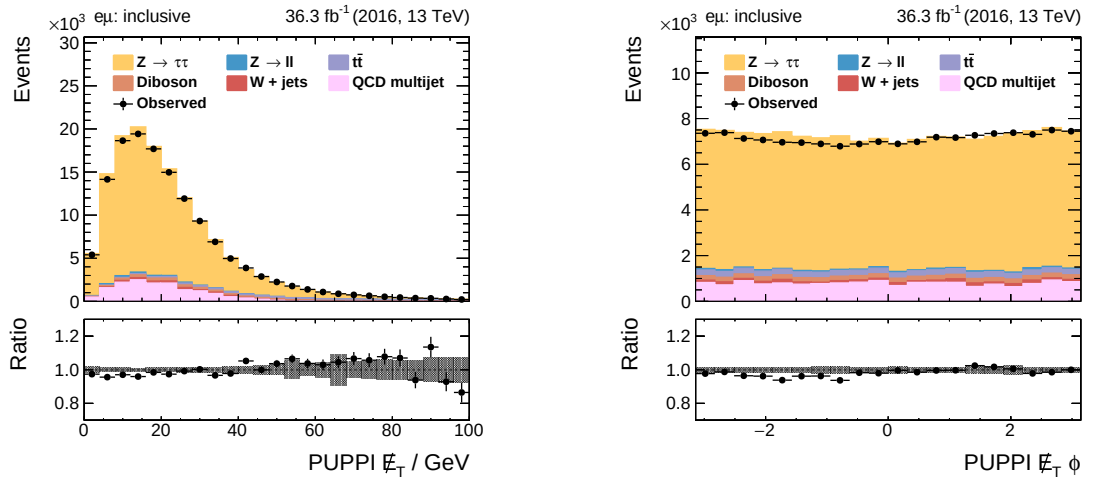

Figure B.23: Distributions of the transverse missing energy (*left*) and azimuthal angle of the transverse missing momentum (*right*) in $\tau_e\tau_\mu$ channel.

Appendix C

SVfit Performance

C.1 $\tau_\mu\tau_\mathrm{h}$ channel

C.1.1 τ^- positive helicity state

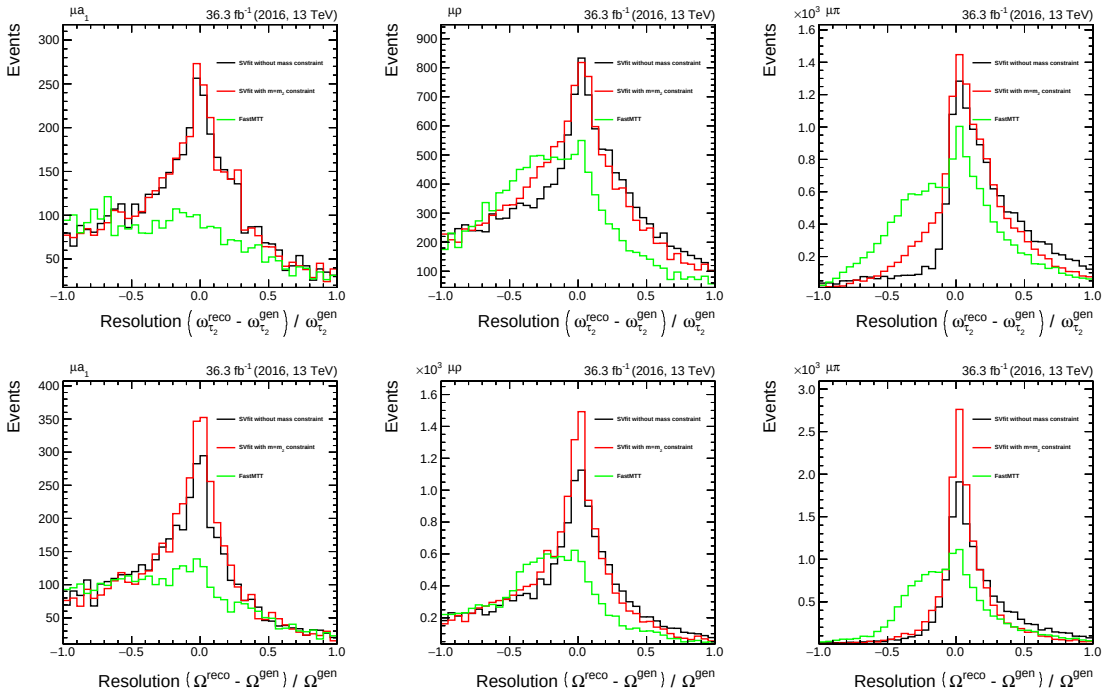

Figure C.1: Reconstruction resolution for optimal observables obtained based on $Z \to \tau_R^- \tau_L^+$ events in the $\tau_\mu\tau_\mathrm{h}$ channel.

C.1.2 τ^- negative helicity state

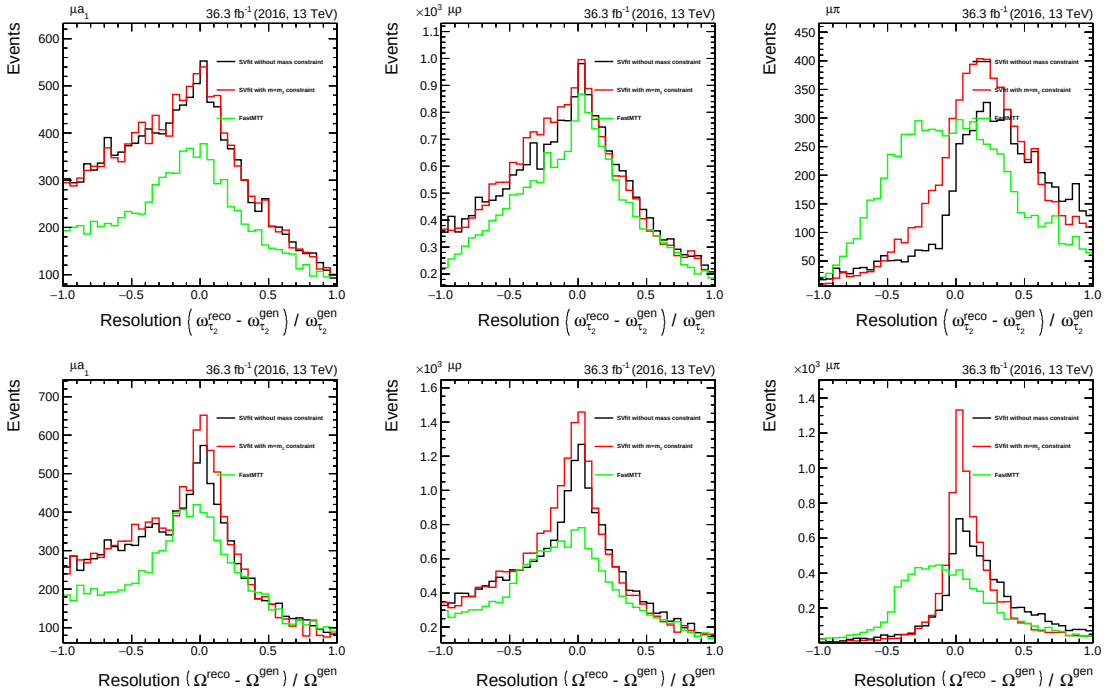

Figure C.2: Reconstruction resolution for optimal observables obtained based on $Z \to \tau_L^- \tau_R^+$ events in the $\tau_\mu\tau_\mathrm{h}$ channel.

C.2 $\tau_e\tau_h$ channel

C.2.1 Inclusive helicity state

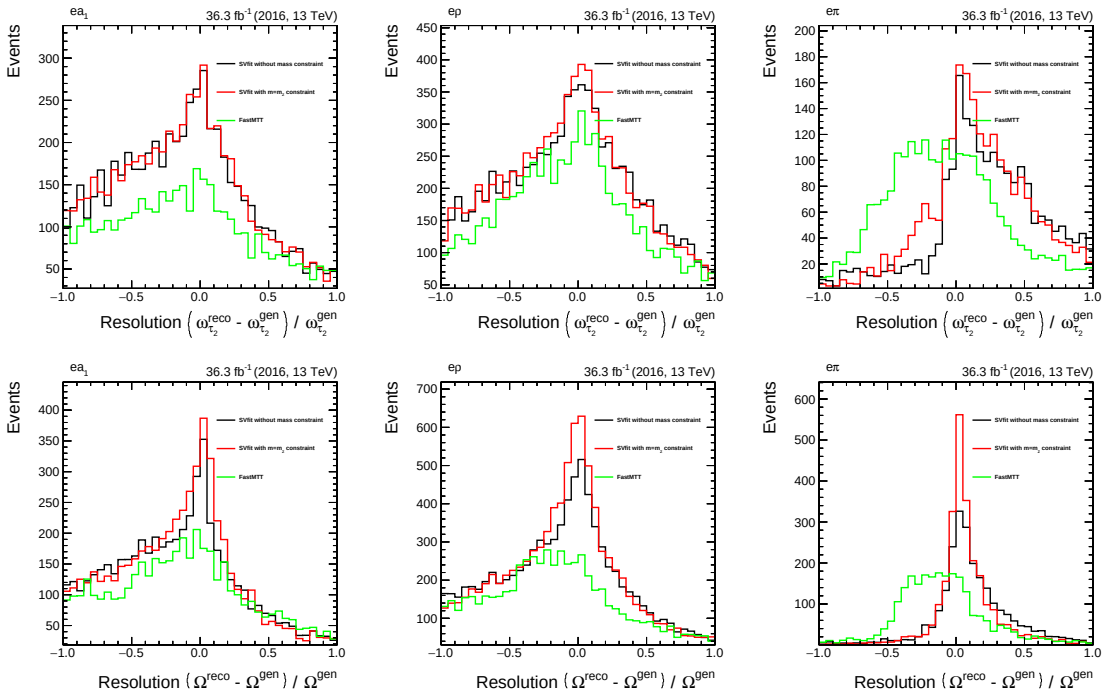

Figure C.3: Reconstruction resolution for optimal observables obtained based on $Z \to \tau\tau$ events in the $\tau_e\tau_h$ channel.

C.2.2 τ^- positive helicity state

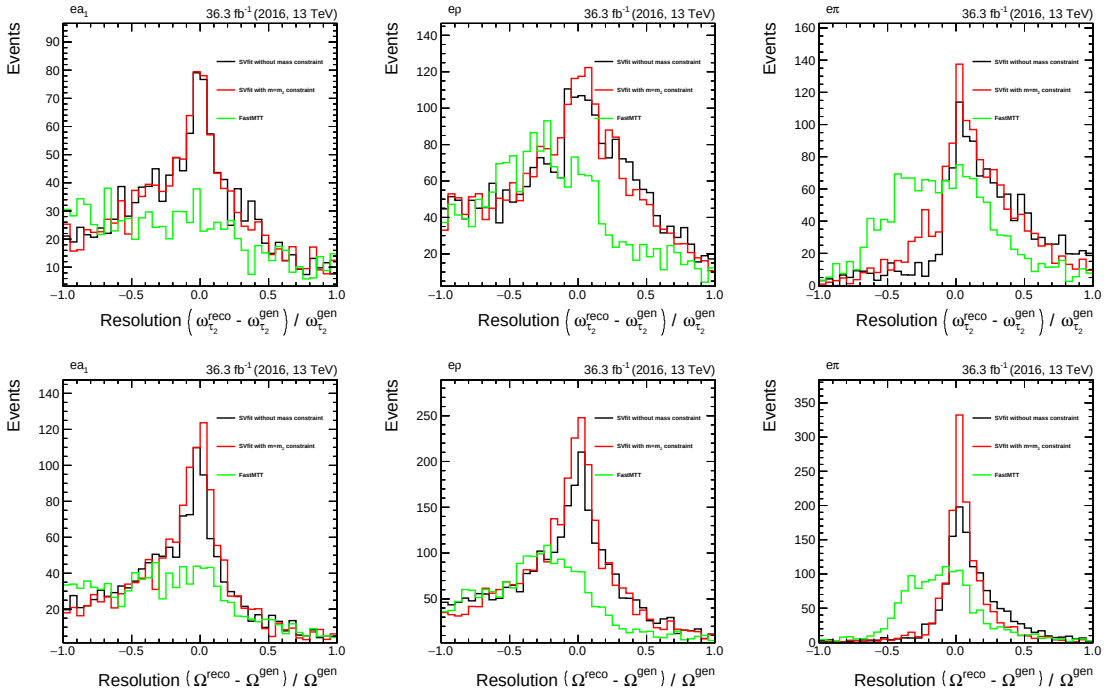

Figure C.4: Reconstruction resolution for optimal observables obtained based on $Z \to \tau_R^- \tau_L^+$ events in the $\tau_e\tau_h$ channel.

C.2.3 τ^- negative helicity state

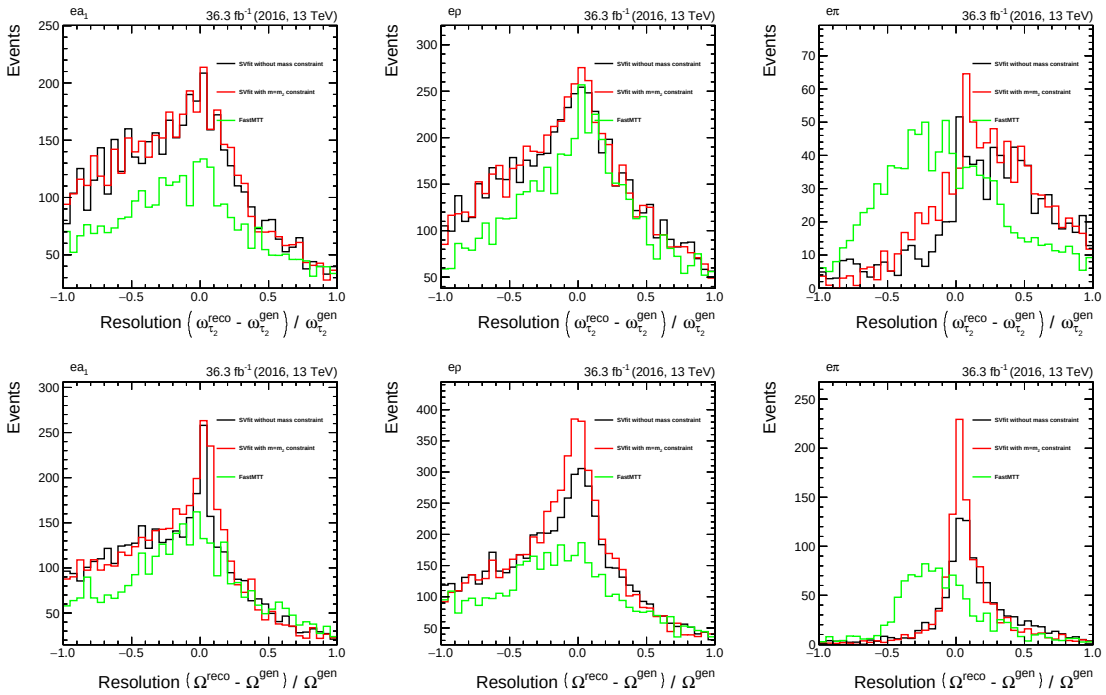

Figure C.5: Reconstruction resolution for optimal observables obtained based on $Z \to \tau_L^- \tau_R^+$ events in the $\tau_e\tau_h$ channel.

C.3 $\tau_h\tau_h$ channel

C.3.1 Inclusive helicity state

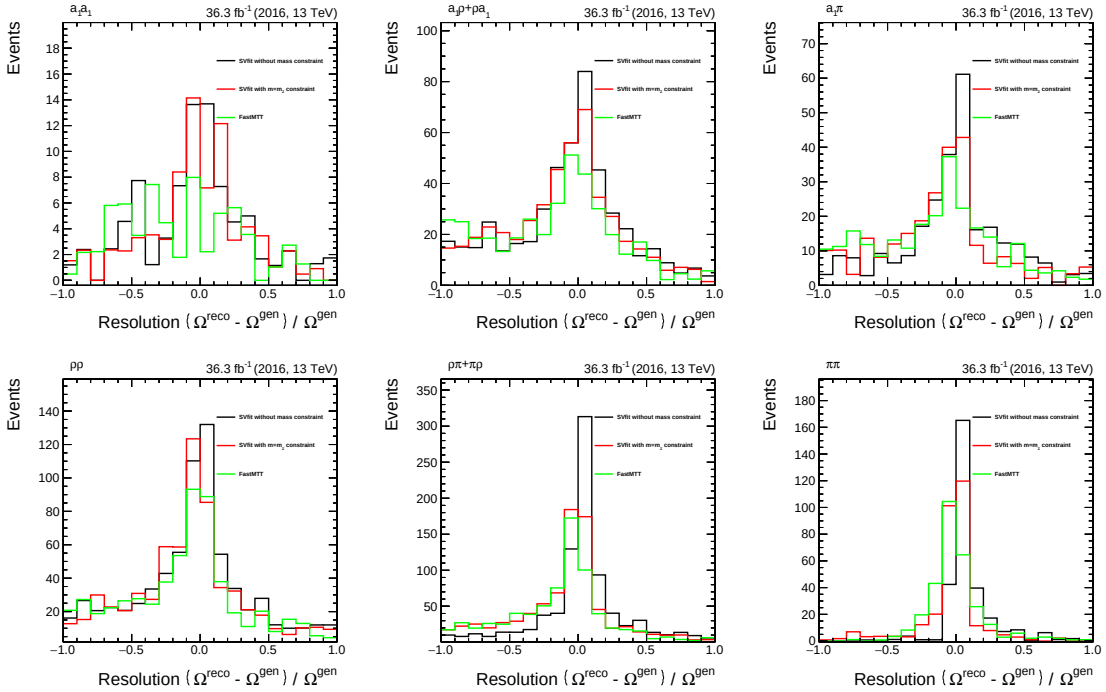

Figure C.6: Reconstruction resolution for optimal observables obtained based on $Z \to \tau\tau$ events in the $\tau_h\tau_h$ channel.

C.3.2 τ^- positive helicity state

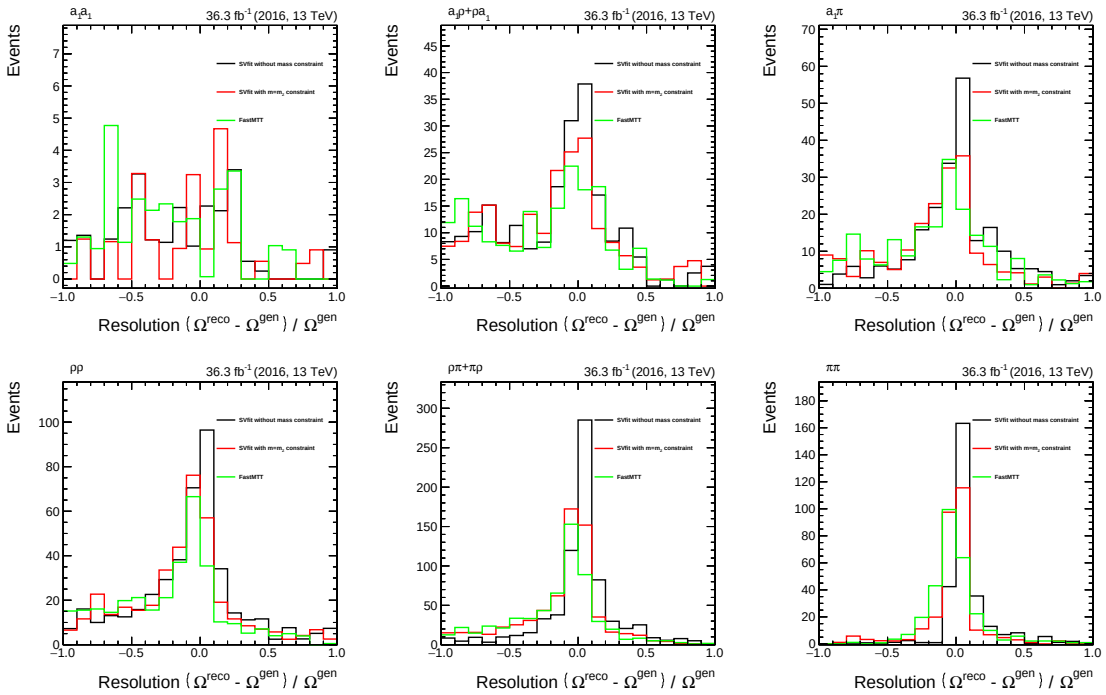

Figure C.7: Reconstruction resolution for optimal observables obtained based on $Z \to \tau_R^- \tau_L^+$ events in the $\tau_h\tau_h$ channel.

C.3.3 τ^- negative helicity state

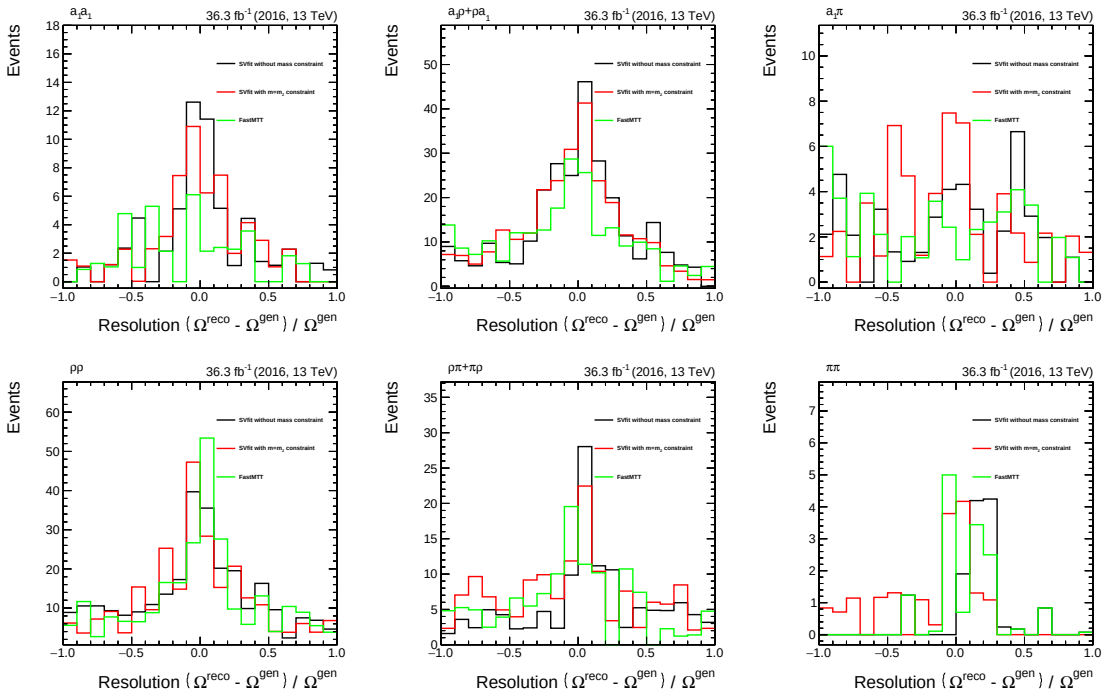

Figure C.8: Reconstruction resolution for optimal observables obtained based on $Z \to \tau_L^- \tau_R^+$ events in the $\tau_h\tau_h$ channel.

C.4 $\tau_e\tau_\mu$ channel

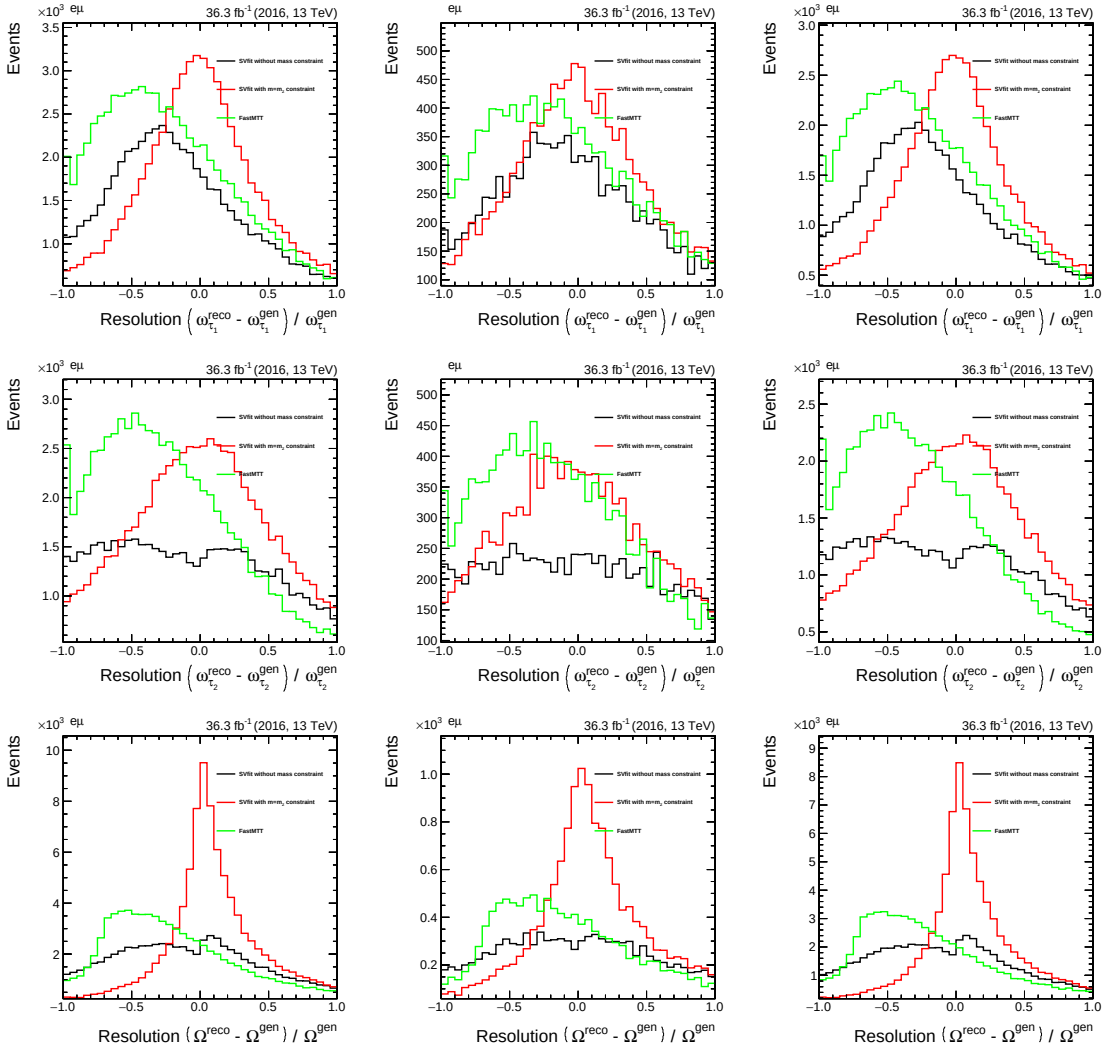

Figure C.9: Reconstruction resolution for optimal observables obtained based on $Z \to \tau\tau$ (*left*), $Z \to \tau_R^- \tau_L^+$ (*centre*) and $Z \to \tau_L^- \tau_R^+$ (*right*) events in the $\tau_e\tau_\mu$ channel. Shown are $\omega(e)$ [*top*], $\omega(\mu)$ [*centre*] and $\Omega(e,\mu)$ [*bottom*].

Bibliography

1. Heister, A. *et al.* Measurement of the tau polarization at LEP. *Eur. Phys. J.* **C20,** 401–430. arXiv: hep-ex/0104038 [hep-ex] (2001).
2. Abreu, P. *et al.* A Precise measurement of the tau polarization at LEP-1. *Eur. Phys. J.* **C14,** 585–611 (2000).
3. Abbiendi, G. *et al.* Precision neutral current asymmetry parameter measurements from the tau polarization at LEP. *Eur. Phys. J.* **C21,** 1–21. arXiv: hep-ex/0103045 [hep-ex] (2001).
4. Acciarri, M. *et al.* Measurement of tau polarization at LEP. *Phys. Lett.* **B429,** 387–398 (1998).
5. Aaboud, M. *et al.* Measurement of τ polarisation in $Z/\gamma^* \to \tau\tau$ decays in proton–proton collisions at $\sqrt{s} = 8$ TeV with the ATLAS detector. *Eur. Phys. J.* **C78,** 163. arXiv: 1709.03490 [hep-ex] (2018).
6. Sirunyan, A. M. *et al.* Particle-flow reconstruction and global event description with the CMS detector. *JINST* **12,** P10003. arXiv: 1706.04965 [physics.ins-det] (2017).
7. Khachatryan, V. *et al.* Reconstruction and identification of τ lepton decays to hadrons and ν_τ at CMS. *JINST* **11,** P01019. arXiv: 1510.07488 [physics.ins-det] (2016).
8. Davier, M., Duflot, L., Le Diberder, F. & Rouge, A. The Optimal method for the measurement of tau polarization. *Phys.Lett.B* **306,** 411–417 (1993).
9. Bianchini, L., Conway, J., Friis, E. K. & Veelken, C. Reconstruction of the Higgs mass in $H \to \tau\tau$ Events by Dynamical Likelihood techniques. *J. Phys. Conf. Ser.* **513,** 022035 (2014).
10. Aaboud, M. *et al.* Measurement of τ polarisation in $Z/\gamma^* \to \tau\tau$ decays in proton–proton collisions at $\sqrt{s} = 8$ TeV with the ATLAS detector. *Eur. Phys. J. C* **78,** 163. arXiv: 1709.03490 [hep-ex] (2018).
11. Cherepanov, V. *Measurement of the polarization of tau–leptons produced in Z decays at CMS and determination of the effective weak mixing angle* PhD thesis (Aachen, Tech. Hochsch., 2016).
12. Cherepanov, V. & Lohmann, W. *Methods for a measurement of τ polarization asymmetry in the decay $Z \to \tau\tau$ at LHC and determination of the effective weak mixing angle* 2018. arXiv: 1805.10552 [hep-ph].

13. *Precision Electroweak Measurements and Constraints on the Standard Model* Dec. 2010. arXiv: 1012.2367 [hep-ex].
14. Abreu, P. *et al.* A Precise measurement of the tau polarization at LEP-1. *Eur. Phys. J. C* **14,** 585–611 (2000).
15. Abbiendi, G. *et al.* Precision neutral current asymmetry parameter measurements from the tau polarization at LEP. *Eur. Phys. J. C* **21,** 1–21. arXiv: hep-ex/0103045 (2001).
16. Acciarri, M. *et al.* Measurement of tau polarization at LEP. *Phys. Lett. B* **429,** 387–398 (1998).
17. Schael, S. *et al.* Precision electroweak measurements on the Z resonance. *Phys. Rept.* **427,** 257–454. arXiv: hep-ex/0509008 (2006).
18. Chatrchyan, S. *et al.* Description and performance of track and primary-vertex reconstruction with the CMS tracker. *JINST* **9,** P10009. arXiv: 1405.6569 [physics.ins-det] (2014).
19. Khachatryan, V. *et al.* Performance of Electron Reconstruction and Selection with the CMS Detector in Proton-Proton Collisions at $\sqrt{s} = 8$ TeV. *JINST* **10,** P06005. arXiv: 1502.02701 [physics.ins-det] (2015).
20. Chatrchyan, S. *et al.* Performance of CMS muon reconstruction in *pp* collision events at $\sqrt{s} = 7$ TeV. *JINST* **7,** P10002. arXiv: 1206.4071 [physics.ins-det] (2012).
21. Khachatryan, V. *et al.* Performance of Photon Reconstruction and Identification with the CMS Detector in Proton-Proton Collisions at $\sqrt{s} = 8$ TeV. *JINST* **10,** P08010. arXiv: 1502.02702 [physics.ins-det] (2015).
22. Khachatryan, V. *et al.* The CMS trigger system. *JINST* **12,** P01020. arXiv: 1609.02366 [physics.ins-det] (2017).
23. Chatrchyan, S. *et al.* The CMS experiment at the CERN LHC. *JINST* **3,** S08004 (2008).
24. Aberle, O. e. a. *High-Luminosity Large Hadron Collider (HL-LHC): Technical design report* https://cds.cern.ch/record/2749422 (CERN, Geneva, 2020).
25. Contardo, D., Klute, M., Mans, J., Silvestris, L. & Butler, J. *Technical Proposal for the Phase-II Upgrade of the CMS Detector* tech. rep. Upgrade Project Leader Deputies: Lucia Silvestris (INFN-Bari), Jeremy Mans (University of Minnesota) Additional contacts: Lucia.Silvestris@cern.ch, Jeremy.Mans@cern.ch (Geneva, June 2015). https://cds.cern.ch/record/2020886.
26. *The Phase-2 Upgrade of the CMS Tracker* tech. rep. (CERN, Geneva, June 2017). https://cds.cern.ch/record/2272264.
27. *The Phase-2 Upgrade of the CMS Barrel Calorimeters* tech. rep. This is the final version, approved by the LHCC (CERN, Geneva, Sept. 2017). https://cds.cern.ch/record/2283187.
28. *The Phase-2 Upgrade of the CMS Muon Detectors* tech. rep. This is the final version, approved by the LHCC. (CERN, Geneva, Sept. 2017). https://cds.cern.ch/record/2283189.
29. collaboration, T. A. *The Phase-2 Upgrade of the CMS L1 Trigger Interim Technical Design Report* tech. rep. This is the CMS Interim TDR devoted to the upgrade of

the CMS L1 trigger in view of the HL-LHC running, as approved by the LHCC. (CERN, Geneva, Sept. 2017). https://cds.cern.ch/record/2283192.

30. *The Phase-2 Upgrade of the CMS DAQ Interim Technical Design Report* tech. rep. This is the CMS Interim TDR devoted to the upgrade of the CMS DAQ in view of the HL-LHC running, as approved by the LHCC. (CERN, Geneva, Sept. 2017). https://cds.cern.ch/record/2283193.
31. *The Phase-2 Upgrade of the CMS Endcap Calorimeter* tech. rep. (CERN, Geneva, Nov. 2017). https://cds.cern.ch/record/2293646.
32. CMS, C. *A MIP Timing Detector for the CMS Phase-2 Upgrade* tech. rep. (CERN, Geneva, Mar. 2019). https://cds.cern.ch/record/2667167.
33. *The Phase-2 Upgrade of the CMS Level-1 Trigger* tech. rep. Final version (CERN, Geneva, Apr. 2020). https://cds.cern.ch/record/2714892.
34. Jansen, H. *et al.* Performance of the EUDET-type beam telescopes. *EPJ Tech. Instrum.* **3,** 7. arXiv: 1603.09669 [physics.ins-det] (2016).
35. Bouquerel, E. *et al.* Design and commissioning of the first two CYRCé extension beamlines. *Nucl. Instrum. Meth. A* **1024,** 166034. arXiv: 2201.10888 [physics.acc-ph] (2022).
36. Deelen, N. *Characterizing detector modules for the Upgrade of the Silicon Tracker of the Compact Muon Solenoid experiment* Presented 18 Oct 2019 (2019). https://cds.cern.ch/record/2707148.
37. Spannagel, S., Meier, B. & Perrey, H. C. *The pxarCore Library - Technical Documentation, Reference Manual, and Sample Applications* tech. rep. (CERN, Geneva, Oct. 2015). https://cds.cern.ch/record/2137512.
38. Langenegger, U. *pXar (pixel Xpert analysis & readout)* version 4.7. Feb. 2021. https://github.com/psi46/pxar/blob/master/main.pdf.
39. Grimault, C. *Reference telescope for detector tests at the 25 MeV proton cyclotron CYRCé at Strasbourg* 8th Beam Telescopes and Test Beams Workshop. 2020. https://indico.cern.ch/event/813822/.
40. Ullrich, T. & Xu, Z. *Treatment of Errors in Efficiency Calculations* 2007. https://arxiv.org/abs/physics/0701199.
41. Eberhard, P. H. *et al. THE tau POLARIZATION MEASUREMENT AT LEP* in *LEP Physics Workshop Geneva, Switzerland, February 20, 1989* (1989), 235–266.
42. Sirunyan, A. M. *et al.* Precision luminosity measurement in proton-proton collisions at $\sqrt{s} = 13$ TeV in 2015 and 2016 at CMS. *Eur. Phys. J. C* **81,** 800. arXiv: 2104.01927 [hep-ex] (2021).
43. https://twiki.cern.ch/twiki/bin/view/CMS/SWGuideMuonIdRun2.
44. https://twiki.cern.ch/twiki/bin/view/CMS/MultivariateElectronIdentificationRun2.
45. Cacciari, M., Salam, G. P. & Soyez, G. The Anti-k(t) jet clustering algorithm. *JHEP* **04,** 063. arXiv: 0802.1189 [hep-ph] (2008).
46. Identification of hadronic tau decay channels using multivariate analysis (MVA decay mode). https://cds.cern.ch/record/2727092 (July 2020).
47. Sirunyan, A. M. *et al. Identification of hadronic tau lepton decays using a deep neural network* Submitted to *JINST*. 2022. arXiv: 2201.08458 [hep-ex].

48. Sirunyan, A. M. *et al.* Identification of heavy-flavour jets with the CMS detector in pp collisions at 13 TeV. *JINST* **13,** P05011. arXiv: 1712.07158 [physics.ins-det] (2018).
49. https://twiki.cern.ch/twiki/bin/viewauth/CMS/BtagRecommendation2016Legacy.
50. Sirunyan, A. M. *et al.* Pileup mitigation at CMS in 13 TeV data. *JINST* **15,** P09018. arXiv: 2003.00503 [hep-ex] (2020).
51. https://twiki.cern.ch/twiki/bin/view/CMS/MissingETOptionalFiltersRun2.
52. Jang, D. *Search for MSSM Higgs decaying to τ pairs in $p\bar{p}$ collision at $\sqrt{s}$ = 1.96 TeV at CDF* PhD thesis (Rutgers U., Piscataway, 2006).
53. Michal Bluj, Guillaume Bourgatte, Andrea Cardini, David Colling, Albert Dow, Mate Farkas, Oleg Filatov, Elisabetta Gallo, Ulrich Goerlach, Clément Grimault, MohammadHassan Hassanshahi, Alexis Kalogeropoulos, Oliver Kuntze, Anne-Catherine Le Bihan, Teresa Lenz, Vinay Krishna, Mareike Meyer, Thomas Mueller, Arun Nayak, Alexander Nikitenko, Alexei Raspereiza, Merijn van de Klundert, Diwakar Vats, Yiwen Wen, Lucas Wiens, Daniel Winterbottom, and Alexander Zotz. *Analysis of the Higgs CP state in τ decays* tech. rep. CMS-AN-19-192 (2019). https://cms.cern.ch/iCMS/jsp/db_notes/noteInfo.jsp?cmsnoteid=CMS%5C%20AN-2019/192.
54. Akhmetshin, A. *et al. Search for the standard model Higgs boson decaying to a pair of tau leptons in 2016 data* tech. rep. CMS-AN-16-355 (2018). http://cms.cern.ch/iCMS/jsp/db_notes/noteInfo.jsp?cmsnoteid=CMS%5C%20AN-2016/355.
55. *Electron and muon scale factor measurements for Higgs to tau tauanalyses* tech. rep. CMS-AN-20-014 (2020). https://cms.cern.ch/iCMS/jsp/db_notes/noteInfo.jsp?cmsnoteid=CMS%5C%20AN-2020/014.
56. Hagiwara, K., Martin, A. D. & Zeppenfeld, D. Tau Polarization Measurements at LEP and SLC. *Phys. Lett. B* **235,** 198–202 (1990).
57. Rouge, A. *Tau decays as polarization analysers* in *Workshop on Tau Lepton Physics* (May 1991), 213–222.
58. Tsai, Y.-S. Decay Correlations of Heavy Leptons in $e^+e^- \to$ Lepton+ Lepton-. *Phys. Rev.* **D4.** [Erratum: Phys. Rev.D13,771(1976)], 2821 (1971).
59. Jadach, S., Was, Z., Decker, R. & Kuhn, J. H. The tau decay library TAUOLA: Version 2.4. *Comput. Phys. Commun.* **76,** 361–380 (1993).
60. Asner, D. M. *et al.* Hadronic structure in the decay tau- —> tau-neutrino pi- pi0 pi0 and the sign of the tau-neutrino helicity. *Phys. Rev.* **D61,** 012002. arXiv: hep-ex/9902022 [hep-ex] (2000).
61. Sjöstrand, T. *et al.* An Introduction to PYTHIA 8.2. *Comput. Phys. Commun.* **191,** 159–177. arXiv: 1410.3012 [hep-ph] (2015).
62. Alemany, R., Rius, N., Bernabeu, J., Gomez-Cadenas, J. J. & Pich, A. Tau polarization at the Z peak from the acollinearity between both tau decay products. *Nucl. Phys.* **B379,** 3–23 (1992).
63. Przedzinski, T., Richter-Was, E. & Was, Z. Documentation of TauSpinner algorithms – program for simulating spin effects in tau-lepton production at LHC. arXiv: 1802.05459 [hep-ph] (2018).

64. Cowan, G., Cranmer, K., Gross, E. & Vitells, O. Asymptotic formulae for likelihood-based tests of new physics. *Eur. Phys. J. C* **71.** [Erratum: Eur.Phys.J.C 73, 2501 (2013)], 1554. arXiv: 1007.1727 [physics.data-an] (2011).
65. https://twiki.cern.ch/twiki/bin/viewauth/CMS/TWikiLUM.
66. The CMS HTauTau group. *Theoretical Uncertainties on Higgs Production via VBF and Gluon Fusion Processes for the $H \to \tau\tau$ Analysis at $\sqrt{s} = 13$ TeV* tech. rep. CMS-AN-16-387 (2016). http://cms.cern.ch/iCMS/jsp/db_notes/noteInfo.jsp?cmsnoteid=CMS%5C%20AN-2016/387.
67. Robert D. Cousins. *Generalization of Chisquare Goodness-of-Fit Test for Binned Data Using Saturated Models, with Application to Histograms* in (2013).
68. Olive, K. A. *et al.* Review of Particle Physics. *Chin. Phys.* **C38,** 090001 (2014).
69. Decamp, D. *et al.* Measurement of the polarization of tau leptons produced in Z decays. *Phys. Lett.* **B265,** 430–444 (1991).
70. Abreu, P. *et al.* A Study of the decays of tau leptons produced on the Z resonance at LEP. *Z. Phys.* **C55,** 555–568 (1992).
71. Alexander, G. *et al.* Measurement of branching ratios and tau polarization from $\tau \to e$ neutrino anti-neutrino , $\tau \to \mu$ neutrino anti-neutrino, and $\tau \to \pi(K)$ neutrino decays at LEP. *Phys. Lett.* **B266,** 201–217 (1991).
72. Tanabashi, M. e. a. Review of Particle Physics. *Phys.Rev.* **D98,** 030001 (2018).
73. Meier, F., Meier, B. & Kästli, H.-C. *PIXEL DTB Testboard for Readout Chips Manual* 2016. https://twiki.cern.ch/twiki/pub/CMS/PixelDTB/DTBmanual.pdf.

Clément Grimault

Mesure de paramètres électrofaibles dans les désintégrations du boson Z en leptons tau et tests de détecteurs pour la jouvence du trajectographe de CMS pour le LHC à haute luminosité

Résumé

Cette thèse se concentre sur la mesure de la polarisation des leptons tau provenant de la désintégration du boson Z. Elle utilise les données de collision proton-proton à une énergie de $\sqrt{s} = 13$ TeV collectées par le détecteur CMS auprès du LHC en 2016, pour une luminosité intégrée de 36,3 fb^{-1}. Cette étude est la première à étendre la mesure de ce paramètre à l'ensemble des canaux de désintégration hadronique du tau qui peuvent être reconstruits par le détecteur CMS.

L'analyse utilise les distributions angulaires entre les produits de désintégration visibles du tau pour caractériser l'état d'hélicité du tau. Pour chaque mode de désintégration du tau, une variable optimale est déterminée, et une attention particulière est accordée à la migration entre les modes de désintégration, qui est la principale source d'erreur systématique de cette analyse. Une étude permet d'estimer l'erreur systématique associée à la modélisation de ces migrations.

Cette thèse fournit également une valeur de l'angle de mélange électrofaible en traduisant la valeur de la polarisation mesurée via des courbes de calibration.

Enfin, elle présente le mini-télescope CHROMini, faisant partie d'un nouveau dispositif expérimental de tests installé auprès de la ligne CMS du cyclotron CYRCé à l'IPHC. Ce dispositif permettra d'évaluer les performances des futurs détecteurs du trajectographe de CMS prévus pour la jouvence du LHC à haute luminosité, avec des taux d'acquisition et d'occupation élevés.

Mots-clé : physique des particules, polarisation, hélicité, angle de mélange électrofaible, lepton tau, détecteur CMS, télescope CHROMini, trajectographe, LHC, haute luminosité.

Abstract

This thesis focuses on the measurement of tau lepton polarisation from Z boson decay. The analysis is based on proton-proton collision data at a center-of-mass energy of $\sqrt{s} = 13$ TeV collected by the CMS detector at the LHC in 2016, corresponding to an integrated luminosity of 36.3 fb^{-1}. This study is the first to extend the measurement of this parameter to all hadronic tau decay channels that can be reconstructed by the CMS detector.

The analysis uses angular distributions between the visible tau decay products to characterise the tau helicity state. For each tau decay mode, an optimal variable is determined, and particular attention is given to the migration between decay modes, which is the main source of systematic error in this analysis. A study estimates the systematic uncertainty associated with the modeling of these migrations.

This thesis also provides a value for the electroweak mixing angle by converting the measured polarisation value using calibration curves.

Finally, it presents the CHROMini mini-telescope, part of a new experimental test beam facility installed on the the CMS beamline at the CYRCé cyclotron at IPHC. This device will evaluate the performance of future CMS tracker detectors for the LHC high-luminosity upgrade, with high acquisition and occupancy rates.

Keywords: particle physics, polarisation, helicity, electroweak mixing angle, tau lepton, CMS detector, CHROMini telescope, tracker, LHC, high-luminosity.